Benemérita Universidad Autónoma de Puebla

FACULTAD DE CIENCIAS FÍSICO MATEMÁTICAS

Posgrado en Física Aplicada

A cellular model for the mechanistic simulation of biological response to radiation damage

Tesis

Para obtener el título de Doctor en Ciencias

Presenta
M.C. Omar Rodrigo García García.

Directores de tesis:

Dr. Eduardo Moreno Barbosa.
Facultad de Ciencias Físico Matemáticas, Benemérita Universidad Autónoma de Puebla.

Dr. José Asunción Ramos Méndez
Department of Radiation Oncology, University of California San Francisco.

Puebla Pue. Mayo 2025

Titulo: A cellular model for the mechanistic simulation of biological response to radiation damage

Candidato a Doctor: M.C. Omar Rodrigo García García

Comité evaluador:

_____
Dr. Benito De Celis Alonso
Presidente

_____
Dr. Juan Francisco Rivas Silva
Secretario

_____
Dr. Jose Miguel Hernández López
Vocal

_____
Dra. Carmen Villagrasa
Vocal externo

_____
Dr. Yann Perrot
Vocal externo

_____
Dr. Ramon Catalán Ortiz
Suplente

_____
Dr. José Asunción Ramos Méndez
Asesor

_____
Dr. Eduardo Moreno Barbosa
Asesor

Resumen

Este trabajo de tesis está enfocado en el estudio de las múltiples etapas de la respuesta biológica al daño producido por radiación. Para ello, se empleó el uso combinado de códigos especializados de simulación computacional basados en Monte Carlo para manejar los diferentes aspectos del fenómeno. Dos proyectos fueron desarrollados: El primero, un modelo de cinética química para la respuesta temprana del medio celular a la radiación centrado en la competencia de los antioxidantes, que reparan químicamente las biomoléculas dañadas, y el oxígeno, que fija el daño, para estudiar la producción de radicales biológicos y los efectos de la tasa de dosis, con dos condiciones correspondientes a una irradiación convencional y a una tasa ultra alta de dosis conocida como irradiación FLASH, y el nivel de oxigenación, con dos condiciones correspondientes a la hipoxia y a la normoxia. El segundo proyecto consistió en el desarrollo de una plataforma computacional multiescalar *todo en uno* para la simulación de la irradiación de una población de células en las que se contempló la producción de lesiones al ADN a partir de la dosis depositada en cada núcleo celular, el proceso de reparación del ADN, la generación de lesiones fatales como producto secundario inevitable de dicha reparación, una red de regulación proteínica centrada en la acción de la proteína p53 que media entre el arresto del ciclo celular, dando tiempo a las células para repararse y así promover su supervivencia, y el procesos de *apoptosis* o muerte programada para aquellas células demasiado dañadas. Los resultados de este proyecto fueron validados con datos experimentales para las curvas de supervivencia de cultivos de células PC-3 de cáncer de próstata bajo una irradiación de rayos X producidos por un LINAC de 4MV.

Dedicatoria

A mis padres, Elsa García Balbuena y Alfonso García Lara, por dotarme con el regalo de la vida y a través de su constante apoyo y enseñanza, de la sabiduría para vivirla de la manera más grata. A mi hermano Héctor que ha sido mi compañero de aventuras todos estos largos años y a toda mi familia, pues me han brindado un hogar inigualablemente feliz, sin ellos nada de esto hubiera sido posible.

A todos mis amigos que me han acompañado en este maratónico viaje, sobre todo a Mauro y William, pues entramos juntos e ingenuos al posgrado sin saber de los retos que nos depararía la academia y por las extrañas coincidencias del destino terminaremos juntos esta larga carrera. Todos ellos me han acompañado en los momentos mas dichosos de la vida y no me han abandonado en los más difíciles.

A mi alma mater la Benemérita Universidad Autónoma de Puebla, que por más de una década ha sido un segundo hogar, y a sus profesores que con un esfuerzo incansable me dieron la formación necesaria para llevar a cabo este logro. De entre ellos los mas importantes han sido mis asesores el Dr. José Ramos Méndez y el Dr. Eduardo Moreno Barbosa, pues su labor no se ha limitado a dirigir este trabajo de tesis, sino a formarme como ser humano e inculcarme un sentido de ética profesional y amor a la ciencia, se lo debo todo a ellos.

De manera más general quiero agradecer a la universidad publica pues es una de las grandes victorias sociales que nos permite a un numero incontable de estudiantes cumplir con nuestros sueños.

Este trabajo marca el punto final de la etapa más importante de mi vida, pero también el punto de partida de la que viene. Esta es mi meta ultima como estudiante, pero apenas el primer paso de lo que espero sea una larga trayectoria profesional y académica. Una vez mas quiero agradecer a todos los involucrados por su invaluable apoyo y a la vida llena de aventuras, logros y goces que afortunadamente me ha tocado tener.

Content

1.Introduction

1.1. Cancer: Worldwide statistics and the situation in Mexico

Cancer is a group of illnesses that can affect almost every organ and tissue of the body. It is characterized by the uncontrolled growth of anomalous cells that cross their normal limits, invading healthy neighborhood tissues or even far-away organs, through a process known as metastasis, which causes most of the cancer-related deaths [World Health Organization (2024)].

Cancer is one of the afflictions that causes more deaths worldwide. According to the World Health Organization (WHO), this is the first or second cause of death in adults younger than 70 years in most countries. Globally, the number of cases is growing rapidly; this can be caused by the decrease in mortality of other types of illness, like cardiovascular diseases, as well as the improvement in lifestyle and socioeconomic conditions of developing countries. These reasons are also associated with population and life expectancy growth, and consequently, a larger elderly population, which is more vulnerable to cancer. *The Human Developing Index* (HDI), an indicator of the economic development of a country, is correlated with the cancer incidence as shown in Figure 1.1 [Sung H., et al (2021)].

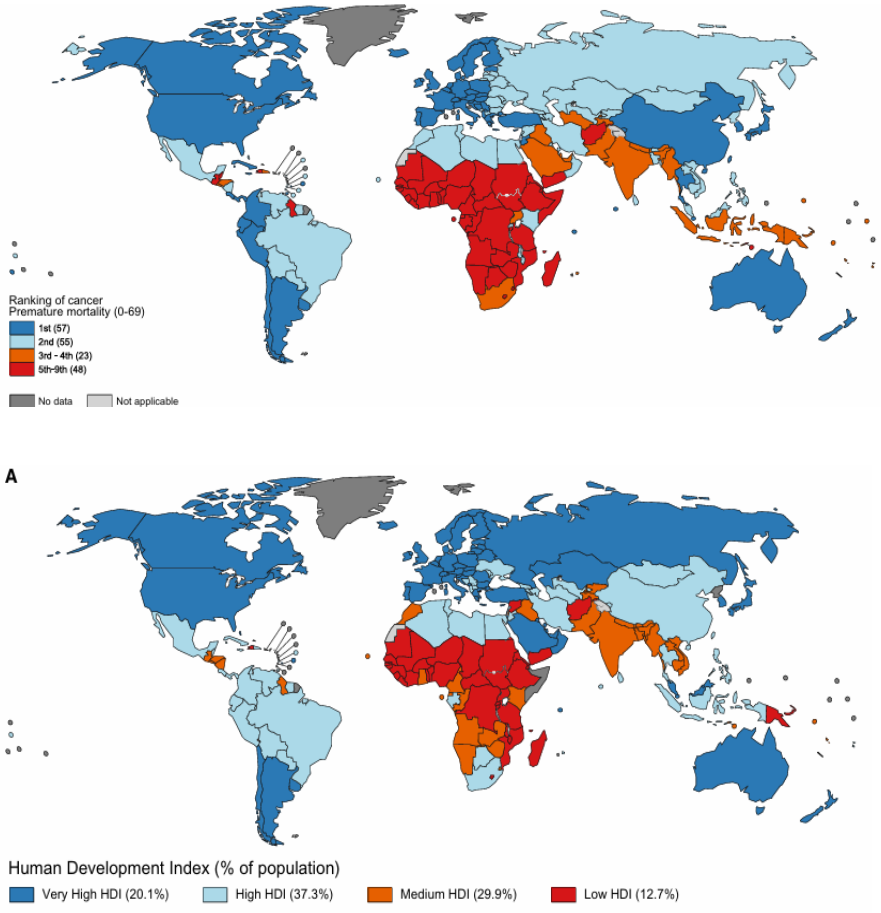

Figure 1.1. Correlation between cancer incidence increasing and the Human Developing Index (HDI). Image taken from [Sung H, et al (2021)]

According to the Global Observatory of Cancer (GLOBOCAN) it is estimated that 19.3 million new cases and around 10 million deaths related to cancer occurred in 2020 [Sung H, et al (2021)]. Breast cancer is the largest cancer diagnosed worldwide (11.7% of the total cases), followed by lung cancer (11.4%), colorectal (10.0%) prostate (7.3%), and stomach (5.6%). However, lung cancer has the largest fraction of the total deaths (18.0%) followed by colorectal (9.4%), liver (8.3%), and stomach (8.3%). For men, the most frequent and deadliest type is lung cancer while for women it is breast cancer, as shown in Figure 1.2.

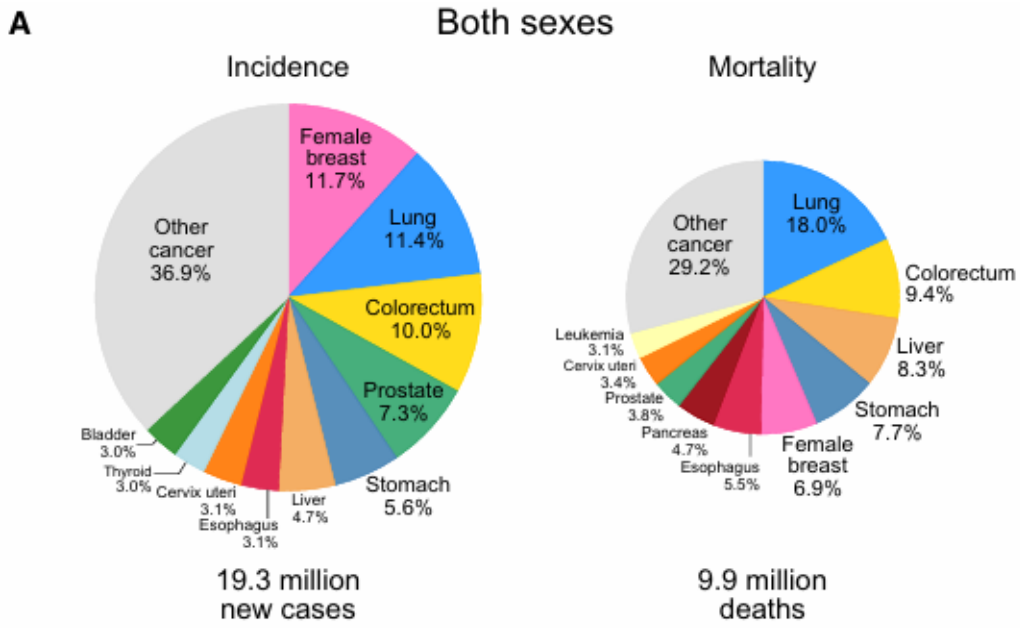

Figure 1.2. cancer incidence and mortality for both sexes. Image taken from [Sung H, et al (2021)].

It is calculated that by 2040 more than 30 million annual cases will be registered and that the least developed nations will be the most affected [Murthy S. S., et al (2024)]. These numbers are attributed to the health systems of those countries which are not prepared to handle the increasing number of patients and do not have the equipment to treat this disease effectively and timely. In contrast, in wealthy countries with more developed health systems the survival for many types of cancer has improved because of the quality of early diagnosis and treatments [World Health Organization (2024)].

1.2. National cancer situation

Mexico is a developing nation with an emerging economy. During 2021, 1.1 million deaths were reported, among them 8% (around 90 thousand) were caused by malignant tumors. According to the Instituto Nacional de Estadística y Geografía (INEGI), cancer related deaths have risen from 6.09 to 7.06 for every 10 thousand people from 2010 to 2021. The most affected entities were Mexico City, Colima, Veracruz and Sonora, while Chihuahua and Morelos where the states with more deaths by tumors [INEGI (2023)], Figure 1.3.

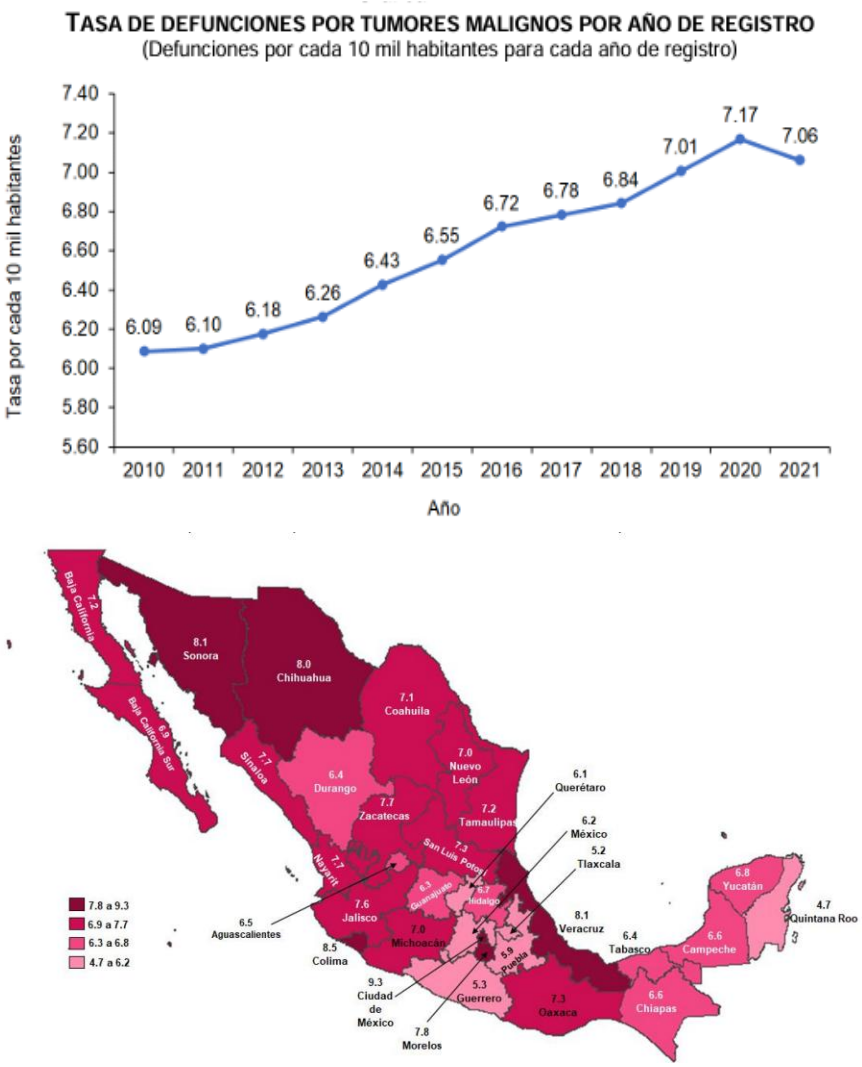

Figure 1.3. Number of cancer related deaths per 10 thousand habitants in Mexico between 2010-2021 and the map showing this quantity per state. Image taken from [INEGI (2023)].

The most common type of cancer depends on sex and age group. Among the youngest portion of the population (between 0-29 years) leukemia is the main cancer related death. From this point the main illness are more specific: for men between 30-59 years the principal type of cancer is colorectal (0.60 deaths per 10 thousand habitants) followed by stomach cancer (0.47). For women in the same group of age the main types are breast and cervix cancer (1.52 and 0.88 respectively).

On the elderly adult group, over 60 years old, the most common type of cancer in men is prostate followed by lung with an incidence of 10.59 and 4.44 per 10 thousand habitants respectively. For women among the same age group, the breast cancer is the most common with 4.18 deaths per 10 thousand habitants, followed by liver and intrahepatic bile ducts malign tumors with 3.29 deaths per 10 thousand habitants [INEGI (2023)].

1.2.1 Radiotherapy infrastructure

It is calculated that in Mexico and Central America, a region formed by 8 countries and 177 million habitants, only 20 radiotherapy facilities with 207 treatment machines exist. These are divided into

171 LINAC and 36 radionuclide teletherapy machines. This equipment is only distributed between 7 of the 8 countries of the region and represents a coverture of 1.167 medical equipment units per million habitants. In contrast, in North America there exists a coverture of 10.751 medical equipment units per million habitants [Abdel-Wahab, M., et al, (2021)].

1.3 Cancer treatment and radiotherapy

There are distinct treatments for this group of illnesses and the most adequate depends on the type, location, growth stage and severity of the tumor. A broad classification of these treatments is in two general categories: *conventional and modern* [Debela D.T., et al (2021)].

Surgery, radiation and chemo therapies are currently the most common treatments, classified as *conventional* therapies. These therapies have a long development history to minimize the risk associated with their use and maximize their effectiveness. For example, chemical substances applied to cancer treatment started in the decade of 1930 with the use of alkylating agents. Its purpose is to supply the drug in a localized way, avoiding its absorption on normal tissue [Arruebo M., et al (2011)]. In the same way, the aim of radiotherapy is to maximize the dose deposited by radiation on cancerous cells and minimize the exposure to healthy tissue, that inevitably exist on the tumor proximity or on the path of radiation [Baskar R., et al (2012)].

The most effective strategy of conventional treatment is the combination of surgery with either radiation or chemotherapy [Debela, D. T., et al (2021)]. In particular, the combined use of surgical intervention with radiotherapy was the basis for treating solid tumors in the 60s [Arruebo M., et al (2011)]. The purpose of radiation applied before surgery (*neoadjuvant therapy*) is the reduction of the tumor size, while the use after surgery (*adjuvant therapy*) focuses on destroying all the remaining malignant cell clusters, too small to be surgically removed [Baskar R., et al. (2012)].

In the other hand, it is calculated that about half of worldwide medical studies are focused on developing novel cancer treatments. These efforts have produced modern therapies, like the so-called targeted therapies. Examples of target therapies are the use of steam cells for the normal tissue recovery after treatment, the use of drugs that interrupt biological functions of specific malignant cell, and the application of specialized antibodies that only attack cancerous tissue while sparing normal cells with immunotherapy techniques [Debela D.T., et al (2021)].

Modern therapies also include the application of conventional techniques in innovative ways. For example, the combined use of radiotherapy with hyperthermia, which is the local increase of temperature of the tumor to increase the radiosensitivity in the affected tissue [Arruebo M., et al (2011), Debela D.T., et al (2021)], or the development of new dose-delivery fractionation schemes. One of the recent proposals for cancer treatment is the use of ultra-high dose rate radiation (FLASH). FLASH radiotherapy consists of delivering a high radiation dose in a pulse of short duration (>40 Gy/s). It has been rediscovered that delivering the dose in ultra-high dose rate regime spare normal tissue while the therapeutic effect on malignant tissue is maintained [Favaudon V., et al (2014), Hughes J.R & Parsons J.L. (2020)].

Approximately half of all cancer diagnoses will be exposed to at least one round of radiation therapy at some point in their treatment [Abdel-Wahab, M., et al, (2021)]. This percentage increases to about 87% for breast cancer patients. Despite the inevitable side effects of radiation damage to healthy cells, tissue and organs, this evidence indicate that radiation is still one of the main therapies against

cancer with a proven high index of effectiveness per cost, taking as an example the treatment of rectal cancer has an estimated $133495 cost per quality-adjusted life-year in the U.S. [Raldow A.C., et al (2019)]. As a result, there are ongoing global efforts to promote their therapeutic use, reducing its side effects and improving its efficacy [Abdel-Wahab, M., et al, (2021), Debela D.T., et al (2021)].

For this purpose, it is essential to understand the effect of radiation on living matter and the mechanisms that drive the biological consequences of irradiation. This understanding allows better and more effective radiation treatments to handle the increased incidence of cancer worldwide, especially in developing countries with limited capacity to respond in terms of infrastructure, qualified personnel and access to resources to face this contemporary challenge [Prager G.W., et al (2018)].

1.4 Radiobiological effect

Radiation is a physical agent used to destroy cancerous cells. The type of radiation employed is known as *ionizing radiation*, which means that its interaction with the matter that it traverses generates charged particles or *ions,* which deposit their energy along its path [Baskar R., et al (2012)]. The critical target for the biological effect of radiation is the genetic material within the cell's nucleus [Casas F., et al (2008), Hall E.J. & Giaccia A.J. (2012)].

However, the formation of biological damage from the physical-chemical interaction of radiation and the mechanism of cellular response to damage occurs in a series of stages on different temporal and spatial scales [Azzam E.I., et al (2012)]. The first stage is physical, and consists on the interaction of particles with water and other molecules that constitute the biological environment, including the genetic material. This physical stage occurs at the nanometric scale and last between femtoseconds to picoseconds in which incident particles ionize or excite the components of the DNA and produce "direct damage". The resulting ionized and excited water molecules can subsequently dissociate into free radicals that can react among them, with the environment and with DNA, breaking its hydrogen bond and causing "indirect damage". This is called the physical-chemical and chemical stages that last between a few picoseconds until around a few nanoseconds after irradiation [Michaels H.B. & Hunt J.W. (1973), Von Sontang C. (2006), Hall E.J. & Giaccia A.J. (2012)].

Cells have different mechanisms for defense and damage response that involve the action of biomolecules naturally present in their environment. Simple molecules such as antioxidants are early responders to radiation, and act in the first seconds to minutes after irradiation. They can intercept free radicals before they can cause further damage, function as hydrogen donors to restore the damaged biomolecules or stop the damage propagation chain to other intact molecules. At the same time the products of this early radiation response are a source of cellular stress that can affect other biological processes and have lethal consequences for the affected cells [Wardman P. (1999), Gebicki J. M. et al (2010)].

Other larger, more complex biomolecules, such as proteins, are involved actively in the biological response to radiation damage that extends to prolonged periods of time in the order of hours to days. Specialized enzymes take part on the repair process of DNA breaks [Hall E.J. & Giaccia A.J. (2012), Chang H.H.Y., et al (2017), Scully R., et al (2019)] while complex protein networks act on parallel to regulate biological functions of the cells such as the cell cycle arrest to promote survival, or programed death for cells that are beyond repair [Wu M., et al (2017), Shibata A. & Jeggo P.A.

(2021), Wang P., et al. (2023]. Figure 1.4 depicts schematically the spatial-temporal distribution of each individual stage.

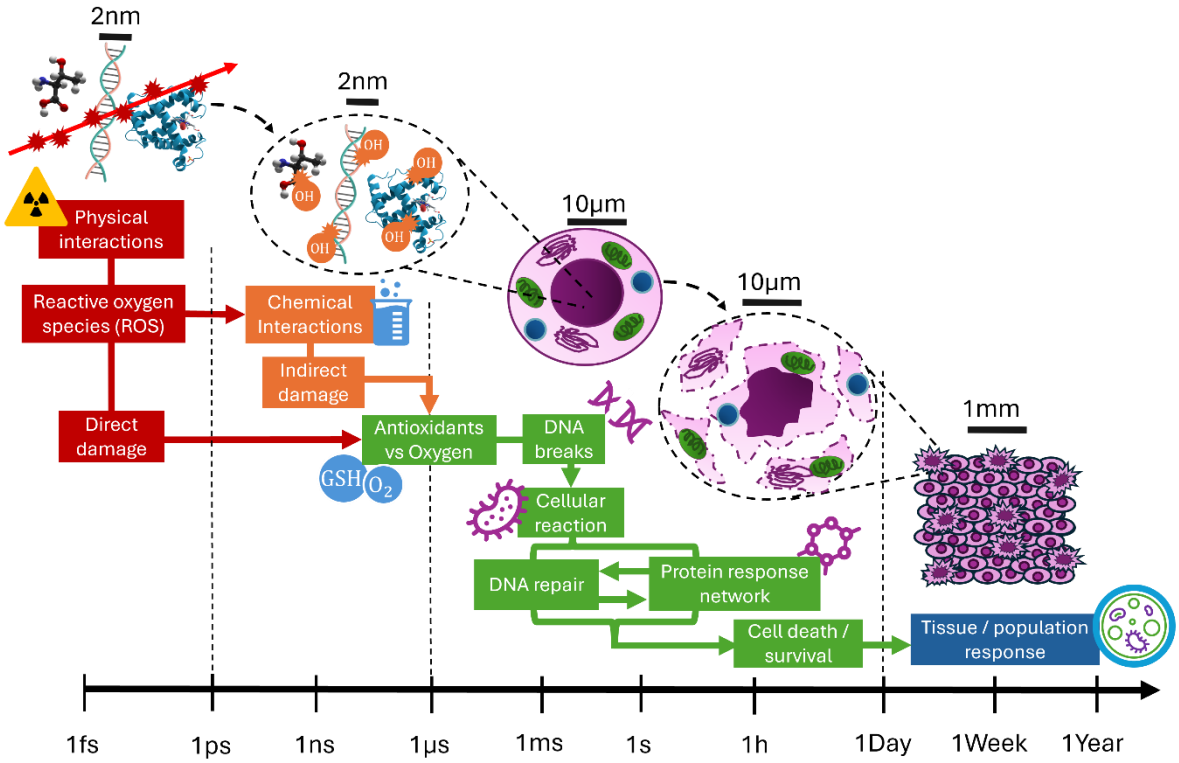

Figure 1.4. Schematics of the multiscale processes of the biological response to radiation. Image adapted from [McMahon S. & Prise K. (2019)]

As depicted in Figure 1.4, the phenomenon of biological response to radiation is a multiscale event. Its characterization requires a detailed description at every level, from the bottom up, starting with the fundamental physical interactions of radiation, that describe the initial conditions for the formation of radiation damage at the molecular level, to the biological response to radiation at the cellular scale, that determinate the ultimate fate of the affected cells: survival or death.

1.5 Study of the radiation effect and its modeling with Monte Carlo computational techniques: The state of the art.

Extensive experimental research has been conducted for decades to understand all aspects of the radiation effects on living tissue. Computational simulations are one of the most powerful tools for the development and testing of theoretical models to describe a natural phenomenon. Its use allows to optimize and resolve unknown parameters to describe the radiation effect. Considering the fact that biological, chemical and physical processes involved in the radiation interaction with living matter are stochastic in nature, the gold standard among the computational tools employed are those based on the *Monte Carlo* (MC) method. The MC method uses random sampling and is suitable for modeling most of the stages of the radiation interaction with biological matter.

15.1 Monte Carlo modeling of radiation interaction in water and DNA

The study of radiation chemistry of water is necessary for the understanding of the biological effects of irradiation. Water is fundamental to life, it is the most abundant liquid on earth's surface representing about 70-80% of the cell's weight [Alizadeh E. & Sanche L. (2012), Hall E.J. & Giaccia A.J. (2012), Plante I. (2021)]. Many chemical processes necessary to life involve water, some of them can be experimentally reproduced and studied on aqueous solutions [Alizadeh E. & Sanche L. (2012)]. It is also an important material for radiation dosimetry in radiotherapy since its energy absorption characteristics are similar to those of the human body [Plante I. (2021)]. Furthermore, the reactions between the chemical species produced by radiation and their kinetic parameters have been studied thoroughly in the context of nuclear energy security research and published in extensive compilations [Buxton G.V., et al (1988), Elliot A.J. (1994), Elliot A.J. & Bartels D. (2009)]. For these reasons and more, water constitutes the basis of any model for the biological response to radiation.

Complementary, *Monte Carlo Track Structure* (MCTS) codes are capable of recreating radiation transport and interaction with matter on the nanometric level, and especially with water [Pimblott S.M. & LaVerne J.A. (1990), Cobut V., et al (1997), Ballarini F., et al (2000), Meesungnoen J. & Jay-Gerin J.P. (2005), Kreipl M.S., et al. (2009), Karamitros M., et al (2011), Schuemann J., et al (2019), Ramos-Mendez J. et al (2018, 2020, 2022)]. MCTS simulations have helped to elucidate details on the modeling of water irradiation such as the thermalization distances of sub-excited electrons produced by charged particles [Goulet T., et al (1990), Kreipl M.S., et al (2009)] or the water dissociation schemes of radiolysis [Ballarini F., et al (2000)]. Nowadays, there exists MCTS algorithms like the *Step by Step* (SBS) transport or the independent reaction times (IRT) [Plante I. (2011,2021)] which efficiently simulate the reaction-diffusion process of chemical species with DNA at the early stages of the irradiation of a biological medium.

Water is also important for the study of DNA radiation damage mechanisms. Experimental methods can consist of *in vitro* assays with DNA suspended in aqueous solution, where the major component of the solution is water. These experiments have been useful to characterize the chemical reactions between DNA's subcomponents and free radicals, their main products and which reactions produce lesions [Balasubramanian B. et al, (1998), VonSontang C. (2006), Dizdaroglu M. & Jaruga P. (2012)]. Moreover, the isolated effect on environmental parameters that influence the quantity of lesions produced by radiation can be studied in water solutions, such as the temperature [Tomita H., et al (1995)], scavenger concentration [Milligan J.R. et al, (1993)] and oxygen dissolved in the solution [Michaels H.B. & Hunt J.W. (1977)].

For decades MCTS codes have been employed in combination with complex geometrical models of genetic material, being refined as years pass, to simulate in detail the DNA radiation damage processes. Simulations range from short DNA segments of a few nanometers in length to a whole cell nucleus with the entire human genome [Charlton D., et a (1989), Tomita H., et al (1998), Friedland W., et al (2003), Dos Santos M., et al (2014), Bernal M., et al (2015), Nikjoo H., et al (2016), Incerti S., et al (2010,2018), Tran H.N., et al (2020), D-Kondo N., et al (2021), Poignant F., et al (2022), Ramos-Méndez J., et al (2022)]. These simulations have helped to determinate details of the direct and indirect DNA damage caused by radiation, such as the energy deposit required to produce breaks [Nikjoo et al. (1997), Bernhardt Ph., et al. (2003), Friedland W. et al (2017), Lampe N. et al

(2018)], the efficiency of radicals to induce strand break a and the separation between consecutive breaks on opposite DNA strands to generate complex lesions such as a *Double Strand Break* (DSB) [Charlton D.E., et al (1989), Nikhoo H., et al (1997), Francis Z., et al (2011)].

Additionally, chemical kinetic models have been employed to describe different aspects of the chemical interactions in aqueous solutions and biological media. Such scenarios range from **a)** reactions between free radicals produced by long irradiation times in pure water, lasting several hours [Elliot A.J. & McCracken D.R. (1990), Pastina B. & LaVerne J.A. (2001)], **b)** early biological response of antioxidants to radiation damage leading to a state of *oxidative* cellular stress [Wardman P. (1999)], or **c)** extensive models for the whole cellular environment [LaBarbe R., et al (2020)].

1.5.2 Biological response modeling

The biological response to radiation, such as the DNA repair or protein response, can be studied experimentally using different optical techniques. For example, fluorescence microscopy techniques use specialized antibodies with fluorescent tags that can attach to proteins of interest, then the time evolution curve of the emitted light intensity can be quantified and correlated to the protein's activity and consequently to the associated biological process [Asaithamby A., et al (2008), Hall E.J. & Giaccia A.J. (2012)]. These time response curves can be employed to develop kinetic models that describe the reactions between proteins involved in the repair of DNA breaks [Belov O.V., et al (2015)] or control networks that mediate between biological radiation response process such as the cell cycle arrest or apoptosis [Ma L., et al (2005), Zhang X.P., et al (2009, 2011)]

Kinetic models can be expressed in the form of a set of coupled differential equations that can be solved by numerical integration using MC techniques, such as the *Gillespie algorithm* [Gillespie D. (1976)]. The Gillespie algorithm was developed in the 70's to simulate the time evolution of well mixed chemical schemes described by a system of coupled differential equations.

The correct function of biological processes is ultimately related to the cells capacity to grow and reproduce indefinitely. Thus, kinetic models can be complemented from experimental parameters such as cell doubling volume periods, or by the surviving number of cell colonies after being irradiated under certain conditions [Hall E.J. & Giaccia A.J. (2012), Chang D.S., et al (2021), Wakisaka Y., et al (2023)]. Those kinds of mesoscopic models require a more sophisticated type of modeling method called Agent-Based.

Agent Based Modeling (ABM) are methods (stochastic or deterministic) that assign rules of interaction to individual entities known as *agents* with their neighbors and their environment. The aim is to study the emerging properties of complex systems. ABMs have been applied in the context of biological research to model epidemiologic, organism's populations or cellular behaviors, from individual cells to entire tissues [Luke D.A. & Stamatakis K.A. (2012)]. For cancer research, ABM codes have been successfully used to simulate the growth and development of vascularized tumors [Shirinifard A., et al. (2009)] and its irradiation [Ruirui Liu et al. (2021)], the invasion of malignant cells to normal tissue [Pramanik D., et al (2021)] and the biochemical signaling of a tumor under a chemotherapy treatment [Jafari Nivlouei S., et al (2022)].

1.5.3 Problem statement

Existing computational modeling methods have proven to be fundamental to individually studying the different aspects that constitute the biological response to radiation. However, a comprehensive multiscale model that accounts for all the biological mechanisms that work in parallel, and that communicate the different spatial-temporal levels into a single solution, is currently lacking.

1.6 Scope of the thesis

The aim of this research work is to validate a multiscale model for the mechanistic simulation of biological response to radiation damage. For this end, two main projects were carried out. In the first project, a kinetic model was developed considering the chemical composition of the cellular environment and the early response of antioxidants against the radiation damage of the constituent biomolecules under different oxygen conditions and radiation dose rates. In the second project, a multiscale framework was validated for the simulation of the main stages of the biological response to radiation at the cell population level.

The foundations for these projects required the combined use of three Monte Carlo computer simulation tools for their implementation. In the first project the combined use of TOPAS [Perl J., et al (2012)], a MCTS code capable of simulating the interaction of radiation with matter as the central pilar of this research work; and Kinetiscope [Hinsberg W. & Houle F. (2020)], a computational tool for solving chemical kinetical models based on the Gillespie algorithm. For the second project, TOPAS was combined with CompuCell3D [Swat M., et al (2012)], an ABM code for the simulation of biological behaviors of a population of cells.

The motivation behind the development of the cell's environment model was the study of some of the main factors that affect the formation of radiation biological damage and the early biological response to it. These factors are the oxygen level in the tissue [Hall E.J. & Giaccia A.J. (2012), Chang D.S., et al (2021)] and the radiation dose rate [Favaudon V., et al (2014), Montay-Gruel P., et al (2019), Hughes J.R & Parsons J.L. (2020)], both are important factors that influence the effectiveness of radiotherapy. The first factor is related to the competition between the oxygen, that fixates the radiation damage, and the chemical repair of antioxidants naturally present on the cell's environment [Becker D., et al (1994)]. The second factor involves the initial density distribution of ionized water molecules, that transform into free radicals capable of inducing chemical damage to the cell's DNA and other important biomolecules, and dependent on dose rate [Wardman P. (2020)]. There is evidence that these two factors are contribute to the "FLASH effect" [La Barbe R., et al (2020), Wardman P. (2020), Favaudon V., et al (2021)]. However, the detailed bio-chemical mechanisms involved in these effects are not yet fully understood [Wardman P. (2020)].

Therefore, in this thesis a chemical kinetic model was developed for studying the effect of dose-rate and oxygenation on the radiation damage to the constituent biomolecules and the response of the two main antioxidants on the cells: Glutathione and ascorbic acid. The dose-rates correspond to conventional and FLASH irradiation modes, and the oxygen concentrations are representing the normoxyc and hypoxic conditions of cells.

Nevertheless, this competition dynamic is only the first stage of the biological response to radiation, and the whole process involves a multitude of biological mechanisms working in parallel and communicating with one another on multiple spatial-temporal scales. Therefore, to study this

multiscale problem, the development of a multiscale model and validation of a new computational platform for the simulation of the irradiation of a cell population were performed. Starting with a defined number of initially seeded cells, the model simulated the cell grown for a given period of time previous to the irradiation [Wakisaka Y., et al., (2023)]. The DNA strand breaks were calculated from the dose deposited in each cell's nucleus during the irradiation stage [Rothkamm K., et al (2003)]. Later, the biological response, consisting of a DNA repair model working in parallel to a kinetic model for the protein network that mediates between cell cycle arrest and apoptosis processes and two cellular death conditions were considered. The accumulation of lethal mis repaired DNA lesions and the apoptosis protein signaling were followed during the post irradiation stage [Stewart R.D. (2001), Ma L., et al (2005)], Zhang X.P. et al (2009,2011)]. Finally, the cell survival fraction was calculated by counting the remaining colonies among the initial seeded cells and validated against experimental data for the survival curve of a PC-3 prostate cancer cell line irradiated with X-rays from a 4MV LINAC [Wakisaka Y., et al., (2023)].

This thesis is structured in 7 chapters, the first one being this introduction. The second one is dedicated to the theoretical framework of this research work in the form of a bibliography review of the models that describe all stages of the radiation effect on a biological medium. The section discusses the fundamental physical-chemical interactions of an incoming particle on an aqueous environment, and the processes of damage to the genetic material at the molecular level. Finally, it is discussed the biological response mechanisms to radiation damage, from the early response of antioxidants to DNA repair and the protein regulation networks.

The third chapter is a description of the methodology developed for this research work. The chapter starts with a review of the three codes employed and their most important computational tools that allowed the integration and simulation of the proposed models. Then the workflow for each of the developed projects is described, and finally, some results of quality control to verify the correct function and implementation of the models are shown.

The fourth chapter presents the obtained results, and the scientific publications produced are enlisted and commented. Finally, the three remaining chapters are dedicated to the discussion, future work and conclusions derived from these results. The expectation of this research work is to aid in the exploration of the theoretical fundaments of the biological response to radiation and the effort to develop emergent technologies for the treatment of cancer based on radiation therapy.

2. Theoretical Framework

2.1 Radiation chemistry of water

To advance the knowledge of the biological effects of ionizing radiation, first it is necessary to describe its action in liquid water, which is the major constituent of living organisms. Water is the most studied liquid both experimentally and theoretically. One of the most important phenomena triggered by radiation is the chemical decomposition or dissociation of ionized and excited water molecules, an effect known as radiolysis [Alizadeh E. & Sanche L. (2012), Azzam E.I., et al (2012)]. Water dissociation produces primary radiolytic species that include free radicals, known as *Reactive Oxygen Species* (ROS), that are responsible for the indirect damage to DNA [Hall E.J. & Giaccia A.J. (2012), Azzam E.I., et al (2012)].

To this end, it is necessary to describe the radiation transport and associate such description with the spatial-temporal energetic distribution of the physical interactions along particle's paths and the time evolution of the primary radiolitic species created by radiation. One fundamental quantity to describe the radiation is the Lineal Energy Transfer (LET), which is a measurement of the ionization density along the particle track [Cobut V., et al. (1996)].

Radiolysis of water for low LET radiation, like X-rays, gamma rays produced by cobalt 60 decay, fast electrons or high energetic protons, at room temperature (25°C) has been widely studied and it's generally well understood [Meesungnoen J. & J Jay-Gerin J.P. (2005)]. Roughly speaking, the modeling of the interaction of radiation water can be divided into four consecutive temporal stages [Azzam E.I., et al (2012), Plante I. (2021)]:

The first is the *physical* stage, where incident charged particles interact with the water molecules of the medium, generating ionized and excited molecules, and secondary electrons distributed in short, very dense and non-homogeneous regions known as *spurs* that surround the main track of the incident particle. This stage occurs on time scales below a few femtoseconds [Meesungnoen J. & Jay-Gerin J.P. (2005), Plante I. (2021)].

These excited and ionized molecules are unstable and decay very quickly, producing primary chemical species like hydrogen ($\mathrm{H}\bullet$), hydroxyl ($\bullet\mathrm{OH}$), dihydrogen ($\mathrm{H_2}$), hydronium ($\mathrm{H_3O^+}$) and hydroxide ($\mathrm{OH^-}$) on the second stage called *physicochemical.* The secondary electrons (sub-excited) are slowed down as they interact with additional water molecules, losing energy until they no longer can produce excitations, reaching the sub-excitation energy. At this point they become trapped (e_{tr}^-) and finally hydrated (e_{aq}^-), this means that they become surrounded by water molecules in a *cage* where they cannot escape [Goulet, T., & Jay-Gerin, J.-P. (1989), Cobut V., et al (1997), I. Plante (2021)].

This initial distribution of primary chemical species is the starting point for the *heterogeneous chemical* stage. In this stage these species diffuse in the medium, react with each to other and with the environment to produce secondary chemical species until around 1 microsecond. After this time, the majority of reactions among radiolitic species have occurred and the surviving species are sufficiently separated to *escape* the highly dense neighborhood of the particle track, transitioning into a *well-mixed* state [Meesungnoen J. & Jay-Gerin J.P. (2005)].

Finally, this new distribution initiates the *homogeneous chemical stage* in the case of an aqueous solution, or the *biological stage* in a physiological system. In this stage, surviving species continue to react triggering the lengthy biological process of radiation response determining the long-term consequences of irradiation [Azzam E.I. et al (2012), I. Plante (2021)]. A more in-depth description of each stage will be developed in the next sections.

2.1.1 Physical Stage

The trajectory of incident particles and the distribution of ionization along their path depends on the physical properties of both the radiation and the traversed material. In general, the interaction of particles with the atoms of the target is described by a probability function known as *cross section*. If we consider a narrow, parallel beam of incident particles p, with initial energy E and traveling on a direction $\vec{r}$, the flux $\dot{\mathrm{N}}_{\mathrm{in}}$ is defined as the number of particles per unit of time and per unit of area,

impacting a target [Nikhoo H., et al (2012), Andreo P., et al., (2017)]. It is assumed that the target is a thin layer of material with a thickness dl formed by $\mathrm{n_T}$ target atoms. The quantity $\dot{\mathrm{N}}_{\mathrm{out}}$ represent the number of particles per unit of time deflected in a certain direction $\vec{r}'$. It is proportional to the initial number of incident particles and the number of target atoms, and the proportionality constant is known as the total cross section of the material Σ_{tot} [Andreo P., et al (2017)]:

$$\dot{\mathrm{N}}_{\mathrm{out}} = \Sigma_{tot} \cdot n_T \cdot \dot{\mathrm{N}}_{\mathrm{in}} \qquad \Sigma_{tot} = n_T \frac{\dot{\mathrm{N}}_{\mathrm{in}}}{\dot{\mathrm{N}}_{\mathrm{out}}}$$

The total cross section has units of length square, and it is considered as the effective area of the objective that the incoming particles "see" in front as they collide. When considering a single target atom ($n_T = 1$) the total cross section reduces to $\Sigma_{tot} = \dot{\mathrm{N}}_{\mathrm{in}}/\dot{\mathrm{N}}_{\mathrm{out}}$ and it can be considered as the total probability that an incident particle interacts with one of the atoms of the material. This interaction provokes a loss of energy and a scatter from the original beam direction. Let us consider a detector that counts the number of particles $\dot{\mathrm{N}}_{\mathrm{d}\Omega dw}$ within a small range of energy dW, that fall on a small section $d\Omega(\theta, \varphi)$ characterized by the direction of the polar θ and azimuthal φ angels. The proportionality constant between $\dot{\mathrm{N}}_{\mathrm{d}\Omega dw}$ and $\dot{\mathrm{N}}_{\mathrm{in}}$ is known as the double differential cross section [Andreo P., et al (2017)]:

$$\dot{\mathrm{N}}_{\mathrm{d}\Omega dw} = \frac{d^2\sigma}{d\Omega dW} \dot{\mathrm{N}}_{\mathrm{in}} d\Omega dW$$

If we integrate this quantity over all the solid angle Ω and all possible loss of energy, between 0 to the energy of the primary particles E, we obtain the microscopic total cross section:

$$\sigma_{tot}(E) = \int_0^E \left(\int_\Omega \frac{d^2\sigma}{d\Omega dW} d\Omega \right) dW$$

Which is a function of the incoming particle energy, and it is composed of the sum the individual cross section $\sigma_i(E)$ of all the possible interaction mechanisms between the particles and the target material. The sum of these quantities describes the total interaction cross section:

$$\sigma_{tot}(E) = \sum_{i=0}^{n} \sigma_i(E)$$

While the individual cross sections $\sigma_i(E)$ describe interaction prosses such as ionization, excitations, elastic collisions, etc. between incoming particles and the atoms of the traversed material, they also describe the production of secondary particles p_{sec} . This means that in certain energy ranges, the cross section of a specific process is larger than others and consequently, that process is more likely to occur than the others. If all the atoms of the target material are considered per unit of mass, the total macroscopic cross section is obtained:

$$\Sigma_{tot}(E) = \frac{N_a}{Z} \sigma_{tot}(E)$$

Where $N_a = 6.022 \times 10^{23} \mathrm{mol}^{-1}$ is Avogadro's number and Z is the atomic number of the material. If we then consider the density ρ of the target, then we can obtain the lineal attenuation coefficient $\mu(E) = \Sigma_{tot}(E)\rho$ which is a macroscopic measurement of the probability of interaction of particle in a small distance dS. The inverse of this quantity is known as the mean free path $\langle S \rangle$ and it

describes the average distance between two consecutive interactions, figure 2.1 [Andreo P., et al (2017)]:

$$\langle S \rangle = \frac{1}{\mu(E)} = \frac{Z}{N_a \cdot \sigma_{tot}(E)}$$

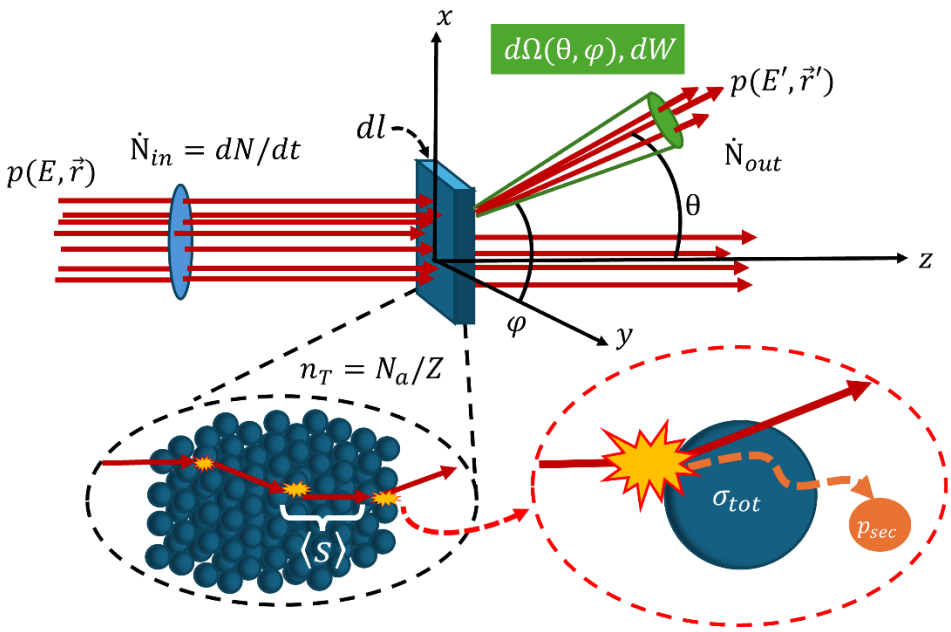

Figure 2.1 schematics of the total cross section of a particle colliding with a material. Image adapted from [Andreo P., et al (2017)]

There are several fundamental quantities that characterize the action of a certain type of radiation with a material. Two important ones are the absorbed dose (D) and the linear energy transfer, LET (L). The first one represents the average energy $d\bar{\varepsilon}$ delivered to a certain material and absorbed per unit of mass dm. The unit of absorbed dose is the Gray (Gy), defined as joule per kilogram (J/kg) [Nikhoo H., et al (2012)]:

$$\mathrm{D} = \frac{\mathrm{d}\bar{\varepsilon}}{\mathrm{dm}}$$

The second quantity is the transfer of energy dE to the medium per length unit dl traveled by the incident charged particles. It has units of kilo electron volts per micrometer, $\mathrm{keV/\mu m}$. This quantity is given by the following expression:

$$L_\Delta = \left(\frac{dE}{dl}\right)_\Delta$$

This quantity considers the contribution of all secondary electrons produced by the primary particles that have a kinetic energy below Δ. For example, L_{100} represents the energy transferred by secondary electrons with a maximum energy of 100 keV while L_∞ represents the contribution of all possible secondary electrons [Nikhoo H., et al (2012)].

In general, particles can be classified in two broad categories: *directly ionizing* and *indirectly ionizing.* Directly ionizing are for charge particles that transmit their energy to the material by direct interactions, usually by numerous Coulomb-force small interactions along its path. Indirectly ionizing is from neutral primary particles (gammas, neutrons) that transmitted their energy to the medium's particles, like free electrons, which are set in motion and produced interactions depositing their energy [Attix F.H. (1986), Chang D.S, et al (2021)]

For a specific type of particles, the interactions they experience and the validity of the models that describe them depend on the energy range considered. The spatial distribution of energy deposits in a medium is known as the *track structure* of the incoming particles [Plante I. (2021)]. For photons, there are 5 relevant effects: Compton scattering, photoelectric effect, Rayleigh scattering, pair production and photo-nuclear interactions. The Rayleigh effect is also known as coherent scattering because photons do not lose energy and only change direction in an elastic collision. Very energetic photons, with energies above 10 MeV, can interact directly with the nucleus of the irradiated target, producing secondary neutrons and radioactivating the material [Attix F.H. (1986)].

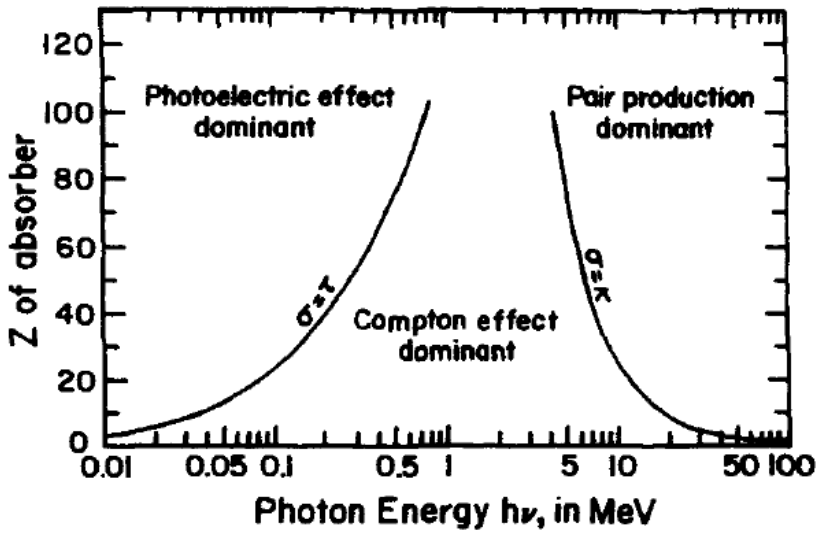

Figure 2.2: relative contribution of the different types of interactions for gamma rays as a function of the energy of the incident photons and atomic number Z of the material. Imagen obtained from [Attix F.H (1986)]

For photons with energies below 1 MeV, like X or gamma rays, the dominant effects are the Compton effect, where photons interact with the electrons of the external shells of the target atoms, transferring a portion of their energy to put them in motion and reducing their wavelength in the process. In the photoelectric effect, the incoming photons rip out the electrons of the inner shells, leaving vacancies that can be filled by external electrons and producing characteristic photons with a wavelength equal to the difference of the atomic shell's energies [Andreo P., et al (2017)]. For energies above 1.022MeV, corresponding to double the rest energy of electrons, the pair production starts to dominate the interaction of photons with the medium, where photons interact with the nucleus of the target atoms and *materialize* into an electron and a positron pair, figure 2.2 and 3.3. All these types of interaction processes produce secondary electrons that can further interact with the material, producing ionizations on their own [Von Sontang (2006), I. Plante (2021)].

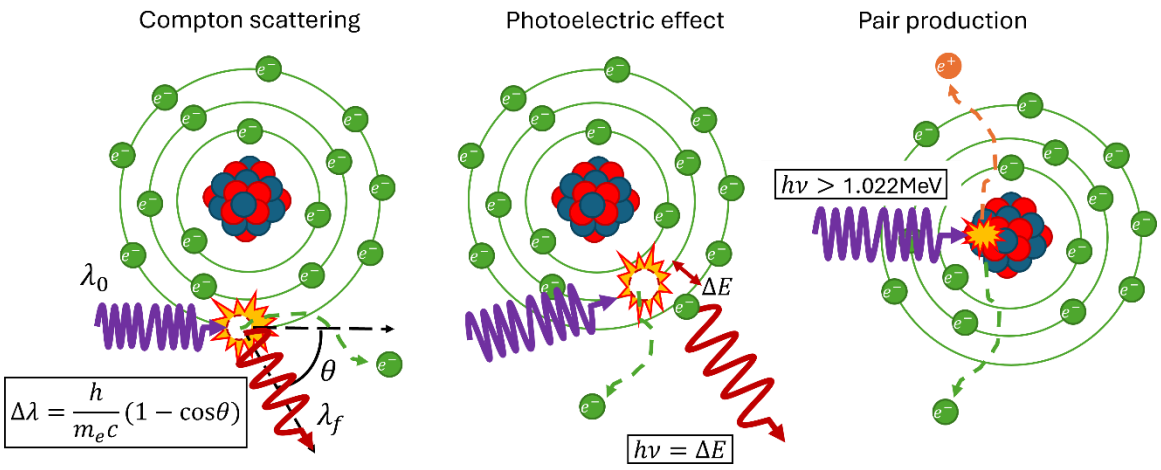

Figure 2.3. Main interactions between photons on the medical energy range. Image adapted from [Attix F.H. (1986)].

Neutral particles interact with a medium in a relatively sparse manner: a neutron or a photon can cross a thin layer of a material without transferring energy or being scattered. In contrast, charged particles interaction with a material is drastically different. These can interact with almost every target atom that it encounters on its path through small but numerous Coulomb interactions, most of them are elastic collisions, that transfer a minuscule fraction of their kinetic energy and change their direction. A useful approximation is to think of this process as a continuous loss of energy similar to a *friction* interaction with the material, this is known as the *Continue Slow-Down Approximation* (CSDA) [Attix F.H. (1986), Andreo P., et al (2017)].

The derivation of the formalism that describes the interactions of charged particles is complex, but they can be simplified by characterizing them in terms of the classical impact parameter b. The impact parameter is the perpendicular distance between the trajectory of the incident particle and the center of the target atom. This distance can be compared with the atomic radius r_a of the material. If b is larger than r_a, then a soft collision can take place and the charged particle will interact with the whole atom, exciting one of its electrons to a higher energy level or even ejecting it from the valence shell, causing an ionization. If the parameter b is about the same as r_a, then it is more likely that the particle interacts with a single electron of the atom's inner shells and ejects it, causing an ionization event. On the other hand, if $b < r_a$ the charged particle experiments a Coulomb-Force interaction with the atomic nucleus, it can lead to an elastic scattering with no energy transfer, or suffer an inelastic radiative interaction, emitting a secondary photon and slowing down in the process, this phenomenon is known as *Bremsstrahlung* or breaking radiation [Attix F.H. (1986), Andreo P., et al (2017)].

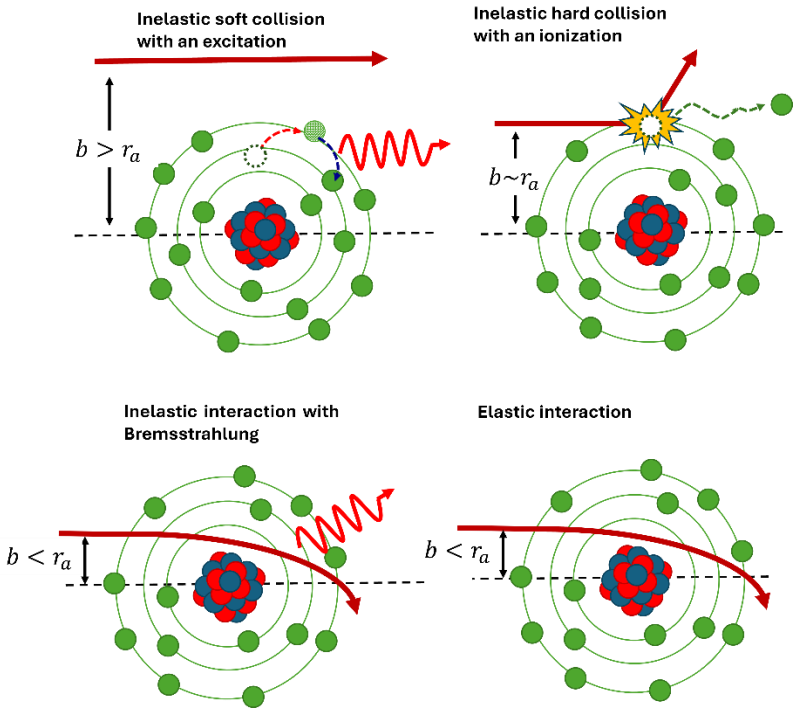

Figure 2.4. Main interactions between charged particles with the atoms of a target material image adapted from [Attix F.H. (1986)].

The expected value for the energy loss dE rate per unit of path length dl traveled by a particle p with initial energy E traversing a material with atomic number Z is known as *stopping power* $S(E)$, with units of MeV/cm and given by the expression:

$$S(E) = \left(\frac{dE}{dl}\right)_{p,E,Z}$$

This quantity can be subdivided into two terms that consider the energy spent by the incident particles on collision events, known as the *collision stopping power*, and photon emission events, called *radiative stopping power*. The photons created by the radiative events carry the energy away from the track of the particle while the energy spent on collisions contributes to the ionization and excitation of the atoms of the irradiated material and to the deposited dose along the particle track as a consequence [Attix F.H. (1986)]. If the density ρ of the material is considered the mass collision power, denoted by the sub index c, is obtained and it can be expressed by:

$$\frac{S(E)_c}{\rho} = \left(\frac{dE}{\rho dl}\right)_c = \frac{N_A Z}{A}\int_{W_{min}}^{W_{max}} W\frac{d\sigma}{dW}dW$$

Where Z is the atomic number, N_A is the Avogadro's number and N_A/A represent the number of atoms of the material per gram, $d\sigma/dW$ is the differential cross section for the inelastic collisions that end up in an energy transfer $W$with the atomic electrons, the limits of the integral are the minimum and maximum energy transfers respectively. The whole term ZN_A/A is the number of electros per gram of target material. [Andreo P., et al (2017)]. This expression can be separated into two terms that represent the soft and hard collisions:

$$\left(\frac{dE}{\rho dl}\right)_c = \frac{N_A Z}{A}\left[\int_{W_{min}}^{W_c} W\frac{d\sigma^{soft}}{dW}dW + \int_{W_c}^{W_{max}} W\frac{d\sigma^{hard}}{dW}dW\right]$$

Where W_c is an energy threshold that separates the energy transfer for hard and soft collisions. Both terms can be expressed using the Bethe formula for soft and hard collisions [Attix F.H. (1986), Andreo P., et al (2017)], for particles heavier than electrons is given by:

$$\frac{S(E)_c^{soft}}{\rho} = 2\pi r_e^2 m_e c^2 \frac{N_A Z}{A}\cdot\frac{z^2}{\beta^2}\left[\ln\left(\frac{2m_e c^2\beta^2 W_c}{(1-\beta^2)I^2}\right) - \beta^2\right]$$

$$\frac{S(E)_c^{hard}}{\rho} = 2\pi r_e^2 m_e c^2 \frac{N_A Z}{A}\cdot\frac{z^2}{\beta^2}\left[\ln\left(\frac{2m_e c^2\beta^2}{W_c(1-\beta^2)}\right) - \beta^2\right]$$

here r_e and m_e are the classical radius and mass of the electron respectively, c is the speed of light and $\beta = v/c$ where v is the particle velocity and z its charge. Finally, I is the mean excitation energy of the materials atoms. Both expressions can be combined to give the total mass stopping power [Attix F.H. (1986), Andreo P., et al (2017)]:

$$\frac{S(E)_c}{\rho} = 4\pi r_e^2 m_e c^2 \frac{N_A Z}{A}\cdot\frac{z^2}{\beta^2}\left[\ln\left(\frac{2m_e c^2\beta^2}{I(1-\beta^2)}\right) - \beta^2\right]$$

The collision stopping power described by the Bethe equation takes into account the general inner electronic structure of the material through terms like the mean ionization energy and the total electron number per gram of the target material. However, the details of the electron distribution of the target atoms are not present in this approach. To calculate the specific probabilities that a certain ionization or excitation interaction occurs shell-by-shell cross sections models for the atoms of the material are needed. Bethe's theory, based on the first-order Born approximation, also provides an expression for the non-relativistic differential cross section for the inelastic interaction which includes the details of the electronic structure of the target material [Andreo P., et al (2017)]:

$$\frac{d^2\sigma}{dQdW} = 2\pi r_e^2 m_e c^2 \frac{z^2}{\beta^2}\frac{1}{WQ}\frac{df(Q,W)}{dW}$$

Where Q is the recoil energy of the target electrons equal to the kinetic energy transferred in the collision, and $df(Q,W)/dW$ is the *generalized oscillator strength* function (GOS). The GOS characterizes the entire response of the material's atoms to the inelastic interactions, and it is independent of the projectile. It is also related to the dielectric properties of the material and is interpreted as the density of oscillators (or more specifically, the effective number of electrons) that participate in an interaction with recoil energy Q per unit of energy transfer dW. For a given material of atomic number Z, if all the possible ionizations and excitations processes that transfer energy are considered, the Bethe sum rule is satisfied [Fernaéndez-Varea J.M., et al (2005), Andreo P., et al (2017)]:

$$\int_0^\infty \frac{df(Q,W)}{dW}dW = Z$$

The GOS is directly related with the *Dielectric Response Function* (DRF) $\varepsilon(W,Q)$, a classical electrodynamic quantity that characterizes a material [Fernaéndez-Varea J.M., et al (2005), Andreo P., et al (2017)], as follows:

$$\frac{df(Q,W)}{dW} = \frac{2Z}{\pi E_p^2} W \left(1 + \frac{Q}{m_e c^2}\right) \mathrm{Im}\left(\frac{-1}{\varepsilon(W,Q)}\right)$$

Where $E_p = \hbar\sqrt{4\pi n_e e^2/m_e}$ is the plasma energy of a homogeneous free-electron gas with an electron density n_e equal to the studied material, and specifically for water it has a value of 21.47 eV. Finally, the $\mathrm{Im(W,Q)}$ term is known as the *Energy Loss Function* (ELF), a characteristic distribution of energy transferred to the material that needs to be experimentally determined by techniques like the electron spectroscopy for the specific electronic structure of a material. In the limit of $Q \to 0$, where no momentum is transferred to the electrons of the material, the $\mathrm{Im(W,Q)}$ becomes the *Optical Energy Loss Function* (OELF) [Andreo P., et al (2017)].

The electronical structure of the water molecule has been studied experimentally through its X-ray emission spectrum and complemented by a theoretical model based on the Hartee-Fock method, identifying several molecular orbits usually called $1b_1$, $3a_1$, $1b_2$, $2a_2$ and $1a_1$ shown in figure 2.5 [Guo J-H., et al. (2002)].

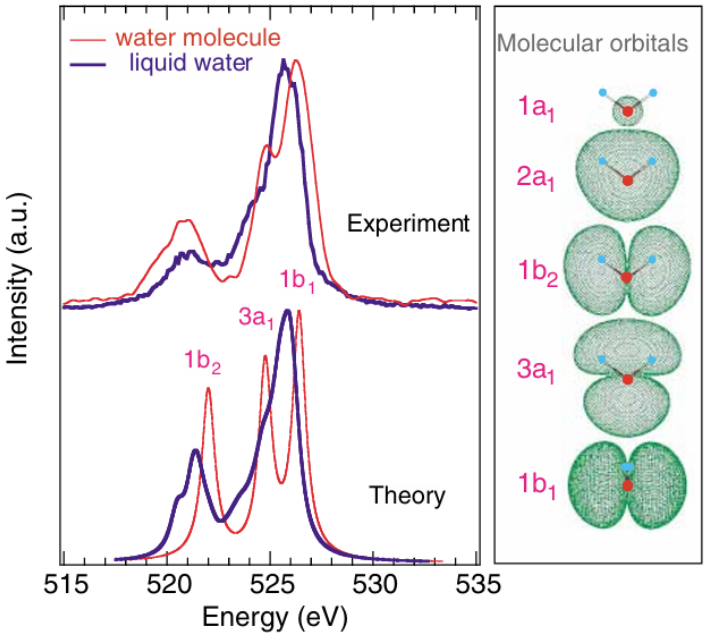

Figure 2.5. Molecular orbits of water. Image taken from [Guo J-H., et al. (2002)]

Furthermore, the energy loss function has been obtained experimentally for liquid water on the optical limit by [Heller J.M., et al (1973)] using the reflection of ultraviolet photos up to energies between 7.6 and 25.6eV and on gas phase by [Diercksen G.H.F., et al (1982)]. Then, the ELF (figure 2.6) can be decomposed into the contributions of each interaction mechanism, like excitations and ionizations, to construct an expression for the cross section of every process [Kutcher G.J. & Green A.E.S. (1976), Cobut V., et al (1997)].

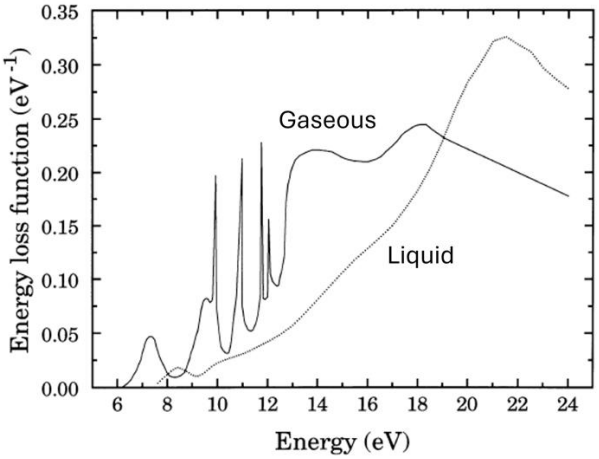

Figure 2.6. ELF for the liquid and gaseous phase of water. Image adapted from [Cobut V., et al (1997)].

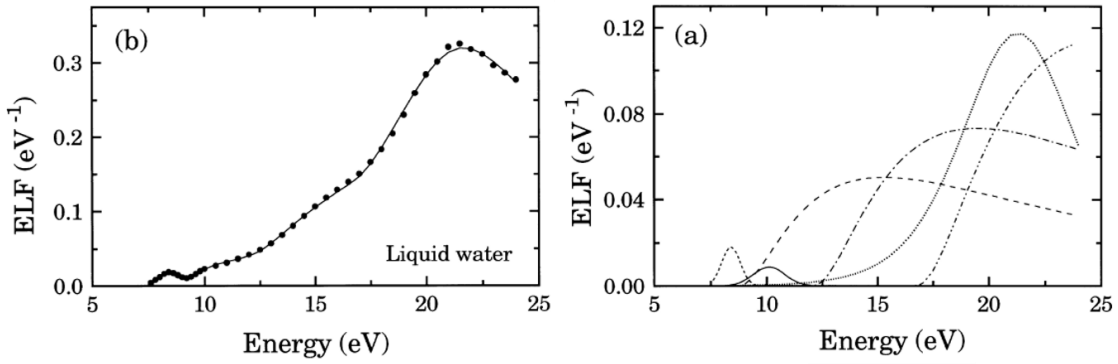

Figure 2.7. Decomposition of the ELF for the liquid of water into the components for the different ionizing and excitation process where the dotted line … represents the collective "plasmon" excitation state, dashed --- and continue___ lines the $\tilde{A}^1B_1$and $\tilde{B}^1A_1$ electronic excitation states respectively, while the long dashed _ _ _, dot-dashed -.-.-. and dashed-double dotted ..-..-.. lines represent the $1b_1$, $3a_1$ and $1b_2$ ionizations respectively. Image adapted from [Cobut V., et al (1997)].

Complementary, Monte Carlo Track-Structure codes have used models based on these approaches for the transport and interaction of radiation with water simulation and applied them to study the different aspects of the physical and chemical effects of ionizing radiation that lead to DNA damage at the subcellular and molecular level under different irradiation conditions for decades. These codes include MOCA8b [Charlton D., et a (1989)], DBREAK [Tomita H., et al (1998)], PARTRAC [Friedland W., et al (2003)], KURBUK [Nikjoo H., et al (2016)], Geant4-DNA [Incerti S., et al (2010,2018)], RITRACKS [Plante I., et al (2019)], DaMaRiS [Warmenhoven J.W., (2019)], and TOPAS-nBio [Schuemann J., et al (2019)]. This last one represents the central pillar of this research work.

The complete physical stage for water can be briefly summarized as follows: around 1 fs ($1 \times 10^{-15} s$) incident particles interact with the electrons that occupy the multiple energy levels of the water molecules and eject them, producing ionized molecules in the process [Cobut V., et al (1997), Ballarini F., et al (2000), Plante I. (2021)] denoted as:

$$H_2O \rightarrow H_2O^+ + e^-$$

High LET radiation can produce molecules with multiple ionizations (H_2O^{2+}, H_2O^{3+}…), however, the probability of producing multiple events reduces with each additional ionizations and the majority of them occur on the interior of heavy ions tracks [Meesungnoen J. & Jay-Gerin J.P. (2005), Plante I. (2021)]. On the other hand, the interactions where the energy transfer is not enough to ionize the water molecules lead to excited states [Cobut V., et al (1997), Ballarini F., et al (2000), Plante I. (2021)], denoted by:

$$H_2O \rightarrow H_2O^*$$

There exist multiple excited states of the water molecule, however, for the radiolysis process the important ones are the excited electronic states $\tilde{A}^1B_1$ and $\tilde{B}^1A_1$in addition to multiple vibrational and rotational excited states characterized by diffuse bands and Rydberg series in the spectroscopic studies of optical and electron scattering on water [Claydon C.R., et al (1970), Plante I. (2021)].

2.1.2 Physical-chemical stage

The ionized and excited molecules are unstable, and they reorganize very quickly by different mechanism, like relaxation, autoionization and dissociation, during the physical-chemical stage that last until around $1 \times 10^{-12}s$ after irradiation [Cobut V., et al (1997), Ballarini F., et al (2000), Plante I. (2021)]. When excited and ionized molecules dissociate, the fragments share the kinetic energy produced by the breaking of the molecular bonds. They travel for a small distance of a few Armstrong until they thermalize [Cobut V., et al (1997)]. Free electrons produced during the physical stage also undergo a similar thermalization process, losing energy until they become trapped by water molecules and eventually, they become hydrated electrons (e_{aq}^-), meaning that they are surrounded by water molecules in a configuration that they cannot escape [Ballarini F., et al (2000), Plante I. (2021)]

In order to model this stage, it is necessary to determinate the values for the probability and the species produced by each type of dissociation event, as well as the thermalization distance of the water molecule fragments and electrons [Ballarini F., et al (2000)]. However experimental data is limited because of the time and spatial scale of the process involved. In response, Mote Carlo computer simulation has been used complementary to test theoretical models and optimize their variables to match the experimental data observed at longer times, progressively improving the models [Cobut V., et al (1997), Ballarini F., et al (2000)].

In the case of ionized molecules, the water cations H_2O^+have a very short lifetime of about 10fs where a sequence of electrons transfers from neighbor water molecules to the hole of the H_2O^+ occur. During this time, it undergoes a random walk with an average *migration distance* of 1.375 nm, and eventually a proton (H^+) transfer from another water molecule occurs, producing a pair of hydronium (H_3O^+) and hydroxyl (OH) radicals [Cobut V., et al (1997), Plante I. (2021)]:

$$H_2O^+ + H_2O \rightarrow H_3O^+ + OH$$

It has been theorized that multiple ionized molecules dissociate into different products, for example the double ionized water molecule can decay into a pair of proton and hydroxide (OH^-) [Cobut V., et al (1997)], or it can react with two neighbor water molecules to form two hydronium radicals and one oxygen atom on the ^3P ground state [Plante I. (2021)]:

$$H_2O^{2+} \rightarrow H^+ + OH^- \quad \text{or} \quad H_2O^{2+} + 2H_2O \rightarrow 2H_3O^+ + O(^3P)$$

Free electrons can recombine with their parent water cation and produce an excited water molecule that will experience its own reorganization processes [Cobut V., et al (1997), Plante I. (2021)]:

$$H_2O^+ + e^- \rightarrow H_2O^*$$

On the other hand, the reorganization process of excited molecules can be non-dissociative relaxations. In this process, the molecule returns to its non-excited state and the excess energy (ΔE) is transferred to the neighboring water molecules, or drive dissociative decays, breaking the molecule into several products; or produce an autoionization process, where the molecule breaks into the same pair of H_3O^+ and OH as an ionization [Cobut V., et al (1997), Plante I. (2021)].

The specific probabilities for the branching decays of each excited state are difficult to obtain experimentally in liquid water and little information is available [Cobut V., et al (1997), Ballarini F., et al (2000), Kreipl M.S., et al (2009)]. However estimated information for the decay products and their occurrence were performed on water vapor photolysis [Claydon C.R., et al (1971)] and used as a dissociative scheme in MC simulations by [Cobut V., et al (1997)].

In [Ballarini F., et al (2000)] the different approaches and dissociation schemes used by several groups on MC simulations are shown with the objective of reproducing the picosecond chemical yields of the radiolytic species.

The dissociation scheme adopted in this work is the one revised by [Kreipl M.S., et al (2009)] based on [Ballarini F., et al (2000)] work. The main difference is that the excited state $\widetilde{B}^1A_1$ decays into a pair of dihydrogen (H_2) and oxygen (O), the later reacts rapidly with a water molecule producing two hydroxyl radicals. This dissociation scheme has been used in numerous publications since, for example [Karamitros M., et al (2011), Schuemann J., et al (2019), Ramos-Mendez J. et al (2018, 2020, 2022)] and it's presented in table 2.1.

Table 2.1. Water dissociation scheme

State	Process	Probability (%)	Products
Ionization (H_2O^+)	Dissociative decay	100	$H_3O^+ + OH \xrightarrow{+e^-} H_2O$
	Recombination	-----	
Excitation (H_2O^*)			
$\widetilde{A}^1B_1$	Dissociative decay	65	$OH + H$
	Relaxation	35	$H_2O + \Delta E$
$\widetilde{B}^1A_1$	Auto ionization	55	$H_3O^+ + OH + e^-_{aq}$
	Dissociative decay	15	$H_2 + O \xrightarrow{+H_2O} H_2 + 2OH$
	Relaxation	30	$H_2O + \Delta E$
Rydberg series/ diffuse band	Auto ionization	50	$H_3O^+ + OH + e^-_{aq}$
	Relaxation	50	$H_2O + \Delta E$

Lastly, the free secondary electrons produced by radiolysis not only recombine with its parent cation but also travel and interact with the medium, ionizing and exciting other water molecules in its path independently until they reach the sub-excitation energy, at around 7.4 eV [Goulet T., & Jay-Gerin J.P. (1989), Cobut V., et al (1997)]. This excess kinetic energy is then lost by inelastic interactions until

it is around 0.2eV when they achieve thermal equilibrium with the environment [Cobut V., et al (1997)].

The thermalization process only last approximately $10^{-13}s$. The probability of recombination and the distribution of thermalization distances, dependent on the energy of the electrons, were calculated using Monte Carlo simulations [Goulet T., et al (1990)]. The scattering cross sections of water were obtained on experiments performed on amorphous ice and later corrected for the liquid phase of water [Michaud M. & Sanche L. (1987), Goulet T. & Jay-Gerin J.P. (1989)]. To simplify the simulation of the thermalization process the traveled distance by sub-excitation electrons can be sampled from a gaussian distribution [Kreipl M.S., et al (2009)], following the results published by [Goulet T., et al (1990)].

2.1.3 Heterogeneous chemical stage

This stage extends from the end of the physicochemical stage, around $10^{-12}s$, until the chemical species have reached a homogeneous distribution, in pure water it is around $10^{-6}\,s$. Here the primary radiolitic species $\mathrm{H^{\cdot}}, \mathrm{OH^{\cdot}}, \mathrm{H_2}, \mathrm{H^+}, \mathrm{OH^-}$ are initially distributed in the proximity of the particle track and the time evolution of the individual molecule's positions are governed by the Einstein's diffusion equation [van Zon J.S., et al (2005), Plante I. 2021]:

$$\frac{\partial}{\partial t}p(\vec{r},t|\vec{r}_0) = D\nabla^2 p(\vec{r},t|\vec{r}_0)$$

The function $p(\vec{r},t|\vec{r}_0)$ is the probability distribution that a certain molecule is located on the position $\vec{r}$ at the time t, conditioned by its initial position $\vec{r}_0$, while D represents its diffusion coefficient. The position of the particle is $\vec{r} = \vec{r}_0$, at the initial time $t = 0$, can be represented by the initial condition $p(\vec{r}, t \to 0|\vec{r}_0) = \delta(\vec{r} - \vec{r}_0)$ where δ is the Dirac delta function. Another boundary condition is the probability that a certain displacement to occur diminishes with distance, this means that the probability that the molecule travel long distances is cero and can be represented by $p(\vec{r} \to \infty, t|\vec{r}_0) = 0$. Considering these conditions, the solution of the diffusion equation can be obtained using the Green's function for diffusion (GFDE), [van Zon J.S., et al (2005), Plante I. (2021)]:

$$p(\vec{r},t|\vec{r}_0) = \frac{1}{(4\pi Dt)^{3/2}}\exp\left[-\frac{(\vec{r}-\vec{r}_0)^2}{4Dt}\right]$$

In the case that the molecule is under the influence of an external force field $\vec{F}(\vec{r})$, an extra term that considers its action can be added to the equation:

$$\frac{\partial}{\partial t}p(\vec{r},t|\vec{r}_0) = D\nabla^2 p(\vec{r},t|\vec{r}_0) - D\beta\nabla\cdot\left[p(\vec{r},t|\vec{r}_0)\vec{F}(\vec{r})\right]$$

Where $\beta = k_B T$, k_B is the Boltzmann constant and T the temperature. This expression is known as the Debye-Smoluchowski Equation (DSE) and for the 1-dimensional case with a constant electrostatic field $F(x) = c$, this expression is reduced to:

$$\frac{\partial}{\partial t}p(x,t|x_0) = D\left(\frac{\partial^2}{\partial x^2} + \beta c\frac{\partial}{\partial x}\right)p(x,t|x_0)$$

If then we consider the following variable change [Agmon N. (1984)]:

$$q(x,t|x_0) = p(x,t|x_0)\exp[Dc\beta(x - x_0 + Dc\beta t)]$$

It can be shown that the solution for the DSE can also be obtained using the Green's function, given by:

$$p(x,t|x_0) = \frac{1}{(4\pi Dt)^{1/2}}\exp\left[-\frac{(x - x_0 + D\beta ct)^2}{4Dt}\right]$$

This example can be generalized to 3 dimensions if each component of the force vector is taken separately. To extend this formalism to a group of molecules dissolved on a solution, a reaction between two chemical species A and B can be written in general as:

$$A + B \rightarrow P$$

The diffusion-reaction theory can be employed to describe these types of reactions. Considering the independent diffusion of two molecules and several conditions necessary for the reaction to occur. One condition is that the intermolecular distance that separates both species must be smaller than their reaction radius. If we have a pair of molecules A, B in the initial positions $\vec{r}_{A_0} = (x_{A_0}, y_{A_0}, z_{A_0})$ and $\vec{r}_{B_0} = (x_{B_0}, y_{B_0}, z_{B_0})$, then the time evolution of their position is given by their respective diffusion equation [van Zon J.S., et al (2005), Plante I. (2021)]:

$$\frac{\partial}{\partial t}p_A(\vec{r}_A, t|\vec{r}_{A_0}) = D_A\nabla_A^2 p_A(\vec{r}_A, t|\vec{r}_{A_0})$$

$$\frac{\partial}{\partial t}p_B(\vec{r}_B, t|\vec{r}_{B_0}) = D_B\nabla_B^2 p_B(\vec{r}_B, t|\vec{r}_{B_0})$$

The fact that each diffusion process is independent tells us that the probability to find the molecules on the respective positions $\vec{r}_A$ and $\vec{r}_B$, at a certain time t, is the product of both probability distributions $p_A \cdot p_B$, written as:

$$p(\vec{r}_A, \vec{r}_B, t|\vec{r}_{A_0}, \vec{r}_{B_0}) = p_A(\vec{r}_A, t|\vec{r}_{A_0}) \cdot p_B(\vec{r}_B, t|\vec{r}_{B_0})$$

Then, as we multiply and re-arrange the equations for each molecule diffusion we obtain the following expression:

$$\frac{\partial}{\partial t}p(\vec{r}_A, \vec{r}_B, t|\vec{r}_{A_0}, \vec{r}_{B_0}) = [D_A\nabla_A^2 + D_B\nabla_B^2]\, p(\vec{r}_A, \vec{r}_B, t|\vec{r}_{A_0}, \vec{r}_{B_0})$$

Where we can take the term $\widetilde{D} = D_A\nabla_A^2 + D_B\nabla_B^2$ known as the *diffusion operator* [Plante I. (2021)]. The quantity of interest is the intermolecular distance $\vec{r} = \vec{r}_B - \vec{r}_A$, that can be used along the variable $\vec{R} = b\vec{r}_B + a\vec{r}_A$, with a, b constants that will be determined; to perform a coordinate transformation. The inverse transformations in terms of the original coordinates are:

$$\vec{r}_A = -\frac{b}{a+b}\vec{r} + \frac{1}{a+b}\vec{R} \quad \text{and} \quad \vec{r}_B = \frac{a}{a+b}\vec{r} + \frac{1}{a+b}\vec{R}$$

Therefore, the differential operator Nabla of the new coordinate system is:

$$\nabla_r = \nabla_A\frac{d\vec{r}_A}{d\vec{r}} + \nabla_B\frac{d\vec{r}_B}{d\vec{r}} = -\frac{b}{a+b}\nabla_A + \frac{a}{a+b}\nabla_B$$

$$\nabla_R = \nabla_A \frac{d\vec{r}_A}{d\vec{R}} + \nabla_B \frac{d\vec{r}_B}{d\vec{R}} = \frac{1}{a+b}\nabla_A + \frac{1}{a+b}\nabla_B$$

And the original differential operators can be rewritten as:

$$\nabla_A = a\nabla_R - \nabla_r$$

$$\nabla_B = b\nabla_R + \nabla_r$$

If we square them, we can obtain the Laplacian operator as:

$$\nabla_A^2 = a^2\nabla_R^2 + \nabla_r^2 - 2a\nabla_R \cdot \nabla_r$$

$$\nabla_B^2 = b^2\nabla_R^2 + \nabla_r^2 + 2b\nabla_R \cdot \nabla_r$$

Which are useful to redefine the diffusion operator as:

$$\widetilde{D} = (D_A a^2 + D_B b^2)\nabla_R^2 + (D_A + D_B)\nabla_r^2 + 2(D_B b - D_A a)\nabla_R \cdot \nabla_r$$

If then, we choose $a = \sqrt{D_B/D_A}$ and $b = \sqrt{D_A/D_B}$, this differential operator simplifies to:

$$\widetilde{D} = (D_A + D_B)\nabla_R^2 + (D_A + D_B)\nabla_r^2$$

This implies that the probability density function that determines the original diffusion process of both molecules can be described as two independent processes in the new coordinate system $p(\vec{r}, \vec{R}, t|\vec{r}_0, \vec{R}_0) = p(\vec{r}, t|\vec{r}_0) \cdot p(\vec{R}, t|\vec{R}_0)$. And more importantly, one of those expressions is in terms of the intermolecular distance $\vec{r}$, which can be used to test the reaction radius condition for the chemical reaction to occur and can be solved using the GFDE [van Zon J.S., et al (2005), Plante I. (2021)]. Thus, the diffusion equation for $\vec{r}$ can be expressed as:

$$\frac{\partial}{\partial t} p(\vec{r}, t|\vec{r}_0) = D\nabla_r^2 p(\vec{r}, t|\vec{r}_0)$$

With $D = (D_A + D_B)$ is the sum of the diffusion coefficients of the reactants involved. It is important to note that reactions can occur between all types of molecules. In the case of a reaction between charged molecules, they experience an electrostatic force that must be taken into account as part of the reaction conditions [Planet I. (2011, 2021)]. Using the Debye-Smoluchowski equation, the electrostatic force can be represented by the gradient of a potential $U(\vec{r})$ that depends on the intermolecular distance $\vec{r}$. This means that the force applied to molecule B is $\vec{F} = \nabla_{\mathrm{B}} U$, while for molecule A it will be $-\vec{F} = \nabla_{\mathrm{A}} U$ [van Zon J.S., et al (2005)]. In this case, the probability density function that describes the evolution of the molecule's position follows the DSE:

$$\frac{\partial}{\partial t} p(\vec{r}_A, \vec{r}_B, t|\vec{r}_{A_0}, \vec{r}_{B_0}) = \left[D_A\nabla_A^2 + D_B\nabla_B^2 + \beta(D_A\nabla_{\mathrm{A}} - D_B\nabla_{\mathrm{B}}) \cdot \vec{F}\right] p(\vec{r}_A, \vec{r}_B, t|\vec{r}_{A_0}, \vec{r}_{B_0})$$

It can be shown that using the same coordinate transformation the differential operator that describe the electrostatic force $D_A\nabla_{\mathrm{A}} - D_B\nabla_{\mathrm{B}}$ can be written as $(D_A + D_B)\nabla_r = D\nabla_r$ [Plante I. (2021)] and the component of the DSE equation that depends on the intermolecular radius can be written as:

$$\frac{\partial}{\partial t} p(\vec{r}, t|\vec{r}_0) = D\nabla_r \cdot \left[\nabla_r - \beta\vec{F}\right] p(\vec{r}, t|\vec{r}_0)$$

Depending on the type of molecules involved in the reaction, they can be classified into four categories considering neutral or charged molecules and if the reaction is partially or completely controlled by diffusion [Plante I. (2011,2021)]. The simplest case, type I, are the reactions between neutral molecules totally controlled by diffusion. This means that the force between molecules is zero $\vec{F} = 0$ and a reaction only occurs if the intermolecular distance is smaller than the reaction radius when a collision takes place. The solution of the Debye-Smoluchowski equation, taking the dependence on the intermolecular angles θ, ϕ by separated [Plante I. (2016)], while the dependence on the magnitude of the vector r can be solved with GFDE resulting on the following probability distribution function:

$$4\pi r r_0 p_I(r,t|r_0) = \frac{1}{\sqrt{4\pi Dt}}\left\{\exp\left[-\frac{(r-r_0)^2}{4Dt}\right] - \exp\left[-\frac{(r+r_0-2\sigma)^2}{4Dt}\right]\right\}$$

Then, the probability that the molecules survive, meaning that the distance between molecules is always larger than the reaction radius σ, is given by the integral of the distribution from this value $r = \sigma$ up to infinity, $r = \infty$ [van Zon J.S., et al (2005)]:

$$S_I(t|r_0) = \int_\sigma^\infty 4\pi r^2 p_I(r,t|r_0)dr$$

Consequently, the probability of reaction $P_I(t|r_0)$ on a certain time t, starting from an initial separation r_0 is given by the complementary probability of this integral, described by the expression:

$$P_I(t|r_0) = 1 - \int_\sigma^\infty 4\pi r^2 p_I(r,t|r_0)dr = \frac{\sigma}{r_0} Erfc\left(\frac{r_0-\sigma}{\sqrt{4Dt}}\right)$$

Where $Erfc(z)$ is the complementary error function defined as:

$$Erfc(z) = \frac{2}{\sqrt{\pi}}\int_z^\infty \exp(-t^2)dt$$

The relationship between the solution for the probability of reaction and the macroscopic observed reaction rate is given by the next expression [Rice S.A. (1984), Plante I. (2011)]:

$$k_{obs} = 4\pi\sigma D$$

In order to obtain the proper probability function that describes the solution for each type of reaction, specific boundary and reaction conditions need to be established. Thus, the DSE will take different forms. In general, the theory of diffusion and the solution by Green's function are the necessary tools to solve the different equations that describe each type of reaction. There exists detailed literature that describes the mathematical procedure and background to develop the solution [van Zon J.S., et al (2005), Plante I. (2011,2021)]. However, the specific solution for all types of reactions is beyond the scope of this section.

Nevertheless, there is an extra type of reaction of particular interest for this research work. The reactions between the molecules that escaped the spur and the bulk of the aqueous solution, called *background reactions*. The molecules in the bulk are homogeneously distributed and exist at a concentration much higher than those of the free radicals produced by radiation. This type of reaction can represent the action of solvents added intentionally to the solution, like the dimethyl

sulfoxide (DMSO) or tris-hydroxyethyl-aminomethane (Tris) which are used as cryoprotectant for DNA suspended on solution [Milligan J.R. et al (1993), Tomita H., et al (1995)]; or biomolecules naturally present on the cellular medium, since they can reach concentrations of about 1 mol per liter [Michaels H.B. & Hunt J.W. (1978), Labarbe R., et al(2020)]. For this type of reaction, the probability P_{VI} in a small-time interval Δt for a molecule A to react with a concentration of molecules B in the medium is given by:

$$P_{VI}(\Delta t) = 1 - \exp(-k \cdot [B]\Delta t)$$

Where [B] is the concentration, k is the reaction rate between the chemical specie A and the medium constituent B. It is assumed that, since the concentration $[B]$ is much larger than $[A]$, the reactions $A + B$ will not significantly change $[B]$, therefore the quantity $k \cdot [B]$ is a constant known as *scavenging capacity* with units s^{-1}. If the time step is sufficiently small, the probability of reaction can be approximated to [Plante I. (2021)]:

$$P_{VI}(\Delta t) = k[B]\Delta t$$

2.1.3.1 Models for the heterogeneous chemistry of pure water

The kinetic parameters, including the diffusion coefficient D, reaction radius σ and reaction rates k, for the radiolitic species have been studied in depth up to temperatures of 300° and compiled in the past, since they were important in the research of the radiation chemistry of nuclear reactors, especially for the corrosion effects by free radicals [Buxton G.V., et al (1988), Elliot A.J. (1994), Elliot A.J. & Bartels D. (2009)]. A list of these parameters is provided next, on table 2.2.

Table 2.2. Kinetic parameters for the radiolitic species.

Symbol	Name	D (10^9 nm^{2}s^{-1})	σ(nm)
e_{aq}^-	Aqueous electron	4.9	0.50
OH	Hydroxyl	2.2	0.22
H	Hydrogen	7.0	0.19
H_3O^+	Hydronium	9.46	0.25
H_2	Dihydrogen	4.8	0.14
OH^-	Hydroxide	5.3	0.33
H_2O_2	Hydrogen peroxide	2.3	0.21
O_2	Oxygen	2.4	0.17
O_2^-	Superoxide anion	1.75	0.22
HO_2	Hydroperoxide	2.3	0.21
HO_2^-	Diloxanide	1.4	0.25
O^-	Oxide radical ion	2.0	0.25
O_3	Ozone	2.0	0.20
O_3^-	Ozonide ion	2.0	0.20
$O(^3P)$	Atomic oxygen on the ^{3}P ground state	2.0	0.20

The complete chemical scheme that describes every possible reaction between radiolitic species is vast [Elliot A.J. & McCracken D.R. (1990), Pastina B. & LaVerne J.A. (2001)]. However, it has been proven that a reduced scheme of 10 principal reactions, presented on table 2.3, and used on a multitude of MCTS codes, is sufficient to reproduce experimental results for the concentration of radiolytic species within 1 microsecond, corresponding to the end of the heterogeneous chemical

stage, [Pimblott S.M. & LaVerne J.A. (1990), Ballarini F., et al (2000), Kreipl M.S., et al. (2009), Karamitros M., et al (2011), Schuemann J., et al (2019), Ramos-Mendez J. et al (2018, 2020, 2022)].

Table 2.3. Reduced chemical scheme for the main reactions on pure water

No	Reaction	$k(\mathrm{M^{-1}s^{-1}})$
R_1	$e^-_{aq} + e^-_{aq}\ (+ 2H_2O) \rightarrow H_2 + 2OH^-$	6.36×10^9
R_2	$e^-_{aq} + H_3O^+ \rightarrow H + (H_2O)$	2.11×10^{10}
R_3	$e^-_{aq} + H\ (+H_2O) \rightarrow OH^- + H_2$	2.50×10^{10}
R_4	$e^-_{aq} + OH \rightarrow OH^-$	2.95×10^{10}
R_5	$e^-_{aq} + H_2O_2 \rightarrow OH + OH$	1.10×10^{10}
R_6	$H_3O^+ + OH^- \rightarrow (2H_2O)$	1.13×10^{11}
R_7	$H + H \rightarrow H_2$	5.03×10^{10}
R_8	$H + OH \rightarrow (H_2O)$	1.55×10^{10}
R_9	$H + H_2O_2 \rightarrow OH + (H_2O)$	9.00×10^7
R_{10}	$OH + OH \rightarrow H_2O_2$	5.50×10^9

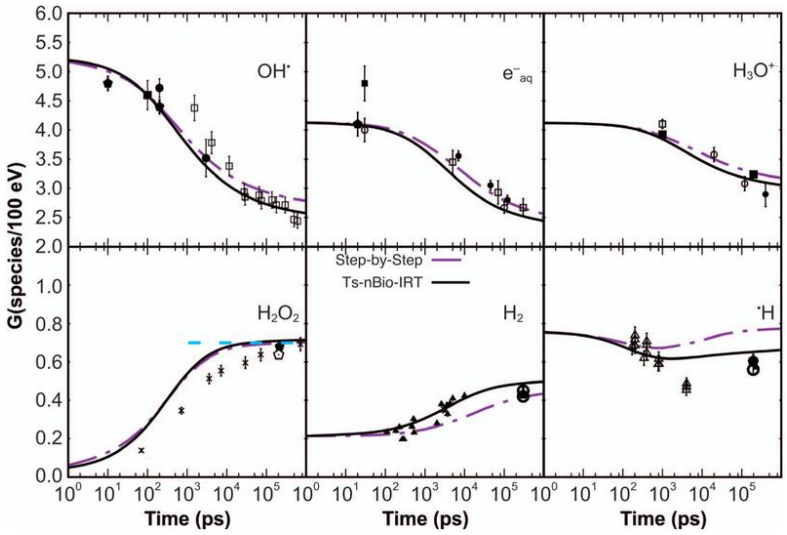

Figure 2.8. Time evolution of several radiolitic species using TOPAS-nBio compared to experimental data. Image taken from: [Schuemann J., et al (2019)]

2.1.4 Chemical yields quantified by the G value.

The quantity used to describe the yield of chemical species X in radiation chemistry is the G-Value $G(X)$. The G value is defined as the number N_X of chemical molecules produced or lost per 100eV of energy deposited in the medium [Buxton G.V., et al (1988), Plante I. (2021)]:

$$G(X) = \frac{N_X}{100eV}$$

This quantity is dependent on time and particle type. For comparison with experimental data, the escape yield G_X is used and is defined as the G value at the system steady state [Pastina B. & LaVerne J.A. (2001), Plante I. (2021)]. The Gx can be used as the starting point for the simulation of processes that extend for longer periods of time (hours or days), like the long-term accumulation of hydrogen peroxide on pure water under different radiation rate conditions [Wardman P. (2020)] or the

mechanisms of biological response to radiation [Labarbe R., et al (2020)]. Considering that the density of water is 1kg/L, and the equivalence of joule to electron volts is $1\mathrm{J} = 6.242 \times 10^{18}\mathrm{eV}$, then the Gx can be reported in units of molar concentration per deposited dose, which is convenient for the simulation of the production of radicals dependent on a specific dose rate ($\mathrm{Gy/s}$) [Wardman P. (2020)], as follows:

$$1molecule/100eV = 0.1036\ \mu\mathrm{M/Gy}$$

Table 2.4. Escape yields for the radiolitic species under γ-rays irradiation, data taken from [Pastina B. & LaVerne J.A. (2001) & Wardman P. (2020)]

Symbol	$N_{mol}/100eV$	$\mu\mathrm{M/Gy}$
$\mathrm{e_{aq}^-}$	2.26	0.269
H	0.66	0.068
$\mathrm{H_2}$	0.45	0.046
OH	2.70	0.280
$\mathrm{H_2O_2}$	0.70	0.073
$\mathrm{HO_2}$	0.02	0.002
$\mathrm{H_3O^+}$	3.10	0.320
$\mathrm{OH^-}$	0.50	0.052

2.1.5 Homogeneous chemical stage

Around one microsecond after irradiation, the radiolitic species have reacted and diffused sufficiently in the medium to reach a homogeneous distribution. These surviving species can further react between them and with the molecules present in its environment [Plante I. (2021)]. Considering this new distribution, it is possible to apply other methods to model the next chemical stage. Specifically, with the theory of chemical kinetics, based on the mass action law, which states that the rate of a reaction is proportional to the product of the active masses of the reactants involved [Saunders N. & Miodownik A.P. (1998)].

Under these conditions, chemical reactions can be represented as differential equations. We need to consider several parameters in order to accurately describe each reaction. These parameters include the molecularity, which is the number of molecules involved in the reaction; the stoichiometry, which is the relationship between the molecular weights before and after the reaction occurs; the rate law, which is a mathematical expression that describes the reaction rate; and the order of the rection, which is the total sum of the powers of the reactive concentration inside of the rate law [Atkins P. (2006)].

Using the same example as the heterogeneous chemical stage section, let us consider the reaction $A + B \rightarrow P$. This is a bimolecular reaction since it involves two molecules, the stoichiometry is based on the conservation of mass, this means that the molecular weight of the reactants should be the same as the products [Atkins P. (2006)]. Therefore, a more precise stoichiometry diagram that describes this reaction will be:

$$A + B \rightarrow AB$$

Rate laws should be determined experimentally. However, for some elemental reactions these laws can be directly deduced from the reaction's stoichiometry, meaning that the rate is proportional to the product of the concentration of the reactants involved (in this case $[A][B]$). In the same way, if

a bimolecular reaction involves two molecules of the same type, for example $2A \rightarrow A_2$, the reaction rate will also be proportional to the product $[A][A]$, which can be written as the square of the concentration $[A]^2$. The constant of proportionality k between the rate of time change of the product's concentration with the product of the reactants concentrations is called the reaction's rate constant [Atkins P. (2006)]:

$$\frac{d}{dt}[P] = k[A][B]$$

The order of the reaction is the sum of the powers of the reactant's concentrations. Here both $[A]$ and $[B]$ have order 1, therefore the total order of the reaction is 2. The same is true for a bimolecular reaction with the same type of molecules $2A \rightarrow A_2$. Since the concentration $[A]$ is squared in the rate law, it is also a second order reaction described by:

$$\frac{d[A_2]}{dt} = k[A][A] = k[A]^2$$

Processes like the constant spontaneous generation or degradation of a molecule do not depend directly on the concentration of any reactive, therefore they are order zero reactions and their rate laws can be represented as:

$$\rightarrow A, \quad \frac{dA}{dt} = k_{gen} \qquad or \qquad A \rightarrow , \quad \frac{dA}{dt} = -k_{deg}$$

As seen in previous sections, one of the most important types of reactions is the one that occurs with the molecules that constitute the medium. In the heterogeneous chemical stage, the reaction between the chemical specie A with the medium molecule B that have a much larger concentration $[B]$ mediated by a reaction rate k; it can be represented as a first order reaction:

$$\frac{d[A]}{dt} = -K_B[A]$$

Where the constant $K_B = k[B]$ is the scavenger capacity of the molecule B. Despite the fact that the molecules on a complex reaction scheme can react with a multitude of other species present in the system and not exclusively with the molecules in the medium, the solution of this type of reaction's differential equations provide a useful measure of the mean life $t_{1/2}$ of the initial concentration of the chemical specie $[A]_0$ in the presence of a scavenger with concentration $[B]$ and indicate the approximate time that it will survive in the environment [Atkins P. (2006)]:

$$\frac{d[A]}{[A]} = -K_B dt \Leftrightarrow \ln\left(\frac{[A]}{[A]_0}\right) = -k[B]t \Leftrightarrow t_{1/2} = -\frac{1}{k[B]} \cdot \ln\left(\frac{[A]_0/2}{[A]_0}\right) = \ln(2)/k[B]$$

The reactions that involve a higher number of molecules will have a corresponding molecularity, stoichiometry and order. Therefore, their rate law should reflect the total number of reactants as a consequence. However, rate laws do not always correspond to the stoichiometry of the reaction, and it is possible that a reaction that involves just two molecules has a very complex rate equation. One of the most relevant examples for this research work is the case of enzyme activation.

Enzymes are specialized proteins that are distributed homogeneously in the cellular environment. They have active sites where a certain substrate, that can be an organic or inorganic compound, can

attach and change the conformation of the enzyme in order to perform a biological process [Atkins P. (2006)].

Experimentally, it has been observed that the reaction rate v between the Enzyme E and substrate S is proportional to the concentration of the enzyme $[E]$, for low concentrations of the substrate it is proportional to $[S]$, but for high concentrations it saturates to a certain value v_{max}. The kinetics of the Michaelis-Menten mechanism reproduce this behavior of this reaction [Atkins P. (2006)] and it is described by the expression:

$$v = k[E]\frac{[S]}{M + [S]}$$

Here M is the so-called Michaelis constant that characterizes the action of the enzyme over the substrate, it has units of molar concentration $(\mathrm{mol/L})$. It can be observed that at lower substrate concentrations ($[S] \to 0$) the reaction rate is directly proportional to $[S]$:

$$\text{if } [S] \ll M \text{ then } \frac{1}{M + [S]} \approx \frac{1}{M} \iff \lim_{[S]\to 0} v = \frac{k}{M}[E][S]$$

While v_{max} is the saturation value in the limit of the equation where the substrate is very high ($[S] \to \infty$), meaning:

$$\text{if } [S] \gg M \text{ then } \frac{[S]}{M + [S]} \approx 1 \iff \lim_{[S]\to \infty} v = k[E] = v_{max}$$

This type of reaction cannot be classified into a specific order but can be used to model the interaction of complex biomolecules like proteins [Atkins P. (2006)].

2.1.5.1 Models for the homogeneous chemistry of pure water

In the case of pure water, the reactions between radiolitic species are numerous. In [Pastina B. & LaVerne J.A. (2001)], a kinetic model for the complete chemical reaction scheme of water radiolysis was proposed based on a previous model by [Elliot A.J. & McCracken D.R. (1990)]. It consists of about 70 different reactions and was applied to reproduce the time evolution and final long-term concentration of hydrogen peroxide under different irradiation conditions including gamma rays, 5MeV helium ions, 2 and 10 MeV protons.

The first group of reactions in the scheme are the acid-base reactions, shown in Table 2.5, a set of dissociation-recombination processes that are in equilibrium, characterized by a forward and backwards reaction rate. It is notable the dissociation of water and recombination of hydroxide and protons $(\mathrm{H_2O} \leftrightarrow \mathrm{H^+ + OH^-})$ a reaction that maintains the equilibrium of $\mathrm{H^+}$ and $\mathrm{OH^-}$ ions neutral, associated with the pH of water [Elliot A.J. (1993), Elliot A.J. & Bartels D.M (2009)].

Table 2.5. Acid-base equilibrium reactions

$k_{fw}(M^{-1}s^{-1})$	Forward reaction / Backwards reaction	$k_{bk}(s^{-1})$
1.4×10^{11}	$H^+ + OH^- \leftrightarrow (H_2O)$	2.53×10^{-5}
5.0×10^{10}	$H^+ + HO^- \leftrightarrow H_2O_2$	1.12×10^{-1}
1.3×10^{10}	$H_2O_2 + OH^- \leftrightarrow HO_2^- + (H_2O)$	3.22×10^{9}
2.2×10^{7}	$H + OH^- \leftrightarrow e_{aq}^- + (H_2O)$	1.9×10^{1}

2.3×10^{10}	$e_{aq}^{-} + H^{+} \leftrightarrow H$	3.9
1.3×10^{10}	$OH + OH^{-} \leftrightarrow O^{-} + (H_2O)$	2.72×10^{9}
1.0×10^{10}	$O^{-} + H^{+} \leftrightarrow OH$	1.26×10^{-1}
5.0×10^{10}	$O_2^{-} + H^{+} \leftrightarrow HO_2$	1.345×10^{6}
5.0×10^{10}	$HO_2 + OH^{-} \leftrightarrow O_2^{-} + (H_2O)$	1.03×10^{3}

The next group are the chemical reactions (Table 2.6) between chemical radiolytic species, when neighboring water molecules are involved or are the product of the reaction it is denoted as (H_2O) since water molecules are not tracked.

Table 2.6. Chemical Reactions

Reaction	$k_{obs}(M^{-1}s^{-1})$	Reaction	$k_{obs}(M^{-1}s^{-1})$
$e_{aq}^{-} + OH \rightarrow OH^{-}$	3.0×10^{10}	$OH + O_3^{-} \rightarrow 2O_2^{-} + H^{+}$	6.0×10^{9}
$e_{aq}^{-} + H_2O_2 \rightarrow OH + OH^{-}$	1.1×10^{10}	$OH + O_3 \rightarrow HO_2 + O_2$	1.1×10^{8}
$e_{aq}^{-} + O_2^{-} + (H_2O) \rightarrow HO_2^{-} + OH^{-}$	1.3×10^{10}	$HO_2 + O_2^{-} \rightarrow HO_2^{-} + O_2$	8.0×10^{7}
$e_{aq}^{-} + HO_2 \rightarrow HO_2^{-}$	2.0×10^{10}	$2HO_2 \rightarrow H_2O_2 + O_2$	7.0×10^{5}
$e_{aq}^{-} + O_2 \rightarrow O_2^{-}$	1.9×10^{10}	$HO_2 + O^{-} \rightarrow O_2 + OH^{-}$	6.0×10^{8}
$2e_{aq}^{-} + (2H_2O) \rightarrow H_2 + 2OH^{-}$	5.5×10^{9}	$HO_2 + H_2O_2 \rightarrow OH + O_2 + (H_2O)$	5.0×10^{-1}
$e_{aq}^{-} + H + (H_2O) \rightarrow H_2 + OH^{-}$	2.5×10^{10}	$HO_2 + HO_2^{-} \rightarrow OH + O_2 + OH^{-}$	5.0×10^{-1}
$e_{aq}^{-} + HO_2^{-} \rightarrow O^{-} + OH^{-}$	3.5×10^{9}	$HO_2 + O_3^{-} \rightarrow 2O_2 + OH^{-}$	6.0×10^{9}
$e_{aq}^{-} + O^{-} + (H_2O) \rightarrow 2OH^{-}$	2.2×10^{10}	$HO_2 + O_3 \rightarrow HO_3 + O_2$	5.0×10^{8}
$e_{aq}^{-} + O_3^{-} + (H_2O) \rightarrow O_2 + 2OH^{-}$	1.6×10^{10}	$2O_2^{-} + (2H_2O) \rightarrow H_2O_2 + O_2 + 2OH^{-}$	1.0×10^{2}
$e_{aq}^{-} + O_3 \rightarrow O_3^{-}$	3.6×10^{10}	$O_2 + O^{-} + (H_2O) \rightarrow O_2 + 2OH^{-}$	6.9×10^{8}
$H + O^{-} \rightarrow OH^{-}$	1.0×10^{10}	$O_2^{-} + H_2O_2 \rightarrow OH + O_2 + OH^{-}$	1.3×10^{-1}
$H + HO_2^{-} \rightarrow OH + OH^{-}$	9.0×10^{7}	$O_2^{-} + HO_2^{-} \rightarrow O^{-} + O_2 + OH^{-}$	1.3×10^{-1}
$H + O_3^{-} \rightarrow OH^{-} + O_2$	1.0×10^{10}	$O_2^{-} + O_3^{-} + (H_2O) \rightarrow 2O_2 + 2OH^{-}$	1.0×10^{4}
$2H \rightarrow H_2$	7.8×10^{9}	$O_2^{-} + O_3 \rightarrow O_3^{-} + O_2$	1.5×10^{9}
$H + OH \rightarrow (H_2O)$	7.0×10^{9}	$2O^{-} + (H_2O) \rightarrow HO_2^{-} + OH^{-}$	1.0×10^{9}
$H + H_2O_2 \rightarrow OH + (H_2O)$	9.0×10^{7}	$O^{-} + O_2 \rightarrow O_3^{-}$	3.6×10^{9}
$H + O_2 \rightarrow HO_2$	2.1×10^{10}	$2O^{-} + H_2O \rightarrow HO_2^{-} + OH^{-}$	1.0×10^{9}
$H + HO_2 \rightarrow H_2O_2$	1.8×10^{10}	$O^{-} + O_2 \rightarrow O_3^{-}$	3.6×10^{9}
$H + O_2^{-} \rightarrow HO_2^{-}$	1.8×10^{10}	$O^{-} + H_2 \rightarrow H + OH^{-}$	8.0×10^{7}
$H + O_3 \rightarrow HO_3$	3.8×10^{10}	$O^{-} + H_2O_2 \rightarrow O_2^{-} + (H_2O)$	5.0×10^{8}
$2OH \rightarrow H_2O_2$	3.6×10^{9}	$O^{-} + HO_2^{-} \rightarrow O_2^{-} + OH^{-}$	4.0×10^{8}
$OH + HO_2 \rightarrow O_2 + (H_2O)$	6.0×10^{9}	$O^{-} + O_3^{-} \rightarrow 2O_2^{-}$	7.0×10^{8}
$OH + O_2^{-} \rightarrow OH^{-} + O_2$	8.2×10^{9}	$O^{-} + O_3 \rightarrow O_2^{-} + O_2$	5.0×10^{9}
$OH + H_2 \rightarrow H + (H_2O)$	4.3×10^{7}	$O_3^{-} + H^{+} \rightarrow O_2 + OH$	9.0×10^{10}
$OH + H_2O_2 \rightarrow HO_2 + (H_2O)$	2.7×10^{7}	Inverse reaction/decomposition	$k_{obs}(s^{-1})$
$OH + O^{-} \rightarrow HO_2^{-}$	2.5×10^{10}	$H + (H_2O) \rightarrow H_2 + OH$	1.1×10^{1}
$OH + HO_2^{-} \rightarrow HO_2 + OH^{-}$	7.5×10^{9}	$O_3^{-} \rightarrow O_2 + O^{-}$	3.3×10^{3}
$OH + O_3^{-} \rightarrow O_3 + OH^{-}$	2.6×10^{9}	$HO_3 \rightarrow O_2 + OH$	1.1×10^{5}

These models for the physical-chemical interactions for the different stages of the water radiolysis process constitute the initial conditions for the radiation effect on a biological environment. However, it is necessary to model their interaction with DNA and other important biomolecules to study the long-term consequences of the biological response to radiation.

2.2 DNA Damage

2.2.1 DNA Structure and organization

Desoxyribonucleic Acid (DNA) is the main target of radiation to induce a radiobiological effect that includes cell death and mutations. DNA is a macromolecule with a natural helix structure with two strands. This configuration was proposed in 1953 by James Watson and Francis Crick [Hall E.J. & Giaccia A.J. (2012)]. The smallest possible unit of DNA is known as a *nucleotide*, it has three components or sub-units: a simple sugar molecule called deoxyribose (2-deoxy-D-ribose-C5H10O4), an inorganic phosphate group and a nitrogenous base [Hall E.J. & Giaccia A.J. (2012), Alizadeh E., et al (2012)].

The DNA strands consist of a support backbone made of alternate units of sugar-phosphates. Deoxyribose is a monosaccharide arranged on a *furanose* ring made of 5 carbons and one oxygen atom. The carbons in this ring are numbered from 1' to 4' in the clockwise direction from the oxygen position and the 5' carbon is externally attached to the 4' inner carbon of the ring [Alizadeh E., et al. (2012)].

This sugar molecule is the center piece of the nucleotide since it can join the nitrogenous bases with a *glucoside* bond (C-N) on the 1' carbon of the furanose ring. Two consecutive sugars are joined though a phosphate group with a *phosphodiester* bond that connects the 5' carbon of one deoxyribose with the 3' of the next one [Alizadeh E. & Sanche L. (2012)]. This gives the DNA molecule strands a natural *orientation* or *directionality* called 3'5' that influences the process of division and DNA repair [Oh J-M. & Myung K. (2022)].

Two of the four nitrogenous bases, Thiamine (T) and Cytosine (C) are pyrimidines, with a single-ring structure; while the two remaining, Adenine and Guanine, are purines with a double-ring structure. The nitrogenous bases on opposite strands are complementary, meaning that an Adenine is always coupled with a Thiamine while a Cytosine attaches a Guanine. The two strands are held together by hydrogen bonds between the complementary nitrogenous bases. The Guanine is joined with three bonds while the union of Adenine with Thiamine has only two. A couple of these bases are known as a base-pair (bp), figure 2.9, and their linear sequence of assembly determines the heritable genetical information coded in the DNA molecule [Hall E.J. & Giaccia A.J. (2012), Alizadeh E. & Sanche L. (2012)].

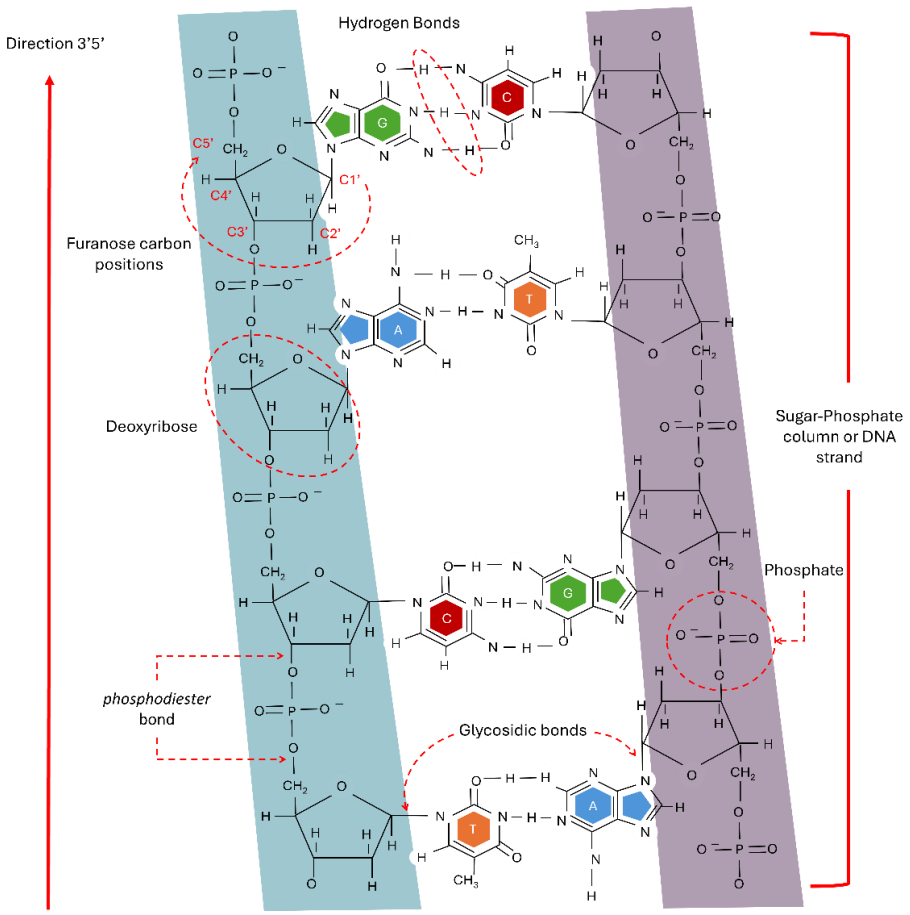

Figure 2.9. structure of the DNA, image adapted from [Sanche L. (2008)] and [Alizadeh E. & Sanche L. (2012)]

Nuclear DNA is compacted and organized in several scales. The double helix, primary structure of DNA, is coiled around a group of specialized proteins known as *histones*. Each group consists of 4 pairs of different histones H2A, H2B, H3 and H4, forming an *octane*. Every 165 bp the DNA wraps two super-helical turns into an octane and forms a *nucleosome*. This DNA-protein complex is called chromatin and is composed of approximately the same molecular wight of genetic material and proteins. It forms a secondary "string of beads" geometrical structure. This fiber is organized into two levels of compactness, a condensed form called *heterochromatin,* and an open form called *euchromatin.* These density levels influence the accessibility to certain regions of DNA, and consequently, the gene expression [Felsenfeld G. & Groudine M. (2003)]. The DNA organization is shown in figure 2.10.

DNA organization and compactation depend on the cell mitotic phase. For non-dividing cells in the interphase, the genetic material is distributed homogeneously in the nucleus. Once the DNA is replicated into two sister chromatin fibers, the DNA condenses into individual compact regions called *chromosomes* in the prophase. The sister chromatins are joined in the chromosome *centromere.* Two structures called *centrosomes* form and start to move to opposite poles of the cell by the lengthening of the microtubules between them, called mitotic spindles. Next, in the proto-metaphase the nuclear membrane starts to open and the microtubes penetrate the nucleus attaching to the centrosomes in one extreme, and several of them bind to the chromosomes in the

other extreme or will collide with the spindles growing in the opposite direction. Then, in the metaphase the chromosomes migrate to the center of the cell and their centromeres align along an imaginary line called *metaphase plate,* equidistant to both centromeres. The sister chromatins break and start to be pulled back to the opposite sides of the cell in the anaphase, at the end both halves of the cell have an equal quantity of genetic material. Finally, in the Telophase two nucleus form, a nuclear membrane reappears and encircle both groups of chromosomes. DNA also starts to decondense, and the spindles degrade. Finally, the cytoplasm divides and form two daughter cells [Rehman I., et al (2023)], this process is shown on figure 2.10 below.

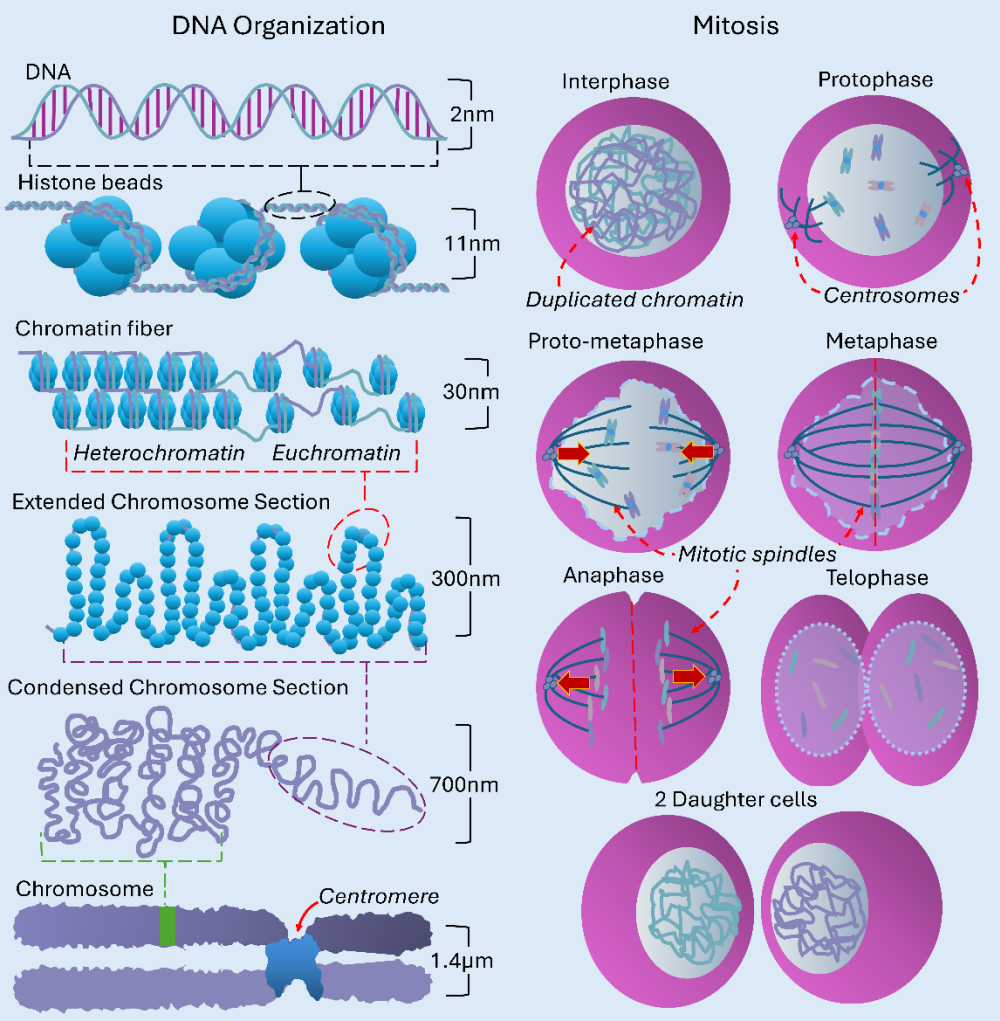

Figure 2.10. **Left**: different levels of DNA organization and compaction. **Right**: different phases of the mitosis process. Images adapted from [Felsenfeld G. & Groudine M. (2003)] and [Gilchrist D.A. (2024)]

The integrity of the genetic material is fundamental for the completion of the mitotic process and any non-repaired or miss-repaired lesion to the DNA is potentially lethal to the cell since it can interfere in the cellular division process.

2.2.2 Direct and indirect DNA Damage

DNA damage by ionizing radiation occurs by two mechanisms: physical and chemical. When radiation directly deposits energy in the DNA molecule, it can ionize its independent components

producing direct or *physical* damage. On the other hand, when radiation interacts with the molecules in the DNA's environment, it can dissociate them and produce free radicals that in turn can react with the genetic material, breaking the DNA chemical bonds and generating indirect or *chemical* damage [Alizadeh E. & Sanche L. (2012)]. The proportion of these effects in the total damage depends on the type of radiation employed and especially on the particle's LET [Meesungnoen J. & Jay-Gerin J.P. (2005), Hall E.J. & Giaccia A.J. (2012)].

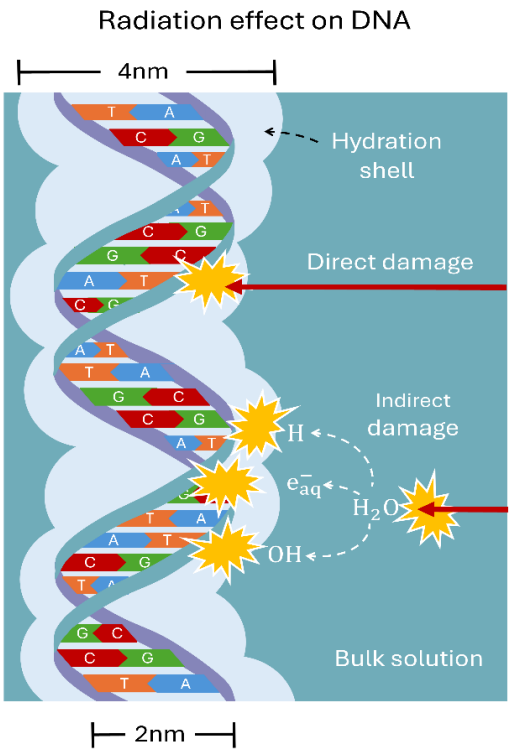

Figure 2.11. DNA direct and indirect damage scheme. Image adapted from [Hall E.J. & Giaccia A.J. (2012)]

Direct DNA damage contribution is challenging to determinate experimentally. For instance, small sequences of denatured DNA with several thousand base pairs (bp) length have been irradiated in ultravacuum conditions. The samples are suspended on thin films of amorphous ice to simulate the structure of water that surrounds the genetic material. Different freeze biomolecules and gases atmospheres, like oxygen or nitrogen, are used to recreate the cellular environment. These experiments have quantified the direct DNA damage by low energy electrons [Friedland W., et al (2017), Alizadeh E. & Sanche L. (2012)].

Complementary to these experimental results, computer simulations based on MC have been employed to study the direct DNA damage mechanism. These studies test theoretical models in order to find the unknown parameters involved in the interaction between radiation and the genetic material. Specifically, geometrical models of DNA overlapped with precalculated spatial distributions of energy interactions generated by MC radiation transport codes have been employed to study different models for the inductions of lesions in the DNA [Charlton D.E. et al (1986), Nikhoo H., et al (1997), Bernhardt Ph., et al. (2003), Edel S., et al (2006), Meylan S., et al (2017)].

Simulations indicate that the sensible target for the direct damage is the volume occupied by a phosphate group and its first hydration shell. The first hydration shell (approximately 4nm in radius) is the water molecule layer that encapsulates the DNA, figure 2.12 [Nikhoo H., et al (1997), Bernhardt Ph., et al. (2003), S. Meylan S., et al (2017)].

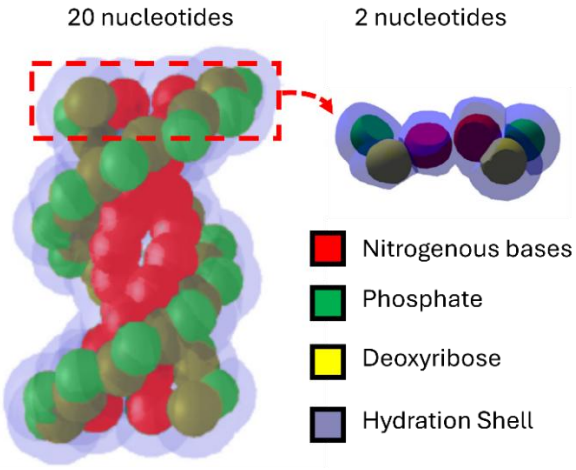

Figure 2.12. geometrical model for a DNA segment, their main components and the hydration shell that envelops the genetic material. Image adapted from [Meylan S., et al (2017)].

The models for direct damage have employed a probability value dependent on an energy threshold. For example, a step function has been reported where the probability of damage is zero for energies below the threshold and 100% for energies above it, resulting in values between 16eV by [Bernhardt Ph., et al. (2003)] and 17.5eV by [Nikjoo et al. (1997)]. Another example is the use of a ramp function, which is zero for all energy deposits below certain minimal value u_{min}, then it increases linearly until 100% at a maximum energy deposit value u_{max}. For this approach, the simulation resulted in values of $u_{min} = 5eV$ and $u_{max} = 37.5eV$, see figure 2.13 [Friedland W. et al (2017), Lampe N. et al (2018)]

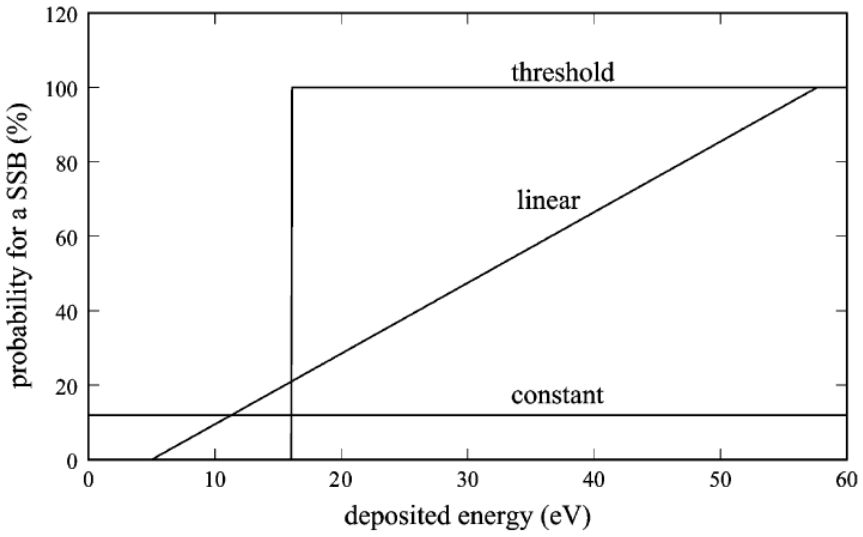

Figure 2.13. Different models for the probability of direct DNA damage as a function of the deposited energy. Image taken from [Bernhardt Ph., et al. (2003)]

However, in a homogeneous mixture of substances, the radiation energy absorbed by each of its components is approximately proportional to the molecular weight of each constituent. Therefore, in water solutions containing DNA at a concentration of 500 $\mathrm{mg/l}$, an example of an invitro solution with a value in between the average bacterial pathogens ($\sim 1.2 \mathrm{mg/l}$) [Khan D., et al (2023)] and eukaryote cells ($\sim 10000 \mathrm{mg/l}$) [Sprague B. L., et al (2006)] DNA nuclear concentrations; under gamma-ray irradiation approximately ~99.5% of the deposited energy will be absorbed by the water, and just ~0.5% by DNA. For these conditions, the majority of DNA damage will be produced indirectly by the free radicals produced by radiolysis, and just a small fraction by direct ionization of DNA [Von Sontang C. (2005)].

Indirect damage occurs when the incoming radiation interacts with the environment that surrounds DNA. This medium includes water, dissolved salts, biomolecules and oxygen [Alizadeh E. & Sanche L. (2012)] The products of water radiolysis capable of reacting with the DNA's components include OH, H and $\mathrm{e_{aq}^-}$. In particular, hydroxyl (OH) free radicals are neutral molecules with high affinity for electrons. OH radicals can *abstract* or remove hydrogen atoms from biomolecules, e.g., proteins, lipids and especially from components of DNA. This result in the formation of biological radicals in the process [Alizadeh E. & Sanche L. (2012)]. In addition, OH can be attached to a biomolecule and form *adducts*, modifying the internal conformation of the molecule [Dizdaroglu M. & Jaruga P. (2012].

DNA sub-units are complex molecules formed by several carbon atoms with hydrogen bonded to them. Therefore, free radicals can react with hydrogen atoms on multiple sites. Both the probability of reactions and their main products depend on the *attacked* site. Some products can experiment a chain of reactions that branch into several stable end points, and some of them can only form on the presence or absence of oxygen in the medium [Dizdaroglu M. & Jaruga P. (2012) Pogozelski W.K. & Tullius T.D. (1998)].

In general, if radicals react on the nitrogenated bases, they will be integrated into their structure and generate adducts, modifying the conformation of the base without breaking the DNA. On the other hand, the abstraction of hydrogen from the deoxyribose on the sugar-phosphate backbone can generate Strand Breaks (SB) [Alizadeh E. & Sanche L. (2012)]. However, there are exceptions to the rule depending on the attacked site of the DNA sub-units.

In [Dizdaroglu M. & Jaruga P. (2012)], an in-depth analysis was performed of the reactions between the DNA's components, their reaction rates, branching reactions and their main products. Taking the thymine as an example, the OH radical can attack this nitrogenated bases with a reaction rate of $\mathrm{k_{T-OH}} = 6.4 \times 10^9 \mathrm{M^{-1}s^{-1}}$ in two sites: 5' and 6' forming adducts $5-\mathrm{OH}$ and $6-\mathrm{OH}$ with probabilities of 60% and 30% respectively, the remaining 10% of the times OH radicals react with the methyl group $(\mathrm{CH_3})$ [Dizdaroglu M. & Jaruga P. (2012)].

Thymine reacts with aqueous electrons and hydrogen with reaction rates of $\mathrm{k_{T-e_{aq}^-}} = 1.8 \times 10^{10} \mathrm{M^{-1}s^{-1}}$ and $\mathrm{k_{T-H}} = 6.8 \times 10^8 \mathrm{M^{-1}s^{-1}}$respectively. The final product of both reactions is the adduct 5,6-hydrotiamina. However, these reactions can only occur in the absence of oxygen, since both $\mathrm{e_{aq}^-}$and H react with $\mathrm{O_2}$ with a reaction rate of about $\mathrm{k_{O_2}} = 2.0 \times 10^{10} \mathrm{M^{-1}s^{-1}}$, which is above the rate with the nitrogenous base [Dizdaroglu M. & Jaruga P. (2012)].

The adduct $5-\mathrm{OH}$ can abstract an hydrogen from its bond with the deoxyribose, transferring the damage to the sugar-phosphate backbone and possibly provoking a strand break. Both 5 and 6 OH adducts can react with free hydrogen atoms to form hydroxy-hydrothymines, which are stable products. However, if the medium contains dissolved oxygen, it inhibits the formation of these products and promotes the formation of peroxyl radicals instead, because the reaction has a rate controlled by diffusion with an approximate value of $k_{O_2} \approx 2.0 \times 10^9 M^{-1}s^{-1}$. One of the main stable products shared by both 5,6 OH adducts, in the absence of oxygen, and their peroxyl radicals in the presence of oxygen, is the thymine glycol [Dizdaroglu M. & Jaruga P. (2012].

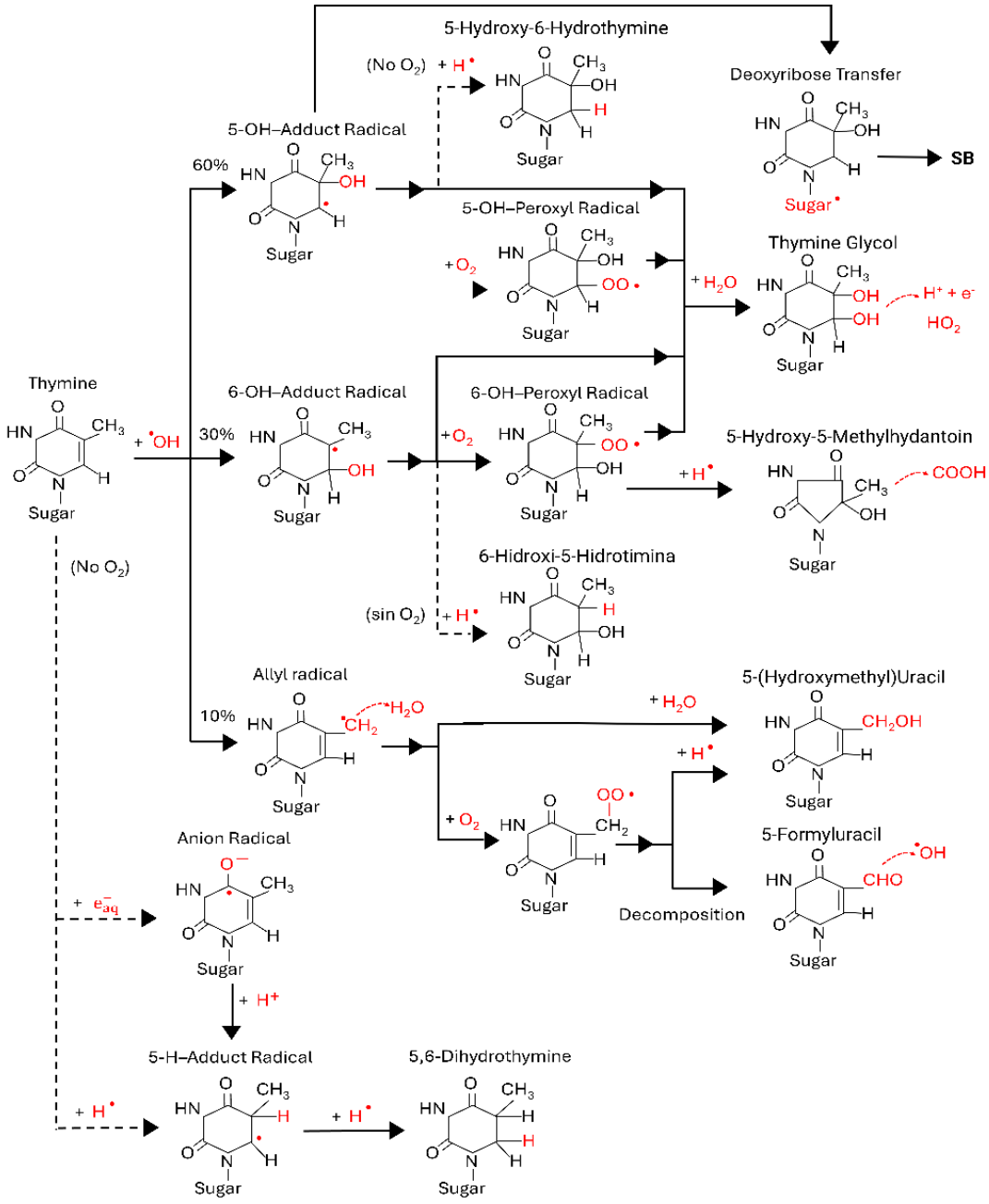

Figure 2.14. branching reactions between Thiamine with OH, e_{aq}^- and H radicals. Image adapted from [Dizdaroglu M. & Jaruga P. (2012].

On the other hand, the reaction of free radicals with the deoxyribose is dominated by OH. Thus, OH is the major mediator of indirect damage by ionizing radiation, and especially the strand breaks produced by the hydrogen abstraction in some sites of the sugar molecule [Balasubramanian B. et al, (1998)]. OH can react with every carbon site (1'-5') in the furanose ring with a general reaction rate of $k_{OH-DR} = 2.5 \times 10^{9} M^{-1} s^{-1}$. However, the exact value and probability of reactions depends on the exact site attacked. The radicals produced experience several transformations that can branch into different final products. In general, they can be classified as strand breaks (SB) or modified sugars where DNA is not broken [Pogozelski, W. K., & Tullius, T. D. (1998), Dizdaroglu M. & Jaruga P. (2012)].

Furthermore, some of those products can either occur in the presence of oxygen (in an aerobic environment), in the absence of it (in an anaerobic medium), or in both environments. Values for the probability of hydrogen abstraction P_r at each site are not absolutely defined. These values, instead, fall within an experimental range, but a general order has been found as follows:

$$P_r(H5') > P_r(H4') > P_r(H3') \approx P_r(H2') \approx P_r(H1').$$

It was also observed that the hydrogen sites more exposed to the medium, and consequently to the OH attacks, are the ones on the 4' and 5' carbon sites [Balasubramanian B. et al, (1998)]. It is important to note that: the majority of the products in any of the hydrogen abstraction sites of the damaged deoxyribose, end up breaking the bond with the nitrogenated base producing a free base in the process, figure 2.15 [Pogozelski W.K. & Tullius T.D. (1998)].

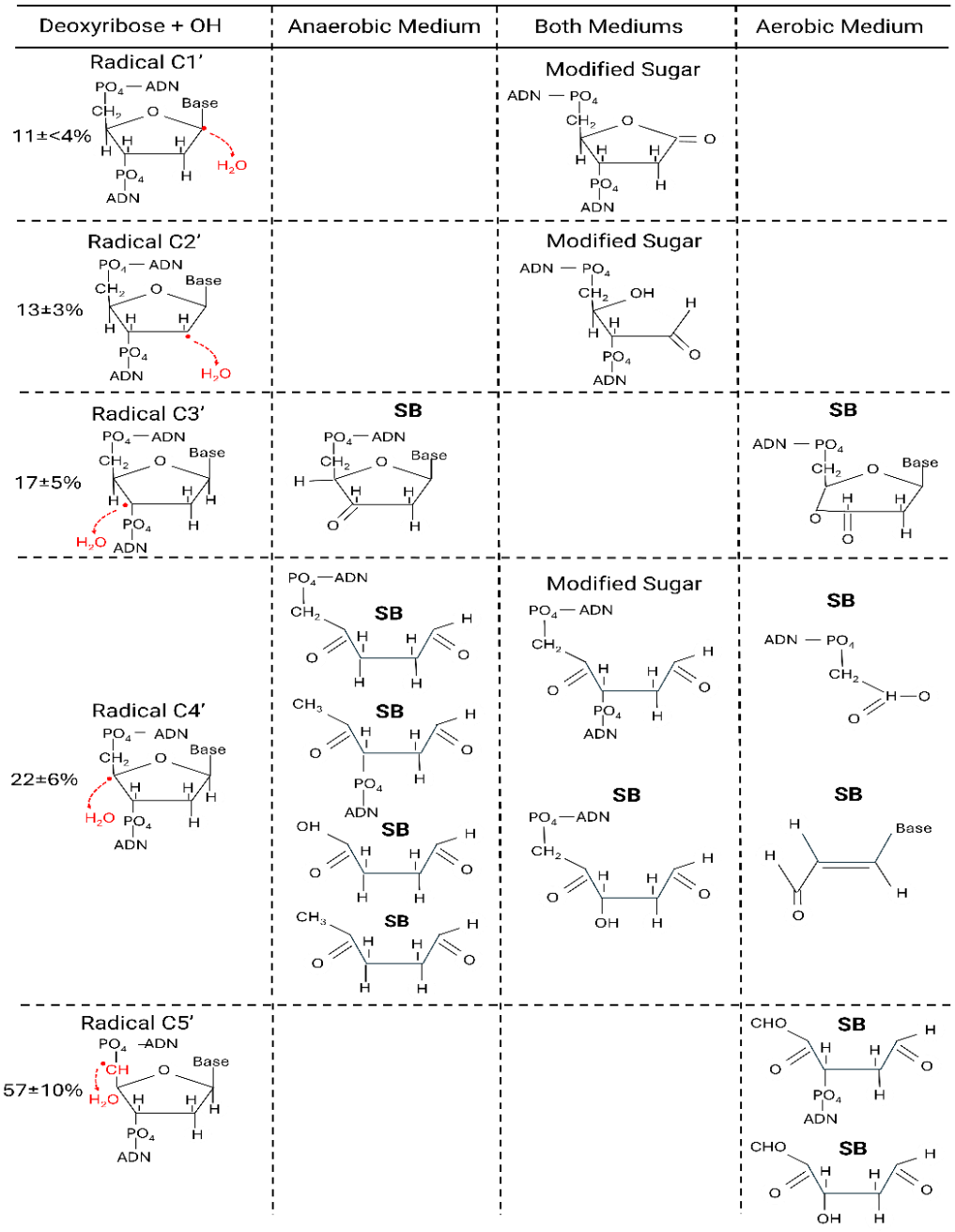

Figure 2.15. Main products of the OH-deoxyribose radicals. Image adapted from [Pogozelski W.K. & Tullius T.D. (1998)].

The previous description shows that radiation induces a wide range of lesions. However, the majority of them do not put in danger to the damaged cells because they can be effectively repaired by biological mechanism. Only those lesions that produce clustered strand breaks represent a real risk to cells since they can produce permanent consequences in the DNA conformation [Hall E.J. & Giaccia A.J. (2012)]. Therefore, a useful approximation to model the complex process of chemical lesions, is to consider the DNA as a single target that can react with free radicals with general reaction rates, and only a fraction of those attacks produce strand breaks, characterized by a probability known as a *damage efficiency* ε_{OH} [Mark F., et al (1989), Milligan J.R., et al (1993)].

In the work by [Michaels H.B. & Hunts J.W. (1973)], a general reaction rate between OH and DNA was derived with a value of $4.0 \times 10^8 \mathrm{M}^{-1}\mathrm{s}^{-1}$. This value was consistent with experiments carried out 20 years later by [Milligan J.R., et al (1996)], where it was observed that the value of this reaction rate was dependent on the scavenging capacity S_{OH} of the solution studied. The reactions follow a second order chemical kinetics. In the range of $10^5 - 10^9 \mathrm{s}^{-1}$ this dependence can be approximated by the next function [D-Kondo J.N., et al (2021)], shown on figure 2.16:

$$k_{OH-DNA} = 1.32 \times 10^7 (\mathrm{S_{OH}})^{0.29}$$

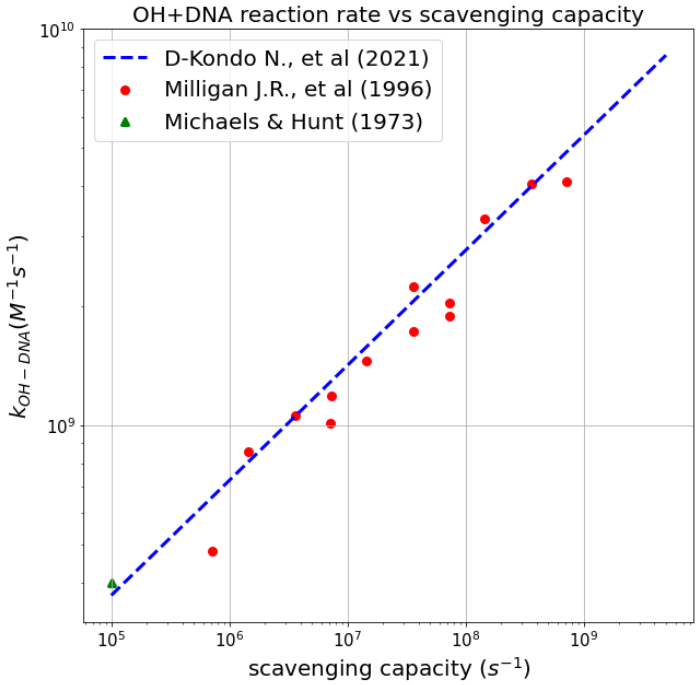

Figure 2.16. $\mathrm{OH} + \mathrm{DNA}$ reaction rate as a function of the aqueous solution scavenging capacity, experimental data are from [Michaels H.B & Hunts J.W. (1973)] and [Milligan J.R., et al (1996)], fitting function from [D-Kondo J.N., et al (2021)].

In another work by Milligan, the efficiency of OH to induce single strand breaks was measured obtaining a value of $\varepsilon_{OH} = 12\%$ [Milligan J.R., et al (1993)]. A similar value was used by [Nikhoo H. et al (1997)] in Monte Carlo computer simulations to reproduce the yield of strand breaks in short DNA segments (73nm, 216bp) irradiated with electrons. This value was obtained by assuming that 20% of all reactions between OH and DNA occurred in the sugar-phosphate backbone while the remaining 80% happened with the nitrogenated bases; another consideration was that reactions with the bases didn't produce any DNA breaks. As only 65% of the reactions with deoxyribose lead to DNA breaks, the computationally derived damage efficiency was 13% ($0.2 \times 0.65 = 0.13$). Later, in [D-Kondo N., et al (2021)], a value of 13.77% was obtained was determined using Monte Carlo Track Structure simulation using pUC19 plasmids (2686 bp) irradiated by gamma-rays from a cobalt 60 source.

The proximity of the breaks inside the DNA internal structure is also a fundamental factor that determines the severity of the damage by radiation. The more complex lesions are more difficult to repair and have a higher probability of causing permanent biological consequences [Nikhoo H., et al (1997)]. An isolated strand break is known as a Single Strand Break (SSB). If another break occurs at

a large enough distance, it will be considered as two separate lesions. It is classified as an SSB+ if it happens in the same strand or as a 2SSB if the break is on the opposite strand. On the other hand, if two breaks occur on opposite strands separated by a short distance of 10 base pairs (~3.4nm), they will form a Double Strand Break (DSB) [Charlton D.E., et al (1989), Nikhoo H., et al (1997), Francis Z., et al (2011)].

DSB are the type of lesions that are more dangerous for cells since they can break DNA into two separate sections, which can result in the loss of genetical information. Furthermore, if DSBs are not properly repaired, these lesions can lead to mutations, carcinogenesis or cellular death [Hall E.J. & Giaccia A.J. (2012), Chang, H.H.Y, et al (2017)]. If multiple SB lesions occur in proximity of one another, in a region of about ~10bp length, *complex* or *clustered* lesions will form, and when DNA break it will leave free fragments of different sizes. The length of the fragments is a factor that determinates the repair mechanism used by the cell to attempt its repair [Chang, H.H.Y., et al (2017)]. Some examples of the variety of lesions produced by radiation are presented next in figure 2.17.

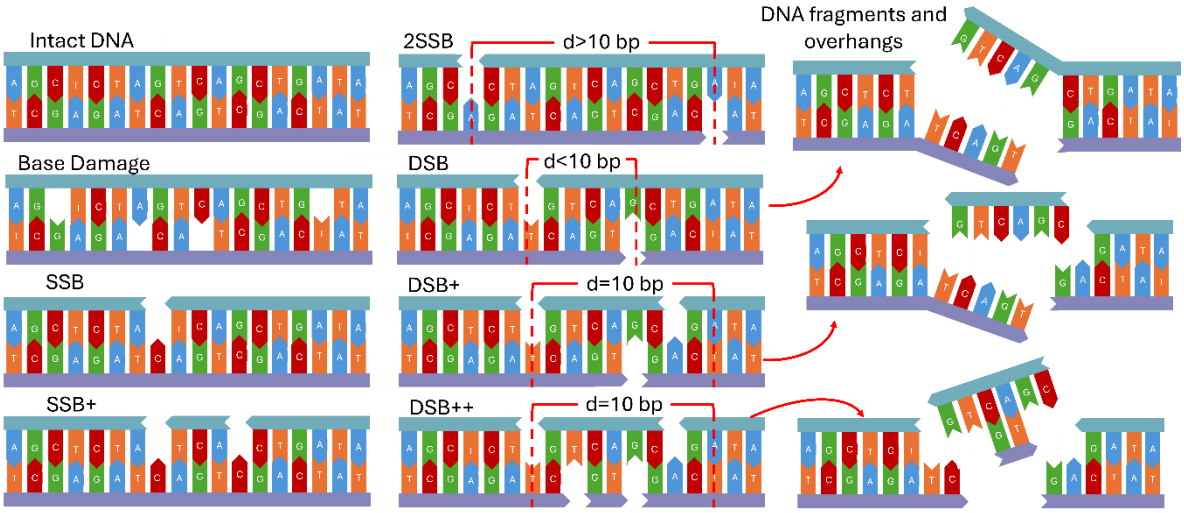

Figure 2.17. Examples of a variety of lesions with different complexities. Image adapted from [Nikhoo H. et al (1997)] and [Chang, H.H.Y., et al (2017)].

In order to study the number of breaks produced by radiation, different experimental methods have been employed. For example, in vitro studies employed small, closed DNA sequences called plasmids with lengths of several thousands of bp. Plasmids are convenient systems to study the isolated effects of certain parameters that affect the overall number of DNA breaks produced by radiation. That is due to its relative easiness to be extracted, purified and suspended in solutions at large concentrations for irradiation and radiochemical study. The single and double strand breaks can be measured with a standardized technique called gel electrophoresis [Milligan J.R., et al (1993); Tomita H., et al (1995)].

Intact plasmids in an aqueous solution are found in a supercoiled state. Breaks in the sugar-phosphate backbone produce geometrical changes in its molecular conformation. If only Simple Strand Breaks occur, the plasmid loses the inner tension that makes it supercoiled geometry and *relaxes*, becoming circular. A DSB provokes the closed structure of the plasmid to open, so it becomes lineal. If multiple DSBs occur, the lineal form fragmentates into multiple short lineal segments [Sanche L. (2008)]. These different forms and fragments of plasmids diffused differently in a type of

gel known as *agarose* subject to a uniform constant electric field. The field attracts the plasmids, as well as the DNA fragments, and separates them by size. Then, the different fragment size groups can be studied by optical methos such as fluorescence [Hall E.J. & Giaccia A.J. (2012)].

On the other hand, double strand breaks in living cell's DNA, are detected by specialized proteins that are activated in order to start the repair process. It is possible to introduce modified antibodies with a fluorescent marker that can attach to those damage response proteins and measure their activity using fluorescence microscopy. One of the key proteins is the Histone X of the $2\mathrm{HA}$ family ($\mathrm{H2AFX}$), which is activated as a response to DSBs and transforms into the variant $\gamma\mathrm{H2AFX}$, where the marked antibodies can join. The intensity of the fluorescence foci of these histones is an indicator of the number of DSBs produced by radiation and its time evolution of the repair process, figure 2.18 [Asaithamby A., et al (2008), Hall E.J. & Giaccia A.J. (2012)].

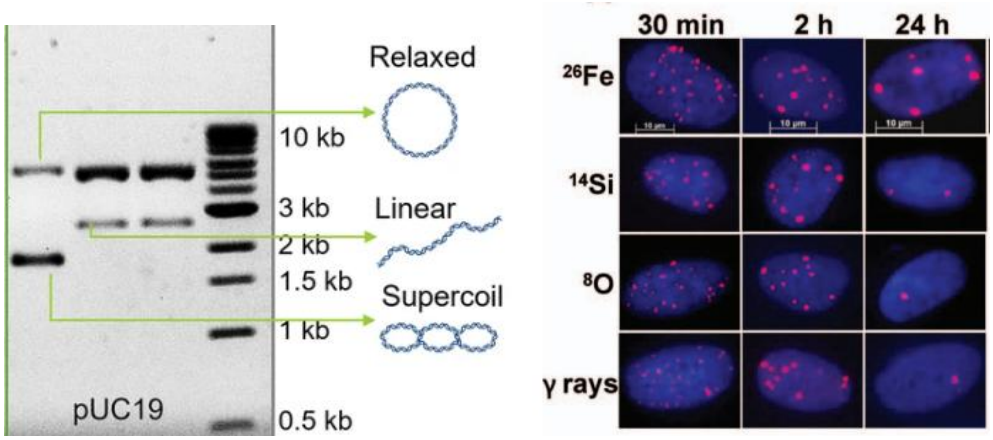

Figure 2.18. **Right.** Gel electrophoresis assay where the different forms of plasmids form into lines according to the plasmid fragments sizes, image was taken from [Mohammad N., et al (2024)]. **Left**. Time evolution of the γH2AFX foci fluorescence for different radiation qualities, image was taken from [Asaithamby A., et al (2008)]

For decades Monte Carlo Track Structure codes have been employed to simulate the different stages of the water radiolysis to calculate the spatial distribution of DNA breaks induced by direct and indirect actions of radiation in geometrical models of DNA, ranging from small DNA segments, complete plasmids, chromatin fibers, and whole cell nucleus [Charlton D., et a (1989), Tomita H., et al (1998), Friedland W., et al (2003), Dos Santos M., et al (2014), Bernal M., et al (2015), Nikjoo H., et al (2016), Incerti S., et al (2010,2018), Tran H.N., et al (2020), D-Kondo N., et al (2021), Poignant F., et al (2022), Ramos-Méndez J., et al (2022)].

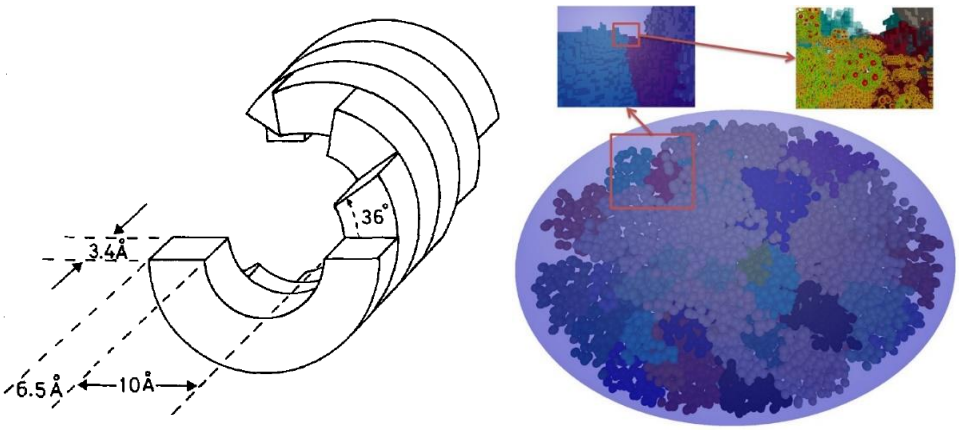

Figure 2.19 evolution of the DNA models, from a short segment constructed by cylindrical sections to the complete human genome inside a cell nucleus. Images taken from [Charlton D., et a (1989)] and [Meylan S., et al (2017)].

2.2.3 Radiation effect quantification and some influence factors

The effect of radiation can be evaluated qualitatively with specific endpoints at different scales. For example, at macroscopic scales the lethality on a population under uniform irradiation can be evaluated for each type of radiation conditions by the necessary dose to kill half of the population after certain observation period, this quantity is known as the mean lethal dose (LD_{50}) [Hall E.J. & Giaccia A.J. (2012)].

At the cellular level, shown in *invitro* assays, survival curves connect the absorbed dose by certain types of radiation with the percentage of a cell population that maintain the capacity to divide indefinitely after being irradiated, known as the *clonogenic state* [Hall E.J. & Giaccia A.J. (2012), Chang D.S., et al (2021)]. This condition for survival is related with the fact that some cells can "survive" the radiation. That is, cells can maintain their metabolic functions, but have lost the capacity to reproduce, sustaining a perpetual state of the cell cycle arrest known as *senescence*. Other cells may survive for a few division cycles but ultimately die mainly by *mitotic catastrophe*. Therefore, just the cells capable of producing large colonies are counted as survivors. This endpoint is also convenient since this type of colonies can be observed and counted with the naked eye [Hall E.J. & Giaccia A.J. (2012), Chang D.S., et al (2021)].

Experimentally, a quantity known as *plating efficiency* needs to be taken into account because some of the cells that were seeded do not survive the transport from the incubator recipient to the assay plate where they will be irradiated. Therefore, a control population that will not be irradiated is needed to obtain this percentage factor to correct the survival measured on the experiment [Hall E.J. & Giaccia A.J. (2012), Chang D.S., et al (2021)].

The Lineal Quadratic model (LQ) has been employed to describe the survival curves under different irradiation conditions. This model indicates that the dependence of this quantity S with the deposited dose D has two components: one that increases linearly with a coefficient α that dominates at low doses; and a squared term with a coefficient β that is predominant at higher doses, figure 2.20 [Hall E.J. & Giaccia A.J. (2012), Brahme A., et al. (2014), Chang D.S., et al (2021)]. The response follows the exponential form:

$$S(D) = e^{-\alpha D - \beta D^2}$$

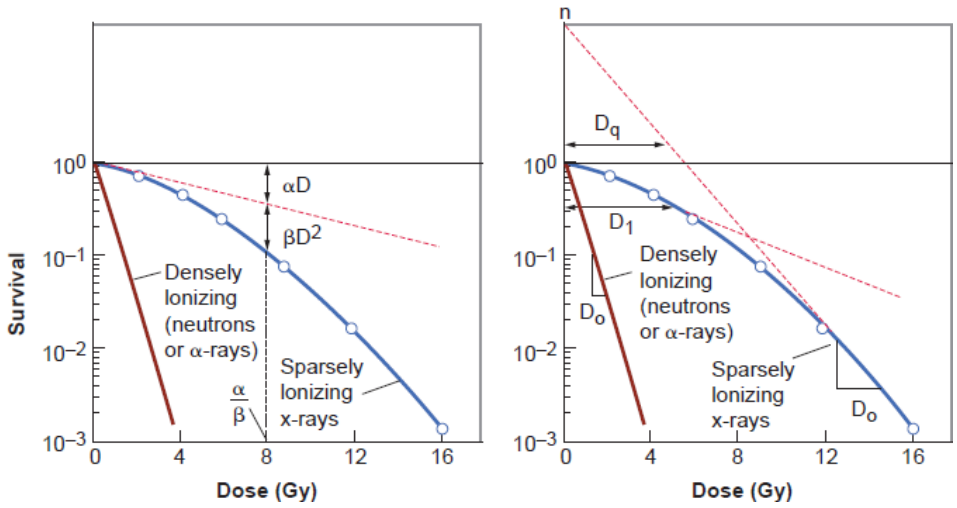

Figure 2.20. Schematics of typical survival curves demonstrate the effect of two different radiation types: low LET X-rays and high LET neutrons or α-rays, and the main characteristics of the curve including its relationship with the LQ model. image taken from [Hall E.J. & Giaccia A.J. (2012)].

In general, cell survival depends on a multitude of factors including the characteristics of the radiation used, and consequently, the physical-chemical interactions between incident radiation, DNA and its environment. The fractionation of dose also has an impact on the effectiveness of the tissue irradiation. On the biological side, the mechanisms of detection and repair of DNA breaks are interconnected with regulatory processes such as the cell cycle. For example, cell arrest plays a fundamental role in the survival of cells, considering the fact that the radiation sensitivity of a type of cell changes as its division cycle progresses since different repair mechanisms are available on specific stages. Secondary biological factors, such as the heterogeneity of tissue, temperature or oxygen availability also impact the effectivity of radiation on the irradiated cells [Hall E.J. & Giaccia A.J. (2012), Brahme A., et al. (2014), Chang D.S., et al (2021)].

At a molecular level, the number of DSBs produced in DNA suspended on solution is also used as an endpoint to quantify the effect of different modifiers such as oxygen concentration [Iraimoudi S.A. et al (1996)], temperature [Tomita K., et al (1995)] or DNA density measured by the supercoiling degree of plasmids [Milligan J.R., et al (1993)]. Various factors can influence the number of lesions caused by radiation. To study the isolated effect of each factor, it is essential to keep all other irradiation conditions constant and measure the number of DNA breaks normalized by dose as a function of the variable studied to quantify the damage modification.

In order to characterize the modification of a variable, a useful quantity employed is the Relative Biological Effect (RBE). RBE is defined as the ratio between the dose required to produce a biological effect by certain reference radiation D_{reff}, measured by a specific endpoint; divided by the dose of the tested irradiation conditions D_{test} necessary to induce the same biological effect [Hall E.J. & Giaccia A.J. (2012), Brahme A., et al (2014), Chang D.S., et al (2021)], given by the expression

$$\mathrm{RBE} = D_{reff}/D_{test}$$

This quantity serves as a comparison point for different irradiation configurations. In the next subsections a few of these factors will be briefly reviewed.

2.2.3.1 Quality of radiation characterized by LET

It is important to consider the different types of radiation since distinct particles may have a very different effect even if the same dose is deposited in a biological target. The Lineal Energy Transfer (LET) is a measurement of the density of ionization produced on a medium by certain type of incident particles and is a useful quantity to characterize the quality of radiation [Hall E.J. & Giaccia A.J. (2012), Chang D.S., et al (2021)].

The type of radiation that is usually employed as a reference radiation are the X-rays produced by a 250kV source (LET of ~2.0keV/µm), or gamma rays from a cobalt 60 source (LET of ~0.2keV/µm) [Hall E.J. & Giaccia A.J. (2012), Chang D.S., et al (2021)].

As the radiation's LET increases the survival fraction decreases [Hall E.J. & Giaccia A.J. (2012)]. The RBE grows until it reaches a maximum after 100 keV/µm, equivalent to an ionization every 2nm, which coincides with the DNA diameter, and is considered an optimal LET value for cell killing. After ~200 keV/µm, the RBE starts to reduce since the densely ionizing radiation produce more damage than it's required to kill a cell, and globally fewer cells are killed per unit dose leading to an *overkill* effect, figure 2.21 [Chang D.S., et al (2021)].

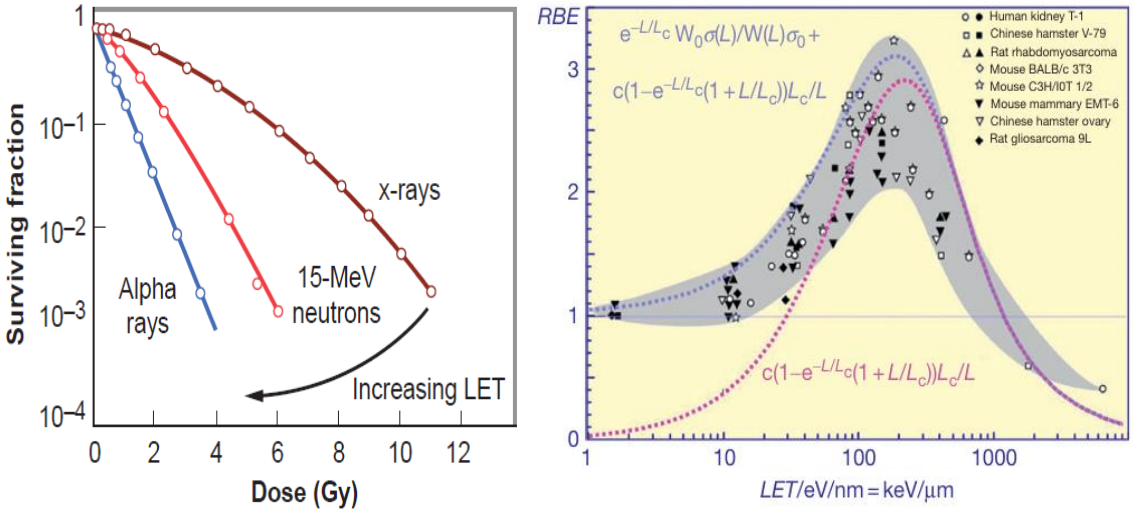

Figure 2.21. **Left**: different survival curves for distinct LET radiation types showing the decrease on survival fraction as LET increases. **Right**: RBE as a function of LET showing a maximum at 100keV/µm. Images taken from [Hall E.J. & Giaccia A.J. (2012)] and [Brahme A., et al (2014)] respectively.

At the molecular level, it is important to consider the differences in LET of the radiation used since the spatial distribution of the energy deposits determinate the initial conditions for the reactions between radiolitic chemical species. In addition, the time evolution of the concentration of these species also affects the DNA damage produced [Cobut V., et al. (1996), Taucher-Scholz G. & Kraft G. (1999), Meesungnoen J. & Jay-Gerin J.P. (2005)].

For example, MC simulations validated against experimental data for the radiolysis of water under high LET radiation, demonstrated that the dense ionization clusters left by the particle's tracks produced close groups of free radicals in close proximity. This proximity increases the probability of reaction neutralizing some species (by reforming water molecules) and reducing their chemical yields in general. There are several important exceptions: The yield of the radicals HO_2 and O_2^-,

related by the reaction $O_2^- + H^+ \leftrightarrow HO_2$, increase. This is caused because HO_2 need $O(^3P)$ to form, by the reaction $OH + O(^3P) \rightarrow HO_2$. Theoretically, $O(^3P)$ is only produced by a double ionized water molecule $H_2O^{2+} + 2H_2O \rightarrow 2H_3O^+ + O(^3P)$ or is the product of a triple ionized molecule $H_2O^{3+} + 3H_2O \rightarrow 3H_3O^+ + HO_2$. Multiple ionizations have been postulated to only occur by high LET radiation [Meesungnoen J. & Jay-Gerin J.P. (2005)]. Another important case is hydrogen peroxide. Its yield increases until a LET value of ~100keV/μm due to the recombination of nearby hydroxyl radicals by the reaction $OH + OH \rightarrow H_2O_2$ and decreases at higher LET values since OH can also react with $O(^3P)$ to form HO_2 [Meesungnoen J. & Jay-Gerin J.P. (2005)]. This behavior can be observed below on figure 2.22.

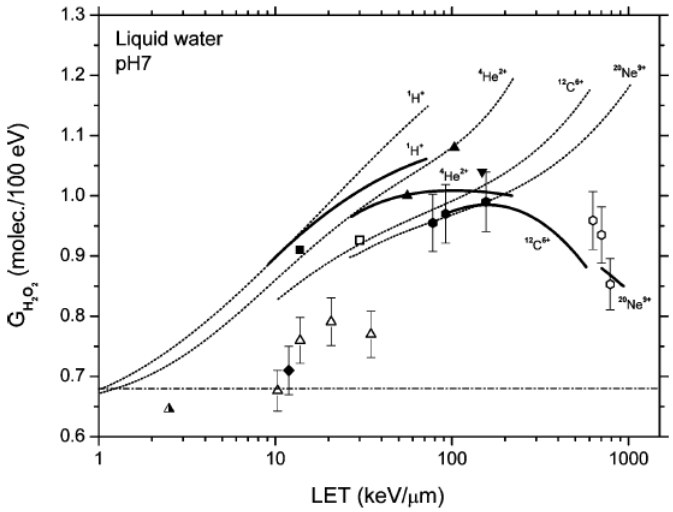

Figure 2.22. G-value of H_2O_2 as a function of LET. Image taken from [Meesungnoen J. & Jay-Gerin J.P. (2005)].

Moreover, for the same absorbed dose, the total number of DNA breaks also decreases as LET increases even if the probability of inducing both a SSB and DSB increases with LET for any type of radiation. That probability is characterized by the cross section for lesion induction per incident particle. However, as the density of ionization increases with LET, the DNA breaks also occur closer to each other and produce more complex lesions, which can become non repairable DSBs or mis-joined chromosomal fragments, associated with the mortality of cells. Therefore, the increase of cell killing is related with the complexity of the lesions the high LET radiation produces rather than the total number of DNA breaks, figure 2.23 [Blakely E.A. (1992), Taucher-Scholz G. & Kraft G. (1999)].

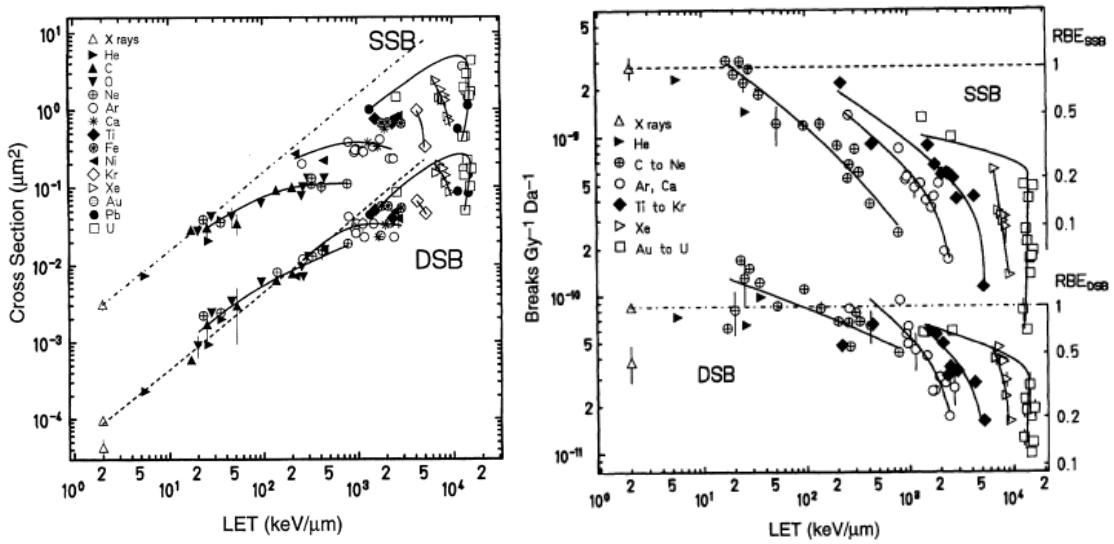

Figure 2.23. dependance of the cross section for the induction of SSBs DSBs and the total number of lesions produced by different types of radiation as a function of their LET, image taken from [Taucher-Scholz G. & Kraft G. (1999)].

In living cells, complex damage correlation to mortality has been confirmed by experiments in vitro. When DNA damage occurs on cells, the histones H2AX phosphorylate in the lesion site and transform into γ-H2AX. The time evolution of the amount of active histones is an indicator of the repair process and can be measured by fluorescent stained antibodies that attach to the γ-H2AX foci. The time evolution curves of intensity can be studied with microscopy imaging techniques as described before. The action of other proteins, like the p53 Binding Protein 1 (53BP) that responds directly to the DSBs sites, can also be studied with this technique. The γ-H2AX foci that remain after 24 hours of continuous DNA repair are indicative of the irreparable lesions produced on a cell. The fraction of irreparable lesions depends on the radiation LET. For example, for high LET iron ions, 40% of the cells presented γ-H2AX foci 24 hours after irradiation, while only around 1% of cells irradiated with low LET γ-rays presented residual fluorescence. This can be explained since the high ionization density along the tracks of high LET particles are close from one another, figure 2.24, and this proximity can cause clustered lesions that are more difficult or impossible to repair [Asaithamby A., et al (2008)]

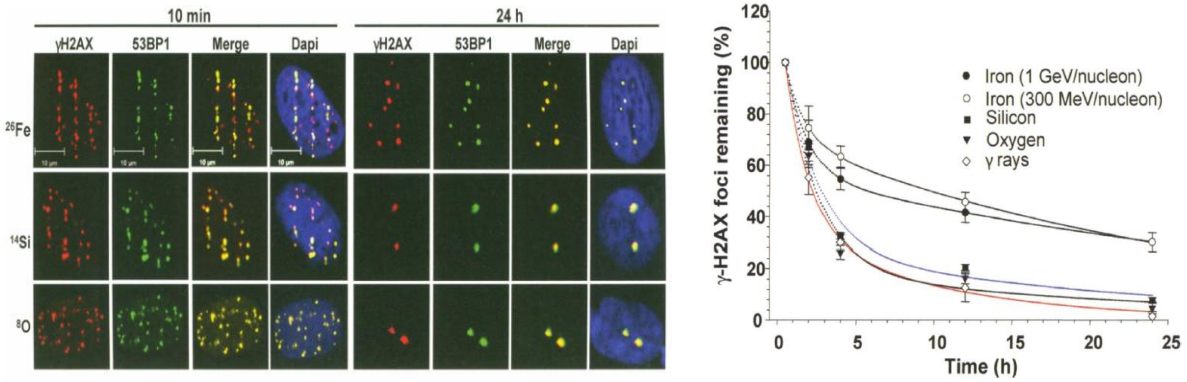

Figure 2.24. **Right**. Fluorescence of several damage response proteins 10 minutes and 24 hours after irradiation with different types of radiation. **Left**. Time evolution for the percentage of remaining γ-H2AX foci for several radiation qualities. Images taken from [Asaithamby A., et al (2008)].

2.2.3.2 Temperature and the hyperthermia effect

Temperature is a radiosensitizer, this means that it increments the effectivity of damage by radiation in a tissue [Oei A. L., et al. (2015)]. In the therapeutical context, increasing the temperature has been used in combination with conventional radiotherapy for a technique known as *hyperthermia,* which consists of a local increase of temperature in the affected tissue in the 39°C to 45°C range [Datta N. R., & Bodis, S. 2019].

Multiple mechanisms for the temperature influence on the radiation damage have been identified at different scales. For example, the increase in temperature is itself a factor that promotes cell mutations and affects multiple biological processes, like the assembly of essential proteins for the repair and replication of the DNA, interfering with the natural cell cycles. Temperature can also directly damage the cell membrane and trigger the apoptosis process [Kaur P., et al. (2011), Oei A. L., et al. (2015)]

At the molecular level, temperature also influences the quantity of DNA breaks that radiation produces. Temperature affects the mobility of the molecules suspended in a solution (characterized by their diffusion coefficient D) and the reactivity between them (characterized by the reaction rate k) [Tomita K., et al (1995)]. In the work of [Elliot A.J. & Bartels D. (2009)] it was reported a compilation of experimental measured values of the reaction rates and diffusion coefficients for temperatures from 25°C to 300°C. In order to describe the temperature dependence for the diffusion coefficient of other radiolitic species, the *self-diffusion* of water is employed. This consists in the scaling of the measured diffusion coefficients at room temperature (25°C) of certain chemical specie X multiplying it by the ratio of the water diffusion coefficient at the desired temperature divided by its value at 25°C [Eliot A.J (1994), Hervé du Penhoat M.A. et al (2000)], as follows:

$$D_X(T) = D_X(25°\mathrm{C}) \times \frac{D_{H_2O}(T)}{D_{H_2O}(25°\mathrm{C})}$$

Experiments have also shown that the escape yields for the $\bullet\mathrm{OH}$ radical increases with the temperature, which might influence the number of indirect DNA breaks [Spinks J.W.T. & Woods R.T. (1990). Eliot A.J (1994)] The effect of temperature on the radiation chemistry of water using computer simulations compared with experimental data in the range 0-45°C can be observed on figure 2.25.

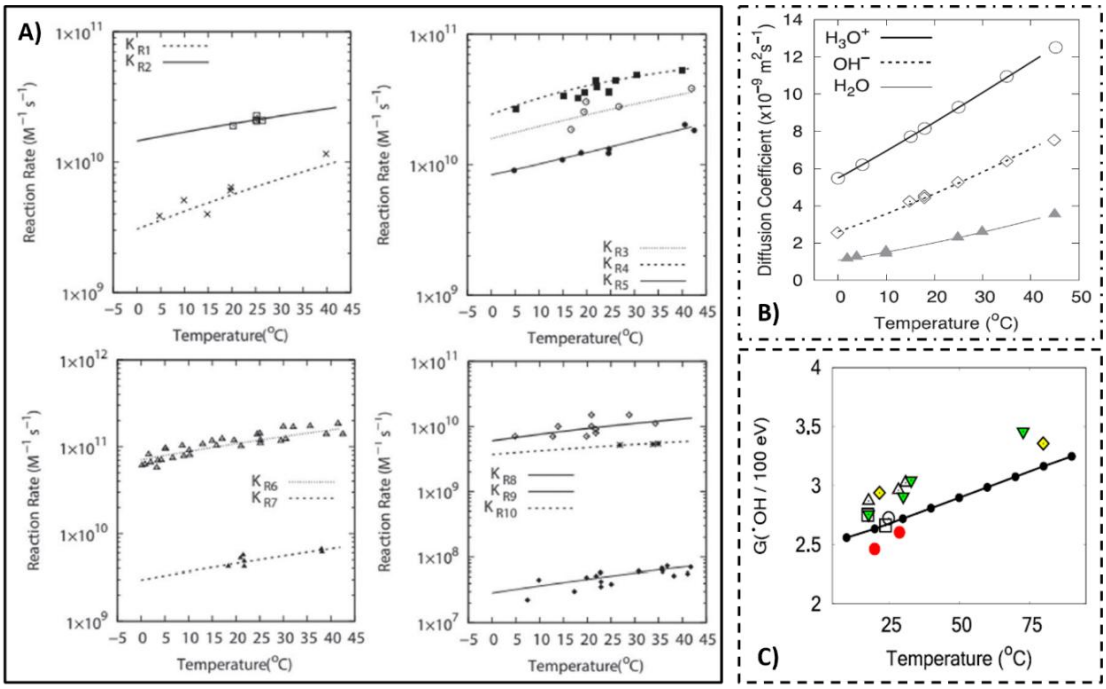

Figure 2.25. effects of the temperature on the kinetics of the radiochemistry of water. **A)** the reaction rate for the main 10 reactions (the order is the same as table 2.3 in section 2.1.4. **B)** the diffusion coefficients for $\mathrm{OH}^-, \mathrm{H_3O}^+$ and $\mathrm{H_2O}$ as a function of temperature, data was compiled in [Elliot A.J. & Bartels D. (2009)]. **C)** the escape yield of OH calculated with TOPAS MCTS simulation and validated against experimental data. images were taken from [Ramos-Méndez J., et al (2022)].

Tomita et al., [Tomita K., et al (1995)] used pBR322 plasmids (4364 base pairs of length) suspended in an aqueous solution with TRIS (an organic compound that protects the DNA in freezing conditions and functions as an OH scavenger) at concentrations between 1mM to 100mM. The plasmids were irradiated with gamma rays produced by a cobalt-60 source. The number of single and double DNA breaks produced by irradiation was used as an endpoint to check the effect of temperature in the range -20 to 42°C. The authors reported the number of lesions normalized by deposited dose and molecular weight of the plasmid measured in units $10^{-10}\mathrm{Gy}^{-1}\mathrm{dalton}^{-1}$, figure 2.26.

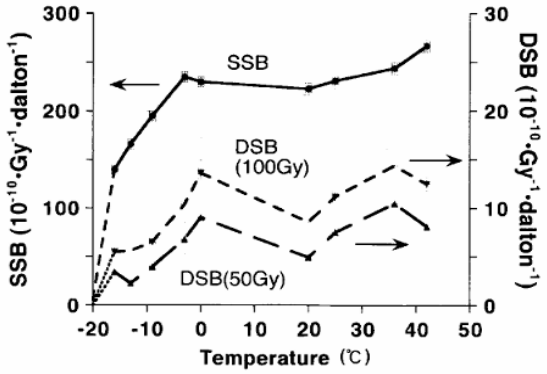

Figure 2.26. The number of SSBs and DSBs as a function of temperature normalized by absorbed dose and molecular weight of the plasmid. Image taken from [Tomita K., et al (1995)]

Complementary, Monte Carlo Track Structure simulations using the TOPAS-Bio code were used to simulate the temperature dependence of DNA DSB and SSB using pUC19 (2686 bp) plasmids. The plasmid concentration (29.75µg ml^{-1} DNA concentration) and scavenging capacity of the media reproduced the experimental conditions of [Tomita K., et al (1995)]. The temperature varied in the 5-45°C range, and ^{60}Co gamma rays irradiation was used. The Monte Carlo simulations allowed to retrieve an improved resolution to stablish a DNA damage rate. The simulation setup and results of this publication can be seen in the figure 2.27 below:

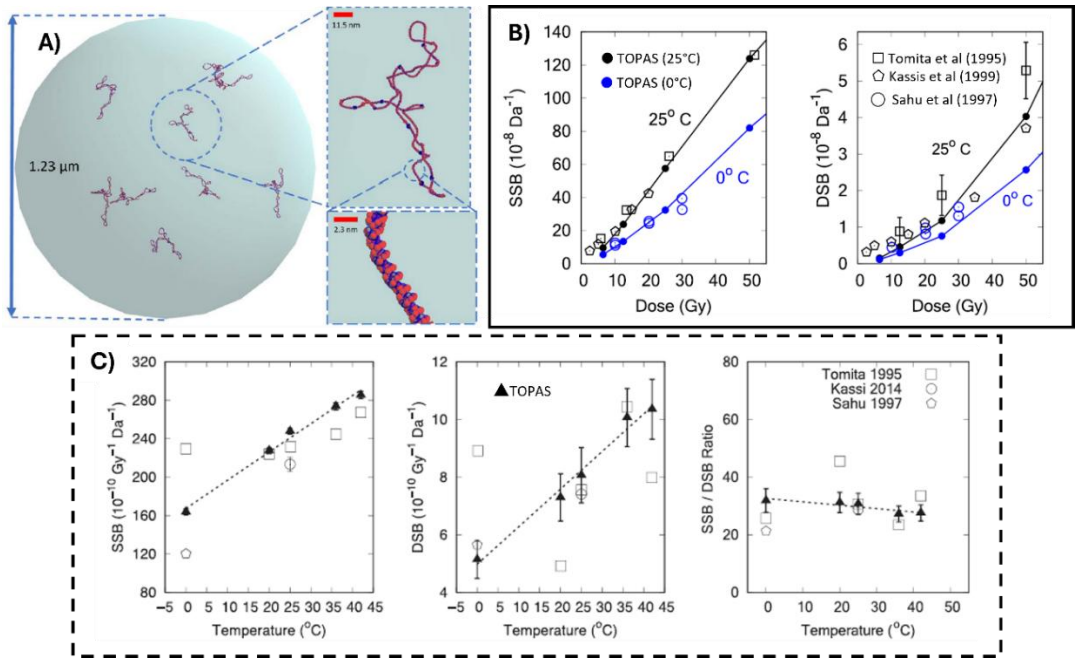

Figure 2.27. **A)** Simulation configuration with a 1.23 µm diameter sphere containing 9 pUC19 geometrical models to match the DNA concentration of the solution. **B)** DNA breaks as a function of deposited dose at two temperatures 0 and 25°C. **C)** DSBs and SSBs as a function of temperature compared with experimental data. Image taken from [Ramos-Méndez J., et al (2022)].

This paper was part of this research work in the exploration of models that were used in the final version of this PhD thesis. The contributions for this PhD work, was the first implementation of the reaction rates and diffusion coefficients of the radiolytic chemical species as a function of the temperature [García García, O.R., et al (2020)].

Lastly, higher temperatures also increase the solubility of oxygen in a solution [Tomita K., et al (1995)]. It also improves the oxygenation of a tissue [Datta N. R. & Bodis S. (2019)] which is another radiosensitizer factor that influences the effectiveness of radiation biological damage.

2.2.3.3 The scavenging capacity of aqueous solutions

In vitro assays that use plasmids in aqueous solutions, as an approximation for the cellular medium, are convenient models to study the isolated effect of a variable measuring the number of DNA breaks produced by radiation as an endpoint. For example, studies using DMSO (an OH scavenger) were performed to determinate the reaction rate of the $\mathrm{OH} + \mathrm{DNA}$ reaction. The OH radical is the major

contributor to indirect DNA damage. As the scavenging capacity of the solution increases, the DMSO molecules compete with the DNA to react with the OH radicals [Milligan J.R, et al (1993, 1996)], this is:

$$\mathrm{DMSO} + \mathrm{OH} \xrightarrow{k_{DMSO}} \mathrm{products}$$

$$\mathrm{DNA} + \mathrm{OH} \xrightarrow{k_{DNA}} \mathrm{products}$$

Thus, the number of SSBs produced depends on the concentration of DMSO. Through the competition dynamics and using the reaction rate between the DMSO and OH, the unknown reaction rate k_{DNA} can be deduced using the single strand break yield G(SSB) [Milligan J.R, et al (1993, 1996)], following the expression:

$$\frac{1}{G(\mathrm{SSB})} = \frac{1}{G_0(\mathrm{SSB})} + \frac{k_{DMSO}[\mathrm{DMSO}]}{k_{DNA}G_0(\mathrm{SSB})[\mathrm{DNA}]}$$

Where $G_0(\mathrm{SSB})$ is the yield of Single Strand Breaks without any DMSO. The results showed that the number of SSBs decreased as the DMSO concentration on the solution increased, and that the k_{DNA} reaction rate had a dependency on the scavenging capacity of the medium, this can be seen on figure 2.28 below:

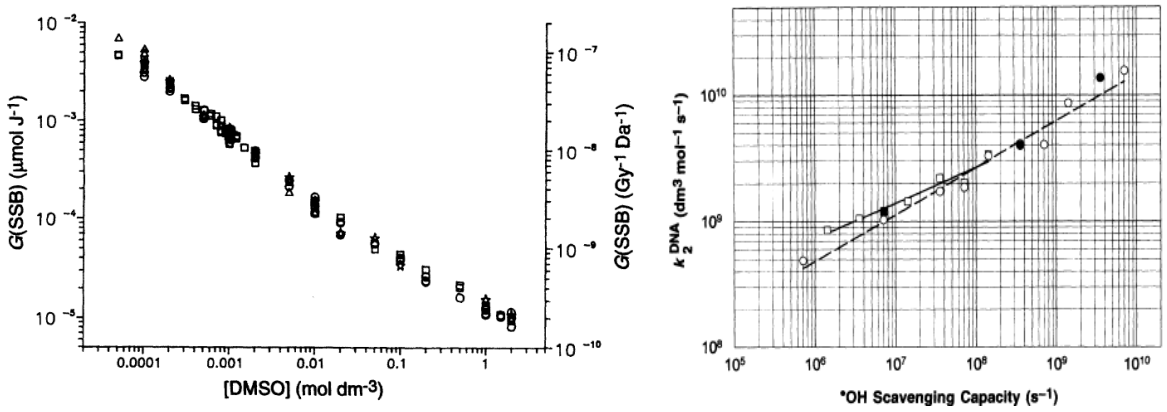

Figure 2.28. **Left:** Number of SSBs as a function of DMSO concentration. **Right**: k_{DNA} value as a function of the scavenging capacity of the medium. Images taken from [Milligan J.R, et al (1993, 1996)]

More recently, computer simulations using TOPAS-nBio were used to simulate the DNA breaks in pUC18 plasmids under $^{137}\mathrm{Cs}$ irradiation on a range of $10^6 - 10^{10} s^{-1}$ scavenging capacity. The results were used to confirm the efficiency of OH radical to induce SSB within 10% of the measured data [Ramos-Mendez J., et al (2022)].

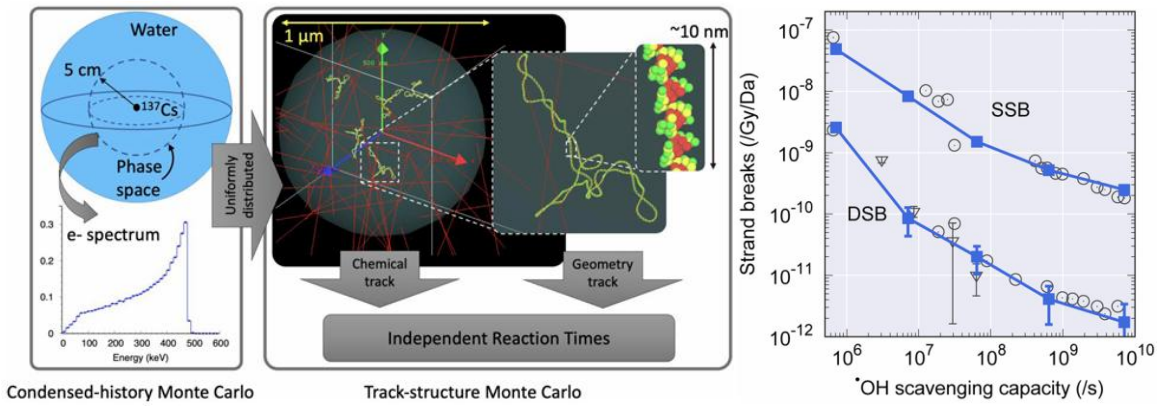

Figure 2.29. **Left.** Simulation configuration on TOPAS to simulate the ^{137}Cs irradiation of pUC18 plasmids to study the (**Right)** DNA breaks (SSB and DSBs) induction as a function of the scavenging capacity of an aqueous solution. Image taken from [Ramos-Mendez J., et al (2022)].

These results are relevant for the present research work since they indicate that the presence of homogeneously distributed molecules on an aqueous solution affect the escape yields of radiolitic species and modify the general chemical interactions that occur on pure water. And, that first order reactions can be employed to describe the effect of multiple molecules that can act as free radical scavengers such as the cellular environment.

2.2.3.4 Oxygen and its competence with antioxidants

Oxygen is one of the more effective agents to modify the biological effect of radiation. Among the biologically relevant chemical agents, oxygen is the one that induces the more dramatic change. Using the concept of relative biological effects, the influence of oxygen can be quantified as the comparison of the dose needed to produce a certain effect under anoxic conditions, to the dose needed to produce the same effect under normoxic conditions. This ratio is known as the *Oxygen Enhancement Ratio* (OER) [Hall E.J. & Giaccia A.J. (2012), Chang D.S., et al (2021)].

The explanation for this effect comes from DNA damage at the molecular level and the response of the cell environment. Briefly, cells have dissolved antioxidants in their medium, like sulfur containing compounds called thiols, usually represented as RSH. When chemical damage occurs by the abstraction of hydrogen atoms from the DNA components ($\mathrm{DNA}^{\bullet}$), these antioxidants can donate their hydrogen to revert the damage, forming thiyl radicals ($\mathrm{RS}^{\bullet}$). This process is known as DNA chemical repair [Becker D., et al (1994)]. On the other hand, oxygen can react with the damaged DNA and form peroxyl radicals ($\mathrm{ROO}^{\bullet}$) that cannot be repaired by the antioxidants and consequently *fixing* the damage [Becker D., et al (1994), Hall E.J. & Giaccia A.J. (2012), Chang D.S., et al (2021)]:

$$\mathrm{DNA}^{\bullet} + \mathrm{RSH} \rightarrow \mathrm{DNA} + \mathrm{RS}^{\bullet}$$

$$\mathrm{DNA}^{\bullet} + \mathrm{O}_2 \rightarrow \mathrm{DNAOO}^{\bullet}$$

This effect has been quantified in vitro assays using aqueous solution with plasmids with different concentrations of thiols, like cysteamine (CyaSH) or glutathione (GSH), which is the most abundant thiol inside cells and considered as the main natural cellular radioprotector [Ayene I.S., et al (1996)]. To that end, the number of DNA breaks per unit dose (figure 2.30) has been used as an endpoint to measure the effect of oxygen on different concentrations of GSH. The results are indicative of the

oxygen competition with the GSH to fix or repair the DNA breaks respectively [Becker D., et al (1994), Ayene S.I., et al (1995,1996)].

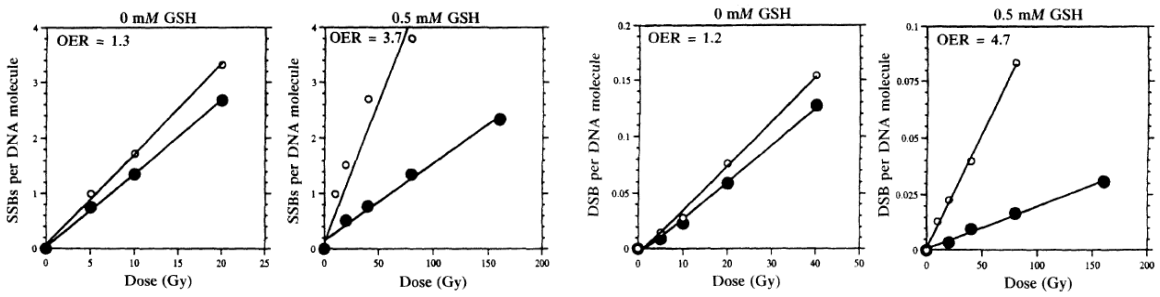

Figure 2.30. Number of SSBs and DSBs as a function of dose in anoxic conditions (●) using a nitrogen and oxygen (○) atmospheres, changing the concentration of GSH from 0 to 0.5μM. Images taken from [Ayene S.I., et al (1995)]

The OER is radiation type specific since the effect of oxygen is directly related to the chemical damage. Low LET radiation, like X-rays or gamma rays, mainly produces DNA breaks by the indirect effect, and are greatly affected by the presence of oxygen; thus have a large OER value. High LET particles, like heavy ions or protons, mainly produce lesions by the direct effect, then these are less impacted by oxygen and consequently have a small OER. OER is better observed in clonogenic cell survival curves, figure 2.31. [Hall E.J. & Giaccia A.J. (2012), Brahme A., et al (2014)]

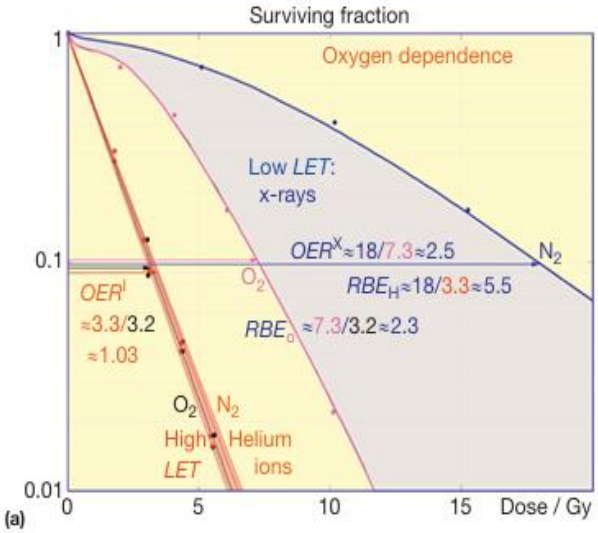

Figure 2.31 survival curves demonstrating the relative biological effect of oxygen and the OER for two types of radiation: low LET X-rays and high LET helium ions. Image taken from [Brahme A., et al (2014)]

The combined effect of oxygen and LET has been studied with Mone Carlo methods elsewhere [Stewart R.D., et al (2011)]. The competence between oxygen fixation and chemical repair of DNA lesions was performed using a probability function p_r that describes the removal of DNA breaks dependent on the oxygen concentration $[O_2]$ and radiation quality:

$$p_r(x,[O_2]) = 1 - \frac{[O_2] + K_{O_2}}{[O_2] + M(x)K_{O_2}}$$

Where:

$$M(x) = M_0 - \frac{M_0 - 1}{1 + (q/x)^r}$$

The term $(1 - 1/M)$, represents the maximum fraction of $\mathrm{DNA}^{\bullet}$ that can be chemically repaired under anoxic conditions, $\mathrm{K}_{\mathrm{O}_2}$ is the concentration of O_2 where half of said maximum is repaired and $x = \left(Z_{eff}/\beta\right)^2$ is a parameter related with the incident particle's radiation quality, with Z_{eff} its effective charge and β the particle's velocity relative to the speed of light in vacuum. On the $M(x)$ expression M_0 is the maximum breaks chemically repairable, and $(q/x)^r$ is a factor that corrects this number by the quality of radiation used, where the parameters M_0, q and r were adjusted to match the experimental data.

For low LET radiation the value of $(q/x)^r$ is large, and the number of possible repairable lesions is maximized. In contrast, the fact that high LET produces more direct DNA breaks that cannot be chemically repairable is reflected by a small $(q/x)^r$ value that minimizes $M(x)$. The results of this study are presented in terms of the Hypoxia Reduction Factor (HRF), that represents the number reduction of DNA breaks as O_2 concentrations decrease and is indicative that the fixation-repair competition favors the chemical repair on hypoxic conditions [Stewart R.D., et al (2011)].

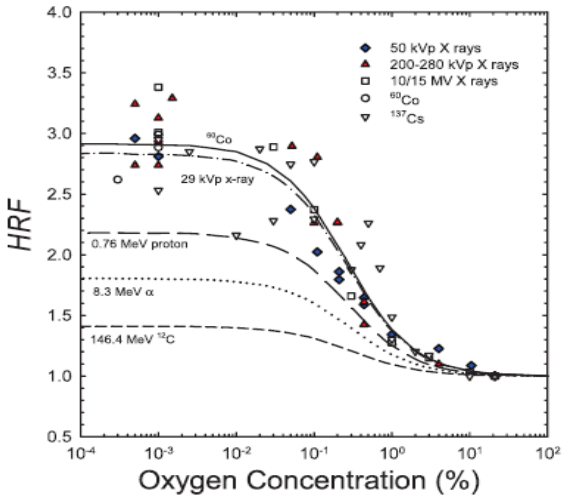

Figure 2.32. Results for the simulation of the Hypoxia Reduction Factor compared with experimental results. Image taken from [Stewart R.D., et al (2011)]

2.2.3.5 Radiation dose rate and the FLASH effect

The rate at which radiation is delivered to the tissue is also a factor to consider. However, its effect is complex and may seem counterintuitive in some cases. For high dose rates, the survival curves have a pronounced fall as the absorbed dose increases, indicating that more cells are killed as dose rate increases. The rise in survival at lower dose rates is linked with the repair of the Sub-Lethal Damage (SLD). However, if the dose rate is lowered again within a certain range, the continuous irradiation may coincide with the cell cycle transition, *redistributing* the DNA damage to a more radiosensitive stage of the cell cycle like the G2 phase. Then, if the dose rate is lowered again, below this critical range, the cells can escape this G2 phase and divide, thus, the newborn cells compensate the cell killing by radiation and the survival curve becomes flatter. However, these effects are sensitive to the type of irradiated cell [Hall E.J. & Giaccia A.J. (2012)].

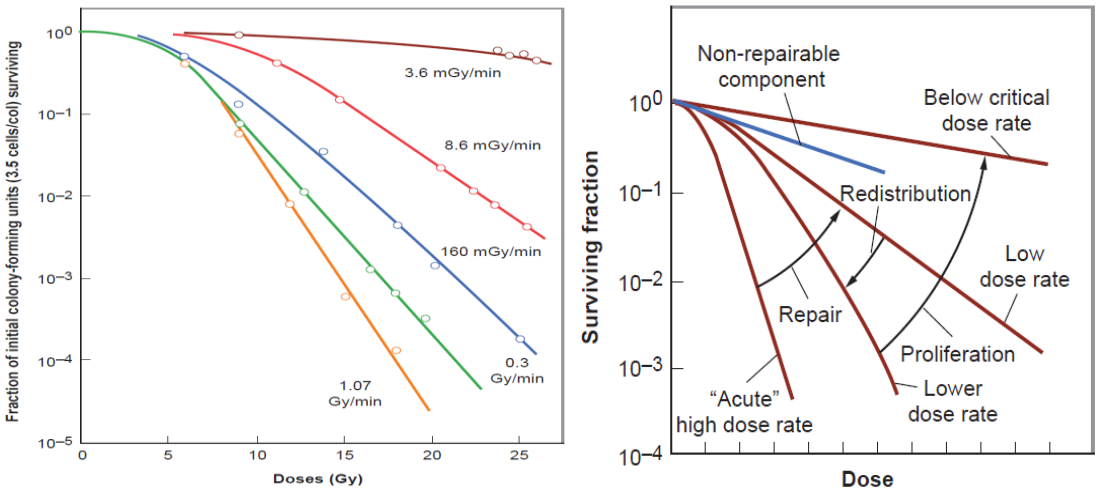

Figure 2.33. **Left:** decrees in the survival of Chinese hamster CHL-F cells ass the dose rate grows. **Right**: general effect of the dose rate and the factors that modify it. Images taken from [Hall E.J. & Giaccia A.J. (2012)].

Nevertheless, there is an important exception in the cell killing behavior dependent on dose rate which occurs at ultra-high dose rates: the FLASH effect. The FLASH effect consist in delivering radiation doses on very short pulses, within milli or microseconds, resulting in ultrahigh dose rates of $10^2 - 10^6 \mathrm{Gy/s}$, in comparison with conventional radiotherapy with values around $0.1 - 0.01\ \mathrm{Gy/s}$ [Favaudon V., et al (2014), Adran G., et al (2019)]. This irradiation modality has proven to reduce the toxicity associated with conventional irradiation in normal tissue, sparing healthy cells while maintaining the normal damage to malignant cells [Favaudon V., et al (2014), Montay-Gruel P., et al (2019), Hughes J.R & Parsons J.L. (2020)].

The first evidence of this effect dates way back to the 70's, where high dose rates on rat skin irradiation not only caused less adverse effects (reddening of the skin to complete necrosis) but they also started to appear at higher doses [Field S.B. & Bewley D.K. (1974)]. More recently, the FLASH effect has been observed in mice and other animal model assays. This type of treatment has proven to protect lungs from radiation-induced fibrosis, blood vessels and bronchi from apoptosis, and skin from radiation lesions like necrosis, ulceration and inflammation. In implants of neck and breast cancerous cells on mouse, a technique known as xenografts, FLASH therapy has proven to be as effective as conventional irradiation for tumoral control [Favaudon V., et al (2014), Hughes J.R & Parsons J.L. (2020)]. This therapy has also been shown to spare memory and brain functions in adult mice and development of zebra fish embryos [Montay-Gruel P., et al (2019)]. Furthermore, there is a documented successful FLASH treatment of a cutaneous lymphoma on a human patient, adding to the evidence in favor of the potential clinical applications of this irradiation mode [Hughes J.R & Parsons J.L. (2020)].

Early observations noted that the irradiated tissue with ultrahigh dose rates presented a "transient hypoxia" [Hendry J. H., et al (1982)]. Nowadays, one hypothesis is the *oxygen depletion* by Flash irradiation. This hypothesis considers that in the presence of oxygen, the indirect radiation damage ultra-high dose rate exposure consumes all the available oxygen in the normal cell's environment, faster than reoxygenation, producing a temporary radioprotective state. This is consistent with the fact that malignant tissue, that exists in a constant state of hypoxia, is more radioresistant than healthy tissue [Favaudon V., et al (2014), Hughes J.R & Parsons J.L. (2020)]. Other theories consider

the cell's immune response, and specifically the reduction in the production of the *Transforming Growth Factor Beta* ($\mathrm{TGF}-\beta$), which is a protein that serves as an extracellular signal for the inflammatory response [Favaudon V., et al (2014), Hughes J.R & Parsons J.L. (2020)].

However, the exact biochemical mechanisms responsible for the FLASH effect are still not completely understood as mechanistic models driven by experimental evidence are required [Hughes J.R & Parsons J.L. (2020)].

LaBarbe et al., proposed physicochemical model of reaction kinetics that supports the theory of peroxyl radical recombination as the main determinant of the FLASH effect [LaBarbe R., et al (2020)]. The model was presented for different dose rates. The model considers the experimentally measured G-values, in water, for $\mathrm{H_3O}$,H,$\mathrm{H_2}$,$\mathrm{H_2O_2}$,$\mathrm{e_{aq}^-}$ and OH in $\mu\mathrm{M/Gy}$. It uses a scheme of 26 reactions between the radiolytic species to represent the radiation chemistry of the water inside the cell's environment. Next, it considered a constant concentration of 1mol/L of general biological molecules RH, that account for DNA, protein, lipids and all the dissolved organic substances in the cellular medium in a global way [LaBarbe R., et al (2020)]. The biological molecules can be attacked by H,$\mathrm{e_{aq}^-}$ and OH radicals (with reaction rates of $\mathrm{k_{R-H}} = 1.0 \times 10^8$, $\mathrm{k_{R-e_{aq}^-}} = 1.4 \times 10^8$ and $\mathrm{k_{R-OH}} = 1.0 \times 10^9 \mathrm{M^{-1}s^{-1}}$, respectively) produce biological radicals $\mathrm{R^\bullet}$, that can be chemically repaired by GSH (with an initial concentration of 6.5mM and a rate of $k_{GSH} = 300/s$). In addition, GSH can also intercept OH at a rate of $\mathrm{k_{dOH}} = 1.0 \times 10^{10} \mathrm{M^{-1}s^{-1}}$. The repair of radicals competes with $\mathrm{O_2}$ (concentration of 50µmol/L), that produce peroxyl radicals ($\mathrm{ROO^\bullet}$), and with a recombination process ($2\mathrm{R^\bullet} \rightarrow \mathrm{R=R}$). Finally, the peroxyl radicals react with other intact biomolecules and propagate the damage ($\mathrm{ROO^\bullet + RH \rightarrow ROOH + R^\bullet}$). These can decay into a bimolecular recombination ($2\mathrm{ROO^\bullet \rightarrow O_2 + ROH + RO}$) and can be intercepted by other antioxidants like the vitamin C ($\mathrm{ROO^\bullet + XSH \rightarrow ROOH + XS^\bullet}$) terminating the chain reaction. A scheme for the all the mechanism involved working together can be seen in figure 2.34 [LaBarbe R., et al (2020)].

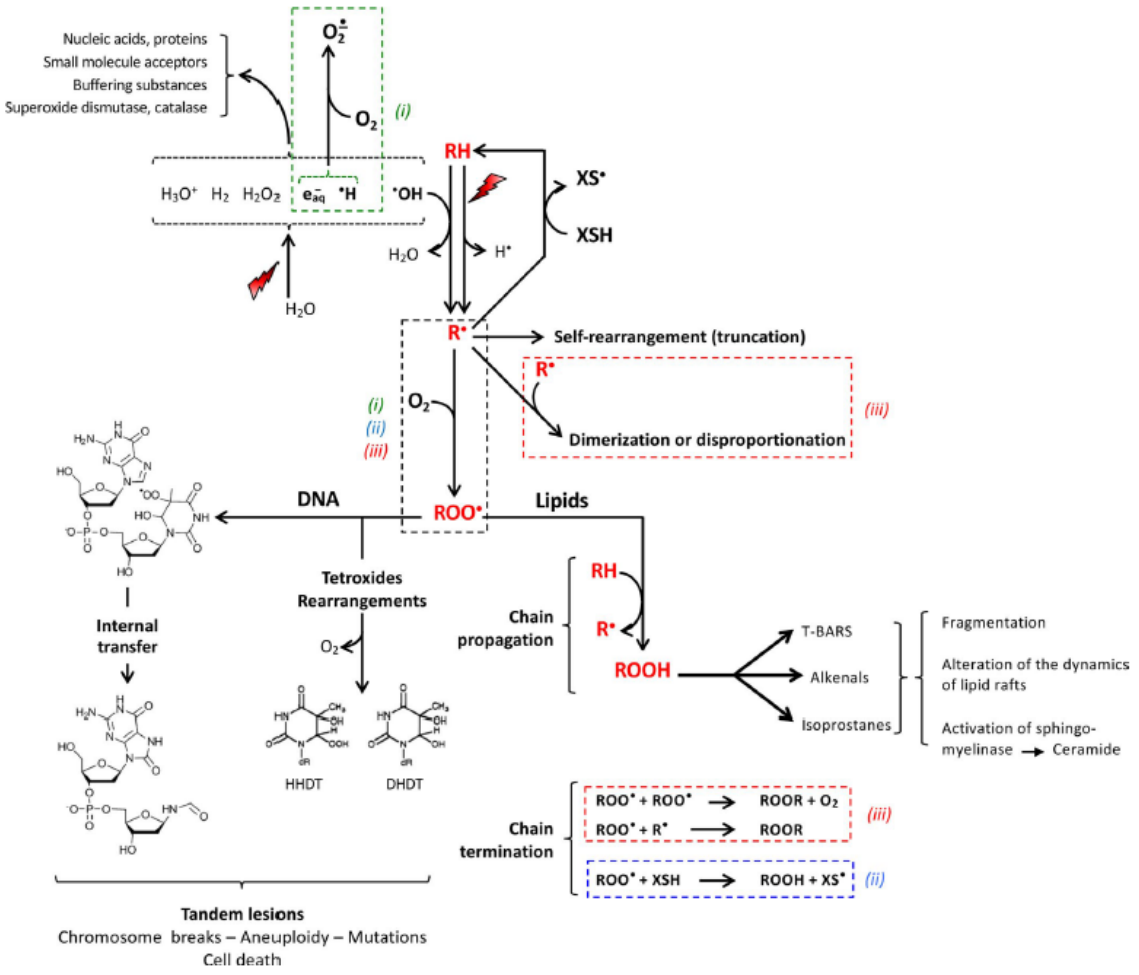

Figure 2.34. Scheme of the cellular environment model proposed by [LaBarbe R., et al (2020)] to investigate radiation damage under different dose rate irradiation conditions.

The metric that the authors choose to evaluate the biological radiation effect is the accumulation of peroxyl radicals, assuming that the general biomolecules (RH) represent the global composition of the cellular environment. The $\mathrm{ROO}^{\bullet}$ accounts for both the fixed DNA breaks by oxygen and the peroxidation of lipids in the cell membrane that can tear it and lead to cellular death. Thus, the normalized *Area Under the Curve* ($\mathrm{AUE}_{\mathrm{norm}}$), defined as the integral of the time evolution of $[\mathrm{ROO}^{\bullet}]$ from 0 to the maximum simulation time T_{sim}, represents the accumulation of these fixed lesions. The AUC are used in a model for the *Normal Tissue Complication Probability* (NRCP), presented as a function of the dose rate, that was compared to experimental data. The results reported, shown on figure 2.35, indicate that $\mathrm{AUE}_{\mathrm{norm}}$ could be an early indicator of long-term adverse effects on the normal tissue [LaBarbe R., et al (2020)].

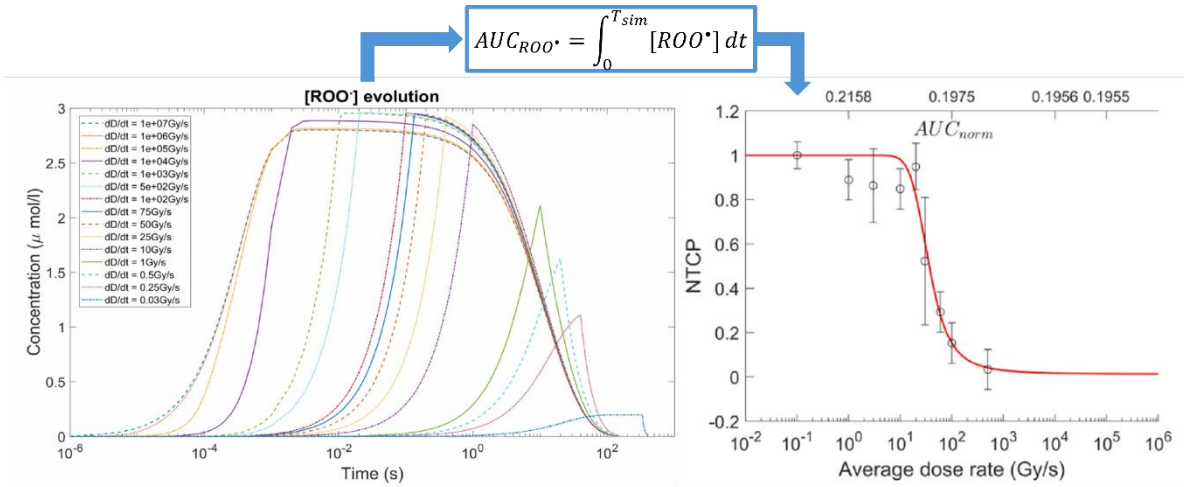

Figure 2.35. (**Left)** Time evolution of the concentration of peroxyl biological radicals, this curve integrated over the simulated time gives the $\mathrm{AUC_{ROO}}$ expression which is feuded into a model for the (**Right)** Normal Tissue Complication Probability and compared to experimental data. Images taken from [LaBarbe R., et al (2020)].

Thus, the model from LaBarbe considers a multitude of the mechanisms involved in the early chemical stage of the biological response to radiation. It has been compared with other current models that focus on the different possible explanations for the FLASH effect, [Favaudon V., et al (2021)].

Nevertheless, it has several drawbacks. For instance, the G-values that characterize the initial free radical production are from pure water. G-values are sensitive to the scavenging capacity of the medium. Considering that the cellular environment has a scavenging capacity's value estimates as approximately $3.4 \times 10^8 s^{-1}$, all the $\mathrm{e_{aq}^-}$ and OH radicals will be swept by the biomolecules at the microsecond time scales [Ramos-Méndez J., et al (2020)]. In addition, while the reaction model is representative of what occurs in a single cell, NTCP models are based on patient population. Thus, such extrapolation needs to be interpreted with caution.

On the other hand, computational simulations performed in water to study the effect of dose rates have been reported. For example, the dose rate also modifies the escape yield at a few microseconds and the long-term concentration of the radiolytic chemical species. MCTS simulations using TOPAS-nBio have been employed to reproduce and validate the time evolution of the radiolytic species under FLASH and conventional pulsated radiation sources [Shin et al. 2025]. It was observed, in water, that the chemical yield of some species, especially hydrogen peroxide, is higher using FLASH in comparison to conventional irradiation with the same delivered dose. The main reactions under FLASH pulses that contribute to the accumulation of $\mathrm{H_2O_2}$ are the recombination of hydroxyl radicals $\mathrm{2OH \rightarrow H_2O_2}$, in a period of a few microseconds, and then the reaction $\mathrm{O_2^- + O_2^-(+2H_2O) \rightarrow H_2O_2 + O_2 + OH^-}$ once sufficient $\mathrm{O_2^-}$ has been produced by other reactions lasting several minutes, [D-Kondo J.N., et al (2023)].

This difference on the final concentration of species can be explained by the fact that, even if the total number of ionizations are produced by both FLASH and CONV for a same overall dose, the higher radiation rate will generate larger concentration of free radicals within a shorter time interval than conventional irradiation, and this will affect the chemical reaction pathways [Wardman P.

(2020)]. A comparison of the results for the final hydrogen peroxide concentration for FLASH and conventional irradiations as a function of the delivered dose and initial oxygen concentration of the solution, retrieved 1000s after the beginning of the simulations, are shown below on figure 2.36.

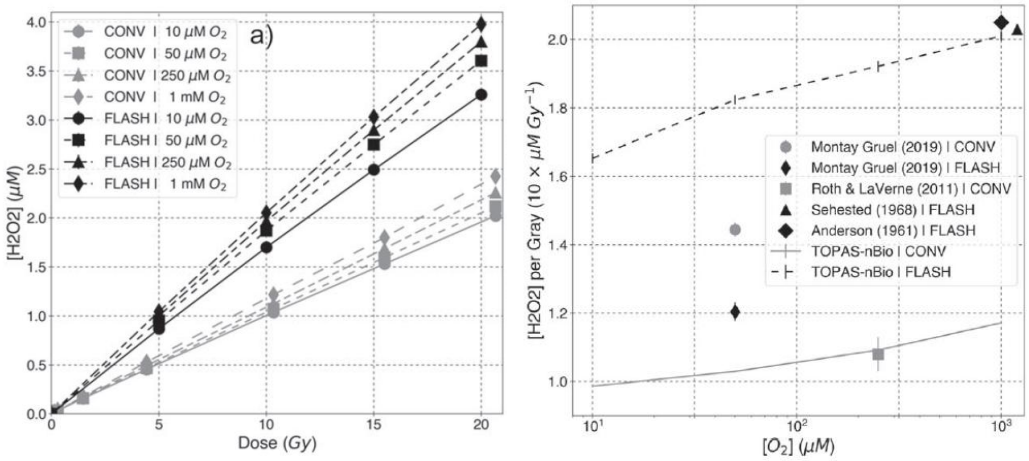

Figure 2.36 results for $[H_2O_2]$ recovered 1000s after the beginning of the irradiation as a function of delivered dose and initial oxygen concentration for CONV and FLASH irradiations using the MCTS simulation code TOPAS. Images were taken from [D-Kondo J.N., et al (2023)].

These results indicate that the same chemical yields cannot be used for the simulation of the radiation biological damage by just changing the dose rate of FLASH or CONV irradiations, like the simulation configuration used on [LaBarbe R., et al (2020)]. The final drawback of this model is that, despite the fact that the accumulation of peroxyl biological radicals correlates with the NTCP, a well-defined biological effect of radiation; this model doesn't explicitly simulate the effect of biological response mechanisms to radiation damage, like the DNA repair [Belov O., et al (2015)] or the protein networks that control the cell cycle and apoptosis signals [Zhang X.P., et al (2011)], which are fundamental process that determines the survival of an affected cell. Thus, to better understand the biological effects of the dose rate, and the variables that influence the irradiation effectiveness in general, a model for the cellular environment and its radiation damage response that consider these multiscale factors was proposed in this research work.

2.3 Biological response to radiation

Cells have two main defense systems to repair the radiation damage to biomolecules (DNA breaks) that act on different temporal stages. First, the early chemical repair by antioxidants present in the cell's environment that competes with free radicals and oxygen to prevent repair and stop the propagation of the chemical damage lasting a few seconds after irradiation. Second, the long-term enzymatic repair that involves complex networks of reactions between specialized proteins, starting once the chemical damage is settled and lasting from hours to days [Von Sontang C. (2006), Hall E.J. & Giaccia A.J. (2012), Chang D.S., et al (2021)].

The most dangerous DNA lesions from radiation are the DSBs, because the unrepaired or miss-repaired breaks can lead to the formation of chromosomal aberrations (associated with mutations), carcinogenesis and cellular death. The main mechanisms of DSBs repair are the Homologous Recombination (HR) and Non-Homologous End Joning (NHEJ).

The HR repair is a fast and error free repair pathway that takes the sister chromatin fiber as a template to repair and replace the missing genetic information of the damaged DNA region, but its only present during late-S and G2 cell cycle stages, when DNA replication is happening [Hall E.J. & Giaccia A.J. (2012), Chang D.S., et al (2021)].

On the other hand, the NHEJ is a slow and *prone to errors* repair mechanism that is available through all cell cycle stages. Here, the two broken ends of the DSBs will be processed by several repair enzymes that cut and replace the damaged bases in the DNA overhangs to match the complementary bases on the other end and then ligate the processed ends to close the gap. As a consequence, this process can cause loss of genetic information and mutations. Furthermore, in the case of closely generated DSBs the repair process can erroneously ligate two different DSBs ends and produce an aberration at the chromosome level, a lesion that might be lethal for the cell [Hall E.J. & Giaccia A.J. (2012), Chang D.S., et al (2021)].

The activation of repair enzymes influences other radiation response protein networks that work in parallel to DNA repair that controls different biological processes. In particular, the biological signaling network centered around the tumoral control protein p53 regulates the division cycle arrest while DNA is repaired, promoting the survival of the cell; or the triggering of the apoptosis process for excessively damaged cells that are beyond repair [Wu M., et al (2017), Tsabar M., et al (2020), Wang P., et al (2023)].

In the following sections a more detailed explanation of each process will be provided and some models that have been developed to reproduce the behavior of the radiation response biological mechanisms.

2.3.1 Oxidative Stress

The free radicals are a normal byproduct of the cell's biological functions. However, if an external source, like ionizing radiation, produces more radicals than the cells can normally handle lead the cell to a state known as *oxidative stress*. The accumulation of the products of these reactions can generate radio sensitizing conditions, like the increase of cellular toxicity, leading to the apoptosis process [Pizzino G, et al. (2017)]; and the depletion of antioxidants that can protect the cells if another source of stress is presented [Gebicki J. M. et al (2010)].

In "Thiyl radicals in Biology: Their Roles as a 'Molecular Switch' Central to Cellular Oxidative Stress" by [Wardman P. (1999)] a model for the effect of the main antioxidants, the ascorbic acid (AscH^-), better known as vitamin C, and the glutathione (GSH) was proposed. The sulfur bond to hydrogen ($\mathrm{S-H}$) present in thiol antioxidants is weaker than the carbon-hydrogen bond present in all intact biomolecules (RH) and in the missing sites of the radicals produced by hydrogen abstraction ($\mathrm{R}^\bullet$) after radiation indirect effect. Therefore, the damage is repairable by the hydrogen donation process, generating a thiyl radical ($\mathrm{GS}^\bullet$) as a byproduct:

$$\mathrm{R}^\bullet + \mathrm{GSH} \rightarrow \mathrm{RH} + \mathrm{GS}^\bullet$$

The measured rates for this chemical repair process for different biomolecules are between 5.0×10^7 to $2.0 \times 10^8 \mathrm{M}^{-1}\mathrm{s}^{-1}$. The thiyl can recombine to form the stable form of oxidized glutathione ($2\mathrm{GS}^\bullet \rightarrow \mathrm{GSSG}$). The reduced GSH form exists in equilibrium with its anionic form (GS^-)[Wardman P. (1999), Galano A. & Alvarez-Idaboy J.R. (2011)] as follows:

$$\mathrm{GSH} \rightleftarrows \mathrm{GS}^- + \mathrm{H}^-$$

This later form can react with thiyl radicals to form disulfide radical anions ($\mathrm{GS} + \mathrm{GS}^- \rightarrow \mathrm{GSSG}^-$) and eventually with oxygen to contribute with the yield of oxidized glutathione and superoxide radical ($\mathrm{GSSG}^- + \mathrm{O}_2 \rightarrow \mathrm{GSSG} + \mathrm{O}_2^-$) [Wardman P. (1999)] the ratio of GSH in its reduced and oxidized forms ($\mathrm{GSH/GSSG}$) is of the cellular toxicity, with a value of 8.1±2.7 for healthy adults [Perricone C. et al (2009)]. This model also considers the action of Superoxide Dismutase (SOD) that helps with the synthesis of oxygen and hydrogen peroxide as a byproduct, from superoxide radicals through the process of catalysis [Wardman P. (1999), LaBarbe R., et al (2020)]:

$$2\mathrm{O}_2^- + (2\mathrm{H}^+) \xrightarrow{\mathrm{SOD}} \mathrm{H}_2\mathrm{O}_2 + \mathrm{O}_2$$

However, thiols are not the most effective antioxidants in the cells. The ascorbic acid, the most important antioxidant in plants and in mammalian lungs [Shen J., et al (2021)] can compete with this oxidized glutathione production for the reaction with thiyl radicals and recycle the glutathione, forming ascorbyl radical, a harmless byproduct [Wardman P. (1999)]:

$$\mathrm{GS}^\bullet + \mathrm{AscH}^- \rightarrow \mathrm{GSH} + \mathrm{Asc}^-$$

The model proposed by [Wardman P. (1999)] starts with the initial concentration of glutathione ($2500\mu\mathrm{M}$), ascorbate acid $400\mu\mathrm{M}$, Oxygen ($40\mu\mathrm{M}$) and SOD ($4\mu\mathrm{M}$) in tissue, then it follows several pathways for the products of the antioxidant's response to the oxidative stress in a 27-reaction scheme and register the final concentration of several chemical species 100s afterward, presented below on Figure 2.37.

Equation	k_f[a]	k_r[a]
[damage + GSH] → GS•	0.1 μmol dm^{-3} s^{-1}	
GSH ⇌ GS^- + H^+	6.3 s^{-1}	1×10^{10}
GS• + GS• → GSSG	7.5×10^8	
GS• + GS^- ⇌ $(GSSG)^{\bullet -}$	6.2×10^8	1.8×10^5
GS• + O_2 ⇌ GSOO•	2.0×10^9	6.2×10^5
$(GSSG)^{\bullet -}$ + O_2 → GSSG + $O^{\bullet -}$	5.1×10^8	
GS• + $AscH^-$ → GS^- + $Asc^{\bullet -}$ [+ H^+]	6×10^8	
GSOO• + $AscH^-$ → $GSOO^-$ + $Asc^{\bullet -}$ + H^+	1×10^8 (?)	
$O_2^{\bullet -}$ + $O_2^{\bullet -}$ [+ $2H^+$] → H_2O_2 + O_2	2.5×10^5	
$O_2^{\bullet -}$ + $AscH^-$ [+ H^+] → H_2O_2 + $Asc^{\bullet -}$	1.5×10^5	
$O_2^{\bullet -}$ + SOD [+ H^+] → 1/2H_2O_2 + 1/2 O_2 [+SOD]	3×10^9	
$Asc^{\bullet -}$ + $Asc^{\bullet -}$ ⇌ Asc^b + $AscH^-$ [+ H^+]	1×10^6	0.1
$Asc^{\bullet -}$ + $O_2^{\bullet -}$ [+ 2 H^+] → Asc + H_2O_2	2.6×10^8	
$O_2^{\bullet -}$ + GSH → GSO• [+OH^-]	1×10^3 (?)	
GSO• + GSH → GSOH + GS•	1×10^5(?)	
GSOO• + GSH → GSO• + GSOH	2×10^6	
GSOO• → GS• (O) (O)	2×10^3 s^{-1}	
GS•(O) (O) + O_2 → GS(O)(O)OO•	5×10^8 (?)	
GS(O)(O)OO•[+ H^+] → GSO_3H + $O_2^{\bullet -}$	1×10^4 (?)	
GSO• + $O_2^{\bullet -}$ [+ H^+] → GSOH + O_2	1×10^7 (?)	
GS• [+ OH^-] → $H_2NC^\bullet$ $(CO_2^-)\cdots SH$	1.3×10^3 s^{-1}	
$H_2NC^\bullet$ $(CO_2^-)\cdots SH$ + O_2 → $H_2NCOO^\bullet(CO_2^-)\cdots SH$	1×10^9	
$H_2NCOO^\bullet(CO_2^-)\cdots SH$ → $O_2^{\bullet -}$ + products	1.5×10^5 s^{-1}	

	Possible tissue levels
Glutathione (total)	2500
Ascorbate	400
Oxygen	40
SOD	4
Dehydroascorbate	4.8
Ascorbyl radical	0.22
GSSG	0.10
H_2O_2	0.32
GSOH	0.05
GSO_3H	0.01
GSOOH	0.19
GSH product[a]	0.05
GS• thiyl radical	4×10^{-7}
$O_2^{\bullet -}$ radical	1×10^{-7}
$(GSSG)^{\bullet -}$ radical	5×10^{-8}
GSSO• radical	5×10^{-8}

Figure 2.37. Original reaction scheme, initial concentration and final concentration of chemical species 100s after the start of the simulation. Images taken from [Wardman P. (1999)]

It is important to note that biological damage is not explicitly modeled. Instead, it is represented by a constant production of thiyl radicals ($\mathrm{GS}^\bullet$) with a value of $0.1\mu\mathrm{M}/s$. To extend this chemical repair model we need to explicitly simulate how the radiolitic chemical species produced by radiation damage the constituent biomolecules of the cellular environment and compete with antioxidants repair and neutralization. Thus, the first step is to identify which biomolecules constitute the cellular environment.

2.3.2 Cellular environment composition and its radiochemical damage

Living organisms have a wide variety of biomolecules naturally present in their cellular environment that perform many different functions. In general, the radicals H, OH and e^-_{aq} can damage all biomolecules that constitute the cellular medium, abstracting hydrogen bonded to their carbon atoms and producing biological radicals [Michaels H.B. & Hunts J.W. (1978)]. The biomolecules considered in this research work are grouped into five general families: DNA, RNA, nucleotides, proteins and amino acids. Values for the concentration of these components on the cell's nucleus, their reaction rates are provided in [Michaels H.B. & Hunts J.W. (1978)] and shown in table 2.7.

Table 2.7. Concentration of the biomolecules families considered and their reaction rate with radiolytic species that can damage them, information obtained from [Michaels & Hunts (1978)]

Biomolecule	Concentration (M)	$k_{e^-_{aq}}$ $(M^{-1}s^{-1})$	k_{OH} $(M^{-1}s^{-1})$	k_H $(M^{-1}s^{-1})$	Product
DNA	0.058	1.5×10^8	4.0×10^8	2.0×10^7	$DNA^\bullet$
RNA	0.15	2.0×10^8	1.0×10^9	4.0×10^7	$RNA^\bullet$
Protein	0.75	1.0×10^8	5.0×10^8	3.0×10^5	$Pr^\bullet$
Amino acid	0.05	1.0×10^8	2.0×10^9	3.0×10^6	$Am^\bullet$
Nucleotide	0.032	7.0×10^9	5.0×10^9	2.0×10^8	$Nc^\bullet$

Antioxidants (RSH) can react to the radiation effect in several ways. In a preventive role, RSH intercepts those radicals $(RSH + OH \rightarrow H_2O + RS^\bullet)$ before they can damage other biomolecules. As chemical repair responders, these donate their hydrogen to restitute the attacked biomolecules and revert the radiation damage $(RSH + R^\bullet \rightarrow RH + RS^\bullet)$. Finally, if there is oxygen present on the environment, then RSH competes with the antioxidants to react with the biological radicals and produce peroxyl radicals $(ROO^\bullet)$. In turn, these can abstract hydrogen from other intact biological molecules and propagate the damage in a reaction chain, antioxidants can then react with peroxyl radicals, forming hydroperoxyl radicals $(ROOH)$ and terminate the propagation of damage. Another biological radical termination pathway can be the recombination, where two of these radicals react and form a double covalent bond $(R = R)$ [Gebicki J. M. et al (2010)]. A schematic of this whole process is shown on figure 2.38.

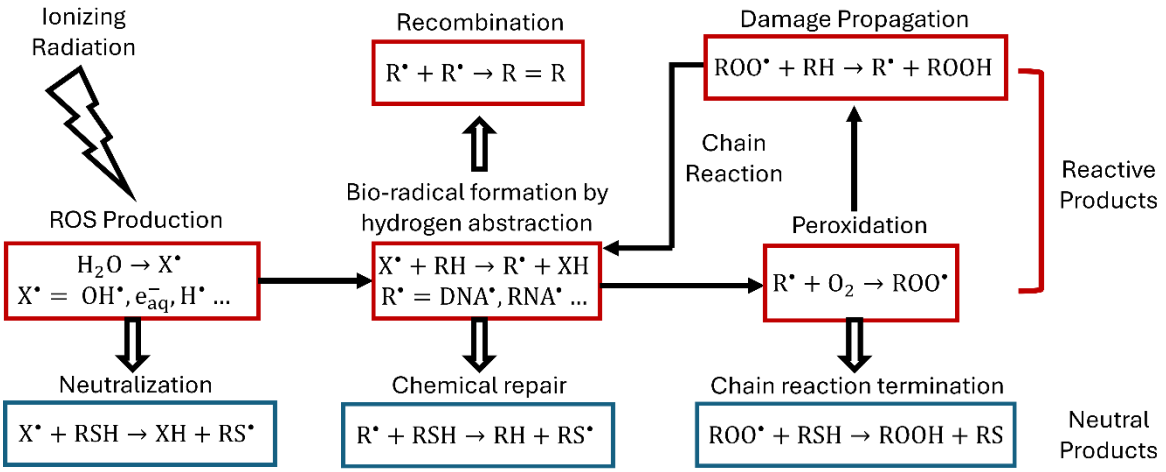

Figure 2.38. General scheme of the antioxidant action on the biological radicals produced by radiation on the cell's environment, arrows represent chemical reaction steps while double arrows represent termination reactions.

To account for the first role of antioxidants, the reaction rate between both GSH and $\mathrm{AscH^-}$ with free radicals was searched in the literature. An extensive study of the reactions and their rates with free radicals was reported elsewhere [Shen J., et al (2021)]. Vitamin C exists in two forms, ascorbic acid ($\mathrm{AscH_2}$) and ascorbate ($\mathrm{AscH^-}$) which exist in equilibrium ($\mathrm{AscH_2} \rightleftarrows \mathrm{AscH^-} + \mathrm{H^+}$). Their total concentration in human cells is $100\mu\mathrm{M}$ spread in $[\mathrm{AscH_2}] = 60\mu\mathrm{M}$ and $[\mathrm{AscH^-}] = 40\mu\mathrm{M}$. For simplicity and considering that the oxidative stress model only accounts for $\mathrm{AscH^-}$, we assumed that all vitamin C in the system is in the later form. Both forms of vitamin C can react with OH, $\mathrm{O_2^-}$and $\mathrm{HO_2}$ to produce $\mathrm{Asc^-}$ radicals and other byproducts. We choose the larger value for each reaction rate provided to represent the neutralization action of this antioxidant. In turn, these ascorbyl radicals can react with $\mathrm{O_2^-}$ and $\mathrm{HO_2}$ and produce Dehydroascorbic Acid (DHA) and $\mathrm{HO_2^-}$ as byproducts, the information for the value of the reaction rates and products is provided in table 2.8.

On the other hand, GSH has a concentration in tissue of $2.5\mathrm{mM}$; and the values for the glutathione reaction rate with $\mathrm{O_2^-}$ and OH were found in [Wardman P. (1999)]. The last parameter $k_{OH} = 1.0 \times 10^{10}\mathrm{M^{-1}s^{-1}}$ is consistent with the one measured by [Eriksen T.E. & Fransson G. (1988)] with a value of $1.4 \times 10^{10}\mathrm{M^{-1}s^{-1}}$ and later calculated using computer simulations by [Galano A. & Alvarez-Idaboy J.R. (2011)] with a value of around $1.1\times 10^{10}\mathrm{M^{-1}s^{-1}}$. The last author also calculated the reaction rate for the $\mathrm{GSH} + \mathrm{HO_2}$ reaction, but no experimental value was provided for comparison, therefore we didn't consider this reaction. The information for the reactions chosen is presented below in table 2.8.

Table 2.8. Reaction rates ($\mathrm{M^{-1}s^{-1}}$) for the main antioxidants with OH, $\mathrm{O_2}$ and $\mathrm{HO_2}$ and their byproducts

Antioxidant	k_{OH}	Byproducts	$k_{O_2^-}$	Byproducts	k_{HO_2}	Byproducts
GSH [2.5 mM]	1.4×10^{10}	GS	2.0×10^{2}	$\mathrm{GSO} + \mathrm{OH^-}$	----------	----------
$\mathrm{AscH^-}$[60µM]	1.0×10^{10}	$\mathrm{Asc^-}$	5.0×10^{4}	$\mathrm{Asc^-} + \mathrm{HO_2^-}$	1.25×10^{6}	$\mathrm{Asc^-} + \mathrm{H_2O_2}$
$\mathrm{AscH_2}$[40µM]	7.9×10^{9}	$\mathrm{Asc^-} + \mathrm{H^+}$	1.6×10^{4}	$\mathrm{Asc^-} + \mathrm{H_2O_2}$	1.22×10^{7}	$\mathrm{Asc^-} + \mathrm{H_2O_2} + \mathrm{H^+}$
$\mathrm{Asc^-}$[0.0µM]	----------	----------	2.6×10^{8}	$\mathrm{DHA} + \mathrm{HO_2^-}$	5.0×10^{9}	$\mathrm{DHA} + \mathrm{HO_2^-}$

The other two roles of antioxidants (the chemical repair and termination of the damage propagation) involve reactions with the damaged biomolecules in the cellular environment. However, the chosen biomolecular families contemplate large collections of complex macromolecules. Therefore, the approach taken to generalize the action of the antioxidants on each of these general groups in this research work was to search for available information in the literature for the reaction rates of the chemical repair, peroxidation, recombination, and other processes for representative molecules of each family. These can be the most abundant one in the cellular environment or a set of well-studied biomolecules that can be averaged. These representative values are then extrapolated to the whole family and explained in the next sections.

2.3.2.1 Protein and Amino acids

Amino acids are the building blocks of larger macromolecules, but they also play an important biological role as "energy storage" and in biochemical signaling. Chemically, these molecules are organic compounds with an *amino* group ($\mathrm{NH_2}$) attached to a carboxyl group (COOH) or sulfonate group ($\mathrm{SO_3}$). There are hundreds of naturally occurring amino acids, but only 20 of them are necessary for the human body and are known as *essential* amino acids. Peptides and proteins are

polymers whose constituent blocks are amino acids. This group of macromolecules plays different important roles for all biological processes. They are involved in metabolism, function as neurotransmitters and biochemical messenger for the intercellular signals [Dietzen D.J. (2018)].

Peptides are short amino acid chains (of about 50 units) that control endocrine and autocrine signals for the appetite, vascular pressure and metabolism of electrolytes, and are part of the radiation response to radiation. For example, the important antioxidant GSH is a tripeptide made of the amino acid glutamate, cysteine, and glycine linked together (Glu-Cys-Gly), being the most abundant antioxidant in cells at around 1-10mM both in tissue and blood [Galano A. & Alvarez-Idaboy J.R. (2011), Dietzen D.J. (2018)].

Lastly, proteins are large amino acid sequences with a wide range of functions. They form support structures of cells, synthesize several necessary biological compounds, and more importantly, they participate in the assembly, replication and repair of the DNA lesions, mediating the biological mechanisms of radiation response [Belov O. et al (2015), Dietzen D.J. (2018), Wang P., et al (2023)].

Proteins have complex structures, but they can be broken into several levels. The primary structure is the lineal sequence of amino acids that forms it. The secondary structure describes the angles between the bonds of the multi-peptides assembly, creating stable structures like the α-helix. The tertiary structure is the 3D geometrical form that results from the folding of the polypeptide secondary structure, forming a super-helix that constitutes a *domain*. Finally, the quaternary structure is the joining of two or more polypeptide domains that form a large complex. There might be other attached structures that provide additional protein functions, such as metals; for example, the iron in the core of hemoglobin enables the transport of oxygen [Dietzen D.J. (2018)].

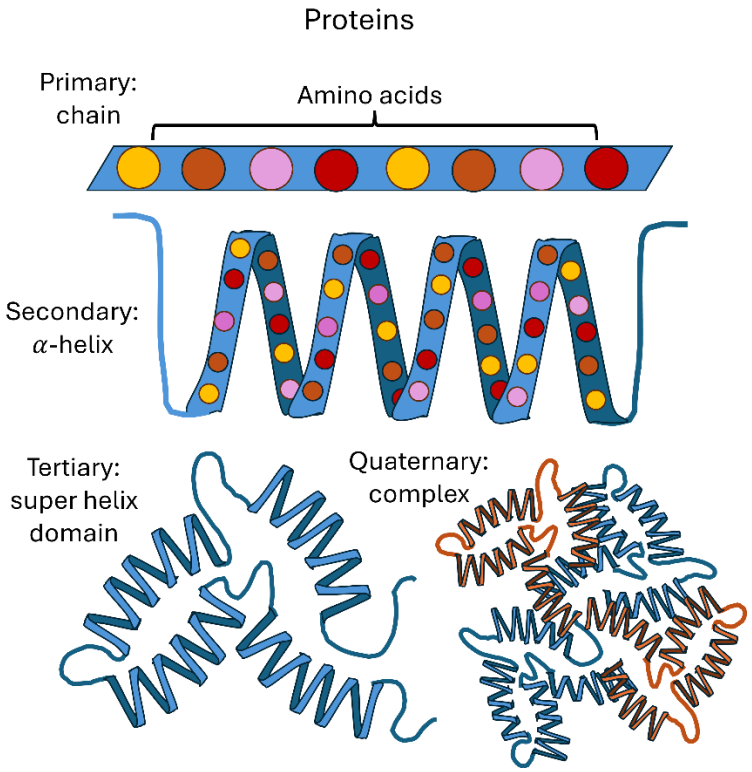

Figure 2.39. Different levels of protein structures. Images adapted from [Alberts B., et al (2002)]

It's been estimated that the human genome codifies around 20,000 different proteins, but the actual number on the cellular environment might be higher since RNA codifies their own proteins [Dietzen D.J. (2018)]. Furthermore, the proteins represent the largest organic component of the cellular environment by far, making them the main secondary target for radiation and the principal indicator of cellular damage under oxidative stress conditions even in the presence of antioxidants [Gebicki J.M. et al (2010)]. This fact makes an extensive study for the characterization of protein damage and its chemical repair a huge challenge.

Nevertheless, lysosomes have been used as a model to represent and characterize the formation of protein radicals by ionizing radiation and their chemical repair by the two main cellular antioxidants, ascorbic acid and glutathione [Nauser T., et al (2005), Domazou A.S, et al (2009), Gebicki J.M. et al (2010)]. Lysosomes are proteins of 129 amino acids in length that form an important part of the immune system of many living organisms including humans [Baron F., et al (2016)]. Therefore, they were chosen as a model protein since they are water soluble, compact and well characterized proteins [Nauser T., et al (2005)].

These research works that use lysosomes as protein representatives [Nauser T., et al (2005), Domazou A.S, et al (2009),Gebicki J.M. et al (2010)] identify several types of protein lesions using FLASH photolysis and $^{60}\mathrm{Co}$ gamma radiolysis to irradiate an aqueous solution containing lysozymes saturated with Nitrous Oxide ($\mathrm{N_2O}$) since the radical $\mathrm{N_3^{\bullet}}$ can directly and selectively damage two of the amino acids that form the model protein, Tryptophan (TrpH) and Tyrosine (TyrOH) to produce their respective amino acids radicals ($\mathrm{Trp^{\bullet}}$ and $\mathrm{TyrO^{\bullet}}$). They can be free amino acid radicals or attached to a protein fragment $\mathrm{Lyz(Trp^{\bullet})}$ or $\mathrm{Lyz(TyrO^{\bullet})}$. The value of the chemical repair rate of the multiple considered lesions on protein and amino acids were provided for GSH with values between 2.4×10^{3} to $1.05\times 10^{5}\ \mathrm{M/s}$ [Nauser T. et al (2005), Gebicki J.M. et al (2010)] and $\mathrm{AscH^{-}}$with values between 1.1×10^{7} to $2.6\times 10^{8}\ \mathrm{M/s}$ [Domazou A.S, et al (2009), Gebicki J.M. et al (2010)].

A comparison of the chemical repair of carbon-centered protein radicals ($\mathrm{Pr^{\bullet}}$), in the absence of oxygen, and peroxyl protein radicals ($\mathrm{PrOO^{\bullet}}$), in the presence of oxygen, was used to determinate that the oxidizing of antioxidants by peroxyl radicals is between 10-20 times greater than for carbon-centered radicals, and a general value for the peroxidation of amino acid containing carbon-center radicals ($\mathrm{Pr^{\bullet}+O_2\rightarrow PrOO^{\bullet}}$) of $1.0\times 10^{9}\mathrm{M/s}$ [Nauser T. et al (2005)] similar to the average of other carbon centered radicals $(2.2\pm 0.1)\times 10^{9}\mathrm{M/s}$ studied in the past [Zhang X., et al (1994)].

In contrast, the smaller value for individual amino acid radicals $\mathrm{Trp^{\bullet}/TyrO^{\bullet}+O_2\rightarrow TrpOO^{\bullet}}$ $\mathrm{/TyrOOO^{\bullet}}$ of $5\times 10^{6}\mathrm{M/s}$ and $2\times 10^{5}\mathrm{M/s}$ were reported [Nauser T., et al (2005)] and values for the recombination of amino acids ($\mathrm{2Am^{\bullet}\rightarrow Am=Am}$) are also provided with a reaction rate of $3.6\times 10^{8}\mathrm{M^{-1}s^{-1}}$[Domazou A.S, et al (2009)], close to the dimerization rate for $\mathrm{TyrO^{\bullet}}$ measured in the past with a value of $4.5\times 10^{8}\mathrm{M^{-1}s^{-1}}$[Jin F., et al (1993)]

To represent all the available information in a single general reaction rate per process, an average was taken when multiple lesions were considered. The values used for the modeling of this biomolecule family is presented on table 2.9.

Table 2.9. Reactions for protein and amino acid radicals

Process	Reaction	k $(\mathrm{M^{-1}s^{-1}})$
GSH chemical repair	$\mathrm{Pr^{\bullet} + GSH \rightarrow PrH + GS^{\bullet}}$	1.05×10^5
	$\mathrm{Am^{\bullet} + GSH \rightarrow AmH + GS^{\bullet}}$	1.1×10^5
$\mathrm{AscH^-}$ chemical repair	$\mathrm{Pr^{\bullet} + AscH^- \rightarrow PrH + Asc^-}$	5.8×10^7
	$\mathrm{Am^{\bullet} + AscH^- \rightarrow AmH + Asc^-}$	1.3×10^8
$\mathrm{Am^{\bullet}}$ Recombination	$\mathrm{2Am^{\bullet} \rightarrow Am = Am}$	4.0×10^8
Biological radical peroxidation	$\mathrm{Pr^{\bullet} + O_2 \rightarrow PrOO^{\bullet}}$	1.0×10^9
	$\mathrm{Am^{\bullet} + O_2 \rightarrow AmOO^{\bullet}}$	3.5×10^6
Peroxyl radical repair	$\mathrm{PrOO^{\bullet} + GSH \rightarrow PrOOH + GS^{\bullet}}$	1.05×10^6
	$\mathrm{AmOO^{\bullet} + GSH \rightarrow AmOOH + GS^{\bullet}}$	1.1×10^6

2.3.2.2 Lipids

Lipids consist of a large family with tens of thousands of different macromolecules central in various biological processes. These are the main building blocks of the cell membrane that delimit and organize the cellular components. In addition, these serve as energy storage and regulate the signaling between intercellular compartments, like the electron transport chain on the mitochondria and extracellular protein signaling process (like the ion channels and pumps) [Gross R.W. & Han X. (2011)].

In the original model for the cellular environment composition, lipids are not considered since they represent just around 3% of the total weight of the cell, and only the radicals produced near the cell's membrane will damage them, making the reaction rate between free radicals and lipids very challenging to measure [Michaels H.B. & Hunts J.W. (1978)]. Therefore, lipids were not included in the current research work.

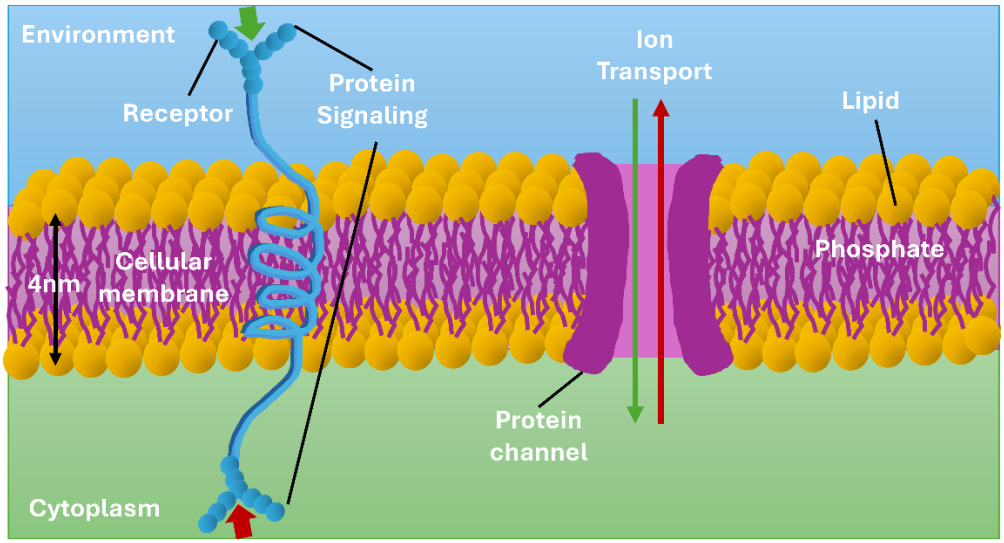

Figure 2.40. general structure of the cell membrane. Image adapted from [Gross R.W. & Han X. (2011)].

However, since lipids are such fundamental biomolecules for the structural integrity and biological functions of the cells, the process of lipid oxidation, chain reaction and chemical repair were investigated and are ready for their implementation in future works. In [Yin H., et al (2011)] was reported an extensive review of the response of lipids to oxidative stress using the linoleate, a member of the fatty-acids family, the principal representative of all lipids. On the other hand, lipids are repaired mainly by vitamin E, a family of eight antioxidants whose more abundant form is the α-Tocopherol in humans, rather than GSH [Niki E. (2021)]. These two research works provide reaction rates for the lipid radical initiation by hydroxyl radicals ($\mathrm{LH + OH \rightarrow L^{\bullet} + H_2O}$), termination of the peroxyl radicals by α-Tocopherol ($\mathrm{LOO^{\bullet} + TH \rightarrow LOOH + T^{\bullet}}$) and recycling of vitamin C radicals by ascorbate ($\mathrm{T^{\bullet} + AscH^{-} \rightarrow TH + Asc^{-}}$). All information available is listed on table 2.10.

Table 2.10. Reactions for protein and amino acid radicals

Process	Reaction	$k\ (\mathrm{M^{-1}s^{-1}})$
Initiation	$\mathrm{LH + OH \rightarrow L^{\bullet} + H_2O}$	1.0×10^{9}
Peroxidation	$\mathrm{L^{\bullet} + O_2 \rightarrow LOO^{\bullet}}$	1.0×10^{9}
Propagation	$\mathrm{LOO^{\bullet} + LH \rightarrow LOOH + L^{\bullet}}$	6.0×10^{1}
Recombination	$\mathrm{2LOO^{\bullet} \rightarrow L - OO - OO - L}$	$1.0 \times 10^{6} - 1.0 \times 10^{7}$
Termination	$\mathrm{LOO^{\bullet} + TH \rightarrow LOOH + T^{\bullet}}$	3.2×10^{6}
Recycling	$\mathrm{T^{\bullet} + AscH^{-} \rightarrow TH + Asc^{-}}$	1.0×10^{6}

2.3.2.3 DNA, RNA and nucleotides

DNA is the main target of radiation, therefore its reactions with multiple radiolytic chemical species, their branching pathways, reaction rates and products have been studied in depth for many decades [Michaels H.B. & Hunt J.W. (1973,1977,1978), Milligan J.R., et al (1993), Von Sontang C. (2005), Dizdaroglu M. & Jaruga P. (2012)]

In addition, the majority of living organisms and viruses have another nucleic acid in their cellular environment, the RNA, that has two structural differences with the DNA, figure 2.41. It is made of a single strand and uses the nitrogenous base Uracil (U) instead of Thymine. The main function of RNA is as the biochemical messenger that translate the information codified in DNA to the amino acid equivalent in the assembly of proteins [Wang D. & Farhana A. (2023)].

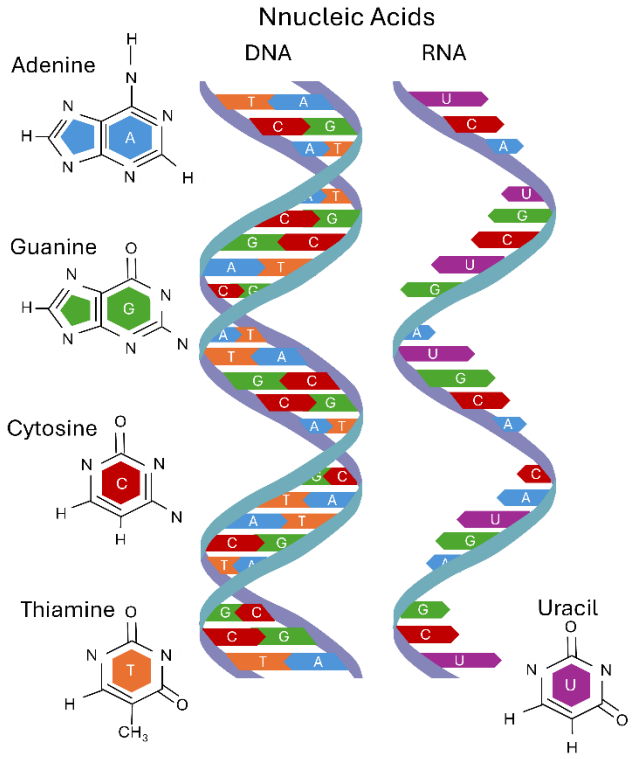

Figure 2.41. Nucleic acids, DNA and RNA, naturally present on living cells, and the nitrogenous bases that make them.

In the indirect damage induction by ionizing radiation to DNA or RNA, oxygen plays a major role. The oxygen effect in DNA damage has been known since the 60's. The survival of bacteria increased in the presence of the sulfhydryl radioprotective compounds cysteine and cysteamine, when it was speculated that these biomolecules acted as hydrogen donors that repair the chemical damage of radiation and competed with oxygen to fix the breaks [Howard-Flanders P. (1960)]

In the 70s experiments were carried out to measure several rate constants for nucleic acids and chains of nucleotides known as *polynucleotides* by [Michaels H.B. & Hunt J.W. (1973)], *s*hown in figure 2.41. This study resulted in a value for the reaction rate of isolated cytosine and O_2 of $2.3 \times 10^9 \mathrm{M}^{-1}\mathrm{s}^{-1}$and for Cytidine-5' Monophosphate (5'-CMP), a pyrimidine ribonucleoside that contains the base cytosine, deoxyribose and a phosphate group, that can form RNA [National Center for Biotechnology Information (2024)] with a value of $1.1 \times 10^9 \mathrm{M}^{-1}\mathrm{s}^{-1}$. Therefore, the rate chosen for the nucleotides is the average of these two quantities. In the other hand [O'Neill P. (1983)] measured the value of the reaction rate between deoxiGuanosine-5' Monophosphate (dGMP) radicals with GSH and other thiols, resulting in a value of $8.0 \times 10^6 \mathrm{M}^{-1}\mathrm{s}^{-1}$ that we adopted for the free nucleotide chemical repair rate.

The rest of the considered polynucleotides are chains of Cytosine, Adenine and Uracil, giving an average reaction rate of $\mathrm{k}_{\mathrm{O}_2} = 4.0 \times 10^8 \mathrm{M}^{-1}\mathrm{s}^{-1}$ for the oxygen fixation process.

Rate Constants for the Reaction of O_2 with ·OH Adducts

Solute	*Wavelength* (*nm*)	*k* (M^{-1} sec^{-1})
Cytosine	425	2.3×10^9
5′-CMP	425	1.1×10^9
Poly C	425	3.8×10^8
Poly U	380	4.8×10^8
Poly A	400	2.8×10^8
Single-stranded DNA	400	4×10^8

Figure 2.41. Experimentally measured reaction rates between different polynucleotides and OH. Image taken from [Michaels H.B. & Hunt J.W. (1973)]

The value measured by these authors was also used to solve the Alper-Howard-Flanders formula by [Schulte-Frohlinde D. & Bothe E. (1990)] which is a quantitative description of the oxygen enhancement ratio as a function of the oxygen concentration that takes into account the oxygen fixation and chemical repair by GSH, given by the next expressions:

$$\mathrm{OER} = \frac{\mathrm{m}[\mathrm{O_2}] + \mathrm{K}}{[\mathrm{O_2}] + \mathrm{K}}$$

$$\mathrm{m} = \frac{\mathrm{k_{rep}}[\mathrm{GSH}] + \mathrm{k_f}[\mathrm{F}]}{\mathrm{k_f}[\mathrm{F}]}$$

$$\mathrm{K} = \frac{\mathrm{k_{rep}}[\mathrm{GSH}] + \mathrm{k_f}[\mathrm{F}]}{\mathrm{k_{O_2}}}$$

Where m is the maximum OER possible in a given system, and K is the concentration of oxygen to obtain half of the m enhancement effect, $\mathrm{k_{rep}}$ and $\mathrm{k_{O_2}}$ are the reaction rates for the chemical repair and oxygen fixation process respectively, while F and $\mathrm{k_f}$ are parameters that describe an *inherit* radiosensitizer process of the system ($\mathrm{DNA^{\bullet}} + \mathrm{F} \xrightarrow{k_f} \mathrm{damage}$) [Schulte-Frohlinde D. & Bothe E. (1990)]. However, due to the experimental observation that in complete absence of oxygen a fraction x of the total DNA breaks was not repairable by GSH, a correction for the Alper formula was made to the m term as a function of x [Edgren M., et al (1985)], given by.

$$\mathrm{m'} = \frac{\mathrm{k_{rep}}[\mathrm{GSH}] + \mathrm{k_f}[\mathrm{F}]}{\mathrm{k_f}[\mathrm{F}] + \dfrac{\mathrm{k_{rep}}[\mathrm{GSH}]}{1 + x}}$$

The intrinsic radiosensitizer parameter can also be viewed as the formation of strand breaks process from the DNA radicals that doesn't require oxygen ($\mathrm{DNA^{\bullet}} \xrightarrow{\mathrm{k_{SB}}} \mathrm{SB}$) [Schulte-Frohlinde D. & Bothe E. (1990)], and the terms of the Alper formula can be rewritten as:

$$\mathrm{m} = \frac{\mathrm{k_{rep}}[\mathrm{GSH}] + \mathrm{k_{SB}}}{\mathrm{k_{SB}}} \qquad \mathrm{K} = \frac{\mathrm{k_{rep}}[\mathrm{GSH}] + \mathrm{k_{SB}}}{\mathrm{k_{O_2}}} \qquad \mathrm{m'} = \frac{\mathrm{k_{rep}}[\mathrm{GSH}] + \mathrm{k_{SB}}}{\mathrm{k_{SB}} + \dfrac{\mathrm{k_{rep}}[\mathrm{GSH}]}{1 + x}}$$

In a system with no oxygen, values for the reaction rates were obtained in E. Coli assays by [Schulte-Frohlinde D. & Bothe E. (1990)]. For the formation of strand breaks independent of oxygen $\mathrm{k_{SB}} = 33\mathrm{s}^{-1}$, and chemical repair in cells $\mathrm{k_{rep}} = 0.85 \times 10^{5}\mathrm{M}^{-1}\mathrm{s}^{-1}$; and in aqueous solution, with a close value of $1.6 \times 10^{5}\mathrm{M}^{-1}\mathrm{s}^{-1}$. Furthermore, the authors also provided reaction rate values for the corresponding process on peroxyl DNA radicals. This is the strand break formation ($\mathrm{DNAOO}^{\bullet} \xrightarrow{\mathrm{k'_{SB}}} \mathrm{SB}$) with $\mathrm{k'_{SB}} \approx 5\mathrm{s}^{-1}$ and the chemical repair ($\mathrm{DNAOO}^{\bullet} + \mathrm{GSH} \xrightarrow{\mathrm{k'_{rep}}} \mathrm{DNAOOH} + \mathrm{GS}^{\bullet}$) with $\mathrm{k'_{rep}} = 6 \times 10^{3}\mathrm{M}^{-1}\mathrm{s}^{-1}$. The summary of this information is provided in table 2.11 below.

Table 2.11. Reactions for protein and amino acid radicals

Process	Reaction	$k\ (\mathrm{M}^{-1}\mathrm{s}^{-1})$
GSH chemical repair	$\mathrm{DNA}^{\bullet} + \mathrm{GSH} \rightarrow \mathrm{DNA} + \mathrm{GS}^{\bullet}$	0.85×10^{5}
	$\mathrm{RNA}^{\bullet} + \mathrm{GSH} \rightarrow \mathrm{RNA} + \mathrm{GS}^{\bullet}$	0.85×10^{5}
	$\mathrm{NUC}^{\bullet} + \mathrm{GSH} \rightarrow \mathrm{NUC} + \mathrm{GS}^{\bullet}$	8.0×10^{6}
Radical peroxidation	$\mathrm{DNA}^{\bullet} + \mathrm{O_2} \rightarrow \mathrm{DNAOO}^{\bullet}$	4.0×10^{8}
	$\mathrm{RNA}^{\bullet} + \mathrm{O_2} \rightarrow \mathrm{RNAOO}^{\bullet}$	4.0×10^{8}
	$\mathrm{NUC}^{\bullet} + \mathrm{O_2} \rightarrow \mathrm{NUCOO}^{\bullet}$	1.7×10^{9}
Peroxyl radical repair	$\mathrm{DNAOO}^{\bullet} + \mathrm{GSH} \rightarrow \mathrm{DNAOOH} + \mathrm{GS}^{\bullet}$	6×10^{3}
	$\mathrm{RNAOO}^{\bullet} + \mathrm{GSH} \rightarrow \mathrm{RNAOOH} + \mathrm{GS}^{\bullet}$	6×10^{3}
	$\mathrm{NUCOO}^{\bullet} + \mathrm{GSH} \rightarrow \mathrm{NUCOOH} + \mathrm{GS}^{\bullet}$	6×10^{3}

This information constitutes the chemical contribution to DNA repair by glutathione, which is part of the early biological response to radiation. However, since the integrity of the DNA is crucial for the survival of the cell, living organisms have evolved different DNA repair mechanisms that involve the action of specialized proteins in long-term processes.

2.3.3 Enzymatic repair of DNA

Cells have developed several biological mechanisms to detect different lesions in DNA, then send signals to alert their presence and recruit proteins that can repair them. Other biochemical signals work in parallel to the DNA repair that will delay the cell cycle progression or trigger other processes like apoptosis. Together these mechanisms form the *DNA Damage Response* (DDR) [Stucki M. & Jackson S.P. (2006)].

Simple lesions like base damages and SSBs can be easily repaired since the opposite strand contains the complementary base. Thus, the damaged bases can be removed and substituted with the correct ones by the Base Excision Repair (BER) mechanism. When bulky lesions occur on nearby DNA basis, like radical adducts on several adjacent nucleotides, the *Nucleotide Excision Repair* (NER) pathway recognizes the damage and isolates a region of around 24 to 32 nucleotides to remove the damaged region, synthesizes the missing nucleotides to fill the gap and ligates the DNA. Since these types of repair mechanisms can use the intact strand as a template, there is not a risk of genetic information

loss and the harmful consequences associated with it, like mutations or cellular death [Hall E.J. & Giaccia A.J. (2012), Chang D.S., et al (2021)].

However, when DSBs occur, the DNA is broken into two sections, and the fragmentation of the ends can cause loss of DNA regions [Chang H.H.Y., et al (2017)]. Cells have two main repair pathways for DSBs: The Homologous Recombination and the NHEJ, as described above in section *2.3 Biological response to radiation*. There exists an Alternative end Joining (AltEJ) that activates when the necessary repair proteins for NHEJ are not available, and a repair mechanism called *Single-Strand Annealing* (SSA) that specifically relieves HR when the cells have a deficiency of a protein called RAD51 [Scully R., et al (2019)].

In any case, the first step of the repair pathways is DNA damage recognition. The protein complex MRN made by three proteins, Mre11, Rad50, and Nbs1, is *ubiquitously* distributed in the cell environment, and it binds to DNA breaks. The activity of this protein complex produces two results:

1. It initiates a chemical process known as DSB *end-resection* that cuts the nucleotides in the DNA overhangs in the 5'3' direction and,

2. It activates a fundamental protein for the damage sensor called Ataxia Telangiectasia Mutated (ATM).

ATM was named after the autosomal recessive disorder ataxia-telangiectasia, where the inactivation of this protein causes progressive loss of cerebellar function [Paull T.T. (2015)]. It has been identified as the central piece of the DSBs *sensor*, since it activates proteins that initiate the cell-cycle arrest (like the Checkpoint kinase 2 (Chk2)), the DNA repair (like the KU repair protein recruitment) or the apoptosis processes (like the tumor suppressor protein p53) [Lee J-H. & Paull T.T. (2005)]. The activation of proteins is done by a mechanism called *phosphorylation* in which a phosphate group from an *Adenosine Triphosphate* (ATP) molecule is transferred to a specific site of the protein, changing its conformation and allowing certain function [Nestler E.J. & Greengard P. (1999)]

Another important protein that ATM activates is the histone H2AX, which forms part of the chromatin fiber and transforms it into γ-H2AX in both directions of the DNA breaks. This active histone anchors the *Mediator of DNA damage checkpoint 1* (MDC1) protein that functions as a *platform* or *scaffold* for the recruitment of other repair proteins. The MDC1 propagates the phosphorylation of the H2AX histones across the chromatin fiber for regions that may extend for hundreds of bp, amplifying the recruitment signal of the γ-H2AX [Ghosh R., et al (2018), Scully R., et al (2019), Ruff S., et al (2020)]. The actions of both MDC1 and γ-H2AX are not "essential" for the repair process per se, but they are needed for the full efficiency of both NHEJ and HR repair processes. Furthermore, cells with deficiencies of these proteins show a limited repair capacity [Stucki M. & Jackson S.P. (2006)]. The early DDR stage is shown in figure 2.42.

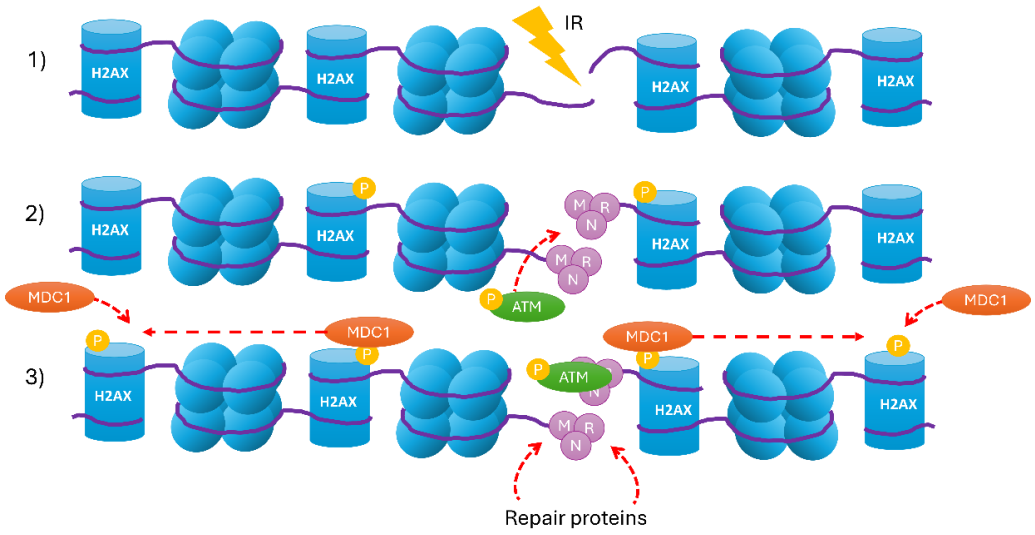

Figure 2.42. Early DDR protein actions **1)** DSBs formation by ionizing radiation, **2)** the MRN protein complex attaches to the DSBs ends and activates the ATM protein that in turns phosphorylate the histones H2AX **3)** then, the protein MDC1 joins the γ-H2AX histone, start the repair proteins recruitment and propagate the phosphorylation of H2AX to amplify the recruitment signal. Image adapted from [Stucki, M., & Jackson, S. P. (2006), Gautam, D., & Moody, C. A. (2016)]

The first repair protein to be recruited is the *heterodimer complex* Ku formed by two proteins Ku-70 and Ku-80, that bind to the DSBs ends, forming a ring that encircles the lesions and initiates the repair process. It is an active part of the NHEJ process, and it is displaced on the HR pathway in the first repair step. The Ku complex has a greater affinity to blunt DSB ends or lesions with short overhangs of less than 20bp rather than DSBs with longer tails, provoking the NHEJ initiation for these complex lesions to be less efficient. The ATM also participates actively in the NHEJ when the Ku complex binds to the DSBs ends and when it is disassembled after ligation. [Bowater R. & Doherty A.J. (2006), Neal J.A. & Meek K. (2011), Chang H.H.Y., et al (2017), Scully R., et al (2019)].

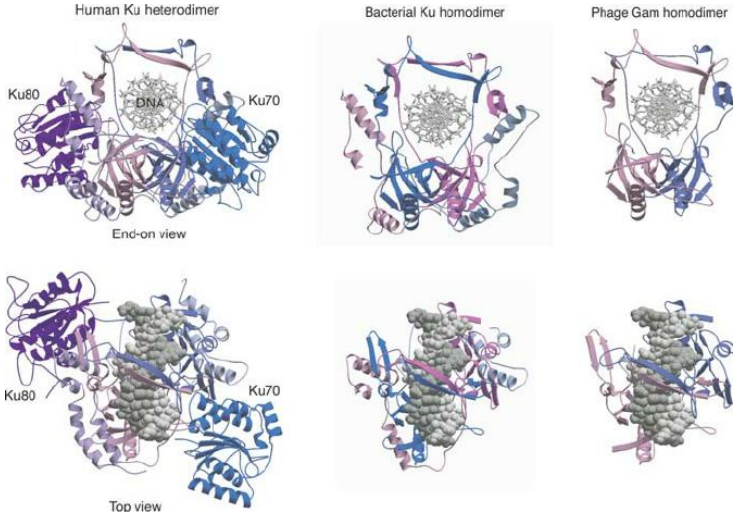

Figure 2.43. Ku complex of humans and bacteria showing the ring structure that encircles the DSBs ends. Image taken from [Bowater R. & Doherty A.J. (2006)]

From this point, the NHEJ mechanism branches into several sub processes that depend on the length and compatibility of the overhangs at the DSBs broken ends, involving several repair proteins that

process them in a specific manner. For example, compatible blunt ends can be directly ligated by the XRCC4–DNA ligase IV complex. On the other hand, when the ends are incompatible, the protein Artemis can perform a resection process to cut a portion of the overhang's boundary while the polymerases Pol μ and Pol λ synthetize new nucleotides in an attempt to generate small regions of *micro homology* that facilitate the ligation of the ends. It is important to note that these enzymes can act in any order, trying to ligate the ends, adding or cutting nucleotides, and consequently, multiple rounds of end processing can happen before a region of microhomology is generated. However, this means that these rounds of repair are error-prone and can generate a multitude of changes in the DNA sequence, producing mutations or mis repairs [Chang H.H.Y., et al (2017)]. The branching pathways and action of these enzymes can be seen below on figure 2.44.

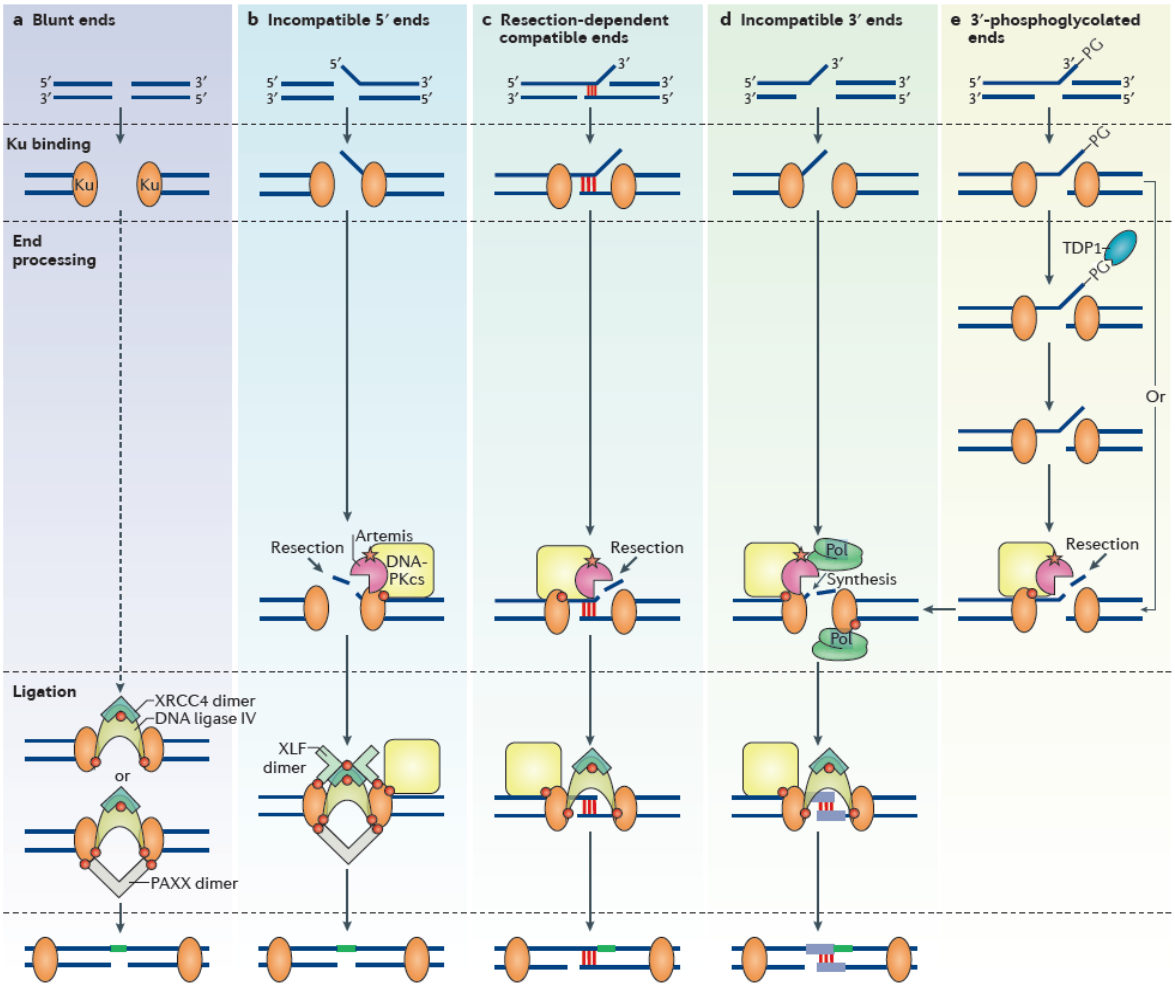

Figure 2.44. NHEJ DNA repair mechanisms and the branching pathways of the enzymes that process the different DSBs ends. Image taken from [Chang H.H.Y., et al (2017)].

Another effect of the Ku binding to the DSBs overhangs is that it prevents the prolonged end resection by the MRN complex, favoring the repair by NHEJ. However, when cells reach the S and G2 phases, where DNA is being replicated and the later stage where two complete copies of the genome exist respectively, the action of the cyclin-dependent kinases (CDK, a protein that control the cell

cycle progression) promotes the extensive end resection by MRN and favors the HR repair mechanism [Hall E.J. & Giaccia A.J. (2012), Chang H.H.Y., et al (2017)].

MRN cut the DSBs ends in the 5'3' direction of the DNA and needs the intervention of the protein CtIP to make a long resection. The complex formed by the exonuclease 1, the endonuclease DNA2, and the Bloom syndrome helicase (EXO1, BLM–DNA2) do the same resect process in the 3'5' direction, and its recruitment displaces the Ku complex. The action of these complexes degrades or *nicks* long regions of up to 300 nucleotides of length. These long DNA tails are rapidly filled or *coated* with the RPA complex that blocks other protein interactions with the DNA. At this point, if the HR repair proceeds, the RPA complex is substituted by the enzyme RAD51 that produces a *nucleoprotein filament* that mediates the process of invasion of the sister chromatin fiber that will be used as a template to reconstruct the DSBs resected ends. As a consequence, the invasion displaces the region of the intact chromatin that will be copied to facilitate the *gene conversion,* creating a region known as a *displacement loop* (D-loop). The polymerase δ (Pol δ) helps in the transfer of genetic information by synthesizing the nucleotide copies on the *nascent strand.* At the end of the HR, a crossover between the intact chromatin fiber and the repaired strand can occur, known as Holliday junctions. These crossovers can be solved by another pair of proteins MMS4 and MUS81 [Hall E.J. & Giaccia A.J. (2012), Scully R., et al (2019)].

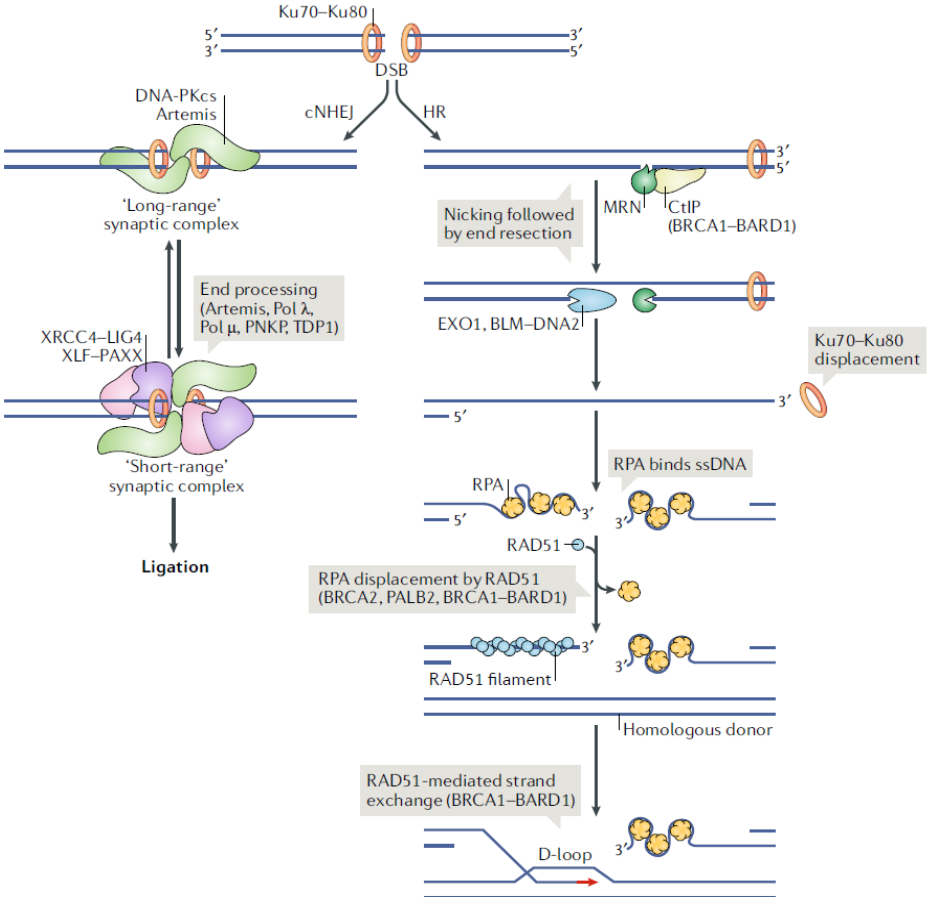

Figure 2.45. repair pathway bifurcation between NHEJ and HR. image taken from [Scully R., et al (2019)].

As DSBs are repaired, an inevitable byproduct are the chromosome translocations. When two DSBs are generated on different chromosomes in close proximity, they can be erroneously joined by DNA repair, causing structural and molecular changes in the chromosomes called *aberrations*, directly responsible for some illnesses like cancer or even cellular death. The details of how these translocations are formed are still debated. There are two hypotheses: The "contact first" and "breakage first". "Contact first" indicates that the broken ends of the DSBs are immobile or have a limited mobility. Therefore, the probability of erroneous joining is maximized for neighbor breaks. On the other hand, the "breakage first" hypothesis indicates that the rupture of DNS provokes that the DSB ends are free to move in a Brownian motion within the nucleus space, making collisions and erroneous joining with distant lesions more probable, on so-called DSBs end clusters [Iarovaia O., et al (2014), Canoy R.J., et al (2022)].

Experimental evidence suggests that in eukaryote cells the mobility of the DSBs ends is restricted to a region of less than 0.5µm around the break, and only in rare cases, about 2% can travel a longer distance of 5µm. This distance is compared to a typical cell nucleus diameter of around 10µm. When the Ku complex fails to attach to lesions, it also improves the mobility of the DSBs ends from 50 to 80 nm/min; in fact, MRN complex, Ku80, and DNA-PK help to stabilize the DSBs. The cellular stage and the DSB repair pathway also affect the frequency of translocations, among many other factors. In stage G1, cells presented more DSB ends clustering while in stages S and G2 no end clustering was observed. In addition, the more faithful repair pathways, like HR and SSA produce less translocations than conventional and alternative NHEJ [Iarovaia O., et al (2014), Canoy R.J., et al (2022)].

Chromosomal translocations can be classified into several categories as well. If the exchange of genetic material is the same, then it is classified as a *reciprocal translocation.* Otherwise, it is called *non-reciprocal*. If a chromosome ends with two centromeres is called a *dicentric* chromosome aberration, while a chromosome without a centromere is called an acentric fragment. And when the translocation of two chromosomes end up with a centromere each but one fuses their long P-arms and the other the short Q-arms it is called a *Robertsonian translocation*. A cell can survive these type of chromosome aberrations, but the short fragment is lost once the cell divides, while the acentric and dicentric chromosomes are often lost because they are either unstable or lethal to the affected cells [Canoy R.J., et al (2022)].

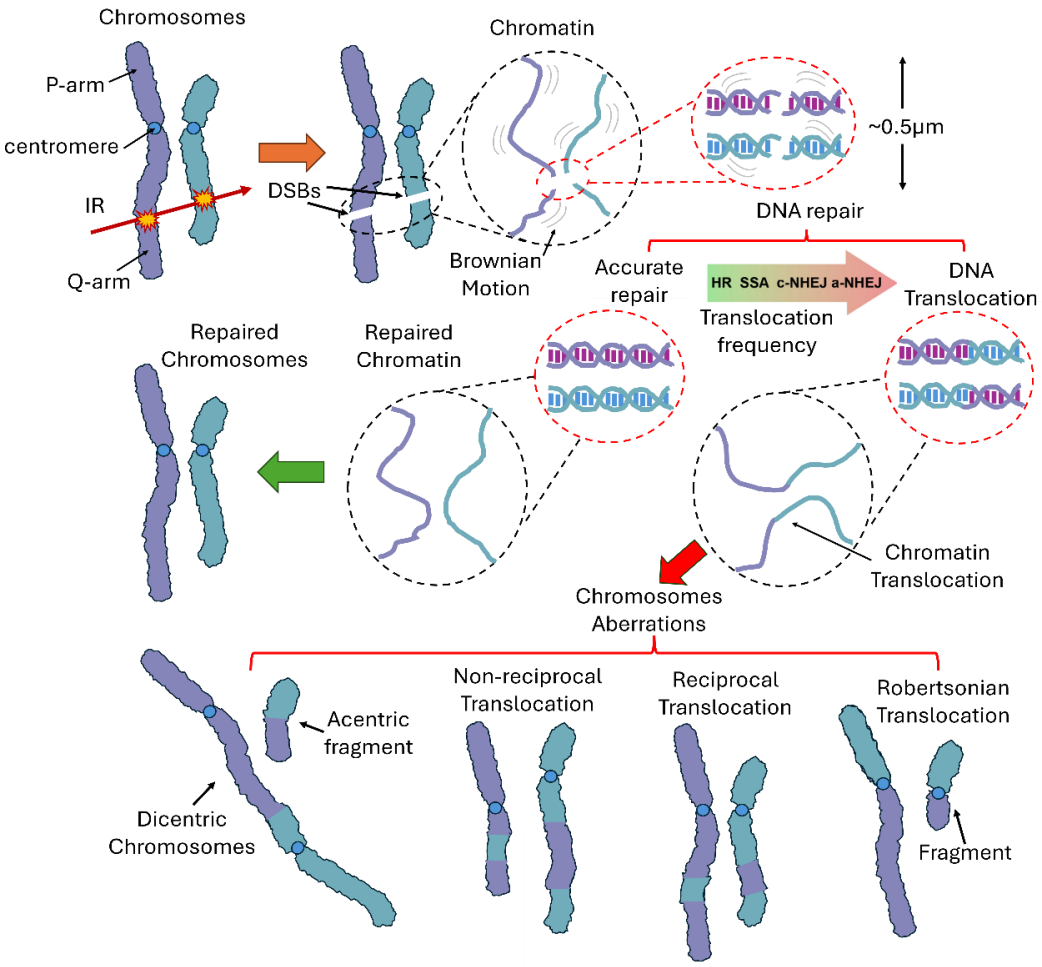

Figure 2.46. scheme for the process of chromosome translocation as a consequence of DSBs repair. Image adapted from [Canoy R.J., et al (2022)].

The modulation of the DNA repair process and the formation of lethal lesions are fundamental to studying the radiation effect on biological systems and determining the ultimate consequences of cell survival or death under irradiation.

2.3.3.1 Kinetic model for the DNA Repair

Belov et al., [Belov O.V., et al (2015)] proposed a kinetic model for the major DSBs repair mechanisms: NHEJ conventional and alternative, HR and SSA. Here, the joining of certain repair protein $\mathrm{P_i}$ to a DSB sites, forming protein complex $\mathrm{DSB} \cdot \mathrm{P_i}$, is simulated in association or dissociation reactions described by coupled differential equations, for example:

$$[\mathrm{DSB}] + [\mathrm{P_i}] \underset{k_{-i}}{\overset{k_i}{\rightleftarrows}} [DSB \cdot \mathrm{P_i}]$$

Where the two direction arrows indicate a reversible process, and the quantities inside square brackets represent the concentration of the protein or complex involved in the reaction in mol per liter units. For instance, the concentration of Ku heterodimer in human cells is $[\mathrm{Ku}] = 9.19 \times 10^{-7}\mathrm{M}$

which is approximately equivalent to 400,000 of these proteins in each cell [Neal J.A. & Meek K. (2011)].

The first step of this model is to calculate the initial number N_0 of DSBs and classify them in two fractions: $(1-f)$ Non-Clustered DSBs ($\mathrm{N_{ncDSB}}$), if two breaks occur on opposite strands of the DNA separated by less than 10bps, and f clustered DSBs ($\mathrm{N_{cDSB}}$) when a DSB is accompanied by other lesions within a distance of 10bps. The production of DSBs depends on the dose rate (dD/dt) multiplied by a function $\alpha(L)$ constructed from a fitting of the average number of DSBs produced by different types of radiation as a function of the LET (L) of the radiation quality used. The fraction f and the portion N_{irr} of irreparable DSBs produced per unit dose is also dependent on the quality of radiation and the authors provide a table with several experimental values for these quantities [Belov O.V., et al (2015)], the expression for the α function is shown next, followed by its graph and the table of the fraction values on figure 2.47:

$$\alpha(L) = ae^{-bL} \quad \text{with} \quad a = 27.5\ \text{DSB and b} = 2.43 \times 10^{-3}\,\mu\text{m/keV}$$

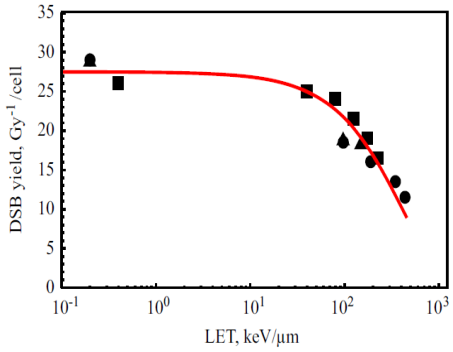

Irrepairable DSBs N_{irr}	fraction f of Clustered DSBs	Type of exposure	LET (keV/µm)
0.01	50.99	γ-rays	~0.2
0.12	50.99	γ-rays	~0.2
0.01	50.99	USX	~0.2
0.43	50.99	X-rays	~0.2
0.2	50.99	X-rays	~0.2
0.33	50.99	X-rays	~0.2
0.04	58.49	^{16}O, 1 GeV/u	14
0.08	69.52	^{28}Si, 1 GeV/u	44
0.1	81.15	^{12}C, 0.029 GeV/u	70
0.2	81.15	^{12}C, 0.029 GeV/u	70
0.4	85.68	^{56}Fe, 1 GeV/u	150
0.58	91.94	^{12}C, 0.0098 GeV/u	170
0.86	91.94	^{12}C, 0.0098 GeV/u	170
0.09	88.77	^{56}Fe, 0.5 GeV/u	200
0.23	88.77	^{56}Fe, 0.5 GeV/u	200
0.3	91.20	^{56}Fe, 0.3 GeV/u	236

Figure 2.47. **Left.** Function $\alpha(L)$ fitted to experimental data of DSB yields as a function of the radiation LET. **Right** table for the irreparable fraction of DSBs and clustered lesions of different types of radiation. images taken and adapted from [Belov O.V., et al (2015)]

The general time evolution of the DSBs is controlled by the following equation:

$$\frac{dN_0}{dt} = \alpha(L)\frac{dD}{dt}N_{ir} - V_{NHEJ} - V_{HR} - V_{SSA} - V_{Alt-NHEJ}$$

Where the V_i terms represent the elimination of DSBs by the different repair mechanisms, each one represented by a consecutive set of reactions that involve the particular repair proteins of each pathway, for example the reactions for the NHEJ are the following: The first step for the NHEJ repair is the joining of the heterodimer Ku complex, given by:

$$[DSB] + [Ku] \underset{k_{-1}}{\overset{k_1}{\rightleftarrows}} [DSB \cdot Ku]$$

With $k_1 = 10.02\mathrm{M^{-1}h^{-1}}$ and $k_{-1} = 5.6 \times 10^{-1}\mathrm{h^{-1}}$. Then the recruitment of two proteins to the lesion sites occurs, the *DNA-dependent protein kinase catalytic subunit* (DNA-PKcs) and Artemis

forming a complex that prevents the degradation of the DSBs ends [Hefferin M.L. & Tomkinson A.E. (2005)] as follows:

$$[DSB \cdot Ku] + [\mathrm{DNA} - \mathrm{PKcs}/Art] \underset{k_{-2}}{\overset{k_2}{\rightleftarrows}} [DSB \cdot Ku \cdot \mathrm{DNA} - \mathrm{PK}/Art]$$

With $k_2 = 5.82 \times 10^5 \mathrm{M}^{-1}\mathrm{h}^{-1}$ and $k_{-2} = 5.26 \times 10^{-1}\mathrm{h}^{-1}$. These two steps are called the *Ku binding*, and the validation of this section of the model is done by comparing the time evolution of the $[DSB \cdot Ku]$ complex against fluorescence microscopy experimental data using Chinese hamster lung fibroblast cells irradiated under X-rays with 27 and 137Gy by [Reynolds P., et al (2012)]. Since the intensity curve is proportional to the activity of the stained Ku80, the comparison is done with the normalization of both the simulated and experimental curves [Belov O.V., et al (2015)], presented on the next images:

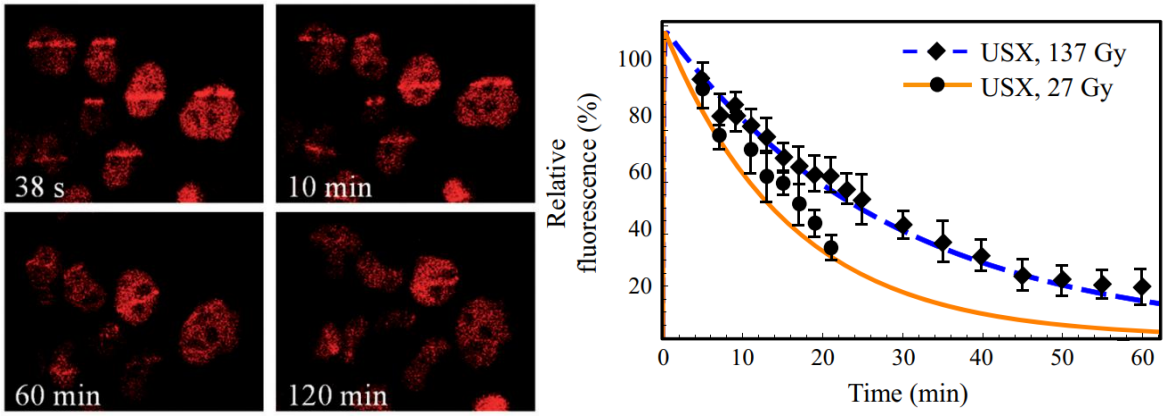

Figure 2.48. **Left.** Experimental evolution of the Ku80 stained proteins of irradiated Chinese hamster lung fibroblast cells, imagen taken from [Reynolds P., et al (2012)]. **Right**. Simulation of the time evolution of the $[DSB \cdot Ku]$ complex compared with the experimental data, image taken from [Belov O.V., et al (2015)].

On the next step, the Artemis protein in the complex is phosphorylated on a non-reversible reaction:

$$[DSB \cdot Ku \cdot \mathrm{DNA} - \mathrm{PK}/Art] \overset{k_3}{\rightarrow} [DSB \cdot Ku \cdot \mathrm{DNA} - \mathrm{PK}/Art^P]$$

With $k_3 = 1.83\mathrm{M}^{-1}\mathrm{h}^{-1}$. Then, two of these complexes, representing the two DSBs ends, join and form a *Bridge*:

$$2 \cdot [DSB \cdot Ku \cdot \mathrm{DNA} - \mathrm{PK}/Art^P] \underset{k_{-4}}{\overset{k_4}{\rightleftarrows}} [Bridge]$$

With $k_4 = 1.38 \times 10^6\ \mathrm{M}^{-1}\mathrm{h}^{-1}$ and $k_{-4} = 3.86 \times 10^{-4}\mathrm{h}^{-1}$. To join the two DSBs ends the DNA-PKcs promote the recruitment of a pair of LigIV proteins, its associated factor XRCC4 and the enzyme XLF. The role of these proteins is to close the gap between the DNA break by ligating its end, and the XLF enzyme helps to align and stimulate the function of the LigIV/ XRCC4. The order of the assembly of this complex is not considered by the model and instead the recruitment is done on a single step [Belov O.V., et al (2015)]:

$$[Bridge] + [LigIV/XRCC4/XLF] \underset{k_{-5}}{\overset{k_5}{\rightleftarrows}} [Bridge \cdot LigIV/XRCC4/XLF]$$

Where $k_5 = 15.24\text{M}^{-1}\text{h}^{-1}$ and $k_{-5} = 8.28\text{h}^{-1}$. The next recruited repair protein is the *PolyNucleotide Kinase Phosphatase* (PNKP), involved in the processing of DSB ends that lack the phosphate group [Chang H.H.Y., et al (2017)]

$$[Bridge \cdot LigIV/XRCC4/XLF] + [PNKP] \underset{k_{-6}}{\overset{k_6}{\rightleftarrows}} [Bridge \cdot LigIV/XRCC4/XLF \cdot PNKP]$$

With $k_6 = 18.6\text{M}^{-1}\text{h}^{-1}$ and $k_{-6} = 1.33\text{h}^{-1}$. The DSBs may have missing nitrogenous bases that form gaps in the ligated DNA strands, the enzyme family of polymerases X made of three members, Tdt, Pol λ and Pol μ, synthetize nucleotides to replace the missing bases and close these gaps [Chang H.H.Y., et al (2017)]. On the kinetic model this is done by considering a general Pol enzyme and done on a single step [Belov O.V., et al (2015)], defined by:

$$[Bridge \cdot LigIV/XRCC4/XLF \cdot PNKP] + [Pol] \underset{k_{-7}}{\overset{k_7}{\rightleftarrows}} [Bridge \cdot LigIV/XRCC4/XLF \cdot PNKP \cdot POL]$$

Where $k_7 = 2.73 \times 10^5\text{M}^{-1}\text{h}^{-1}$ and $k_7 = 3.20\text{h}^{-1}$. The set of reactions that describe this stage of the NHEJ and their parameters were validated against the experimental fluorescence curves of pT2609, stained antibodies that attach to phosphorylated DNA-PKcs, using HSF42 human skin fibroblast cells irradiated under iron ions and gamma-rays measured by [Asaithamby A., et al (2008)], shown next on figure 2.49:

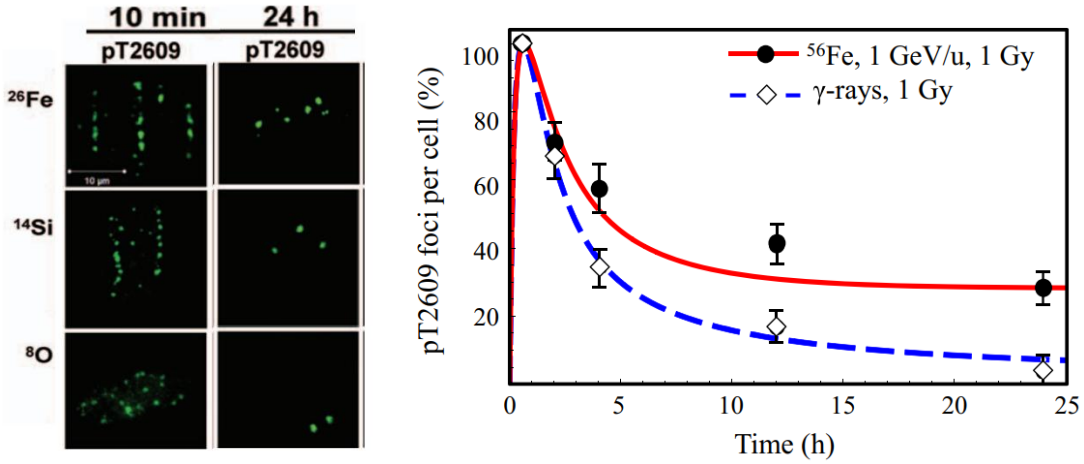

Figure 2.49. **Left.** Time evolution of the pT2609 fluorescence foci, associated with the action of the DNA-PKcs proteins, under different radiation types. Image taken from [Asaithamby A., et al (2008)]. **Right**. Comparison between experimental data and the kinetic model for this stage. Image taken from [Belov O.V., et al (2015)].

Then, after the DSBs are processed, the DNA break is repaired ($dsDNA$), the protein complex disassembly and the repair proteins reintegrate to the cell environment and can participate in the repair of another DSB, represented by the following step with an irreversible rate $k_8 = 5.52 \times 10^{-1}\text{h}^{-1}$:

$$[Bridge \cdot LigIV/XRCC4/XLF \cdot PNKP \cdot POL] \xrightarrow{k_8} [dsDNA] + [LigIV/XRCC4/XLF] + [PNKP] + [POL] + [DNA - PKcs] + [Ku]$$

The same steps of repair reactions and validation against experimental data are done for the rest of DNA repair mechanisms. The whole model, considering all the repair mechanisms, was tested on an *asynchronous* culture, this means that the cells are distributed across the cell cycle accordingly to certain fractions, this also implies that some repair mechanisms will not be available for some cells, for example those on G_0/G_1 and early S phases can only repair their DSBs with the conventional or alternative NHEJ. Then, it was validated against experimental data for γ-H2AX fluorescence curves performed by [Asaithamby A., et al (2008)] shown below on figure 2.50.

$$\text{G}_0/\text{G}_1,\ \text{and early S} \begin{cases} 0.45\ TN_{\text{ncDSB}} \longrightarrow \text{NHEJ}, \\ 0.45\ TN_{\text{cDSB}} \longrightarrow \text{Alt-NHEJ}, \end{cases}$$

$$\text{late S and G}_2/\text{M} \begin{cases} 0.55\ TN_{\text{ncDSB}} \longrightarrow \text{NHEJ, SSA}, \\ 0.55\ TN_{\text{cDSB}} \longrightarrow \text{HR, SSA, Alt-NHEJ}. \end{cases}$$

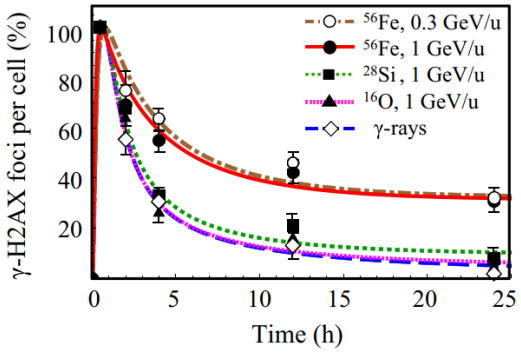

Figure 2.50. **Left.** Cell cycle distribution of the asynchronous cell culture. **Right.** validation of the complete kinetic model against γ-H2AX fluorescence experimental data. images taken from [Belov O.V., et al (2015)].

This model has been implemented on Geant4-DNA and used in combination with geometrical models for whole cells, their nucleus and the genetic material inside. The explicit simulation of the DNA breaks production by the incident radiation was simulated. The DSBs produced are then classified as simple or complex to feed the kinetic model, simulate the repair process of the cells and later feed another model that evaluates their survival [Sakata D., et al (2020), Chatzipapas K.P. et al (2023)].

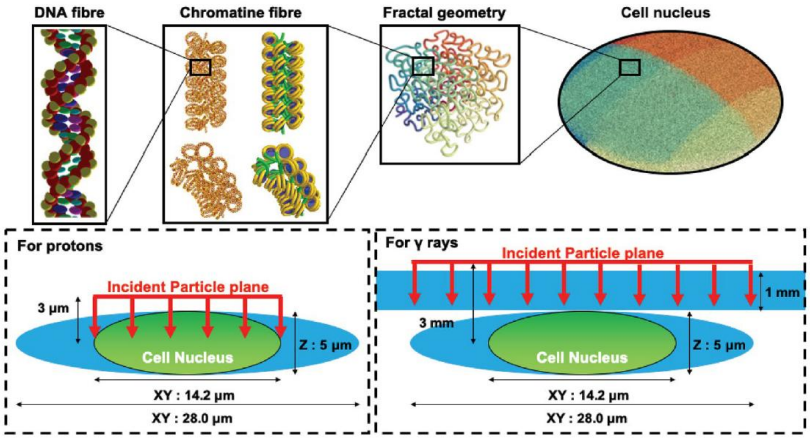

Figure 2.51. Geometrical model of a human fibroblast with a complete genome model on its nucleus, used to explicitly simulate the DNA breaks inside to feed the kinetic repair model and then determinate the cell's survival. Image taken from [Sakata D., et al (2020)].

This is an important model for the explicit DNA repair mechanisms that have been validated against experimental data and applied to MCTS codes on cellular geometrical models where the DSBs generation is explicitly simulated. However, this model doesn't count with a direct evaluation of the cell survival, like lethal lesions generation. To address this, we can explore other alternative models proposed in the past, that simplify the biological mechanisms to their essential components while being equally effective to simulate the DNA repair process and have been successfully validated to evaluate the cell survival for different irradiation conditions.

2.3.3.2 Two Lesions Kinetic model

The Two Lesion Kinetics (TLK) is an approximation for the most important DSB repair mechanism the NHEJ and HR, proposed by [Stewart R.D. (2001)]. It is based on the *Lethal-Potentially Lethal* (LPL) Model [Curtis S.B. (1986)], where the time evolution of two kinds of lesions present on the system is described by a couple of first order, non-lineal differential equations. Here DSBs are considered as *potentially lethal* lesions $\mathrm{L_{DSB}(t)}$, they can be repaired by a lineal term λ_{DSB}. On the other hand, the interaction of two of these lesions can be mis-repaired to produce *lethal lesions* $\mathrm{L_f(t)}$, irreparable and responsible for the cellular death proportional to a quadratic term of the number of DSBs ($\eta_{\mathrm{DSB}}\mathrm{L^2_{DSB}(t)}$). These can also be directly produced by radiation with certain probability Σ_{f}. DSBs are produced constantly with certain probability Σ_{DSB}, proportional to the dose rate $\dot{D}(t)$ of the irradiation, considering the total number of nucleotide pairs in a DNA sequence of length Y [Curtis S.B. (1986), Stewart R.D. (2001)], as follows:

$$\frac{d\mathrm{L_{DSB}(t)}}{\mathrm{dt}} = \Sigma_{\mathrm{DSB}} 2Y\dot{D}(t) - \lambda_{\mathrm{DSB}}\mathrm{L_{DSB}(t)} - \eta_{\mathrm{DSB}}\mathrm{L^2_{DSB}(t)}$$

$$\frac{d\mathrm{L_f(t)}}{\mathrm{dt}} = \Sigma_{\mathrm{f}} 2Y\dot{D}(t) + \eta_{\mathrm{DSB}}\mathrm{L^2_{DSB}(t)}$$

The TLK model extends these ideas by considering two types of potentially lethal lesions: *simple and complex*. Simple lesions, denoted by subscript 1 and associated with DSBs, have only one break in each strand of the DNA; while *complex* identified by the subscript 2, representing DSBs with additional lesions, like base damages, strand breaks or base deletions on the 10bp vicinity that forms it. Each type of lesion is repaired by fast or slow kinetics respectively. The evolution of both types of lesions is described by a pair of first order, non-lineal coupled differential equations that consider a lesion fixation probability ε, a lineal λ and quadratic η repair terms, and a crossover term η_{12} for the interaction between complex and simple lesions, related to the formation of chromosomal aberrations [Stewart R.D. (2001)], following the next pair of equations:

$$\frac{dL_1(t)}{dt} = \dot{D}(t)(2Y\Sigma_1) - [\varepsilon_1 + \lambda_1]L_1(t) - \eta_1 L_1^2(t) - \eta_{12}L_1(t)L_2(t)$$

$$\frac{dL_2(t)}{dt} = \dot{D}(t)(2Y\Sigma_2) - [\varepsilon_2 + \lambda_2]L_2(t) - \eta_2 L_2^2(t) - \eta_{1,2}L_1(t)L_2(t)$$

The accumulation of lethal lesions L_f is characterized by the parameters a, representing the fidelity of lineal repair, for example if $a = 1$ the lineal repair is always correct. While β, γ and γ_{12} represents the fraction of mis repaired damage from lineal and quadratic repairs and crossover interactions respectively. In the case the $\beta = 1$ it means that the lineal mis repair of lesions always produces a lethal lesion. The complementary fraction of these quantities describes the evolution of non-lethal

mutations L_m from repaired lesions. Each one of the 16 parameters considered needs to be adjusted for a specific type of cell [Stewart R.D. (2001)]. The time evolution of both lethal and non-lethal lesions follows the next pair of equations:

$$\frac{dL_m(t)}{dt} = \lambda_1(1-a_1)(1-\beta_1)L_1(t) + \lambda_2(1-a_2)(1-\beta_2)L_2(t)$$
$$+\eta_1(1-\gamma_1)L_1^2(t) + \eta_2(1-\gamma_2)L_2^2(t) + 2\gamma_{12}(1-\eta_{12})L_1(t)L_2(t)$$

$$\frac{dL_f(t)}{dt} = [\lambda_1(1-a_1)\beta_1 + \varepsilon_1]L_1(t) + [\lambda_2(1-a_2)\beta_2 + \varepsilon_2]L_2(t)$$
$$+\eta_1\gamma_1L_1^2(t) + \eta_2\gamma_2L_2^2(t) + 2\gamma_{12}\eta_{1,2}L_1(t)L_2(t)$$

The simplest case, and the one that is solved in the publication considers the following constrictions: 1) $a_1 = a_2 = 0$, meaning that the lineal repair is 100% effective, 2) $\varepsilon_1 = \varepsilon_2 = 0$, meaning that there is not directly production of lethal damage through the *fixation* of lesions and 3) $\gamma_1 = \gamma_2 = \gamma_{12} = \gamma$ and $\eta_1 = \eta_2 = \eta_{12} = \eta$, this means that the parameters for repair and miss repair of the crossover terms is the same for both complex and simple lesions [Stewart R.D. (2001)]. This simplifies the expressions and gives the next system of differential equations:

$$\frac{dL_1(t)}{dt} = \dot{D}(t)(2Y\Sigma_1) - \lambda_1L_1(t) - \eta L_1(t)[\,L_1(t) + L_2(t)]$$

$$\frac{dL_2(t)}{dt} = \dot{D}(t)(2Y\Sigma_2) - \lambda_2L_2(t) - \eta L_2(t)[\,L_1(t) + L_2(t)]$$

$$\frac{dL_f(t)}{dt} = \lambda_1\beta_1L_1(t) + \lambda_2\beta_2L_2(t) + \eta\gamma[\,L_1(t) + L_2(t)]^2$$

$$\frac{dL_f(t)}{dt} = \lambda_1(\beta_1 - 1)L_1(t) + \lambda_2(\beta_2 - 1)L_2(t) + \eta(\gamma - 1)[\,L_1(t) + L_2(t)]^2$$

The evaluation of the cell survival $S(t)$ is then evaluated as an exponential probability sampling dependent on the accumulation of lethal lesions as follows:

$$S(t) = e^{-L_f(t)}$$

Since the expression for the time evolution of L_f has a lineal and a quadratic terms for the simple and complex lesions, which in turn are functions of the deposited dose D, the expression for the cell survival inherits the lineal-quadratic relationship on D, analogous to the classical LQ experimental model for cell populations survival [Stewart R.D. (2001)]. The TLK model has been successfully implemented in Monte Carlo Track Structure codes like Geant4-DNA and used to simulate the survival of a population of cells under different irradiation conditions and the accumulation of chromosomal aberrations linked to cellular death [Douglass M., et al (2015), Zhang Y., et al (2017), Forster J.C., et al (2019)].

However, despite the fact that the TLK is a general representation of the main DSB repair mechanisms of the cell, its use for the cell survival evaluation is not directly related with cellular processes and doesn't take into account other biological radiation response mechanism like the cell

cycle arrest, or *apoptosis* that lead to the final consequences of radiation: The cellular survival or death.

2.3.4 Protein DNA damage response networks

ATM performs (as the DSB detector of the DDR signaling network) the phosphorylation of the tumor control protein p53 [Shibata A. & Jeggo P.A. (2021)]. This protein has been identified as the central piece in the cellular process regulation during the DNA repair [Zhang T., et al (2007), Tsabar M., et al (2020), Wang P., et al (2023)]. Its action is characterized by a series of discrete pulses that result from the competing activation by ATM and deactivation by the protein Mdm2. This is followed by multiple loops of positive and negative feedback of an intricate protein network that mediates during the cell cycle arrest, allowing the damaged cells time to repair and promote its survival. The sustained p53 oscillation triggers the programed cellular death for cells that are beyond repair (apoptosis) process that is initiated by the activation of the enzyme Caspase 3 (Casp3).

The general dynamic of the p53 oscillations is given in two phases. First, a train of pulses that ends when the cell is repaired on time. Second, a sustained high-level saturation that trigger the apoptosis signal [Porter A.G. & Jänicke R.U. (1999), Wu M., et al (2017), Wang P., et al. (2023)]. Experimental fluorescence microscopy images of the p53 level oscillations in in vitro cultures of breast cancer MCF7 cells are shown below on figure 2.52. They were treated with the radiomimetic drug doxorubicin (Dox) that produces DSBs in the same way as ionizing radiation. Two different doses of 0.1 and 10µM were used to demonstrate the different dynamics of the p53 protein levels under moderate and severe DNA damage conditions [Wu M., et al (2017)].

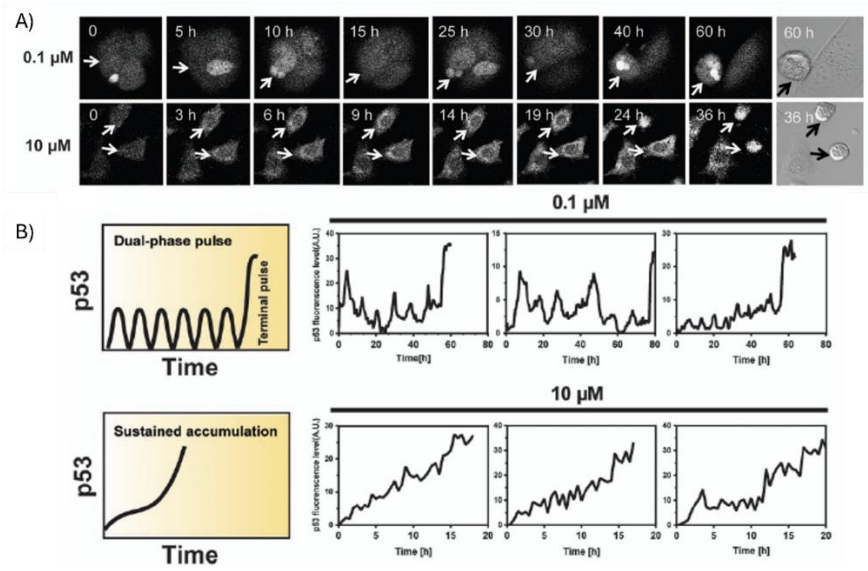

Figure 2.52. **A)** Time lapse of fluorescence microscopy images of the p53 activity on MCF7 cells treated with doxorubicin under 0.5 or 10µM. **B)** single cell time traces of the p53 level and their representative dynamics on the left. Images taken from [Wu M., et al (2017)].

However, the dynamics of this protein network are still not completely understood, and its behavior depends on the type of damage that is generated to the DNA. For example, SSBs produced by UV irradiation generate a single, extended pulse of p53 instead of a train of pulses. The width and height of the pulses increase with UV dose deposited [Wang P., et al (2023)]. On the other hand, alterations

in the p53 pathways are linked to carcinogenesis and other cell abnormalities [Lahalle A., et al (2021)]. A scheme of the p53 protein network can be seen below in figure 2.53.

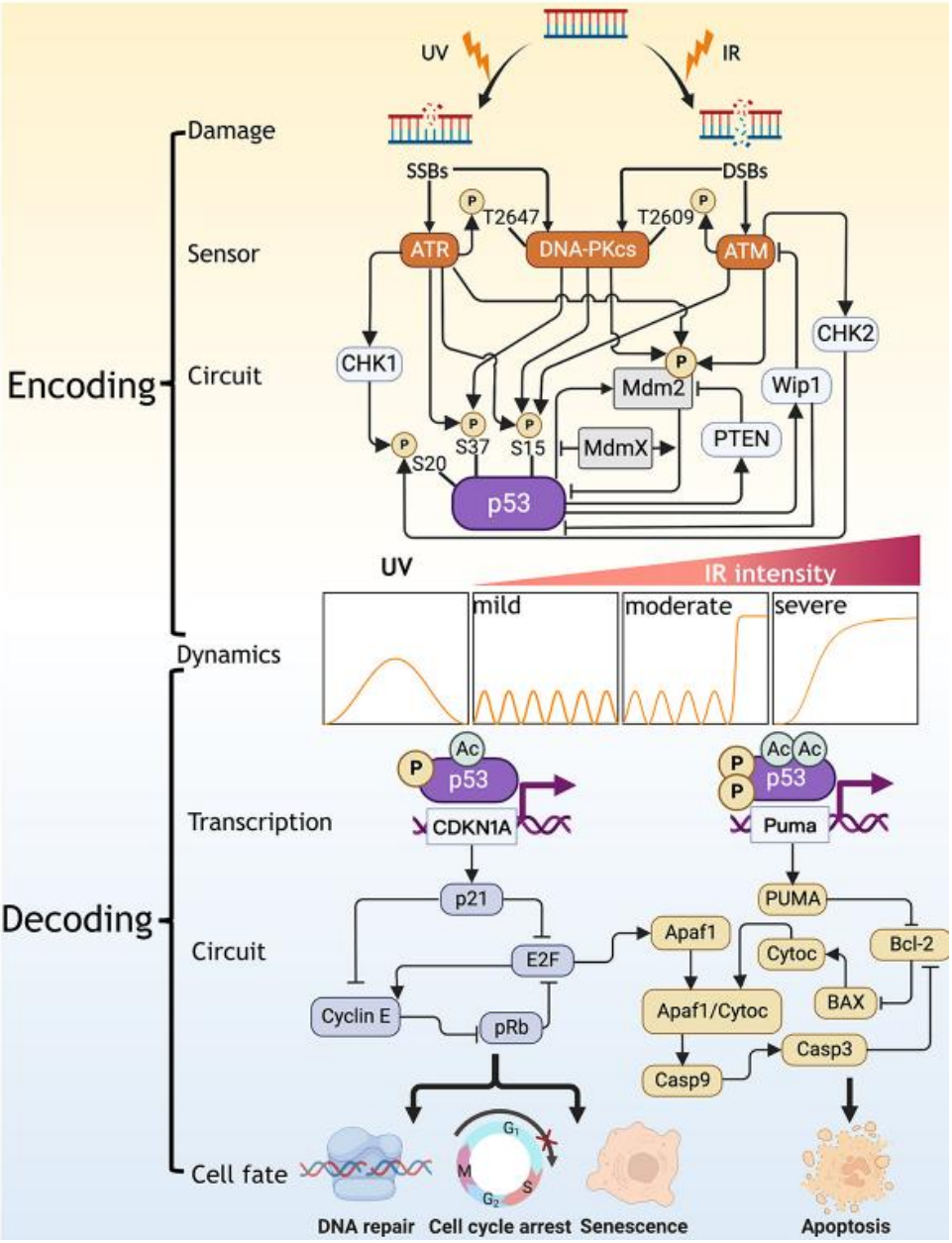

Figure 2.53. Scheme of the p53 protein network and the different outcomes of its functioning [Wang P., et al (2023)]

The incorporation of a MCTS code that simulates the DNA radiation damage on cells that feeds this information to a repair model working on parallel with a protein network model has been reported in the past to study the DDR and determinate the cellular survival or death [Hu A., et al. (2022)]. In that work, the authors presented a multiscale approach to simulate the irradiation and biological response using a single-cell integrating the *Nanodosimetry Simulation Code* (NASIC) based on Geant4, a DNA damage repair model based on the NHEJ pathway [Dolan D., et al (2015)] and a model for the p53 protein network, including its influence on the cell cycle regulation [Hat B., et al (2016)].

Other kinetic models for the action of this protein network coupled to a DNA repair module have been published and validated against experimental data in the past [Ma L., et al (2005), Zhang X.P., et al (2009,2011)] that served as the central piece for the simulation of the cellular biological response to radiation in this research work.

2.3.4.1 p53 Protein network kinetic model.

The model for the p53 protein network adopted is based on the one proposed by [Zhang X.P., et al (2011)]. That model combines four different modules for handling specific aspects of the process. It is a refined version of a previous work [Zhang X.P., et al (2009)], and the first version that proposed the digital response of the p53 pulses as described on [Ma L., et al (2005)]. Briefly, DSBs repair is performed in a module based on the TLK model and detected by the *ATM sensor* module that activates a series of protein reaction cycles that produce a train of p53 pulses in the *feedback control* module. Then, in the *cell fate decision* module, the number of pulses determinates the cell survival if it repairs on time or apoptosis for sustained p53 oscillations that trigger the Casp3 signal. The complete scheme of the protein network, as well as the kinetics of some proteins, resulted from two different irradiation doses (3 and 5Gy), are shown below in figure 2.54.

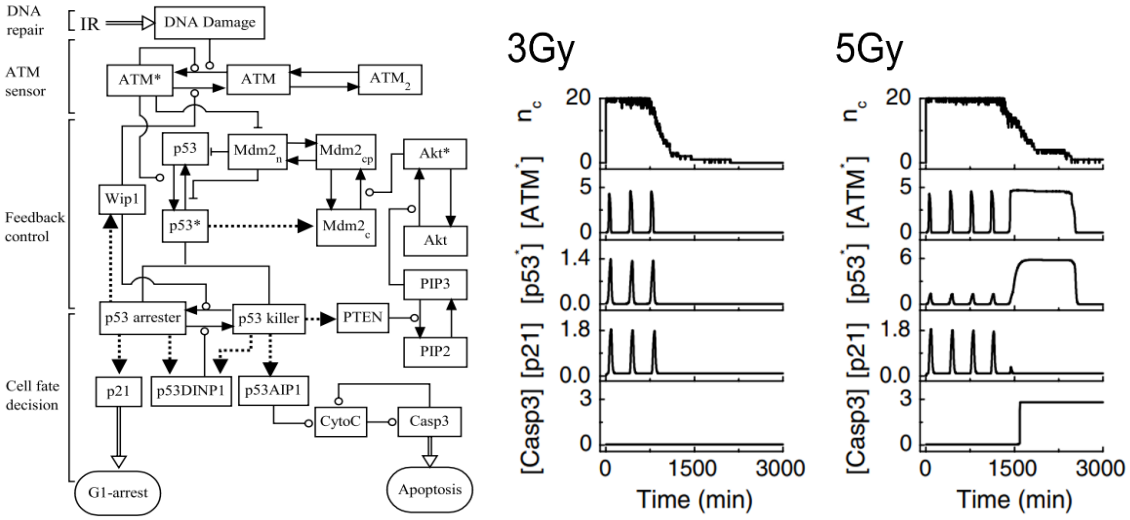

Figure 2.54. **Left**. A scheme of the different modules for the p53 protein network model. **Right**. The kinetics of this model under two doses 3Gy, where the cell repairs on time on only 3 pulses of p53 are generated, and 5Gy, where the sustained p53 oscillation causes the triggering of the Casp3 apoptosis signal. Image taken from [Zhang X.P., et al (2011)].

The first module is the DNA repair model: a stochastic version of the TLK repair model [Stewart R.D. (2011)]. Here the DSBs can transition between three states, intact (DSB), attached to a repair protein complex ($\mathrm{DSB_C}$) and fixed ($\mathrm{DSB_F}$) as the final state.

In addition, this model classifies a fraction $(f-1)$ of the total DSBs as simple, denoted by the subscript 1 ($\mathrm{DSB_1}$), and a fraction f as complex, identified by the subscript 2 ($\mathrm{DSB_2}$), which are handled by a fast and slow repair kinetics respectively. The repair model works in general as follows: If an intact DSB is under repair, then it attaches to a repair protein $\mathrm{N_r}$; meaning that both numbers of DSB and $\mathrm{N_r}$ reduce in 1 and $\mathrm{DSB_C}$ increases in 1. If this process fails, then the repair protein dissociates from the $\mathrm{DSB_C}$, and its total number reduces in 1 while DSB and $\mathrm{N_r}$ increase in 1. Lastly, if the $\mathrm{DSB_C}$ is *fixed,* then it transition to $\mathrm{DSB_F}$ which is increased in 1, the $\mathrm{N_r}$ is liberated and it can

participate in the repair of another DSB, as a consequence the number of $\mathrm{DSB_C}$ decreases in 1 [Zhang X.P., et al (2009, 2011)].

It is important to note two facts about this model. First, the number of available repair proteins $\mathrm{N_r}$, set to 20, is not representative of the real concentration of any proteins inside a cell nucleus. For example, the Ku complex has a concentration of $9.19 \times 10^{-7}\mathrm{M}$ which represents around 400,000 of just this type of proteins per cell [Neal J.A. & Meek K. (2011)]. Nevertheless, this limit of 20 general repair proteins is an approximation to simulate the saturation of the DNA repair mechanisms. Thus, the correct interpretation is that only this quantity of DSBs can be repaired at the same time, instead of only 20 proteins existing on the whole nucleus [Ma L., et al (2005)]. Second, the $\mathrm{DSB_F}$ does not necessarily represent repaired DSBs in a strict sense, since lethal mis-repaired lesions are not considered in this model. Even if these are crucial to the long-term biological consequences of DNA repair and cell survival, it is better to think of them as processed and ligated DSB ends [Ma L., et al (2005)].

The transition between states is handled by probabilities that depend on the number of DSBs in each state, the number $\mathrm{N_r}$ of available repair proteins, the association-dissociation rates $\mathrm{k_i}$ and the time step Δt. The complete original scheme for the probabilities is presented next and the values for each parameter are shown below in table 2.11. [Zhang X.P., et al (2009, 2011)].

$$\mathrm{P(DSB_1 \rightarrow\ DSB_{C1}) = N_r[k_{fb1} + k_{cross}(DSB_1 + DSB_2)]\Delta t}$$

$$\mathrm{P(DSB_2 \rightarrow\ DSB_{C2}) = N_r[k_{fb2} + k_{cross}(DSB_1 + DSB_2)]\Delta t}$$

$$\mathrm{P(DSB_{C1} \rightarrow\ DSB_1)\ =\ k_{rb1}\Delta t}$$

$$\mathrm{P(DSB_{C2} \rightarrow\ DSB_2)\ =\ k_{rb2}\Delta t}$$

$$\mathrm{P(DSB_{C1} \rightarrow DSB_{L1})\ =\ k_{fix1}\ \Delta t}$$

$$\mathrm{P(DSB_{C2} \rightarrow DSB_{L2})\ =\ k_{fix2}\ \Delta t}$$

Table 2.11. Parameters for the DNA repair module

Parameter	Description	value
$\mathrm{N_R}$	Number of repair proteins	20
$\mathrm{k_{fb1}}$	Association rate for repair proteins in fast kinetics	1.3
$\mathrm{k_{fb2}}$	Association rate for repair proteins in slow kinetics	0.13
$\mathrm{k_{rb1}}$	Dissociation rate for repair proteins in fast kinetics	0.3
$\mathrm{k_{rb2}}$	Dissociation rate for repair proteins in slow kinetics	0.03
$\mathrm{k_{fix1}}$	DSB ligation rate in fast kinetics	0.02
$\mathrm{k_{fix2}}$	DSB ligation rate in slow kinetics	0.002
$\mathrm{k_{cross}}$	DSB binary mismatch rate	0.0007
f	Fraction of complex DSB	0.3
$1-f$	Fraction of simple DSB	0.7
Δt	Time step	0.1min

The second module is the *DNA damage sensor*, where the number of DSBs attached to a repair protein complex ($\mathrm{DSB_C}$) influence the activation rate of the (ATM) protein. In undamaged cells, ATM

exists as a dimer (ATM_2) that is in equilibrium with its inactive monomer form (ATM). When DNA damage occurs, this protein activates and transform into ATM^*. This active form phosphorylates the p53 protein. The action of ATM is regulated by the protein of Wip1 that influences its deactivation rate [Zhang X.P., et al (2009, 2011)]. The equations that describe this module are presented next and the values for the parameters involved are shown in table 2.12.:

$$ATM_{tot} = [ATM] + 2[ATM_2] + [ATM^*]$$

$$\frac{d[ATM_2]}{dt} = 0.5 * k_{dim}\,[ATM]^2 - k_{undim}\,[ATM_2]$$

$$\frac{d[ATM^*]}{dt} = k_{acATM}\frac{DSB_C}{DSB_C + j_{nc}} \cdot \frac{[ATM]}{[ATM] + j_{acATM}}[ATM^*] - k_{deATM}\frac{[ATM^*]}{[ATM^*] + j_{deATM}}(1 + [Wip1])$$

Table 2.12. Parameters for the DNA damage sensor module

Parameter	Description	value
ATM_{tot}	Total concentration of ATM	5.0 μM
k_{dim}	ATM dimerization rate	5.0/μM min
k_{undim}	ATM un-dimerization rate	1.0/ min
k_{acATM}	ATM activation rate	1.3/ min
j_{acATM}	Michaelis constant for ATM activation	1.0 μM
k_{deATM}	ATM inactivation rate	0.53/min
j_{deATM}	Michaelis constant for ATM^* inactivation	2.5 μM
j_{nc}	Threshold number of DSB_C for ATM activation	5
$[ATM]_0$	Initial concentration of ATM	2.17 μM
$[ATM_2]_0$	Initial concentration of ATM_2	2.73 μM
$[ATM^*]_0$	Initial concentration of ATM*	0.10 μM

The third module is known as the *feedback control*. It is centered around the action of the p53 protein and consists in several regulatory cycles, the most important involves its activation (p53*) and deactivation. First, it is phosphorylated by active ATM, creating a positive feedback loop, while p53 degrades itself with a constant rate k_{dep53}. Then, the presence of active p53 promotes the production of Mdm2, that in turn degrades p53*, forming a negative feedback cycle. This model considers three forms of Mdm2: Nuclear (Mdm2n), unphosphorylated cytoplasmic form (Mdm2c) and phosphorylated cytoplasmic form (Mdm2cp) [Zhang X.P., et al (2009, 2011)]. The equations that control this module are presented next and the parameters involved are shown in table 2.13.

$$\frac{d[p53^*]}{dt} = k_{acp53_1}\frac{[ATM^*]}{[ATM^*] + j_{ATM}}[p53] - k_{dep53}[p53^*] - k_{dp53s}[Mdm2_n]\frac{[p53^*]}{j_{1p53n} + [p53^*]}$$

$$\frac{d[p53]}{dt} = k_{Sp53} - k_{dp53n}[p53] - k_{dp53}[Mdm2_n]\frac{[p53]}{j_{1p53n} + [p53]} - k_{acp53_1}\frac{[ATM^*]}{[ATM^*] + j_{ATM}}[p53] + k_{dep53}\,[p53^*]$$

$$\frac{d[Mdm2_c]}{dt} = k_{sMdm2_0} + k_{sMdm2}\frac{[p53^*]^4}{j_{p53}^4 + [p53^*]^4} + k_{1Mdm2_s}\frac{[Mdm2_{cp}]}{j_{1Mdm2_s} + [Mdm2_{cp}]} - k_{dMdm2}[Mdm2_c] - k_{Mdm2_s}[Mdm2_c]\frac{[Aktp]}{j_{Mdm2_s} + [Mdm2_c]}$$

$$\frac{d[Mdm2_{cp}]}{dt} = k_{Mdm2_s}[Mdm2_c]\frac{[Akt_p]}{j_{Mdm2_s} + [Mdm2_c]} - k_{1Mdm2_s}\frac{[Mdm2_{cp}]}{j_{1Mdm2_s} + [Mdm2_{cp}]} - k_i[Mdm2_{cp}] + k_o[Mdm2_n] - k_{dMdm2}[Mdm2_{cp}]$$

$$\frac{d[Mdm2_n]}{dt} = k_i[Mdm2_{cp}] - k_o[Mdm2_n] - \left(k_{dMdm2_{n0}} + k_{dMdm2_{n1}}\frac{[ATM^*]}{[ATM^*] + j_{ATM}}\right)[Mdm2_n]$$

$$\frac{d[Akt^*]}{dt} = k_{acAkt}[PIP_3]\frac{[Akt]}{j_{acAkt} + [Akt]} - k_{deAkt}[PIP_3]\frac{[Akt^*]}{j_{deAkt} + [Akt^*]}$$

$$[Akt_{tot}] = [Akt] + [Akt^*]$$

$$\frac{d[PIP3]}{dt} = k_{p2}\frac{[PIP_2]}{[PIP_2] + j_{p2}} - k_{p3}[PTEN]\frac{[PIP_3]}{[PIP_3] + j_{p3}}$$

$$[PIP_2] = [PIP_{tot}] - [PIP_3]$$

Table 2.13. Parameters for the feedback control module

Parameter	Description	Value
$k_{dMdm2_{n0}}$	Basal degradation rate of Mdm2	0.003/min
$k_{dMdm2_{n1}}$	ATM-dependent degradation rate of Mdm2	0.05/min
j_{ATM}	Michaelis constant of ATM* as a kinase	1.0μM
k_{acp53_1}	ATM-dependent activation rate of p53	0.2/ min
k_{dep53}	Deactivation rate of p53	0.1/ min
k_{dp53_s}	Mdm2-dependent degradation rate of p53*	0.01/ min
k_{sp53}	Production rate of p53	0.2μM/ min
k_{dp53_n}	Basal degradation rate of p53	0.05/ min
k_{dp53}	Mdm2-dependent degradation rate of p53	0.7/ min
j_{1p53_n}	Michaelis constant of Mdm2-dependent p53 degradation	0.1μM
k_{sMdm2_0}	Basal production rate of Mdm2	0.002μM/min
k_{sMdm2}	p53-dependent production rate of Mdm2	0.024μM/min
j_{sMdm2}	Michaelis constant of p53-induced Mdm2 production	1.0μM
k_{dMdm2_c}	Mdm2*c* degradation rate	0.003/min
k_{1Mdm2_s}	Dephosphorylation rate of cytoplasmic Mdm2	0.3μM/min
j_{1Mdm2_s}	Michaelis constant of Mdm2 dephosphorylation	0.1μM
k_{Mdm2_s}	Akt-dependent phosphorylation rate of cytoplasmic Mdm2	8/min

j_{Mdm2_s}	Michaelis constant of Akt-dependent Mdm2 dephosphorylation	$0.3\mu M$
k_i	Nuclear import rate of Mdm2cp	$0.06/min$
k_o	Nuclear export rate of Mdm2n	$0.09/min$
k_{acAkt}	Akt phosphorylation rate	$0.25/min$
j_{acAkt}	Michaelis constant for Akt phosphorylation	$0.1\ \mu M$
k_{deAkt}	Akt^* dephosphorylation rate	$0.1\mu M/min$
j_{deAkt}	Michaelis constant for Akt^* dephosphorylation	$0.2\ \mu M$
k_{p2}	PIP2 phosphorylation rate	$0.1\mu M/min$
j_{p2}	Michaelis constant for PIP2 phosphorylation	$0.2\mu M$
k_{p3}	PTEN dependent PIP3 dephosphorylation rate	$0.5/min$
j_{p3}	Michaelis constant for PIP3 dephosphorylation	$0.4\mu M$
PIP_{tot}	Total concentration of PIP2 and PIP3	$1.0\mu M$
Akt_{tot}	total concentration of all forms of Akt	$1.0\mu M$
$[p53]_0$	Initial concentration of inactive p53	0.8 μM
$[p53^*]_0$	Initial concentration of active p53	0.0001
$[Mdm2_c]_0$	Initial concentration of cytoplasmic Mdm2	0.1
$[Mdm2_{cp}]_0$	Initial concentration of phosphorylated cytoplasmic Mdm2	0.4
$[Mdm2_n]_0$	Initial concentration of nuclear Mdm2	0.26
$[Akt]_0$	Initial concentration of inactive Akt	0.06
$[Akt^*]_0$	Initial concentration of active Akt	0.94
$[PIP_2]_0$	Initial concentration of PIP_2	0.11 μM
$[PIP_3]_0$	Initial concentration of PIP_3	0.89 μM
$[PTEN]_0$	Initial concentration of PTEN	0.1 μM

The last module is the cell fate decision. Here two levels of p53 phosphorylation are considered, the primary form is $p53_{arrester}$ which induces cell cycle arrest through the production of p21 and Wip1, this last one also deactivates ATM* and restricts the activation of p53 consequently. The second level of phosphorylation is the $p53_{killer}$ which activates p53DINP1, PTEN and p53AIP1, this last one protein continues the apoptotic pathway until Casp3 is activate, which is considered as the apoptosis condition in this model and the way cell survival or death is evaluated [Zhang X.P., et al (2009, 2011)]. The equations that describe this module are shown below and their parameters are presented on Table 2.14.

$$\frac{d[p53_{killer}]}{dt} = k_{p46}[p53DINP1]\frac{[p53_{arrester}]}{j_{p46} + [p53_{arrester}]} - k_{dp46}[Wip1]\frac{[p53_{killer}]}{j_{dp46} + [p53_{killer}]}$$

$$[p53_{arrester}] = [p53^*] - [p53_{killer}]$$

$$\frac{d[Wip1]}{dt} = k_{sWip1_0} + k_{sWip1}\frac{[p53_{arrester}]^3}{j_{sWip1}^3 + [p53_{arrester}]^3} - k_{dWip1}[Wip1]$$

$$\frac{d[p53DINP1]}{dt} = k_{sDINP1_0} + k_{sDINP1_1}\frac{[p53_{arrester}]^3}{j_{sDINP1_1}^3 + [p53_{arrester}]^3} + k_{sDINP1_2}\frac{[p53_{killer}]^3}{j_{sDINP1_2}^3 + [p53_{killer}]^3} - k_{dDINP1}[p53DINP1]$$

$$\frac{d[PTEN]}{dt} = k_{sPTEN_0} + k_{sPTEN}\frac{[p53_{killer}]^3}{[p53_{killer}]^3 + j_{PTEN}^3} - k_{dPTEN}[PTEN]$$

$$\frac{d[p21]}{dt} = k_{sp21_1} + k_{sp21}\frac{[p53_{arrester}]^3}{j_{sp21}^3 + [p53_{arrester}]^3} - k_{dp21}[p21]$$

$$\frac{d[p53AIP1]}{dt} = k_{sAIP1} + k_{sAIP1}\frac{[p53_{killer}]^3}{j_{sAIP1}^3 + [p53_{killer}]^3} - k_{dAIP1}[p53AIP1]$$

$$\frac{d[CytoC]}{dt} = \left(k_{acCytoC_1} + k_{acCytoC_2}[p53AIP1]\frac{[Casp3]^4}{[Casp3]^4 + j_{Casp3}^4}\right)(CytoC_{tot} - [CytoC]) - k_{deCytoC}[CytoC]$$

$$\frac{d[Casp3]}{dt} = \left(k_{acCasp3_0} + k_{acCasp3_1}\frac{[CytoC]^4}{[CytoC]^4 + j_{cytoC}^4}\right)([Casp3_{tot}] - [Casp3]) - k_{deCasp3}[Casp3]$$

Table 2.14. parameters for the cell fate decision module

Parameter	Description	Value
k_{p46}	phosphorylation rate of p53 arrester	$0.6/min$
j_{p46}	Michaelis constant of p53 arrester phosphorylation	$0.5\mu M$
k_{dp46}	dephosphorylation rate of p53 killer	$0.3/min$
j_{dp46}	Michaelis constant of p53 killer dephosphorylation	$0.2\mu M$
k_{sWip1_0}	Basal induction rate of Wip1	$0.01\mu M/min$
k_{sWip1}	production rate of Wip1 induced by p53 arrester	$0.09\mu M/min$
j_{sWip1}	Michaelis constant of p53 dependent Wip1 production	$0.5\mu M$
k_{dWip1}	Degradation rate of Wip1	$0.05/min$
k_{sDINP1_0}	Basal induction rate of p53DINP1	$0.001\mu M/min$
k_{sDINP1_1}	production rate of p53DINP1 induced by p53 arrester	$0.01\mu M/min$
j_{sDINP1_1}	Michaelis constant for p53 arrester dependent p53DINP1 production	$0.7\mu M$
k_{sDINP1_2}	production rate of p53DINP1 induced by p53 killer and E2F1	$0.07\mu M/min$
j_{sDINP1_2}	Michaelis constant for p53 killer dependent p53DINP1 production	$0.3\mu M$
k_{dDINP1}	Degradation rate of p53DINP1	$0.01/min$
k_{sPTEN_0}	Basal induction rate of PTEN	$0.01\mu M/min$
k_{sPTEN}	p53 killer inducible production rate of PTEN	$0.5\mu M/min$
j_{sPTEN}	Michaelis constant of p53 dependent PTEN production	$1.0\mu M$
k_{dPTEN}	Degradation rate of PTEN	$0.1/min$
k_{sp21_0}	Basal induction rate of p21	$0.01\mu M/min$
k_{sp21}	production rate of p21 induced by p53 arrester	$0.2\mu M/min$
j_{sp21}	Michaelis constant of p53 arrester inducible p21 production	$0.6\mu M$
k_{dp21}	Degradation rate of p21	$0.1/\ min$
k_{sAIP1_0}	Basal induction rate of p53AIP1	$0.01\mu M/min$
k_{sAIP1}	production rate of p53AIP1 induced by p53 killer	$0.32\ \mu M/min$
j_{sAIP1}	Michaelis constant of p53 dependent p53AIP1 production	$1.5\mu M$
k_{dAIP1}	Degradation rate of p53AIP1	$0.1/min$
$k_{acCytoC_0}$	Basal release rate of mitochondrial cytochrome C	$0.001\ /min$

$k_{acCytoC_1}$	p53AIP1 dependent release rate of mitochondrial cytochrome C	$0.9\ /min$
j_{Casp3}	Michaelis constant of caspase 3-dependent cytochrome C release	$0.5\mu M$
$k_{deCytoC}$	Mitochondrial influx rate of cytochrome C	$0.05/min$
$CytoC_{tot}$	Total cytochrome C concentration	$3.0\mu M$
$Casp3_{tot}$	Total caspase 3 concentration	$3.0\ \mu M$
$k_{acCasp3_0}$	Basal activation rate of caspase 3	$0.001\mu M/min$
$k_{acCasp3_1}$	Activation rate of caspase 3	$0.9\mu M/min$
j_{CytoC}	Michaelis constant of cytochrome C dependent caspase 3 activation	$0.5\mu M$
$k_{deCasp3}$	Inactivation rate of caspase 3	$0.07\ \mu M/min$
$[p53_{arrester}]_0$	Concentration of primarily phosphorylated p53 (arrester)	$0.0\ \mu M$
$[p53_{killer}]_0$	Concentration of further phosphorylated p53 (killer)	$0.0\ \mu M$
$[Wip1]_0$	Concentration of wild-type p53 induced protein 1 (Wip1)	$0.2\ \mu M$
$[p53DINP1]_0$	Concentration of p53-dependent damage-inducible protein 1	$0.0\ \mu M$
$[p53AIP1]_0$	Concentration of p53-regulated Apoptosis-Inducing protein 1	$0.1\ \mu M$
$[CytoC]_0$	concentration of cytochrome C	$0.06\ \mu M$
$[Casp3]_0$	Concentration of active caspase 3	$0.05\ \mu M$

This model was validated experimentally for MCF7 human breast cancer cell assays treated with doxorubicin, which is a radiomimetic drug. It was reported that a maximum of 5 pulses was observed for apoptotic cells over a period of 6hr between oscillations [Wu M., et al (2017), Wang, P., et al (2023)]. However it has two related drawbacks, it doesn't consider the lethality of the lesions in the last state (DSB_F) and the survival of the cell is exclusively evaluated by the apoptosis signal by the Casp3 trigger. Nevertheless, this model was adopted as the basis for the biological response of radiation in this research work.

3. Methodology

3.1 Software

Three different specialized codes were employed in the development of this research work: TOPAS, a MCTS code capable of handling the physical-chemical radiation process in an aqueous environment; Kinetiscope, a computational tool for solving the time evolution of kinetic chemical schemes; and CompuCell3D (CC3D), a code for the simulation of biological processes of individual cells or whole populations.

All these codes are free software available for the scientific community and both TOPAS and CC3D are open source that can be extended by users. They are all also based on Monte Carlo methods and are well-established simulation tools for their respective fields of research with long histories of development. They have been used separately to simulate and validate a large variety of systems. Furthermore, used in combination they can complement each other's capabilities and overcome their respective limitations. In the following section a more in-depth description of each software will be provided, the description of the methods that each one uses to solve their simulated models and how we employed and combine them to better understand the biological response to radiation.

3.1.1 TOPAS

TOPAS is a Monte Carlo code for the simulation of radiation transport and interaction with matter [Perl J., et al (2012), Faddegon B., et al (2020)] that wraps and extends the general-purpose MC

toolkit Geant4 [Agostinelli S., et al (2003)], therefore it inherits a lot of their functionalities, like the material database, the geometric components definition and their system of units and equivalences. It counts with a user-friendly interface that simplifies the coding process of a C++ language Geant4 application, and the steep learning curve that comes with it, via a parameter file with a nomenclature convention for different components of the simulation: A parameter name in a TOPAS application file need to be defined by a predefined structure that serve as a security measure in order to ensure that the user define a parameter without ambiguity.

First comes the type of variable defined, “s” means string, “b” is a Boolean, “i” an integer and “d” is a double precision number, this last one also needs a unit added at the end of the parameter name definition. Followed by a “:” after the variable type and a prefix that define their characteristics: “Ge/” for geometry, “So/” for particle sources, “Ph/” for physics, “Sc/” for scoring and “Gr/” for graphics. After this, the name of the parameter can be further specified to different aspects of the object. Finally, the parameter value is assigned after the equal symbol “=” [Perl J., et al (2012)].

For example, if a user wants to construct a cube of water of 1cm of length that registers the dose accumulated in it, a set of instructions that follow this name convention need to be written in the parameter file in the following table:

Table 3.1. Example of a TOPAS parameter file and the structure of the name convention

Command	Description
s:Ge/Cube/Type = "TsBox"	Type of geometrical component
s:Ge/Cube/Material = “G4_Water”	Material for the component
d:Ge/Cube/HLX = 0.5 cm	Component’s half-length in the X direction in cm
d:Ge/Cube/HLY = 0.5 cm	Component’s half-length in the Y direction in cm
d:Ge/Cube/HLZ = 0.5 cm	Component’s half-length in the Z direction in cm
s:Sc/Dosel/Quantity = "DoseToMedium"	Define the quantity registered by the scorer
s:Sc/Dose/Component = "Phantom"	Geometrical component associated to the scorer
s:Sc/ Dose /OutputType = "CSV"	Format of the scored information output file

A modular approach for the TOPAS application development was taken. This facilitate the distribution of work on a research group for individuals that specialize on specific parts of the simulation, like the geometrical model or the radiation source, to focus and develop dedicated files that can be added to a master file that inherits properties to make them work together following a hierarchical control system [Perl J., et al (2012)].

TOPAS has been used extensively on medical physics applications and radio biology research. An extension called TOPAS-nBio has been validated for the simulation of the physical, physical-chemical and chemical stages for the radiolysis of water process, including the intertrack and dose rate effects on the chemical yields of radiolytic species [Ramos-Mendez J., et al (2018), Schuemann J., et al (2019), D-Kondo J.N., et al (2023)]. It has also been used to research factors that influence DNA breaks production on plasmid geometrical models like temperature, the scavenging capacity of the aqueous solution and the compaction degree of the plasmids characterized by the supercoiling grade [D-Kondo N., et al (2021), Ramos-Méndez J., et al (2022)]. TOPAS-nBio is also capable of handling cellular geometries, simulate SSB and DSB production, the subsequent DNA repair and the formation of chromosomal aberration such as dicentric and acentric chromosome fragments [Zhu

H., et al (2023)], the effect of gold nanoparticles in the production of ROS and dose deposition [Rudek B., (2019)] and the cellular nucleus damage produced by the internalization of radioisotopes [Carrasco-Hernandez J., et al (2023)], among many other applications.

3.1.1.1 Methods for solving the reaction-diffusion equation

The explicit computational method for solving this kind of equation requires that all the chemical species produced during the pre-chemical stage of the water radiolysis are followed in time and it is known as Step by Step (SBS). The diffusion of each molecule can be simulated following a random walk, caused by numerous collisions with the molecules of the medium. Here, the position of the molecules, for example in the x-axis, x_i on certain time t "jumps" to a new position x_{i+1} in given time step Δt, characterized by the diffusion coefficient D[Plante I. (2021)] as follows:

$$x_{i+1}(t, \Delta t) = x_i(t) + \zeta_x \sqrt{2D\Delta t}$$

Where ζ_x is a normally distributed random number. The same process can be performed to the y and z components of the position with independent random numbers ζ_y and ζ_z respectively. At each time step the diffusion-reaction equation needs to be solved for every pair of molecules to check if a reaction has occurred. Taking as an example the solution for the Type 1 reactions (on section *2.1.3 Heterogeneous chemical stage*), the probability of reaction between a pair (a, b) of non-charged particles totally controlled by diffusion is sampled for the intermolecular distance $r_0 = |\vec{r}_a - \vec{r}_b|$ in the time Δt and compared to a uniformly distributed number U, if $P_I \leq U$ the reaction occurs, otherwise the solution for the Debye-Smoluchowski equation p_I is used to sample a new intermolecular distance r' for the surviving molecules [Plante I. (2011, 2021)] given by:

$$\text{if} \quad P_I(\Delta t|r_0) = \frac{\sigma}{r_0} Erfc\left(\frac{r_0 - \sigma}{\sqrt{4D\Delta t}}\right) \leq U \in [0,1], \quad (a, b) \text{ react}$$

$$\text{else} \quad r' \text{ sampled from } \; p_I(r', \Delta t|r_0)$$

However, this is a very time-consuming process, since the probability of reaction needs to be checked for every possible pair of molecules each time step: Considering that for N particles in a system the total possible pairs of reactants is $N(N-1)/2$ this becomes very computationally expensive even for a small number of molecules [Plante I. & Devroye L. (2017), Plante I. (2011,2021)]. An alternative method to solve the diffusion-reaction equation without explicitly simulating the full step by step diffusion process considers that each pair of molecules can react independently of the rest of the chemical species present in the system. This approximation is known as the *Independent Reaction Times* (IRT) method and it is a very fast way to calculate the yield of chemical reaction on a heterogeneous distribution from a particle's track, several hundred times faster than the SBS method [Frongillio Y., et al (1998), Plante I. & Devroye L. (2017), Plante I. (2021)]. First, the time of reaction for each pair is calculated by sampling the inverse of the probability of reaction function, for example, for the type I reaction is as follows:

$$P_I(t|r_0) = \frac{\sigma}{r_0} Erfc\left(\frac{r_0 - \sigma}{\sqrt{4Dt}}\right) \Leftrightarrow t = \frac{1}{4D}\left[\frac{r_0 - \sigma}{Erfc^{-1}(r_0\xi/\sigma)}\right]^2$$

Where ξ is a uniform number between [0,1]. Then, if $t = \infty$ the reaction doesn't occur. The times for each pair of reactants is stored in a list and then sorted form in an ascending order and the

algorithm goes one by one performing the reactions, generating the corresponding products and eliminating the pairs that contained unavailable molecules that have already reacted [Frongillio Y., et al (1998), Planet I. (2021)]. One method to determinate the position of the newly created products is to obtain the vector $\overrightarrow{r_r}$ located between the original position of the reactants $\overrightarrow{r_a}$ and $\overrightarrow{r_b}$ weighted by the diffusion coefficients of the molecules a,b involved [Plante I. & Devroye L. (2017)] as follows:

$$\overrightarrow{r_r} = \frac{\sqrt{D_b}}{\sqrt{D_a}+\sqrt{D_b}}\overrightarrow{r_a} + \frac{\sqrt{D_a}}{\sqrt{D_a}+\sqrt{D_b}}\overrightarrow{r_b}$$

If there is only one product, it is placed exactly at $\overrightarrow{r_r}$, but if multiple products are created then they are placed randomly around $\overrightarrow{r_r}$ at the reaction radius σ distance. Then, it samples the reaction time for the products with the other existing molecules and introduces them to the list [Plante I. (2021)]. This process is performed until no possible pairs of reactants exist or until the maximum simulation time is reached.

Both SBS and IRT method are available in TOPAS-nBio [Schuemann J., et al (2019)] and the IRT method has been validated for the simulation of the radiation chemistry of water radiolysis in the presence of scavengers, modeling them as first order reactions with molecules of the background [Ramos-Mendez J., et al (2020a)]. This method has been used to simulate DNA damage with plasmid geometrical models, considering that the centroid of the semi-spheres that represent the sugar-phosphate components of DNA are the initial position of the DNA molecules that will participate in the IRT and potentially generate chemical damage. This approach considers that the DNA is static, meaning that the diffusion coefficient is cero ($D_{DNA} = 0$) [Ramos-Mendez J., et al (2020a), D-Kondo J.N., et al (2023)]. IRT has also been used to simulate the effect of the dose rate and intertrack effect on the time evolution and final chemical yield of the radiolytic species [Ramos-Mendez J., et al (2020b), D-Kondo J.N., et al (2021)].

In this research work, the capability of TOPAS to simulate the irradiation of complex geometries and to incorporate the effect of multiple molecules that constitute an aqueous environment were used to study the irradiation of models for the chemical composition of the cellular medium, and entire population of cells with distinct compartments that represent the nucleus and cytoplasm, calculate the DNA damage from scored quantities like absorbed dose and fed DNA repair and protein networks models for the biological response to radiation.

3.1.2 Kinetiscope

Kinetiscope is a free-to-use scientific software available on multiple platforms, based on the Stochastic Mechanism Simulator MSIM4 [Houle F.A., & Hinsberg W.D. (1995)]. It is a tool for the simulation of chemical kinetic schemes for multiple contexts: From chemist, chemical engineering and material science applications. Therefore, it is not restricted to any specific research area. It has a user-friendly interphase and a simple convention for reaction declaration: It relays on the mass-action principle where all the functions that describe the reaction rates must be integer powers of the involved reactant's concentration, and the law is automatically deduced from the stoichiometry of the reaction [Hinsberg W. & Houle F. (2020)].

The reactants must be separated by a plus signs "+" and if a high order reaction between the same species is declared it must be explicitly declared. For example, a bimolecular reaction of A must be

written as $2A \rightarrow \cdots$ instead of $A + A \rightarrow \cdots$, this same rule applies for the products. In addition, all names can include special characters like "+,*,-" etc. Products are declared after an arrow "=>" and bidirectional reactions can be declared with a double arrow "<=>". The code then will ask for the numerical values for both the forward k_f and backward k_b reaction rate constants and automatically determinate if the units are on $\mathrm{M}^{-1}\mathrm{s}^{-1}$ for 2nd or higher order reactions or s^{-1} for first order, decay or dissociation reactions [Hinsberg W. & Houle F. (2020)].

A simple example for the use of this tool is provided below where a small chemical reaction scheme involving three arbitrary substances A, $B$and C, where A turns into B and B into C with constant rates k_1 and k_2 respectively, finally, the initial concentration of each substance is given by $A_0 = 10.0$, $B_0 = 0.0$, $C_0 = 0.0$. A screenshot of the interface, the use of the nomenclature and writing conventions, and the solution of the system on the graphical tool of Kinetiscope is shown below on figure 3.1.

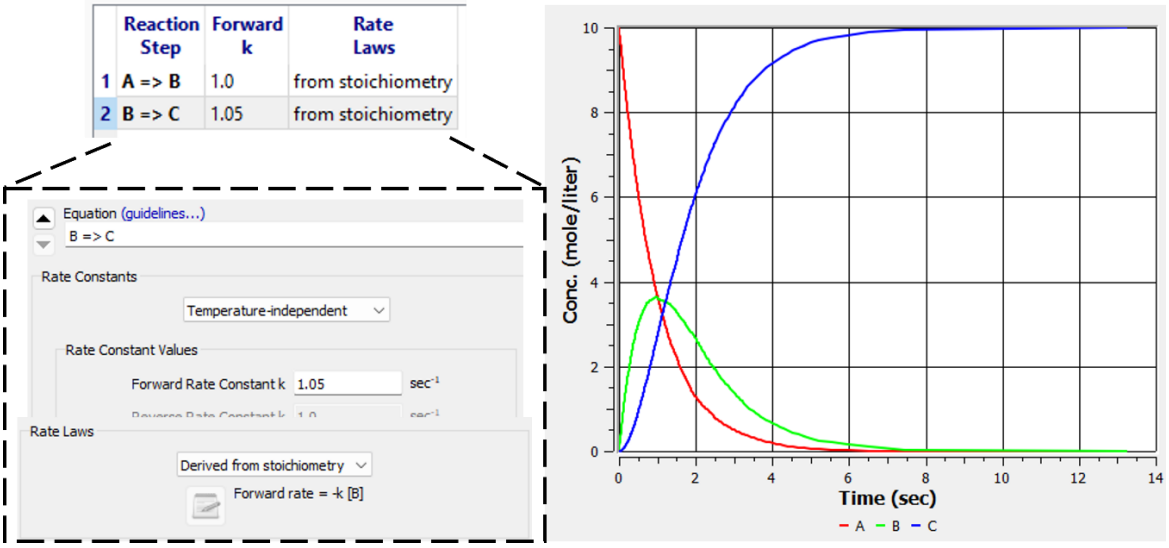

Figure 3.1. Simple example chemical scheme and its time evolution shown on the Kinetiscope interface.

Kinetiscope counts with several internal tools for the simulation of different reaction schemes. The simplest case is the *single reactor model,* where all the reactions and chemical species are contained within the same volume, while the *compartmental* model allows to consider multiple individual volumes with their own set of reactions and species separated from the others with the possibility of communication through *transfer paths,* where species can travel from one compartment to another with specific rates. One additional tool available for compartmental models is the dependence of certain reaction rates on external stimulus. This function can represent the action of an injection, a valve that opens and closes with certain frequency or even the photolysis effect on a compartment [Hinsberg W. & Houle F. (2020)].

A simple example similar to the previous one but considering two compartments, the first one only contains the substance A that is transforming into B with an initial concentration of $A_0 = 10$ and $B_0 = 0$. In the second compartment B can transform into C but both concentrations are equal to zero initially ($B_o = C_0 = 0$). The two compartments are communicated by a "valve" that only allows the transfer of B from the first compartment to the second one and its only "opened" from 1 to 5

seconds. The scheme of the reactions written on Kinetiscope convention, and the time evolution of both compartments can be seen next on figure 3.2, where the immediate transformation of A into B is seen on the first compartment, then after 1 second the valve open and the transfer of B into the second compartment is initiated and last for 4 seconds, this is represented by a *step function* defined by the user on a separate window. Finally, the 1 second delayed conversion of B into C is observed in the second compartment:

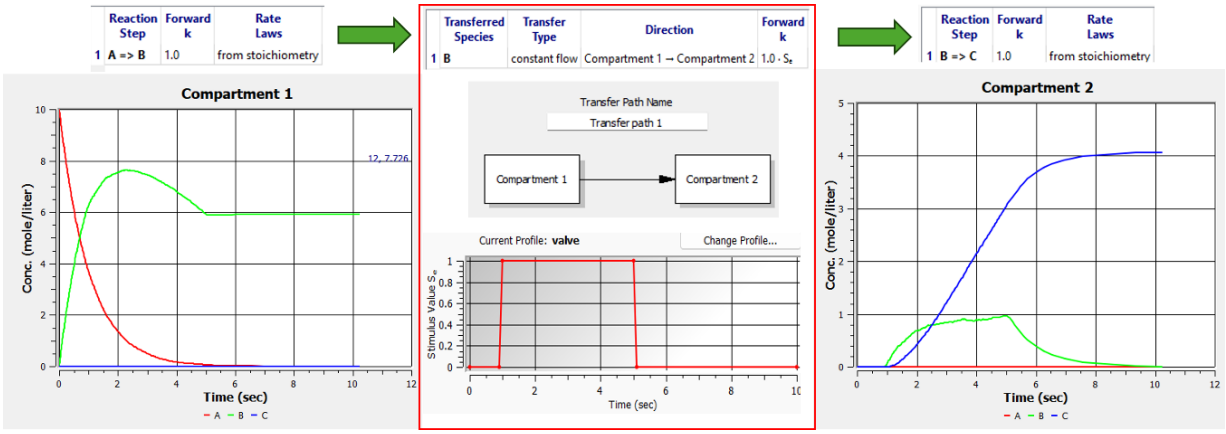

Figure 3.2. scheme and time evolution of a two-compartment system communicated through a valve that only allows the flow of a specific species from one to another and is controlled by a user defined function.

Kinetiscope is a very powerful and versatile tool that can handle the long-term time evolution of a chemical system, from ~1 to several hundreds of seconds. The compartment model with user defined external stimulus can be used to simulate the creation of radiolytic chemical species by a radiation source, and escape yields calculated with TOPAS for different dose rates can be fed into Kinetiscope to simulate both conventional and Flash types of irradiations. Furthermore, even though this is not an open-source code and functions as a "black box", its working core is the Gillespie Algorithm, a stochastic numerical method to solve the time evolution of kinetic chemical schemes. This means that it is compatible with TOPAS, and it was implemented internally to extend its capabilities to simulate the long-term time evolution of the homogeneous chemical stage of aqueous solution radiolysis.

3.1.2.1 Gillespie Algorithm

The Gillespie Algorithm, also known as *Stochastic Simulation Algorithm* (SSA) was developed during the 70's and published in "A general method for numerically simulating the stochastic time evolution of coupled chemical reactions" by [Gillespie D. T. (1976)] for the numerical calculation of the time evolution of any mixture of chemical species distributed homogeneously that interact on a finite scheme of chemical reactions. Using this algorithm the Chemical Master Equation (CME) can be solved using Monte Carlo techniques, equivalent to the analytical solution. The CME is a mathematical expression that describe the time evolution of a chemical system in terms of the probability $P(X,t|X_0,t_0)$ that an initial state X_0, with the number of the j molecules considered $[X_0^1, X_0^2, .. X_0^j]$ at time t_0, will transition to $X_1 = [X_1^1, X_1^2, .. X_1^j]$ at time t_1 [Tran H.N., et al (2013), Gillespie D.T. (1976), Gillespie D.T., et al (2013)].

Briefly, the SSA works on a step-by-step basis, however the time Interval Δt is not fixed by a predefined value, and must be calculated in each step alongside the i-th reaction among the n of the chemical scheme that will occur on the time interval, this is accomplished with the so-called *propensity function* $A(t)$ given by:

$$A(t) = \sum_{i=1}^{n} a_i(t) \quad \text{with} \quad a_i(t) = k_i \, X_{i1}(t) \cdot X_{i2}(t)$$

Here a_i is the individual propensity for the i-th reaction with a rate k_i, and X_{i1}, X_{i2} is the number of molecules involved in the reaction present on the system at the time t. The time step Δt_i will be calculated and the j-th reaction selected by the following process [Gillespie D.T., et al (2013)]:

$$\Delta t_i = \frac{1}{A} \ln\left(\frac{1}{1-\zeta_1}\right) \quad \text{and} \quad j^{th} \text{ reaction selected if } \sum_{i=1}^{j} a_i \geq A\zeta_2$$

With ζ_1, ζ_2 random numbers between [0,1], and the global time of the system is updated $(t_{i+1} = t_i + \Delta t_i)$ this process will continue until the system archive a state of equilibrium or the maximum time predefined is reached. The whole process is schematically represented in figure 3.3. below:

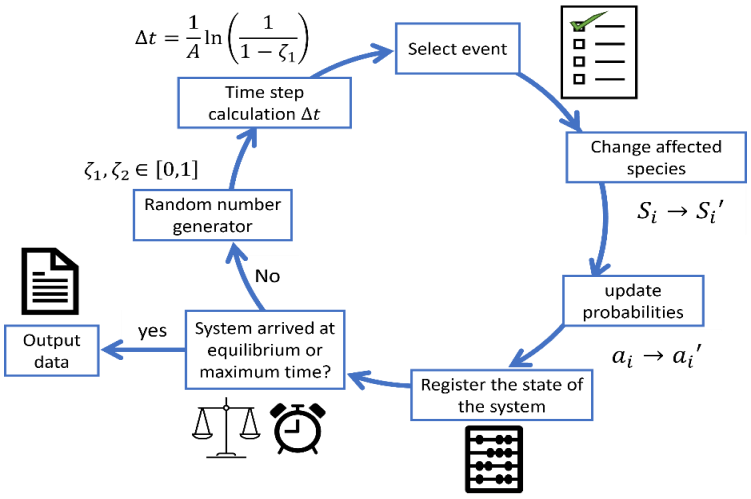

Figure 3.3. Scheme of the SSA operation.

A scheme of chemical reactions can be represented by a system of coupled differential equations and the "usual" method to solve it is with a *deterministic formulation,* using conventional numerical integrators like the Euler or Runge-Kutta methods, viewing the constants k_i as reaction rates (with $\mathrm{M}^{-1}\mathrm{s}^{-1}$ units) and the evolution of the concentration of substances as continuous functions. For example, on a system with N distinct chemical species there will have an equal number of coupled differential equations [Gillespie D.T. (1976,2000)]:

$$\frac{d[S_1]}{dt} = k_1^1[S_1][S_2] + k_2^1[S_3][S_4] + \cdots + k_N^1[S_{N-1}][S_N]$$

$$\vdots$$

$$\frac{d[S_i]}{dt} = k_1^i[S_1][S_2] + k_2^i[S_3][S_4] + \cdots + k_N^i[S_{N-1}][S_N]$$

$$\vdots$$

$$\frac{d[S_N]}{dt} = k_1^N[S_1][S_2] + k_2^N[S_3][S_4] + \cdots + k_N^N[S_{N-1}][S_N]$$

This is sufficient for some heterogeneously distributed chemical systems, however, for sensible systems that might have non-linear kinetics or represent chemically unstable systems, the *stochastic formulation* proposed by the SSA is better suited to describe those systems. Here the k_i constants are interpreted as the probability of reaction per unit of time, and the time evolution of the concentration of the molecules is modeled as a random walk on a n-dimentional Markov system, this means, a chain of events where the probability of transition between an initial state $X_0 = [X_0^1, X_0^2, .. X_0^n]$ to a final state $X_f = [X_f^1, X_f^2, .. X_f^n]$ only depends on the previous state of the system. Then, instead of solving Ndiferentialequations a single so-called *differential-difference* equation needs to be solved with the knowledge requirement of the previous state of the system [Gillespie D.T. (1976)].

3.1.2.2 Fundaments of the SSA

The general problem that the SSA tries to solve is phrased in the original publication [Gillespie D.T. (1976)] as follows: given a volume V that contains N different types of reactive chemical species S_i ($i = 1,2, \dots, N$) and their inert final products, the quantity X_i represent the number of molecules for each type of specie at the current time t. These chemical species can participate in M different reactions R_μ ($\mu = 1,2, \dots, M$), each one of them characterized by a parameter c_μ related to the probability of reaction, the time evolution of the system can be described using a stochastic formulation approach rather than a deterministic numerical one, and it is in fact a more faithful description of the phenomenon. The following table shows some examples of reaction types considered.

Table 3.2. General scheme of different types of reactions

Nomenclature		Type of reaction
$*\rightarrow p$		Spontaneous creation (or external source)
$S_j \rightarrow p$		Spontaneous degradation
$S_j + S_k \rightarrow p$	$j \neq k$	Bimolecular reaction with different reactants
$2S_j \rightarrow p$		Bimolecular reaction
$S_i + S_j + S_k \rightarrow p$	$i \neq j \neq k$	Trimolecular reaction with different reactants
$S_j + 2S_k \rightarrow p$	$j \neq k$	Biomolecular and an extra reactant reaction
$3S_j \rightarrow p$		Trimolecular reaction
	$\vdots$	

It is notable that all possible reactions used in the SSA are unidirectional, meaning that an equilibrium reaction with a forward and backward reactions ($A + B \rightleftarrows AB$) needs to be broken into two independent steps ($A + B \rightarrow AB$ and $AB \rightarrow A + B$).

First, we consider the quantity $c_\mu \delta t$ is defined as the mean probability, at first order in time, that one of the possible pairs of molecules $S_i - S_j$ may react by R_μ in the next time interval δt. In an idealized approximation, all S_i molecules are hard spheres with mass m_i and diameters d_i.

Therefore, collisions between two S_1 and S_2 species will occur if the distance that separate the center of the species is less than $d_{12} = (d_1 + d_2)/2$. If then we take into account, the velocity v_{12} of the molecule S_1 relative to S_2, the first molecule can travers a *collision volume* $\delta V = \pi d_{12} v_{12} \delta t$ centered around the second molecule in this time interval. This means that, in the limit where $\delta t \to 0$, the volume will also become smaller and the probability of colliding and reacting becomes 1 since escaping from the collision volume becomes unlikely.

If we then consider the *well-mixed* condition of the system, meaning that the molecules should be distributed homogeneously, following a uniformly random positions across the whole volume V, like a well-mixed gas. This condition implies that if we place a collision volume δV_{col} in a random position inside the total volume, the probability to find a S_2 molecule inside is $\delta V_{col}/V$ and the average probability that a pair of molecules $S_1 - S_2$ will collide on the next time step is given by:

$$\langle \delta V_{col}/V \rangle = \pi d_{12}^2 \cdot \langle v_{12} \rangle \delta t/V$$

Where $\langle v_{12} \rangle$ is the average velocities of all molecule pairs $S_1 - S_2$ and assuming that the mixture is on thermal equilibrium at a certain absolute temperature T on kelvin, the velocities of the molecules follow a Maxwell-Boltzmann distribution. Thus, this expression can be rewritten as:

$$\langle \delta V_{col}/V \rangle = \pi d_{12}^2 \left(\frac{8\mathrm{k}T}{\pi m_{12}}\right)^{1/2} \delta t/V$$

Where k is the Boltzmann constant and $m_{12} = m_1 m_2/(m_1 + m_2)$ is the reduced mass of the pair of molecules. In the case where all collisions lead to a reaction R_μ the mean probability of reaction per unit time $c_\mu \delta t$ is equal to $\langle \delta V_{col}/V \rangle$. However, on a more realistic approach is to consider that only those pairs of molecules with sufficient kinetic energy, that surpasses certain threshold u_μ^* known as the *activation energy*, will result in a reaction when colliding. Then, the last equation needs to be corrected by an attenuation factor $e^{-u_\mu^*/\mathrm{kT}}$ to account for this effect, and the average reaction probability is rewritten as:

$$c_\mu = \frac{\pi d_{12}^2}{V} \left(\frac{8\mathrm{k}T}{\pi m_{12}}\right)^{1/2} e^{-u_\mu^*/\mathrm{kT}}$$

The well-mixed condition is the key factor supporting the concept of average reaction probability that makes the Gillespie algorithm to work and the whole theory of the stochastic solution for a chemical scheme. This condition is sustained if the elastic events from collisions that don't result in chemical reactions are more frequent than the reactive collisions. Furthermore, the non-reactive collisions redistribute the velocities of the molecules to keep the Maxwell-Boltzmann distribution and ensure the uniformly random distribution of molecules across the volume.

In order to relate the average probability of reaction with the experimentally observed reaction rate k_μ, we need to consider the number X_1, X_2 of molecules S_1, S_2 inside the whole volume V: There are $h_\mu = X_1 \cdot X_2$ distinct combinations of $S_1 - S_2$ molecule pairs, then the probability that a reaction R_μ occurs somewhere inside V in the time interval δt is given by $c_\mu X_1 \cdot X_2 \, \delta t$. Then the average rate of reaction can be expressed in terms of this number of combinations as $c_\mu \langle X_1 \cdot X_2 \rangle$, and considering that the concentration of the substance S_i is written as $[S_i] = X_i/V$, the average reaction rate per volume unit is given by:

$$c_\mu \frac{\langle X_1 \cdot X_2 \rangle}{V} = c_\mu \left(\frac{V}{V}\right) \frac{\langle X_1 \cdot X_2 \rangle}{V} = c_\mu V \frac{\langle X_1 \cdot X_2 \rangle}{V^2} = c_\mu V \left\langle \frac{X_1}{V} \cdot \frac{X_2}{V} \right\rangle = c_\mu V \langle [S_1] \cdot [S_2] \rangle$$

And the observed reaction rate k_μ is defined as the average reaction rate per volume unit divided by the average concentration of the reactants involved, expressed by:

$$k_\mu = c_\mu \frac{\langle X_1 \cdot X_2 \rangle}{V} \cdot \frac{1}{\langle [S_1] \rangle \langle [S_2] \rangle} = c_\mu V \frac{\langle [S_1] \cdot [S_2] \rangle}{\langle [S_1] \rangle \langle [S_2] \rangle}$$

Since there are no correlations between the number of a given type of molecules S_i that could affect the number of molecules of a different type S_j, the average of the product of their concentrations is the same as the product of their average concentrations, meaning that: $\langle [S_i] \cdot [S_j] \rangle = \langle [S_i] \rangle \langle [S_j] \rangle$. This simplifies the previous expression to:

$$k_\mu = c_\mu V$$

However, it is important to note that every type of reaction will have a different number of combinations, for example a bimolecular reaction between the same type of substance $S_1 - S_1$ has a number of combinations $h_\mu = X_1(X_1 - 1)/2$. For very large concentrations this can be approximated to $X_1^2/2$, and it will result in a reaction rate equals to $k_\mu = c_\mu V/2$. Some examples for the total number of combinations between reactants for several types of reactions can be seen on table 3.3.

Table 3.3. Number of combinations between reactants for several types of reactions

Reaction		Number of combinations h_μ
$* \rightarrow p$		1
$S_j \rightarrow p$		$\mathrm{X_j}$
$S_j + S_k \rightarrow p$	$j \neq k$	$\mathrm{X_j \cdot X_k}$
$2S_j \rightarrow p$		$\mathrm{X_j(X_j - 1)/2}$
$S_i + S_j + S_k \rightarrow p$	$i \neq j \neq k$	$\mathrm{X_i \cdot X_j \cdot X_k}$
$S_j + 2S_k \rightarrow p$	$j \neq k$	$\mathrm{X_j \cdot X_k(X_k - 1)/2}$
$3S_j \rightarrow p$		$\mathrm{X_j(X_j - 1)(X_j - 2)/6}$
	$\vdots$	

A final complication occurs when we consider that the substances present on the system can experience multiple types of reactions with different molecules, making the chemical reaction scheme a coupled system.

3.1.2.3 The reaction probability density function

The solution to solve this coupled system is to use the *grand probability function* [Gillespie D.T. (1976)] $\wp(X_1, X_2, \dots, X_N, t)$, a mathematical expression that determine the probability that at a certain time t a number X_1 of S_1 molecules, a number X_2 of S_2 molecules,… and a number X_N of S_N molecules exist in the volume V, alongside the *moments* $X_i^{(k)}(t)$ of this probability function given by:

$$X_i^{(k)}(t) = \sum_{X_1=0}^{\infty} \dots \sum_{X_N=0}^{\infty} X_i^k \wp(X_1, X_2, \dots, X_N, t) \quad \text{with } i = 1,2, \dots, N; k = 1,2, \dots \infty$$

These moments represent *average* quantities over many repetitions of the stochastic evolution of the system from 0 to a given time t, starting from the same initial condition defined by $X_i^{(0)}(0) = \{X_1, X_2 \dots X_N\}$ in an *ensemble*. Specifically, the more useful moments are $k = 1,2$. The first one represents the average number $\bar{X}_i$ of molecules S_i at time t in the whole volume:

$$\bar{X}_i(t) = X_i^{(1)}(t)$$

The second moment $X_i^{(2)}(t)$ can be used to calculate the average fluctuations on the number of molecules relative to the average molecule number, this is the standard deviation σ_i, as follows:

$$\sigma_i(t) = \left\{ X_i^{(2)}(t) - \left[X_i^{(1)}(t) \right]^2 \right\}^{1/2}$$

Then, it is reasonable to assume that the total number of molecules S_i on the volume V at any given time t is between $X_i^{(1)}(t) - \sigma_i(t)$ and $X_i^{(1)}(t) + \sigma_i(t)$. The so-called Chemical Master Equation describes the time evolution of the grand probability function $\wp(X_1, X_2, \dots, X_N, t)$. However, the CMO cannot be solved analytically or numerically in the majority of cases. The method that Gillespie proposed in the 70's was to instead use the *reaction probability density function* $P(\mu, \tau)$, when multiplied by a small time-interval $\delta\tau$ it describes the probability that at a given time t the next reaction that will occur somewhere inside the volume V in the time interval $(t + \tau, t + \tau + d\tau)$ is R_μ. In mathematical terms $P(\mu, \tau)$ is a joint probability density function of the continuous variable $\tau \in (0, \infty)$ and the discrete variable $\mu \in (1,2, \dots, M)$.

To obtain an explicit expression for $P(\mu, \tau)$ we need to consider the number of possible combinations h_μ, with $\mu = 1,2, \dots, M$, between the molecules necessary for the reaction R_μ to occur. A list of examples of the number of reactant combinations for several reactions is shown on table 3.3. in the previous section. Then, we can use h_μ to express the probability that the reaction R_μ will happen in V in the next time interval $d\tau$ as $h_\mu c_\mu d\tau$, then $P(\mu, \tau)$ can be written as a product of the probability $P_0(\tau)$ that no reaction will occur between the interval $(t + \tau)$ multiplied by the probability that the reaction R_μ will occur on the subsequent time interval $(t + \tau, t + \tau + d\tau)$ as:

$$P(\mu, \tau) = P_0(\tau) \cdot h_\mu c_\mu \tau$$

Then, if we divide this $(t + \tau)$ time interval into K sub intervals of equal length $\varepsilon = \tau/K$, the probability that no reaction occurs during ε is given by:

$$P_0(\varepsilon) = 1 - \sum_{\mu=1}^{M} h_\mu c_\mu \varepsilon + O(\varepsilon)$$

Where $O(\varepsilon)$ describes the probability that more than one reaction will happen on the interval ε. Since the sub intervals are equally spaced, the last expression also describes the probability that no reaction will occur between $(t + \varepsilon, t + 2\varepsilon)$ and $(t + 2\varepsilon, t + 3\varepsilon)$… and $(t + (K - 1)\varepsilon, t + K\varepsilon)$. Thus, the probability P_0 on the whole τ interval is:

$$P_0(\tau) = \left[1 - \sum_{\mu=1}^{M} h_\mu c_\mu \varepsilon + O(\varepsilon)\right]^K = \left[1 - \sum_{\mu=1}^{M} h_\mu c_\mu \tau/K + O(\tau/K)\right]^K$$

This is true for any value of $K > 1$, and specifically on the limit where K is very large:

$$P_0(\tau) = \lim_{K\to\infty}\left[1 - \left(\sum_{\pi=1}^{M} h_\mu c_\mu \tau + O(\tau/K)\right)/K\right]^K$$

Since $\tau/K \to 0$ as $K \to \infty$ the probability that more than one reaction occurs within this infinitesimal fraction of time also goes to zero. Using the known equivalence for the limit:

$$\lim_{n\to\infty}\left(1 + \frac{x}{n}\right)^n = e^x$$

We can transform the expression for the probability P_0 as:

$$P_0(dt) = \lim_{K\to\infty}\left[1 - \left(\sum_{\pi=1}^{M} h_\mu c_\mu \tau\right)/K\right]^K = \exp\left(-\sum_{\pi=1}^{M} h_\mu c_\mu \tau\right)$$

Thus, the explicit expression for the probability that the reaction μ from the M that forms the complete chemical scheme will occur on the time interval τ is given by:

$$P(\mu,\tau) = h_\mu c_\mu \tau \cdot \exp\left(-\sum_{\pi=1}^{M} h_\mu c_\mu \tau\right)$$

This probability function can be employed with Monte Carlo techniques to solve the evolution of the system that starts form an initial configuration $\{X_1, X_2 \dots X_N\}_0$ at time $t = 0$ [Gillespie D.T. (1976)], on a simple set of steps:

1) Randomly sample a pair (μ, τ) from the reaction probability density function.
2) Advance the time in τ and change the state $\{X_1, X_2 \dots X_N\}$ accordingly to the reaction μ, for example if the reaction $S_1 + S_2 \to S_i$ occur X_1 and X_2 will decrees in 1 unit each, while X_i will increase in 1. Then, with this new state, the parameters $h_\mu c_\mu$ that control the reactions are recalculated for the next time-interval.
3) If the maximum time t_{max} is reached or there are no more reactants, meaning that all $h_\mu = 0$ the simulation is terminated, otherwise the current state is registered, and the algorithm goes back to step 1.

The study of the Gillespie algorithm fundamentals was carried out not just to better understand the operation of the software employed and the methods for the long-term simulation of chemical systems, but also to implement this algorithm into TOPAS to extend its capacity to simulate the time evolution of the radiolytic species at times longer than a few microseconds, once the homogeneous chemical stage has started.

3.1.3 CompuCell3D

CompuCell3D (CC3D) is an open-source free to use software for the simulation of biological process of cells, it is based on Monte Carlo methods and mainly relies on Python programing language for application development. It works specifically with the Agent-Base Modeling (ABM) approach and the Graner-Glazier-Howeg (GGH) algorithm [Balter A., et al (2007), Swat M., et al (2012)].

ABM codes have been used to simulate the behavior of complex systems consistent on multiple interacting individual elements called "agents" and constructed from the bottom up, assigning rules of interaction between themselves and their environment. The response of the entire system results from the combined contributions of the individual agents, in a term known as *emerging properties* of the system. ABM has been used in multiple contexts, from epidemiology to cellular automata [Luke D.A., et al (2012)].

In the context of cellular biology, ABM has been used to simulate mechanistically the behaviors of individual cells to entire populations [Pleyer J. & Fleck C. (2023)]. The main difference between codes that model cells using ABM approach is the number of individual agents that represent a single cell, for example VCell is a software that use vast groups of individual agents to simulate one or a few cells, this approach is useful to construct geometrical models with great detail to consider multiple compartments that represent different organelles of the cell and the process that occur inside them [Fink C.C., et al (2000)]. On the other hand, codes like Biocellion assign a single agent to each cell that is represented by basic shapes like spheres or cylinders. This allows to simulate huge populations, close to 10^6 cells, reaching the tissue level, sacrificing geometrical accuracy as a compromise [Kang S., et al (2014)].

CC3D is in a middle point where each cell is represented by a moderate number of agents that exist as identical elements on a discretized space or *voxels*. The simulation of biological process, the plasticity of cells and how individual cells interact with their neighbors to form colonies or tissue, depends on a parameter called *effective energy* that encompasses a series of constriction on the cell's volume, length, adhesion to other cells and the response to chemical signaling on its environment. CC3D works on a step-by-step basis, where the effective energy is used to sample the probability to *copy* a voxel on the periphery of a cell to an external neighbor voxel following a Boltzmann distribution, on a process called *index copy attempt*. If the discrete space consists of N different sites, an equal number of N index copy attempts constitute a Monte Carlo Step (MCS) the basic time unit on this code [Balter A., et al (2007), Swat M.H., et al (2012, 2014)].

This method combined with chemical models based on the numerical solution of Ordinary Differential Equations (ODE) applied to describe the diffusion of extracellular chemical signaling in the cellular environment and the internal cellular biochemical networks that control the individual cellular processes make CC3D a powerful tool to simulate all types of biological behaviors at the cell population level [Swat M.H., et al (2012, 2014)].

In a very general description, a CC3D application is made of three files: First, an XML file with the general parameters of the simulation, like the dimensions of the space, the maximum simulation time and a series of *plugins* that declare the simulated biological processes like growth, division or cellular chemical interactions. Second, a Python file where a series of *classes* known as *Steppables* are defined, since they can be called on a step-by-step or a frequency of steps basis. They contain

functions that control the biological process, for example a growth Steppable will contain a function that increases the cells volume at a certain rate and might consider factors like the concentration of nutrients in the ell's environment. Finally, the header file, another Python file that joins the information in the other files and executes the application. It is important to note that on advanced applications the XML and header files can be combined into a single Python file.

Figure 3.3 general structure of a CC3D application with an XML file, containing the general properties of the simulation, like lattice dimensions or cell types, and a Python stoppable file with specific biological process are described such as the growth rate and cellular division conditions.

For the cancer research effort, this software has been employed to simulate the invasion of malignant cells into normal tissue [Pramanik D., et al (2021)], to develop a model for vascularized tumors and the angiogenesis process induced by the hypoxic cells that appear on its core as the tumor grows [Shirinifard A., et al. (2009)], as well as multiscale model for the growth of a tumor under chemotherapy and the biochemical signaling network response to the drug [Jafari Nivlouei S., et al (2022)]. A more in-depth view of the functioning of CC3D, the GGH algorithm and the tools this code provides will be presented in the next sections.

3.1.3.1 Fundaments of the GGH algorithm

The simulation of living tissue, organs and multicellular organisms is a great challenge, since all biological processes at this scale are mediated by intricate networks of intercellular biochemical signaling. Despite this complexity, each individual cell perform a relatively small number of basic tasks: They stick to one another to maintain the tissue integrity, they grow, reproduce and specialize, changing their volume and surface in the process, pushing each other with certain pressure, they absorb and secrete chemical compounds that can be biochemical signals, wastes or nutrients in their environment, and ultimately they die [Glazier J.A., et al (2007)].

In this sense, the problem that the GGH algorithm tries to solve is to simplify the immeasurable networks of molecular interaction that control this list of basic cellular functions in a small number

of key aspects, and model them in a representative manner without making the simulations computationally prohibitively [Swat M.H., et al (2012)].

The origin of the GGH comes from an extension of the Potts and Ising models, originally proposed to simulate the ferromagnetism phenomenon based in the intrinsic magnetic moments or *spins* σ, that can be in two states 1 or -1, of individual atoms in positions $\vec{\imath}(k,l,m)$ on a regular two- or three-dimensional lattice, forming a discrete space with $K, L, M \in \mathbb{N}$ sites. The central idea of these models is that, for a collection $\{\sigma(\vec{\imath})\}$ of atom's spins in the lattice that can only interact with their direct neighbors; the probability P to find them on a specific state is described by a Boltzman distribution in terms of the energy of the configuration $H(\{\sigma(\vec{\imath})\})$ where H is the Hamiltonian of the system [Glazier J.A., et al (2007)] following the next expression:

$$P(\{\sigma(\vec{\imath})\}) = e^{-\frac{H(\{\sigma(\vec{\imath})\})}{kT}}$$

Where k is the Boltzmann constant and T is the temperature of the system in kelvin. H is also known as the *Ising Hamiltonian* and it is given by the sum of interactions J between all the possible spin pairs of direct neighbors [Glazier J.A., et al (2007)]:

$$H(\{\sigma(\vec{\imath})\}) = \frac{1}{2} \sum_{\substack{\vec{\imath},\vec{\jmath} \\ \text{neighbors}}} J[\sigma(\vec{\imath}), \sigma(\vec{\jmath})]$$

In this model it is assumed that the interaction of spins is favorable to aligned spins with an energy $-J$ and penalizes anti-aligned spins with an energy $+J$, and the expression can be rewritten as:

$$H(\{\sigma(\vec{\imath})\}) = -\frac{J}{2} \sum_{\substack{\vec{\imath},\vec{\jmath} \\ \text{neighbors}}} \sigma(\vec{\imath}), \sigma(\vec{\jmath})$$

A modification to this model proposed by Potts R.B. was to consider that spins can be in in q different *degenerate* states, not only 1 or -1 [Potts R.B. (1952), Glazier J.A., et al (2007)] and the expression is modified accordingly:

$$H(\{\sigma(\vec{\imath})\}) = -\frac{J}{2} \sum_{\substack{\vec{\imath},\vec{\jmath} \\ \text{neighbors}}} \{1 - \delta[\sigma(\vec{\imath}), \sigma(\vec{\jmath})]\}$$

Where $\delta(x,y) = 1$ if $x = y$ and $\delta(x,y) = 0$ if $x \neq y$. The importance of this extension is that considering these different states results in spin *dominions*, meaning regions where all the atoms have the same q_i spin state. With these conditions the partition function $\mathcal{Z}$ accounts for the Boltzmann statistics that describe all the possible configurations $\{\sigma(\vec{\imath})\}$ in the system. Furthermore, for an arbitrary function of the system states $f(\{\sigma(\vec{\imath})\})$, the expectation value is given by [Glazier J.A., et al (2007)]:

$$\mathcal{Z} = \sum_{\{\sigma(\vec{\imath})\}} e^{-H(\{\sigma(\vec{\imath})\})/T} \quad \langle f \rangle = \frac{\sum_{\{\sigma(\vec{\imath})\}} f(\{\sigma(\vec{\imath})\}) e^{-H(\{\sigma(\vec{\imath})\})/T}}{\mathcal{Z}}$$

However, this function doesn't have an analytical solution for the majority of systems, therefore a solution needs to be obtained numerically. Due to the large quantity of states, for example a Potts model with N lattice sites and q degenerate spin values there is a total of q^N different configurations, a deterministic numerical method is not computationally practical. As an alternative, Monte Carlo methods are used to start on an arbitrary initial state $\{\sigma(\vec{\imath})\}_0$ and sampling the Boltzmann function to obtain the probability to randomly *jump* between states on a chain of events. A register of the times that each state $\{\sigma(\vec{\imath})\}_i$ is visited is carried out, and after many repetitions the average of this events register converges to the expected value of f. This is known as the Ashkin–Teller method and the explicit transition between the initial state $\{\sigma(\vec{\imath})\}$ to $\{\sigma(\vec{\imath})\}'$ can be represented by the next expression [Glazier J.A., et al (2007)]:

$$\frac{p\left(\{\sigma(\vec{\imath})\} \to \left\{\sigma'^{(\vec{\imath})}\right\}\right)}{p\left(\{\sigma'(\vec{\imath})\} \to \left\{\sigma^{(\vec{\imath})}\right\}\right)} = \frac{e^{-H(\{\sigma(\vec{\imath})\})/T}}{e^{-H(\{\sigma'(\vec{\imath})\})/T}}$$

However, this method is only useful to determinate the most probable states of the system through its expected value and the random jumps between states are not representative of the time evolution of the system. Then, the las major contributor to the improvement of this methodology considered here was the Metropolis algorithm, where instead of randomly jumping between all possible states, only local changes of the configuration were permitted, meaning that the current configuration of the system will only jump to configurations that differs in only one lattice site. Therefore, the chain of events that lead from an arbitrary configuration to the most probable state of the system can be viewed as the time evolution of the whole system in the Metropolis approach [Glazier J.A., et al (2007)]. This process can be enlisted as follows:

1) A random lattice site is chosen, this is called the *target site*, whose position and state are $\vec{\imath}_{target}$ and σ_{target} respectively.
2) A new value for spin of the target site is chosen from the q degenerate states, this is known as the *trial* spin (σ_{trial}).
3) The energy of the current configuration $H_{initial}$ and the trial configuration H_{trial}, meaning if the spin value of the trial lattice site were changed, are calculated.
4) The change of energy on the configuration is calculated as:
$$\Delta H = H_{trial} - H_{initial}$$
5) The probability of accepting this change is sampled from a Boltzmann distribution:
$$p\left(\sigma_{trial} \to \sigma_{target}\right) = \begin{cases} 1 & \text{if } \Delta H < 0 \\ e^{-\Delta H/T} & \text{if } \Delta H \geq 0 \end{cases}$$
6) Repeat

The steps from 1-5 are known as a *spin-copy attempt*. And, on a system with N lattice sites, a MCS is made from N spin-copy attempts.

3.1.3.2. Cellular Potts Model and Effective Energy

The original Potts model served as inspiration to construct a first cellular model where instead of spin values of the atoms on the lattice sites of the system, a generalized state $\sigma(\vec{\imath})$ could represent an index that identifies all the components of a cell on the discretized space. This approach was

baptized as the Cellular Potts Model (CPM) or by the initials of the creator's surnames Glazier, Graner and Hogeweg (GGH) [Glazier J.A., et al (2007), Swat M.H., et al (2012)].

This model was applied to simulate the dynamics of a *generalized cell* with a list of constrictions that determined its plasticity and geometrical characteristics as components of a parameter known as the effective energy, in this context the process of target site selection is renamed as *index-copy-attempt* [Glazier J.A., et al (2007), Swat M.H., et al (2012,2014)]. For example, the contribution of the cell's volume H_{vol} to the effective energy can be expressed as:

$$H_{vol} = \lambda_{vol}\big(V(c) - V_{target}\big)^2$$

Where $V(c)$ is the cell's current volume, V_{target} is the target or *ideal* volume and λ_{vol} is the inverse compressibility constant in units of joule per volume unit. This term is minimized when the volume of the cell is close to the ideal volume and the λ_{vol} parameter is also related to the internal pressure of the cell as follows: $P(c) = -\lambda_{vol}[V(c) - V_{targuet}]$. This means that if the cell is smaller than the target volume the pressure will be positive and the cell will expand, while if it is larger the internal pressure will be negative, and the cell will compress. In the same way, if the cell has a surface constriction it can be written in an analogous form, with $S(c)$ the current cell surface, S_{target} the target or ideal surface and λ_{suf} the inverse membrane compressibility in joule per surface units [Swat M.H., et al (2012,2014)]; as follows :

$$H_{surf} = \lambda_{suf}\big(S(c) - S_{target}\big)^2$$

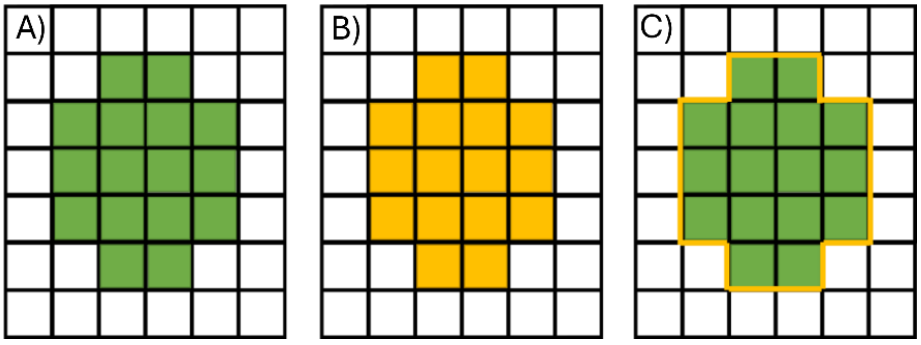

Figure 3.4. **A)** a generalized cell in a certain state where the voxels that will be taken into consideration for the calculation of **B)** the volumetric contribution and **C)** the surface term of the effective energy are marked in yellow.

Therefore, a general term for a cellular constriction in the effective energy can be written as $H_i = \lambda_i\big(K^i(c) - K^i_{target}\big)^2$. This means that the process of index-copy-attempt favors the cell configuration that minimizes each effective energy component and penalizes those states that differ from the ideal cell's characteristics. This means that on a series of MCS the cell will eventually arrange itself into its optimal form.

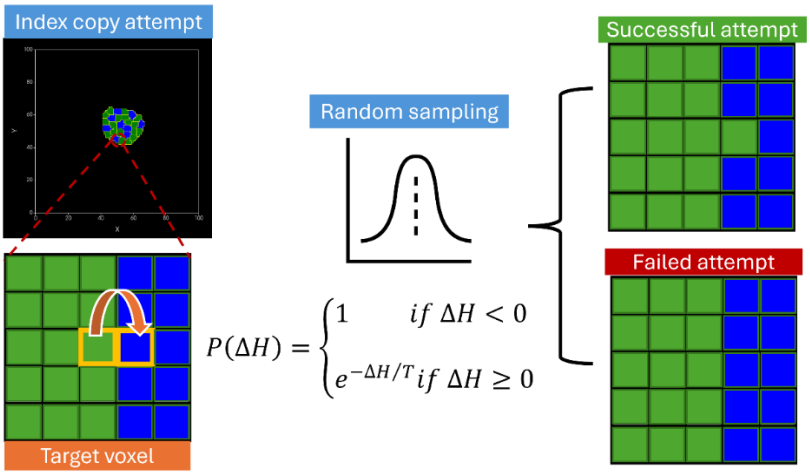

Figure 3.5. Schematics of the index copy attempt process.

An example of the modeling of an intercellular process through the use of the effective energy, is the adhesion to neighbor cells, where the interaction between the contact voxels of two cells can be described by the next expression:

$$H_{bound} = \sum_{\substack{\vec{i}\vec{j} \\ \text{neighbors}}} J[\tau(c(\vec{i}), c(\vec{j}))] \cdot \left[1 - \delta\left(c(\vec{i}), c(\vec{j})\right)\right]$$

Where $J[\tau(c(\vec{i}), c(\vec{j}))]$ is the *contact energy,* in joule per unit area, between the pair of cell types τ. All the voxels of the cells on the sites $\vec{i}$ and $\vec{j}$ are visited but only those in contact are considered, this is denoted by the term $\delta\left(c(\vec{i}), c(\vec{j})\right)$ [Swat M.H., et al (2012,2014)]. A schematic of this process is shown below in figure 3.6.

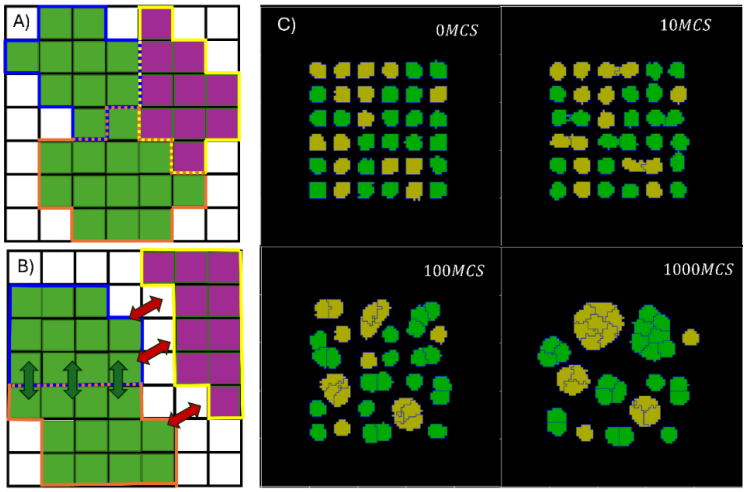

Figure 3.6. **A)** schematics of the contact voxels (dashed lines) involved in the adhesion contribution to the effective energy, two types of cells with different adhesion parameters are considered (green and purple). **B)** Due to the differences in this parameter the adhesion between green cells is preferential (green arrows) while it is repulsive (red arrows) towards purple cells. **C)** a demonstration of the action of adhesion between two types of cells where the preferential adhesion between the same type of cell and repulsion between different type produces clusters of sorted cells by types.

3.1.3.3 initiation of a simulation and cells geometries

CC3D have a default plugin to construct a randomized initial distribution of cells, it can generate square or round “blob” cell distribution shapes, both types of distributions take the list of cells that will be generated, their width and the separation between one another as general arguments to initialize the geometry. In addition, the square distribution needs to consider the limits of the region where it will generate cells on each of the lattice directions, while the circular blob distribution needs the central position and the radius of the region where it will generate cells [Swat M.H., et al (2014)]. An example of these two standard geometry initializers is shown below in figure 3.7.

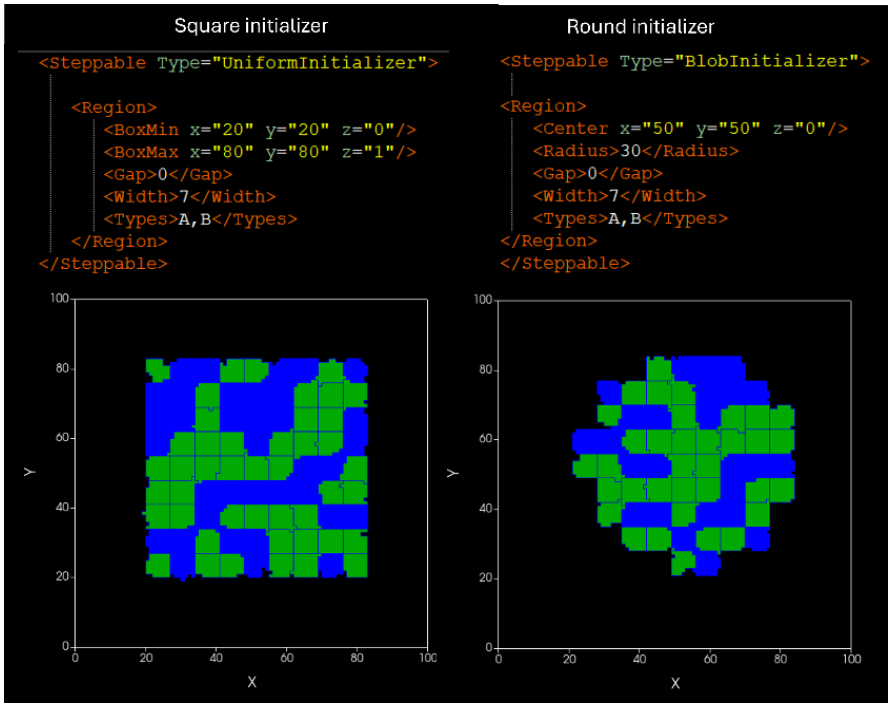

Figure 3.7. The two default geometry initializers in CC3D

However, these types of geometry initializers are very limited when a complex structure needs to be declared as the starting conditions for a simulation. Nevertheless, CC3D count with a tool to initialize from a user defined geometry stored on an external file that follows a special format called *Potts Initializing Format* (PIF) file that consist of a database separated in columns where the first one is dedicated to identifying the cell number, then the cell type by name, then 3 pairs of columns delimitate the minimum and maximum voxel position in each direction [Swat M.H., et al (2014)]. This is a very useful tool for constructing complex geometries that require a shape other than a square or a round blob. PIF file can also be written from another code, like a Python external application, it can also serve as a geometry storage file and a starting point for new simulations. An example of PIF initializer from a Python generated file is shown in figure 3.8.

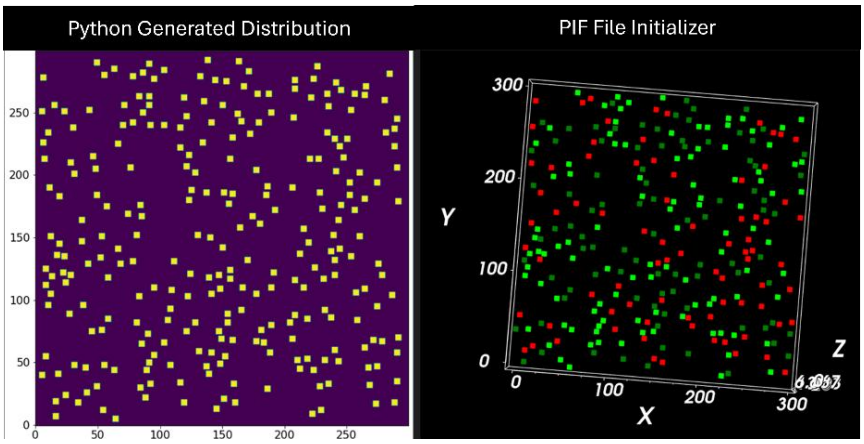

Figure 3.8. PIF initializer from a python generated file.

Another column can be added to the PIF file to identify multiple compartments of a single cell: CC3D have an option to declare that two independent *generalized cells* are different compartments, like the organelles within a cell, of a single joined cell, they evolve together and need two sets of adhesion parameters, one internal between compartments and an external one with other cells [Swat M.H., et al (2014)]. This is useful to construct simple cells with distinct compartments that represent the nucleus and cytoplasm, or taking the example described in [Belmonte, J. M., et al (2016)] to construct very detailed geometry for the trapezoidal cells on the nephron tubules where multiple compartments represent the apical, basal and lateral sections of the cellular membrane, with different adhesion, which have been used to simulate the development of kidney cyst by deficiency of cadherin-8 protein that influence the adhesion between cells. These examples are shown below on figure 3.9.

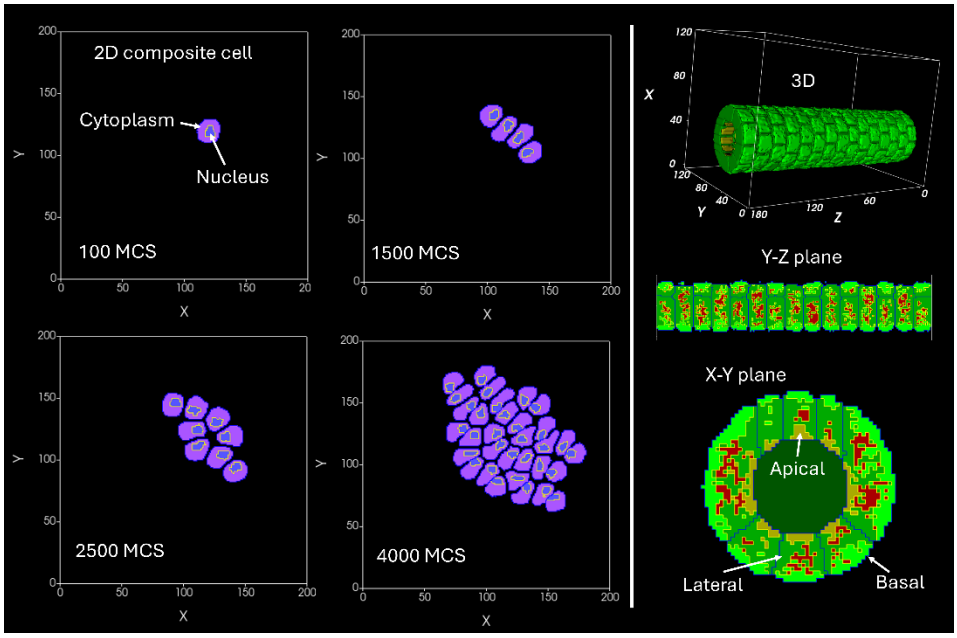

Figure 3.9. examples of multi compartmental cells: **Right.** a simple 2D cell with separate cytoplasm and nucleus compartments that conserves the two compartments as it grows and divides into a tissue. **Left.** trapezoidal cells from kidney tubules with multiple compartments representing different sections of the cellular membrane. Geometry was reproduced from [Belmonte, J. M., et al (2016)].

3.1.3.4 Growth, division and differentiation on CC3D

A basic method that CC3D uses to simulate the growth of a cell is by making its target volume a function of time, in terms of MCS which is the basic time unit in CompuCell3D, then as the simulation progress the GGH algorithm through the index copy attempt will drive the cells to the optimal configuration as $V_{targuet}$ increase or reduces. The simplest case is a constant growth rate k_0 [Glazier J.A., et al (2007), Swat M.H. (2014)] as follows:

$$\frac{dV_{cell}}{dt} = k_0 \quad \Leftrightarrow \quad V_{target}(t) = k_0 \cdot t$$

In the same way, processes that reduce the cell's volume, like necrosis, can be simulated using a negative value for k_0, causing that the target volume decreases as the simulation continues. On the other hand, mitosis can be simulated employing a division condition, that can be declared for the cells that reach certain maximum volume V_{max}, they are added to a Python list and division is performed by distributing the voxels of the original cell c into two halves that will become new separate cells c'. This action has some available options on CC3D, for example division can be performed on along a random axis, on a preferential direction, or through the major or minor axis of the cell [Swat M.H., et al (2014)].

Specialization is another process that can be implemented straight forward: Each cell is assigned to a certain type τ, useful to track the adhesion parameter between neighbor cells among other applications. However, if a chemical change in the environment occurs or at a certain point of the cellular development, specialization can occur, which changes the morphology of the cell and its interactions. This can be simulated on CC3D by changing the cell's type to τ' and with that, their characteristics, for example, different size, shape adhesion parameters, etc. [Swat M.H. (2014)]. A simple example is presented next on figure 3.10. where a steam cell (on blue) grows and divides. The daughter cells are Terminally Defined (on green) and don't grow nor divide, therefore the steam cells don't change on number but produce the constituent cells of the tissue:

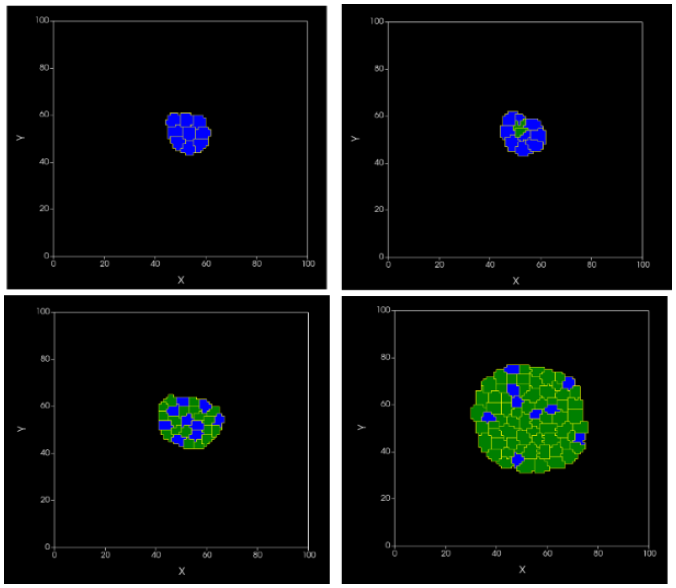

Figure 3.10. Time evolution of the growth, division and specialization processes in CC3D for steam cells (blue) and TD cells (green)

Another simple example on how to combine different simulated biological systems in CC3D is to make the growth rate proportional ($\propto m_0$) to the concentration of an external chemical field $C(\vec{\imath})$, that might represent nutrients in the cellular environment, evaluated in the center of mass of the cell ($\vec{\imath}$):

$$\frac{dV_{cell}}{dt} = m_0 \iff V_{target}(C,t) = m_0 \cdot C(\vec{\imath},t)$$

CC3D has special internal tools to handle the evolution and interaction of this kind of external chemical field [Swat M.H., et al (2014)].

3.1.3.5. External Chemical Field

On a biological environment cells are not isolated. Instead, they exist on a constant interchange of nutrients, waste and biochemical signals that cells absorb and secrete. Thes chemical compounds diffuse in the medium and might produce a concentration gradient that can affect processes like *chemotaxis,* the influence of the mobility of a cell due to the presence of a signal in its environment. The GGH implementation of this type of extracellular interactions is employing a *chemical field* that exists on a parallel lattice $C(\vec{\imath})$ with the same dimensions. The time evolution of this field is handled by a Partial Differential Equation (PDE) that controls the diffusion process of the substance [Swat M.H., et al (2012,2014)]:

$$\frac{\partial C(\vec{\imath})}{\partial t} = D\nabla^2 \cdot C(\vec{\imath}) - k_{decay} \cdot C(\vec{\imath}) + k_{secretion}$$

Where $C(\vec{\imath})$ is the concentration of the chemical field at the lattice site $\vec{\imath}$, D is the diffusion coefficient, the terms k_{decay} and $k_{secretion}$ represent the degradation of the substance in the medium and the cellular secretion process respectively. This equation is solved numerically by the *finite difference* approach by methods like the forward-Euler or Crank‑Nicholson algorithms where the local concentration at each voxel is redistributed to the neighboring sites. Those methods have the advantage of considering different diffusion coefficients, decay and secretion constants and even anisotropic diffusion in adjacent voxels that belong to different types of cells. However, the Euler method becomes unstable when the next condition is met [Glazier J.A., et al (2007), Swat M.H., et al (2012)]:

$$D \cdot \frac{\Delta t}{\Delta x^2} > \frac{1}{2d}$$

Here d is the dimension of the space, for example in a three-dimensional space $1/2d \approx 0.16$, and Δx is the size of the voxel. Therefore, a smaller time step Δt can improve the simulation but make it slower. This method can be exemplified by a simple 2-D diffusion approximation scheme where the concentration of the lattice site on the (i,j) position will be influenced by its neighbors and the local generation g and decay d processes of the substance on a small time-step Δt [Glazier J.A., et al (2007)]:

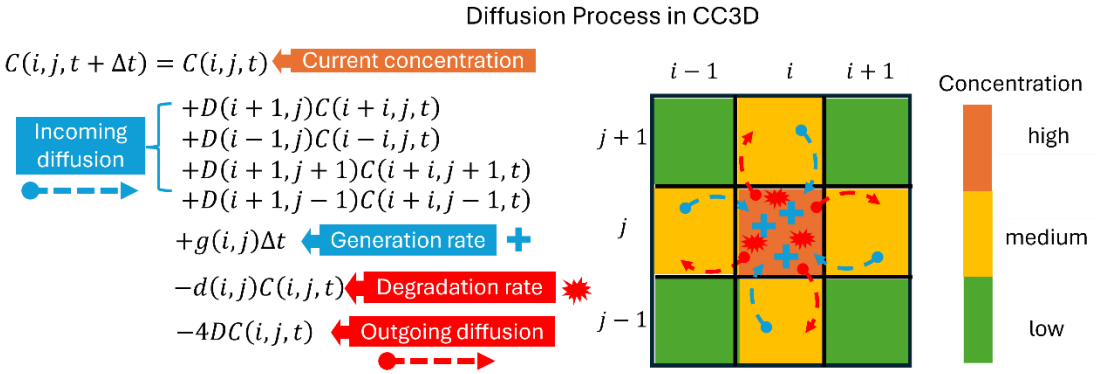

Figure 3.10. Scheme for the chemical diffusion process on CC3D. information taken from [Glazier J.A., et al (2007)]

The initial and frontier conditions for the chemical field can be defined in several ways. Maximum and minimum concentration regions can be declared on opposite sides of the lattice, and a gradient that adjusts to these restrictions will automatically form as the simulation progresses. Constrictions for the derivative of the gradient can be declared as well in the frontiers of the discrete space and periodic conditions can be established, where the chemical substance diffuse until it touches the limit of the space and reappears in the opposite side of the lattice instead of colliding with a solid barrier. An option to declare the concentration field from an external file is also available in CC3D, it needs to follow a four-column format where the first three are the x, y, z positions on the discrete space and the las value is reserved for the concentration of the field [Swat M.H., et al (2014)]. An example of the diffusion of a chemical species is shown below in figure 3.11. accompanied by a graph of the central cut of the distribution.

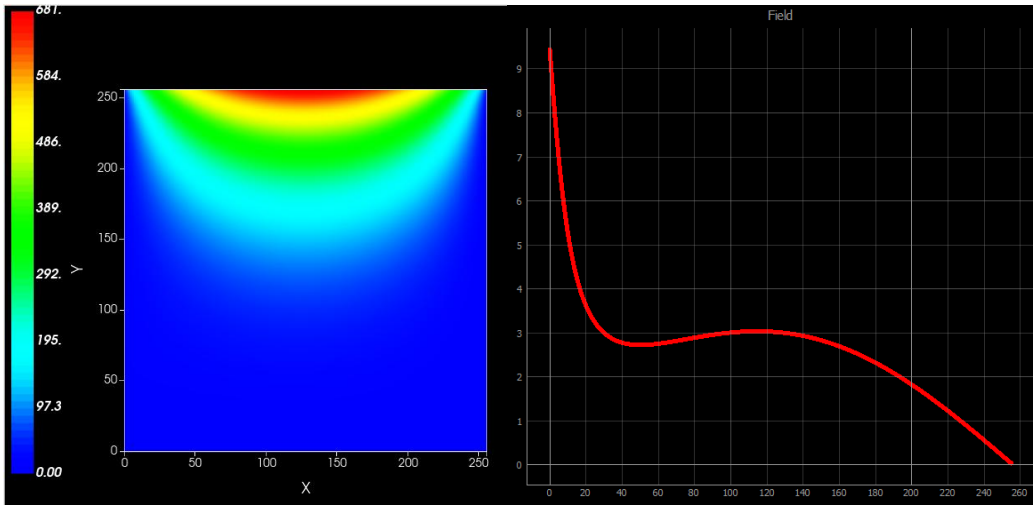

Figure 3.11. **Left.** CC3D simulation of a chemical field with a maximum constant concentration of 700 units on the y=250 and minimum value of 0 units at y=0, and a concentration derivative constriction of zero on both the x frontiers, generating a gradient on the y negative direction. **Right.** The profile of the generated field at the central cut of the y axis.

3.1.3.6 Consumption and secretion of chemical fields

As stated before, cellular growth can be a function of the local concentration of a certain chemical field that might represent nutrients available in the medium. In order to make a more realistic simulation in CC3D, an *uptake* can also be introduced to represent the cellular feeding, here a certain

quantity of the chemical field concentration will be subtracted from all the voxels that constitute a cell. This mechanism can be defined using two parameters: A maximum uptake u_{max} for concentrations above certain saturation concentration C_{sat}, meaning that the cell cannot consume more than this limit even if there are plenty of resources available; and a percentage α for concentrations below the saturation level. Therefore, the time-rate of chemical consumption inside the cell $dC(\vec{\imath})/dt$ is described by a *ramp function,* that increases linearly from 0 to 100% of u_{max} when the value of concentration goes from 0 to C_{sat} respectively [Swat M.H., et al (2014)]. The expression that describes this function and a graphical representation are show below on figure 3.12:

$$u = \min(\alpha \cdot C(\vec{\imath}), u_{max})$$

$$\frac{dC(\vec{\imath})}{dt} = \begin{cases} -\alpha \cdot C(\vec{\imath}) & si \quad C(\vec{\imath}) < C_{sat} \\ -u_{max} & si \quad C(\vec{\imath}) \geq C_{sat} \end{cases}$$

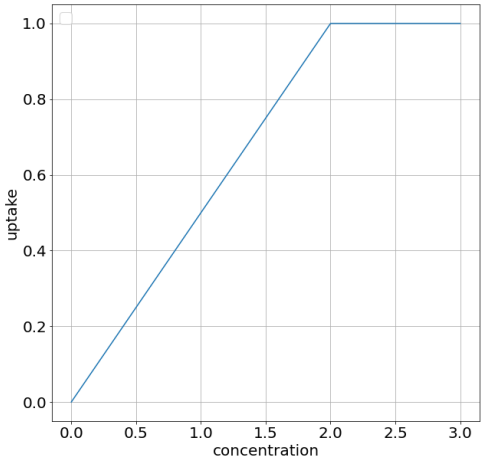

Figure 3.12. Mathematical expression for the uptake function and its graphical representation. Image adapted from [dal Caste P. (2022)].

On the other hand, cells can secrete chemical compounds that might represent signals to communicate with other distant cells, or metabolic byproduct waste. On CC3D a function exists to assign a constant value for the chemical secretion on specific voxels inside the cells so they can contribute to concentration of a chemical field [Swat M.H., et al (2014)], with several options:

1) *secreteInsideCell* – all cell's voxels secrete at a constant rate.
2) *secreteInsideCellConstantConcentration* – all cell's voxels sustain a constant concentration.
3) secreteInsideCellAtBoundary – secretion is done in the interior of the cell on the voxels at the boundary.
4) secreteInsideCellAtBoundaryOnContactWith – secretion is performed inside the cell, at the boundary only in the voxels that are in contact with another predefined type of cell.
5) secreteOutsideCellAtBoundary – the boundary of the cell secretes to the outside.
6) secreteOutsideCellAtBoundaryOnContactWith – secretion is done at the outside of the cell boundary, only in the voxels that are in contact with another predefined cell type.
7) secreteInsideCellAtCOM – secretion is performed at the cell's center of mass.

An example of the evolution on a chemical field in the presence of two types of cells, one secreting constantly a "signal", in the form of a sustained constant concentration in all its voxels, while the other cell is consuming the chemical field, is shown below on figure 3.13:

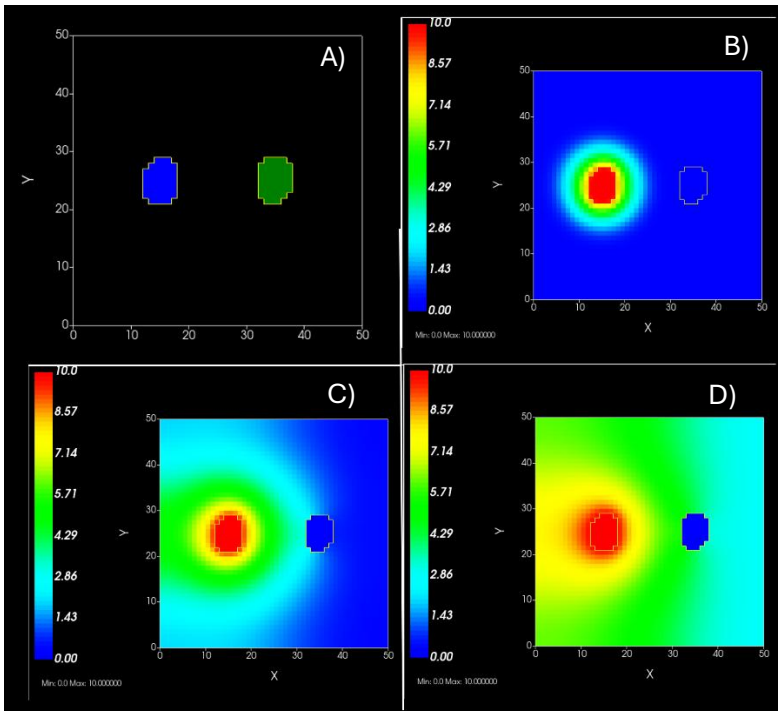

Figure 3.13. A) two different cells, a *secretor* (blue) and an *absorber* (green) of a "chemical signal". B-D) the time evolution of the chemical field as the simulation progresses.

However, the interaction of the chemical signal on the cells can produce a dynamic change in the cellular mobility: Certain biochemical signals like the Vascular Endothelial Growth Factor (VEGF) is secreted by hypoxic cells, especially the ones on the core of a tumor, to promote the growth of new vascular cells that can provide more nutrients or oxygen to the affected tissue. Then, the neovascular cells are attracted to this growth factor and follow the gradient of VEGF concentration as a path to find the hypoxic part of the tissue in a process known as *chemotaxis*. CC3D have specialized functions to simulate these kinds of biological behaviors using a dedicated term for the effective energy [Shirinifard A., et al. (2009), Swat M.H., et al (2014)]

3.1.3.7 Chemotaxis

The chemotaxis process consists in the influence of a cell's mobility by a chemical signal that follows its concentration gradient. This process is crucial for the long-distance communication between cells, allowing that one part of the tissue influences the movement of cells in another extreme of the tissue [Glazier J.A., et al (2007), Swat M.H., et al (2014)].

The method implemented in CC3D to simulate chemotaxis is to include a term of the effective energy H_{chemo} as a function of the concentration of the chemical field $C(\vec{\imath})$ inside the cell. The simplest case is the one directly proportional to $C(\vec{\imath})$, described as:

$$H_{chemo} = \mu_{cell}(c) \cdot C(\vec{\imath})$$

Here μ_{cell} represents the chemotactic response of the cell c to the substance: If $\mu_{cell} > 0$ the cell is attracted to the lattice sites where the chemical field have a greater concentration, while in the opposite case, where μ_{cell} is negative, the cell will be repelled by the chemical substance and flee to the lattice sites with the lest or no concentration of the chemical field [Swat M.H., et al (2014)].

Furthermore, CC3D offers several options to determinate this dependence on the chemical field concentration considering the most convenient representation for each type of cell and the biological process that is being stimulated. The simplest of these is to consider the difference between the chemotactic response of the *source* and *target* voxels, but only the field concentration on the target voxel, the difference in the chemotaxis component of the effective energy is then described by [Swat M.H., et al (2014)]:

$$\Delta H_{chemo} = \left[\mu\left(c_{target}\right) - \mu(c_{source})\right] \cdot C(\vec{\imath}_{target})$$

While a more complex option can be the use of a Hill or Michaelis–Menten function to describe the dependence of the effective energy on the chemotactic response as follows:

$$H_{chemo} = \mu(c) \cdot \frac{C(\vec{\imath})^a}{b + C(\vec{\imath})^a}$$

With a and b constants, and the change on effective energy described by a form that simultaneously considers the chemotactic response and the concentration of both source and target voxels:

$$\Delta H_{chemo} = \left[\mu\left(c_{target}\right) - \mu(c_{source})\right] \cdot \frac{[C\left(\vec{\imath}_{target}\right) - C(\vec{\imath}_{source})]^a}{b + [C\left(\vec{\imath}_{target}\right) - C(\vec{\imath}_{source})]^a}$$

A simple example of the simulation of the chemotactic response is shown below on figure 3.14, where an initially constant and uniform nutrient field being consumed by an ameba that consumes it, creating a random walk where the areas with less nutrients that the ameba has already visited are avoided as the simulation progresses.

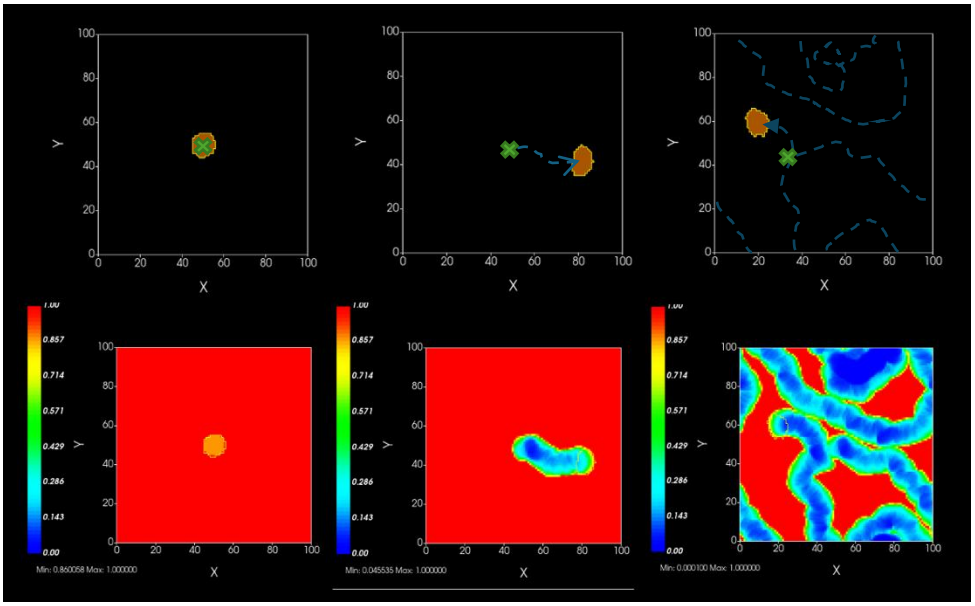

Figure 3.14. Time evolution of the simulation of an ameba feeding on a chemical field of nutrients.

However, these tools can be employed to simulate more complex and important systems for cancer research, like the evolution of vascularized tumors and the chemical signaling on its development.

3.1.3.8 Simulation of a vascularized tumor and Geant4-CC3D coupling

In the past CC3D has been employed to simulate the development of solid tumors, whose cells growth depended on the available oxygen on its environment, on "3D Multi-Cell Simulation of Tumor Growth and Angiogenesis" by Shirinifard A., et al (2009) a model that starts with a single cell, located at the center of a mesh arrangement of normal vascular tissue that provide oxygen, proliferates until it becomes a tumor. An image showing the initial configuration can be seen in Figure 3.15.

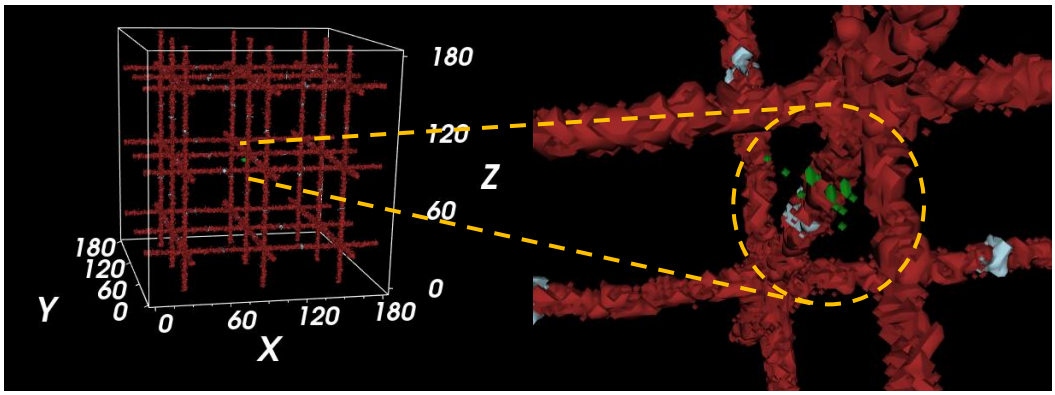

Figure 3.15. initial distribution of normal vascular tissue (red), inactive neovascular tissue (white) and the single tumoral cell at the center of the array (green), geometry reproduced from [Shirinifard A. et al, 2009].

As the tumor grows and the oxygen consumption of the increasing number of cells starts to rise, the central region at its core doesn't receive enough oxygen to continue developing and its cells become hypoxic. In this state the cells secrete a cascade of chemical signals that include the *Hypoxia Induced Factor-1* (HIF1) and the Vascular-Endothelial Growth Factor 1 and 2 (VEGF) that promotes the growth and extension of the close vascular tissue in a process known as *angiogenesis* in an attempt to increase the supply of oxygen to the hypoxic tissue [Shirinifard A. et al, 2009].

This model was employed to simulate tumor growth under two parallel conditions starting with identical initial characteristics, one with the normal angiogenesis process and other with this mechanism deactivated, the growth of both tumors was compared in terms of the total number of each type of cell considered: Normal, hypoxic and necrotic tumor cells, while the vascular cells were divided into normal and neovascular.

The behavior observed for the angiogenesis tumor was separated into several stages; between 0-15 simulated days the tumor grows as a spheroid until it reaches a diameter of about 300µm, here the first active neo vascular cells are seen. From 15 to 30 days the growth of the tumor changes into a cylindrical shape of 350µm length and 300µm of diameter, attaching and rupturing the original vascular array. The tumor also starts to be surrendered by neovascular tissue. Finally, 75 days after the start of the simulation the tumor is completely developed and the neovascular tissue forms a 2D sheet structure that envelops it. In contrast the non-angiogenic tumor never surpass the 200µm diameter on the spheroid growth stage, it develops into a cylindrical shape of 200µm diameter and 350 µm of length, rupturing vascular tissue in the process [Shirinifard A. et al, (2009)]. The images on figure 3.16 show the time evolution and the different growth stages of the angiogenic tumor, and the graphics on figure 3.17. the comparison of the number of cells in both considered cases.

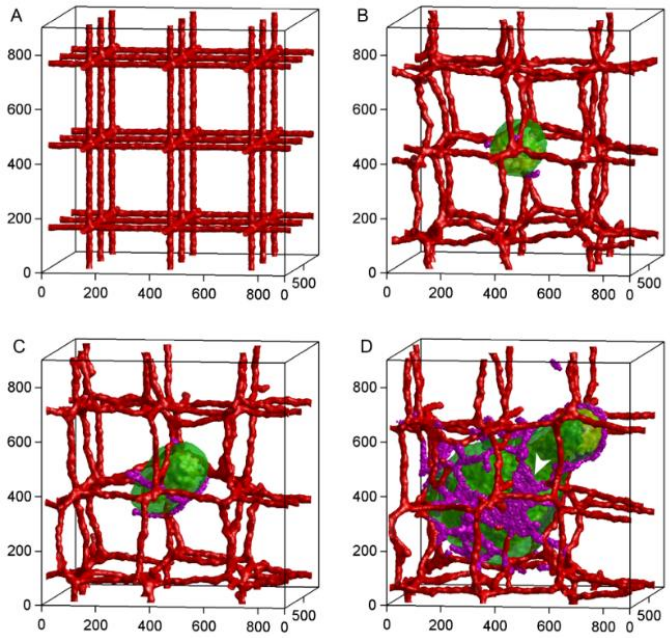

Figure 3.16. Time evolution of an angiogenic tumor where it is observed at A) 0 days, the original normal vasculature. B) 15 days, the spheroid growth stage. C) 30 days, the cylindrical growth stage and D) the fully developed tumor. Image taken from [Shirinifard A. et al, (2009)]

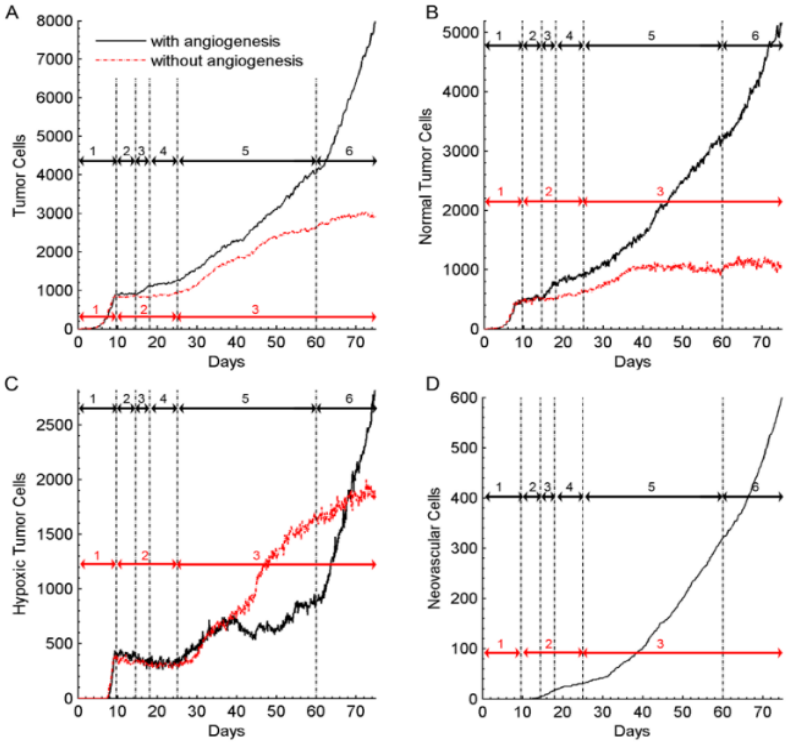

Figure 3.17. comparison of the different types of cells considered on both angiogenic and non-angiogenic tumors. Image taken from [Shirinifard A. et al, (2009)]

Another similar and important research work is “Development of a coupled simulation toolkit for computational radiation biology based on Geant4 and CompuCell3D” by [Lui R., et al. (2021)], where a multiscale platform that combined CC3D with Geant4 was developed, CompuCell3D was used to simulate the growth of a vascularized tumor, feed by an initial distribution of normal vascular tissue and using glucose as a representation to the blood flow. It considered the same angiogenesis mechanism mediated by the VEGF signaling used by [Shirinifard A. et al, (2009)]. The tumor is allowed to proliferate until a certain point when the geometrical information is traduced into a format that Geant4 can read. Then, the irradiation of the tumor is simulated using the Geant4-DNA application RADCELL.

In Geant 4, the geometries of the individual cells are simplified to pairs of concentric spheres, the internal one represents the nucleus while the external one is the cytoplasm. This approximation has been reported to be sufficiently accurate for scoring the absorbed dose in both cell’s compartments [Šefl M., et al (2015), Lui R., et al. (2021)]. After the irradiation is performed, the number of SSBs and DSBs were quantified using the Density-Based Spatial Clustering of Applications with Noise (DBSCAN) clustering algorithm, a method that has been successfully integrated into Geant4 and applied to calculate the number of DNA lesions from the geometrical distribution of ionizations on a cell nucleus based on the distinction of clusters from noise by a predefined distance, usually ~3.2nm which is the distance corresponding to 10bp needed to the formation of a DSB [Francis Z., et al (2011), Dos Santos M., et al (2013), Douglass M., et al (2015)].

The irradiation information is feedback into CC3D, and the simulation continues by considering that cells can be in three states: Arrested, healthy, and dead. The transition between these states was handled by random sampling of a probability distribution, where parameters were adjusted with biological data. The irradiation is performed in different tumor development stages and using various number of dose fractions, microbeams were also employed to test the hyper fractionation of doses, delivering up to 40Gy in 2-5 fractions [Lui R., et al. (2021)], several stages of the tumor growth and the geometry translation into Geant4 is shown on figure 3.18, and the comparison of the time evolution of the number of alive cells between several doses and dose-fractions are presented next on figure 3.19.

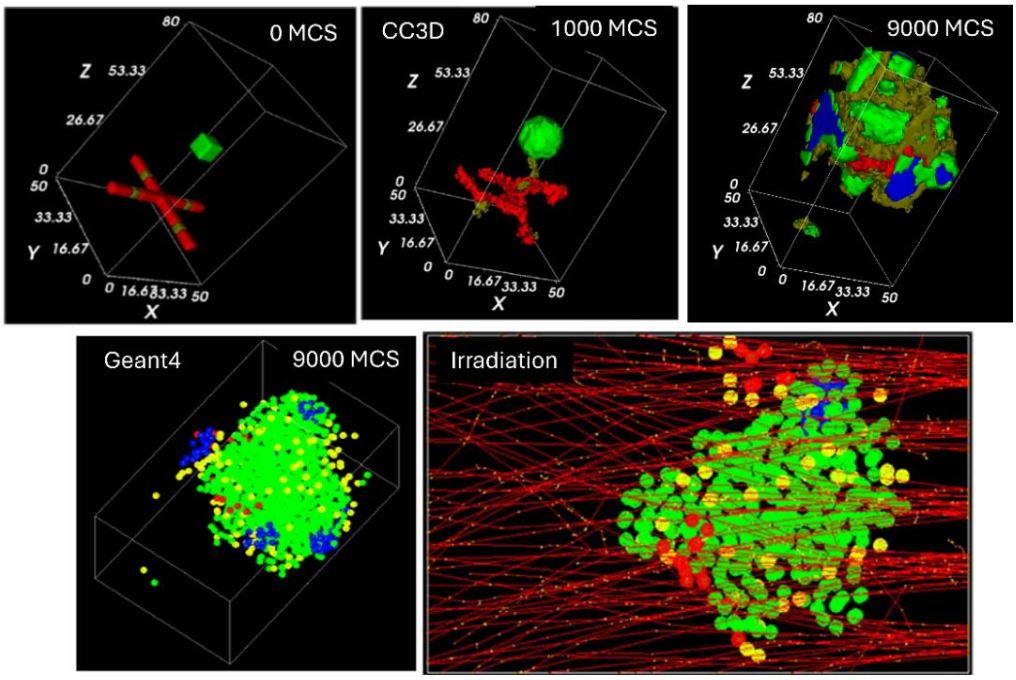

Figure 3.18. Tumor growth at 0-9000 MCS with an equivalence of 1MS=1min, below the translation of the tumor into Geant4 and the irradiation process. Images taken from [Lui R. (2017), Lui R., et al. (2021)]

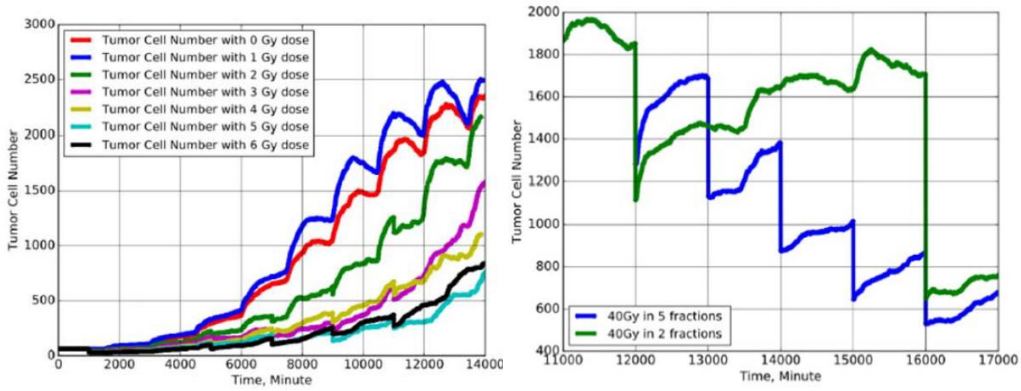

Figure 3.19. time evolution the number of alive cells under different total dose deposits, in a range of 0-6Gy and the comparison between the hype fractionation of 40Gy in 2 or 5 applications. Images taken from [Lui R., et al. (2021)]

Nevertheless, biological processes like DNA repair and the cell radiation damage response were not explicitly simulated in this work. The random sampling method for the cellular state transition made the computational simulation very efficient, and the authors remarked on the extension capabilities of their platform for the implementation of external models in future works [Ruirui Liu et al. (2021)].

Furthermore, CC3D counts with a very powerful and flexible tool for the implementation of internal biochemical signaling networks in the form of coupled differential equations systems that can be solved numerically and assigned to individual cells. They can represent the protein control mechanisms for the biological radiation response and may be interconnected with other biological systems like cellular growth or apoptosis processes.

3.1.3.9. Tellurium: Solving internal differential equation systems

The CC3D methods for handling the diffusion and interaction of external chemical fields in the cell's environment were reviewed briefly in past sections. However, CompuCell3D also has an internal tool called Tellurium, a free open-source platform based on the *RoadRunner* library, that facilitates the construction, simulation, analysis and sharing of kinetic chemical models, especially those oriented to biological systems. It has been implemented in several platforms with user-friendly interfaces like MATLAB or SPYDER, making the transferring of models between codes much easier [Somogyi E.T., et al (2015), Choi K., et al (2018)].

This tool can read a standard type of file called Systems Biology Markup Language (SBML) a data format similar to HTML for the formal definition of biochemical reactions and the differential equations that describe them, it is a free and open-source language [Hucka M., et al (2018)] and it is used by several codes focused on the simulation of different cell biological aspects on several scales, like Vcell [Fink C.C., et al (2000)].

Tellurium also has an internal tool called Antimony, designed to write and translate chemical schemes on SBML to an easy-to-read format on asci, with simple definitions and conventions: Each reaction must have a name with no spaces in between and ended by a colon ":", after that, the involved reactants are declared separated by the plus sign "+", the products are declared after an arrow "->" in a similar way. In addition, both reactants and products names cannot have especial characters like "+", "- ", "*". Finally, the reaction rate is declared after a semicolon ";" and it can be any function, from simple action-mass stochiometric relationships, dependent on the concentrations of the reactants involved in the reaction like bimolecular reactions ($A + B \overset{k_r}{\rightarrow} P; k_r = k[A][B]$), independent of them like spontaneous generations ($\overset{g}{\rightarrow} P$, with g constant) and even dependent on other chemical substances not involved in the reaction, following complex functions like the Michelis-Menten formula [Choi K., et al (2018)]:

$$A + B \overset{k_r}{\rightarrow} P \quad \text{with} \quad k_r = k_{max}\frac{[D]}{[D] + M}$$

In CC3D these SBML models can be associated with particular groups of cells, by index or type of cell, and as global *free-floating* models not associated with any specific cells [Swat M.H., et al (2014)]. A simple example of the use of this tool is provided below where a small chemical reaction scheme involving three arbitrary substances A, $B$and C, where A turns into B and B into C with constant rates k_1 and k_2 respectively. The initial concentration of each substance is given by $A_0 = 2.0$, $B_0 = 0.0$, $C_0 = 0.0$. The analytical solution of this system is given by the next set of equations dependent on time, and the implementation of the scheme, using the Antimony language conventions, followed by the comparison between the Tellurium results and the analytical solution are presented on figure 3.20.

$$A(t) = A_0 \cdot e^{-k_1 \cdot t}$$

$$B(t) = A_0\frac{k_1}{k_2 - k_1} \cdot \left(e^{-k_1 \cdot t} - e^{-k_2 \cdot t}\right)$$

$$C(t) = A_0 - A(t) - B(t)$$

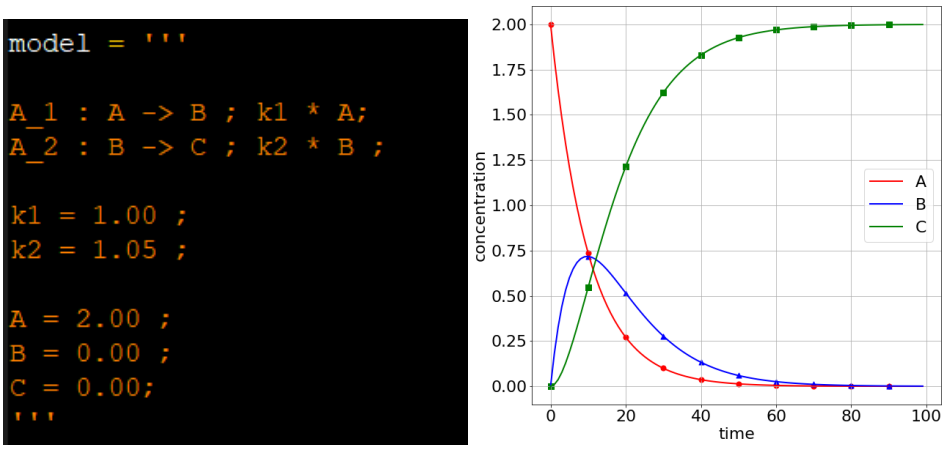

Figure 3.20. **Left**: implementation of the chemical scheme in Antimony language. **Right**: comparison between the Tellurium simulation of the chemical system and the analytical solution.

The importance of this tool for this research work is that existing models for protein networks that controls biological process like the cell cycle or the response to radiation damage can be implemented in a SBML format, assign them to individual cells, extract information to communicate with other simulated behaviors like the cell's growth, DNA repair or apoptosis, and simulate the radiation response of a cell population.

3.2 TOPAS-Kinetiskope Coupling

The combination of TOPAS with Kinetiscope was used to simulate the irradiation of three models under Conventional and FLASH irradiation: A basic pure water model, based on the work of [Wardman P. (2020)] of 28 reactions and revised by [D-Kondo N.J., et al (2023)] presented on table 3.4; pure water plus the biomolecules compiled on tables 2.7, 2.8,2.10 and 2.11 from section 2.3.2 *Cellular environment composition and its radiochemical damage*, and a cellular environment model that encompassed water, biomolecules and antioxidants.

Table 3.4. Chemical reaction scheme used for the simulation of pure water radiolysis

Number	Reaction	Reaction rate k ($M^{-1}s^{-1}$)
1	$H^+ + OH^- \rightarrow (H_2O)$	14.3×10^{10}
2	$H + H \rightarrow H_2$	1.56×10^{10}
3	$H + OH \rightarrow (H_2O)$	2.0×10^{10}
4	$H + H_2O_2 \rightarrow OH + (H_2O)$	0.009×10^{10}
5	$H + e^-_{aq} \rightarrow H_2 + OH^-$	2.5×10^{10}
6	$OH + OH \rightarrow H2O2$	0.55×10^{10}
7	$OH + e^-_{aq} \rightarrow OH^-$	3.0×10^{10}
8	$H_2O_2 + e^-_{aq} \rightarrow OH^- + OH$	1.1×10^{10}
9	$e^-_{aq} + e^-_{aq} \rightarrow OH^- + OH^- + H_2$	1.1×10^{10}
10	$e^-_{aq} + H^+ \rightarrow H$	2.3×10^{10}
11	$H^+ + O_2^- \rightarrow HO_2$	2.1×10^{10}
12	$HO_2 \rightarrow H^+ + O_2^-$	$8.05 \times 10^5\ s^{-1}$

13	$H^+ + O_2^- \rightarrow HO_2$	5.00×10^{10}
14	$e_{aq}^- + O_2 \rightarrow O_2^-$	1.9×10^{10}
15	$H + O_2 \rightarrow HO_2$	2.10×10^{10}
16	$HO_2 + HO_2 \rightarrow H_2O_2 + O_2$	8.3×10^{5}
17	$HO_2 + O_2^- \rightarrow H_2O_2 + O_2 + OH^-$	9.7×10^{7}
18	$O_2^- + O_2^- \rightarrow H_2O_2 + O_2 + OH^-$	4.9×10^{3}
19	$HO_2 + OH \rightarrow O_2 + (H_2O)$	6.00×10^{9}
20	$O_2^- + OH \rightarrow O_2 + OH^-$	8.2×10^{9}
21	$e_{aq}^- + HO_2 \rightarrow H_2O_2 + OH^-$	2.00×10^{10}
22	$e_{aq}^- + O_2^- \rightarrow H_2O_2 + 2\,OH^-$	1.3×10^{10}
23	$H + HO_2 \rightarrow H_2O_2$	1.5×10^{10}
24	$H + O_2^- \rightarrow H_2O_2 + OH^-$	1.8×10^{10}
25	$HO_2 + H_2O_2 \rightarrow OH + O_2$	5.0×10^{-1}
26	$O_2^- + H_2O_2 \rightarrow OH + O_2 + OH^-$	1.3×10^{-1}
27	$OH + H_2 \rightarrow H + (H_2O)$	4.3×10^{7}
28	$OH + H_2O_2 \rightarrow O_2^- + H^+ + (H_2O)$	2.7×10^{7}

TOPAS-nBio was used to simulate individual pulses of a Flash and Conventional radiation sources following the specifications described in [Montay-Gruel et al. (2019)]: for the FLASH source pulses were 1.8µs width, on a 100Hz frequency, meaning that a 0.01 second delay was in between pulses, each one of them delivering 5Gy to the medium, giving as a result $2.78 \times 10^6 \mathrm{Gy/s}$ dose rate. In contrast, the conventional source used 1.0µs of width pulses at a frequency 10Hz, and consequently a separation of 0.1 seconds between pulses, with an overall dose rate of $2.86 \times 10^4 \mathrm{Gy/s}$, meaning that a 10Gy dose delivery required 350 CONV pulses in comparison to 2 FLASH pulses. In TOPAS, the individual pulses were simulated using a gaussian pulse with a Full Width at Half Maximum (FWHM) value of 1.0µs and 1.8µs for CONV and FLASH irradiations respectively, 400 repetitions were performed for every type of irradiation and simulated environment. The TOPAS pulse configuration can be seen below in figure 3.21.

```
# FLASH Pulse Configuration
d:Sc/yield/PrescribedDose     = 5 Gy
s:Sc/yield/PulseDistribution = "Gaussian"
d:Sc/yield/PulseTimeMean      = 0.9 us
d:Sc/yield/PulseTimeFWHM      = 1.8 us
i:Sc/yield/NumberOfPulses   = 1
```

```
# CONV Pulse Configuration
d:Sc/yield/PrescribedDose     = 0.0286 Gy
s:Sc/yield/PulseDistribution = "Gaussian"
d:Sc/yield/PulseTimeMean      = 0.5 us
d:Sc/yield/PulseTimeFWHM      = 1.0 us
i:Sc/yield/NumberOfPulses   = 1
```

Figure 3.21. TOPAS configuration for the CONV and FLASH pulses

The radiation source was simulated with a flat proton beam of 100MeV, since it has been shown that the radiolytic scape yields on pure water produced by this type of irradiation are similar to those produced by gamma rays from a ^{60}Co source [Ramos-Méndez J., et al (2020)]. The irradiated volume was a cube of water with sides of 3µm length. Both geometrical and particle beams can be seen next, on figure 3.22 and 3.23.

```
#################################################################
####################- GEOMETRY PARAMETERS-#####################
#################################################################

Ge/World/HLX = 1.5 um
Ge/World/HLY = 1.5 um
Ge/World/HLZ = 1.5 um
Ge/World/Material = "G4_WATER"

s:Ge/Target/Parent   = "World"
s:Ge/Target/Type     = "TsBox"
s:Ge/Target/Material = "G4_WATER"
d:Ge/Target/HLX = 1.5 um
d:Ge/Target/HLY = 1.5 um
d:Ge/Target/HLZ = 1.5 um
```

Figure 3.22 TOPAS geometrical configuration

```
#################################################################
####################- SOURCE PARAMETERS-######################
#################################################################

d:So/Demo/BeamEnergy = 100 MeV
u:So/Demo/BeamEnergySpread = 0
s:So/Demo/BeamPositionDistribution = "Flat"
d:So/Demo/BeamPositionCutoffX = 1.4 um
d:So/Demo/BeamPositionCutoffY = 1.4 um
s:So/Demo/BeamAngularDistribution = "None"
s:So/Demo/BeamParticle = "proton"
i:So/Demo/NumberOfHistoriesInRun = 50000
```

Figure 3.23. TOPAS particle beam configuration

The chemical scheme was introduced without changes, but oxygen, biomolecules and antioxidant reactions were introduced as first order reactions with constant concentrations. The G-values of the chemical species were retrieved at 100µs after irradiation at the end of the heterogeneous chemical stage. An example of the amino acid chemical configuration and reactions on TOPAS can be seen below in figure 3.24. Since biomolecules are much larger than radiolytic species and consequently have less mobility, they were simulated as static in TOPAS, meaning that their diffusion coefficients were set to 0.

Biomolecule declaration

```
#################################################################
#######                    AMINOACID                 ##############
#################################################################

s:Mo/AminoAcid/Symbol = "AminoAcid"
d:Mo/AminoAcid/DiffusionCoefficient = 0 nm2/s
u:Mo/AminoAcid/Charge = 0
d:Mo/AminoAcid/Radius = 0.3 nm

s:Mo/AminoAcid_R/Symbol = "AminoAcid_R"
d:Mo/AminoAcid_R/DiffusionCoefficient = 0 nm2/s
u:Mo/AminoAcid_R/Charge = 0
d:Mo/AminoAcid_R/Radius = 0.3 nm
```

Reactions with radicals

```
sv:Ch/TOPASChemistry/BackgroundReaction/SolvatedElectron/AminoAcid/Products = 1 "AminoAcid_R"
d:Ch/TOPASChemistry/BackgroundReaction/SolvatedElectron/AminoAcid/ReactionRate = 1.0e8 /M/s
d:Ch/TOPASChemistry/BackgroundReaction/SolvatedElectron/AminoAcid/Concentration = Ch/TOPASChemistry/
AminoAcidConcentration M
i:Ch/TOPASChemistry/BackgroundReaction/SolvatedElectron/AminoAcid/ReactionType = 6
b:Ch/TOPASChemistry/BackgroundReaction/SolvatedElectron/AminoAcid/CompatibleWithStepByStep = "False"


sv:Ch/TOPASChemistry/BackgroundReaction/hydroxyl/AminoAcid/Products = 1 "AminoAcid_R"
d:Ch/TOPASChemistry/BackgroundReaction/hydroxyl/AminoAcid/ReactionRate = 2.0e9 /M/s
d:Ch/TOPASChemistry/BackgroundReaction/hydroxyl/AminoAcid/Concentration = Ch/TOPASChemistry/AminoAcidConcentration M
i:Ch/TOPASChemistry/BackgroundReaction/hydroxyl/AminoAcid/ReactionType = 6
b:Ch/TOPASChemistry/BackgroundReaction/hydroxyl/AminoAcid/CompatibleWithStepByStep = "False"


sv:Ch/TOPASChemistry/BackgroundReaction/Hydrogen/AminoAcid/Products = 1 "AminoAcid_R"
d:Ch/TOPASChemistry/BackgroundReaction/Hydrogen/AminoAcid/ReactionRate = 3.0e6  /M/s
d:Ch/TOPASChemistry/BackgroundReaction/Hydrogen/AminoAcid/Concentration = Ch/TOPASChemistry/AminoAcidConcentration M
i:Ch/TOPASChemistry/BackgroundReaction/Hydrogen/AminoAcid/ReactionType = 6
b:Ch/TOPASChemistry/BackgroundReaction/Hydrogen/AminoAcid/CompatibleWithStepByStep = "False"
```

Figure 3.24. Declaration of a background reaction on TOPAS for the Amino acids biomolecules with the free radicals that can damage it (e^-_{aq}, OH and H).

These escape yields produced by single CONV and FLSH pulses were used to feed Kinetiscope. A compartment model was used with a single volume, and the external stimulus option was employed to simulate a train of pulses. The production rate for a R specie ($d[R]/dt$) is calculated as the G-value in µM/Gy units, multiplied by the dose rate in Gy/s units, resulting in a quantity of chemical species produced by second in µM/s units ($G(R)dD/dt$). Two oxygen concentrations were used 50 and 5 µM to represent normoxic and hypoxic conditions. The time evolution for the radiolitic species and biological radicals was recorded and a scheme of the TOPAS-Kinetiscope coupling is shown on figure 3.25.

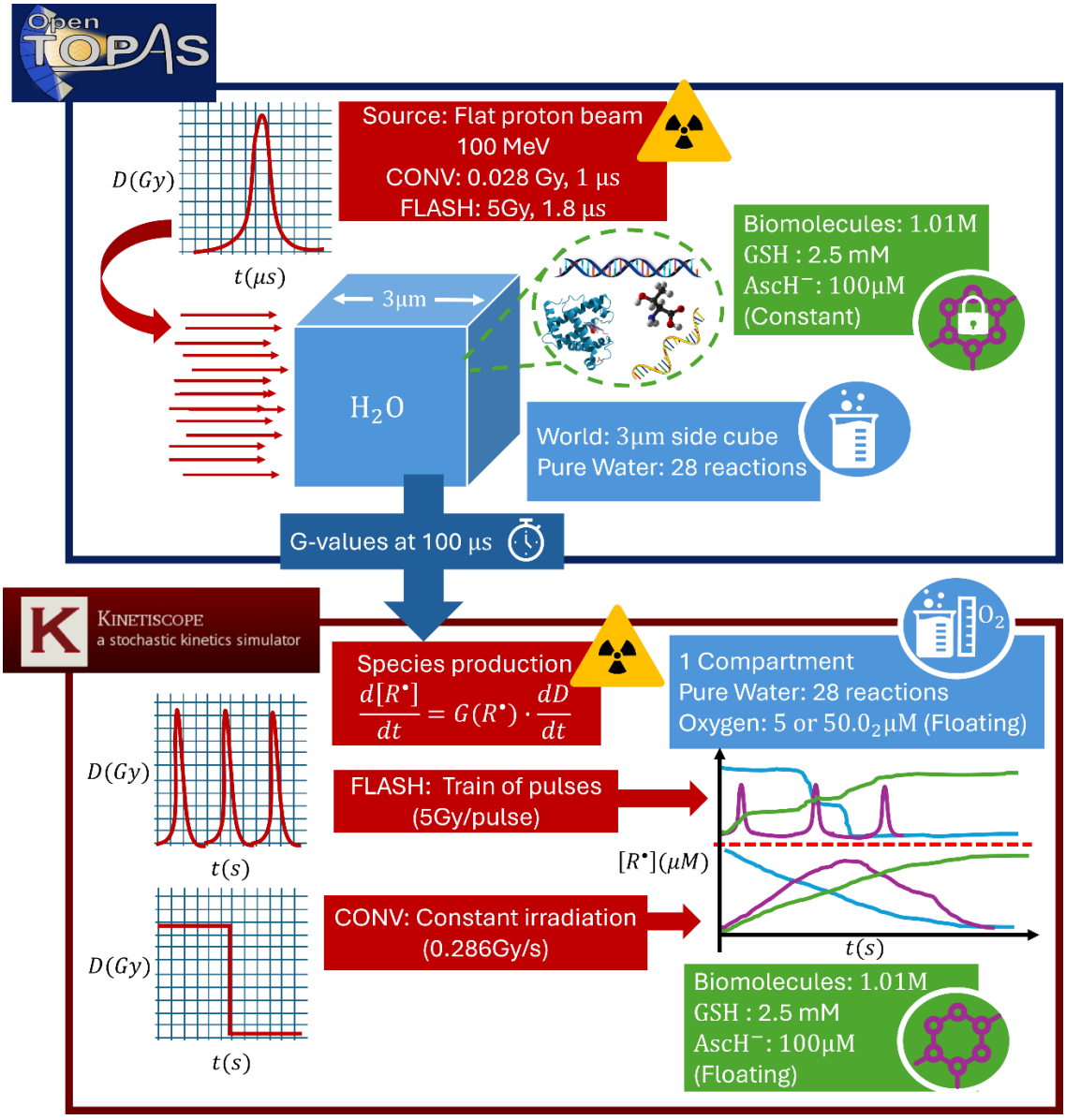

Figure 3.25. scheme of the TOPAS-Kinetiscope coupling where the simulation of CONV and FLASH pulses in pure water, in the presence of biomolecules and the with antioxidants added, were carried out by TOPAS. The G-values obtained were fed to Kinetiscope and using the user defined external-stimulus tool, they were simulated as a train of pulses to continue the long-term simulation of the heterogenous chemical stage.

3.2.1 Prototype for the SSA implementation

One of the main goals of the in-depth study on the fundamentals and operation of the Gillespie algorithm was to implement an *in-house* version inside TOPAS to extend its capabilities for the simulation of the chemical heterogeneous stage of water radiolysis. The first step taken was to develop a prototype in Python language to compare its functioning with Kinetiscope, as a reference code, and then translate this external tool into a dedicated C++ file, the native programing language of TOPAS and Geant4, into the extension library TOPAS-nBio.

To test our implementation, we use the G-Values for pure water reported on [Pastina B. &. LaVerne J. (2001)] table 2.5. on section 2.1.6. *Homogeneous chemical stage* on M/Gy units, to simulate the time evolution of the radiolytic species under a total dose of 0.5Gy for both our Gillespie algorithm implementation and Kinetoscope shown below in figure 3.26. Since it was a preliminary test, we used the main 10 reaction scheme for water radiolysis, described in table 2.2., section 2.1.3.1 *Models for the heterogeneous chemistry of pure water.* However, this main reaction scheme has passed through several iterations with changes and corrections for the reaction rates values, therefore, for this preliminary test the original values from [Pimblott S.M. & LaVerne J.A. (1990)] were chosen, presented next in the Kinetiscope language conventions in figure 3.26. This reduced chemical scheme is sufficient to simulate the phenomenon until the end of the heterogeneous chemical stage at around $1\mu s$, and was chosen instead of the complete ~80 reaction scheme for the sake of simplicity and to focus on the comparison between implementations.

Species	Initial Concentration (mole/liter)	Calculated Initial Number of Particles
eaq-	1.345e-7	2427
H	3.4155e-08	616
H+	1.60425e-07	2895
H2	2.32875e-08	420
H2O	0	0
H2O2	3.6225e-08	654
OH	1.39725e-07	2521
OH-	2.5875e-08	467

	Reaction Step	Forward k	Rate Laws
1	2 eaq- => H2 + 2 OH-	5.5e9	from stoichiometry
2	eaq- + H+ => H	2.3e10	from stoichiometry
3	eaq- + H => H2 + OH-	2.5e10	from stoichiometry
4	eaq- + OH => OH-	3.0e10	from stoichiometry
5	eaq- + H2O2 => OH + OH-	1.1e10	from stoichiometry
6	H+ + OH- => H2O	1.4e11	from stoichiometry
7	2 H => H2	7.8e9	from stoichiometry
8	H + OH => H2O	2.0e10	from stoichiometry
9	H + H2O2 => H2O + OH	9.0e7	from stoichiometry
10	2 OH => H2O2	5.5e9	from stoichiometry

Figure 3.26. **Lef.t** Kinetiscope Initial conditions from the G-values reported on [Pastina B. &. LaVerne J. (2001)] and transformed into M/Gy units, then multiplied by the total dose of 0.5Gy to obtain the initial concentration of each molecule. **Right.** The 10 main reactions scheme for the heterogeneous chemical stage of water radiolysis on Kinetiscope language convention.

One of the aspects that came up in our SSA implementation was the necessity to include a conversion factor c between the number of chemical species X_i and concentrations $[S_i]$ given in mol/l units. This is because the propensity function works with the actual number of molecules and not its molar concentration.

$$[S_i] = c \cdot X_i$$

Kinetiscope initiates with a fixed number of global molecules N_{tot} defined by the user. The default value is 1000, which will be divided among the n declared molecule types according to the declared initial molar concentrations, and a volume of 1 liter is assumed, shown below in figure 3.27. Then, the conversion factor is automatically calculated as the sum of all the concentrations $[S_{tot}]$ divided by the total number of molecules as follows:

$$[S_{tot}] = \sum_{i=1}^{n} [S_i] \quad \Longrightarrow \quad n = \frac{[S_{tot}]}{X_{tot}}$$

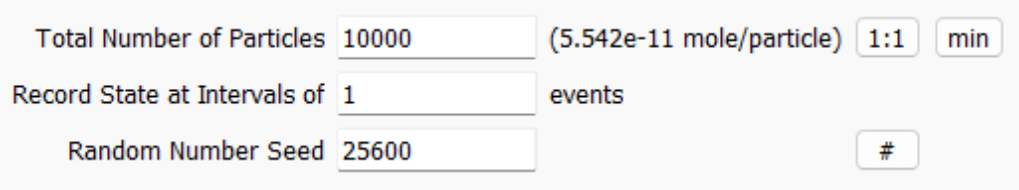

Figure 3.27. Kinetiscope configuration window where the user defines the desired total number of molecules and the conversion factor to mol is automatically calculated.

This was not a problem in our implementation since we took the number provided by Kietiscope as an initial condition. However, once the implementation was translated into TOPAS-nBio this factor needed to be considered. Fortunately, the simulated volume $V$and the number of molecules produced X_i are provided by TOPAS. Then we can compare the previous expression with the formula for the molar concentration to deduce that the factor needed to convert the number of molecules into molar concentration is the following:

$$[S_i] = \frac{1}{N_A V_{(l)}} \cdot X_i \quad \Leftrightarrow \quad c = \frac{1}{N_A V_{(l)}}$$

Where N_A is the Avogadro number and $V_{(l)}$ is the simulated volume measured in liters. Results for the time evolution of our SSA implementation compared to Kinetoscope are presented below. For several chemical species the behavior is essentially the same and the differences at the end of the simulations, at times $t > 10^{-3}s$, can be explained by the stochastic nature of the Gillespie algorithm.

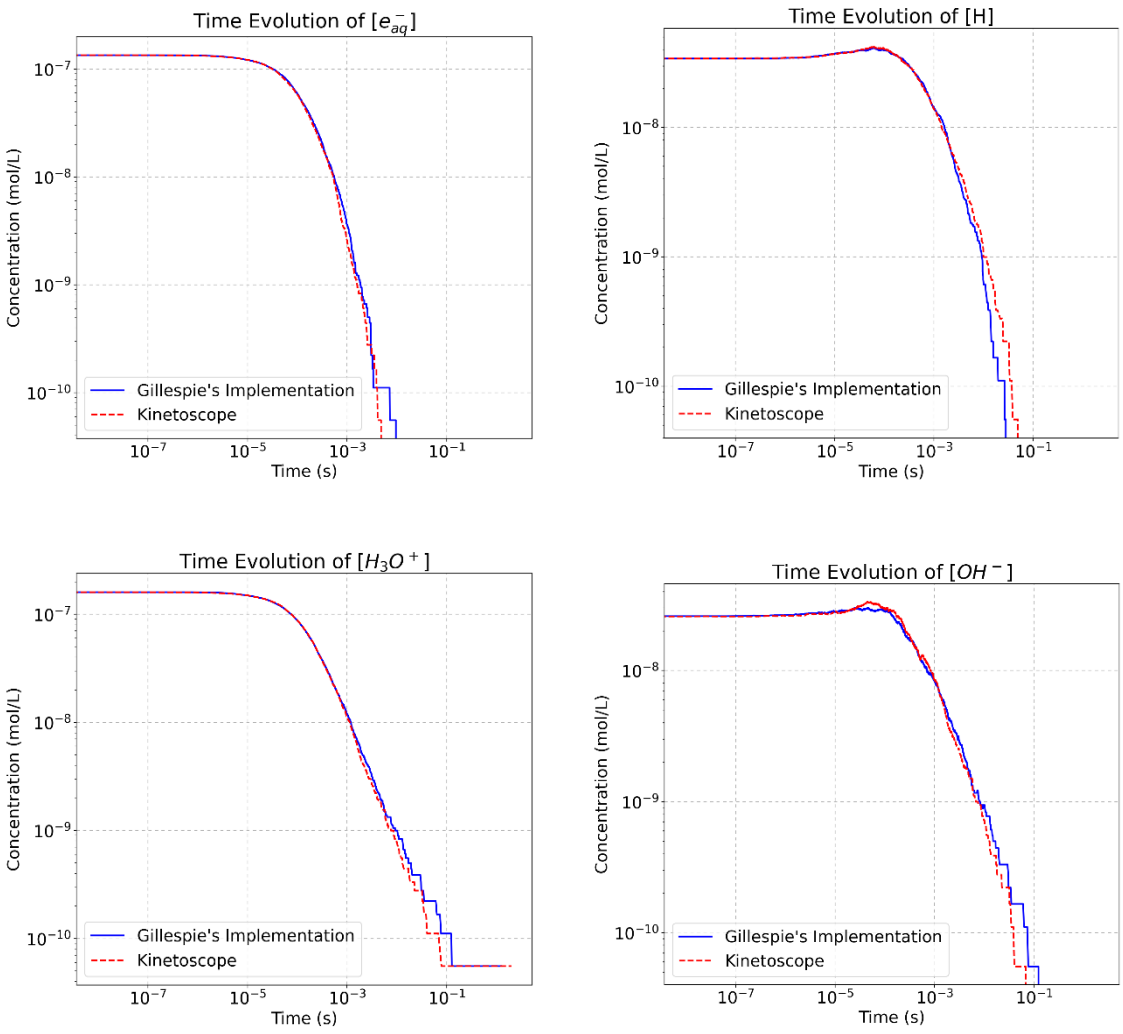

Figure 3.28. comparison of the time evolution of the concentration of e_{aq}^-, H, H_3O^+ and OH^-between our implementation of the SSA (blue solid line) and Kinetiscope (red dashed line).

However other chemical species show small differences: our results for the hydroxyl radical concentration are above the results on kinetoscope for times $t > 10^{-3}s$, and the water molecules, declared to account for several neutralization reactions like $OH + H \rightarrow H_2O$ and $OH^- + H^+ \rightarrow H_2O$, start to being produced at $t > 10^{-7}$ on our implementation, rather than the beginning of the simulation like Kinetiscope, but arrives at the same final concentration. The evolution of these two reactions is shown below in figure 3.29.

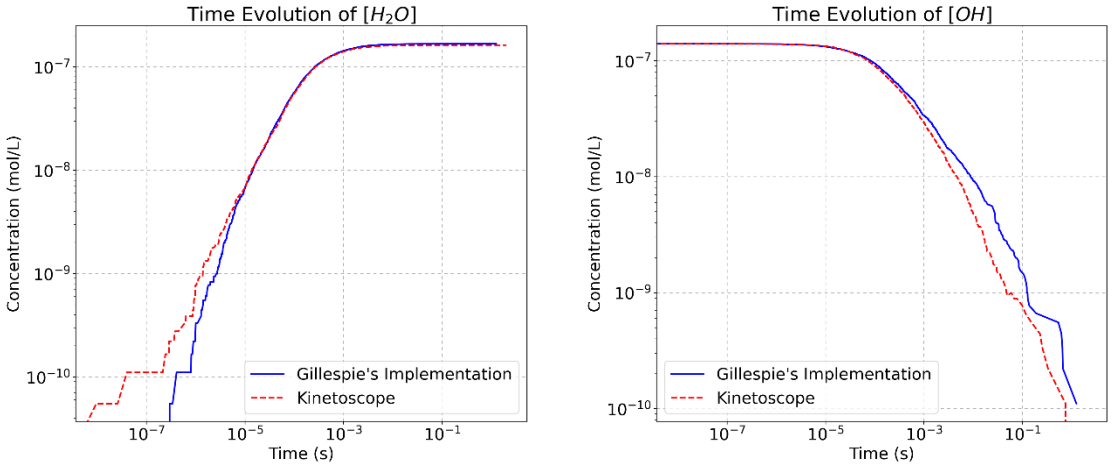

Figure 3.29. Comparison of the time evolution of the species with small differences, $\mathrm{H_2O}$ and OH, between our implementation (blue solid line) and Kinetiscope (red dashed line).

The difference for the final value of $[\mathrm{OH}]$ is related to the next set of results. Two species are significatively different between our implementation of the Gillespie algorithm and the results from the reference code: for $\mathrm{H_2}$ there is a difference of 9.9% and for $\mathrm{H_2O_2}$ of 10.3 % below the value calculated with Kinetiscope, shown on figure 3.30.

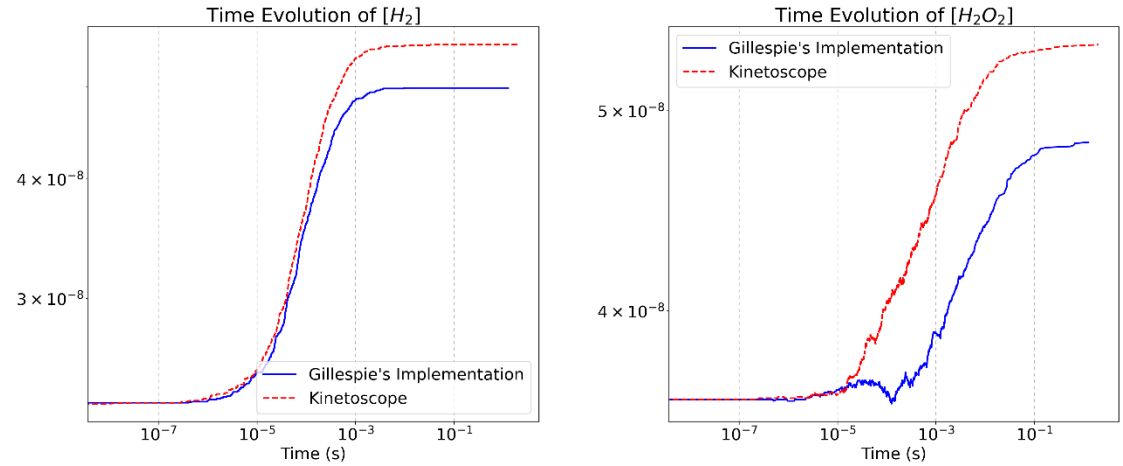

Figure 3.30. comparison of the time evolution of the species that had significant differences, H_2 and $\mathrm{H_2O_2}$, between our implementation (blue solid line) and Kinetiscope (red dashed line).

These differences arise mainly because the principal contributions to the production of both molecules are bimolecular reactions between the same species, $2\mathrm{OH} \rightarrow \mathrm{H_2O_2}$ and $2\mathrm{H} \rightarrow \mathrm{H_2}$. In our implementation the total number of combinations h_μ between the X_i molecules in the system for this type of reactions was set to the exact solution of $h_\mu = X_i(X_i - 1)/2V$ while the solution on Kinetiscope is approximated to the limit when the number of molecules is very large to $h_\mu = X_i^2/2V$. Nevertheless, this first prototype was the basis for the development of a first

TOPAS-nBio implementation on C++ and the differences on the final concentrations were later addressed when the results were published.

3.3 TOPAS-CC3D Coupling

The coupling of TOPAS with CC3D was performed to construct a multiscale platform for the irradiation of a cell population simulation, complementing both codes capabilities and overcome their limitations: TOPAS can incorporate detailed geometrical models for biological structures, from DNA plasmids [D-Kondo N., et al (2021, Ramos-Méndez J., et al (2022)] to whole cells, including the DNA repair and formation of chromosomal aberrations [Zhu H., et al (2020)] among other applications. However, it is not designed to simulate the biological process of the targeted cells like their growth, division or movement.

On the other hand, CC3D is capable of handling all this biological process and more: for instance, DNA repair and p53 protein networks models for the cellular function regulation can implemented into a CC3D application and associated with individual cells using internal tools like Tellurium. However, this code doesn't count with a tool for the simulation of the radiation effect on a biological environment, specifically the production of DSBs. Therefore, this information needs to be externally fed.

The strategy proposed by this research work to couple TOPAS with CC3D was to use the specialized functions on each code to handle the specific stages of a cell population irradiation and the biological response, communicating both software's with the use of compatible files: CC3D simulate the cells growth of an initially *seeded* cells until they reach certain density during a pre irradiation period, the geometrical model is saved into a format that TOPAS can read and assign to a voxelated geometrical component that preserves the information of the cell's types and ID numbers. Then, the irradiation is performed and a quantity of interest, like the deposited dose in each voxel, is saved and processed to calculate the radiation damage done in each cell. This information is transferred back to CC3D to continue with the simulation of the DNA repair and cellular response to radiation that determinates if the cell dies or survives the damage. Finally, the survival curve is registered and compared to experimental data for the validation of the platform. A scheme for the coupling of TOPAS with CC3D is shown below in figure 3.31.

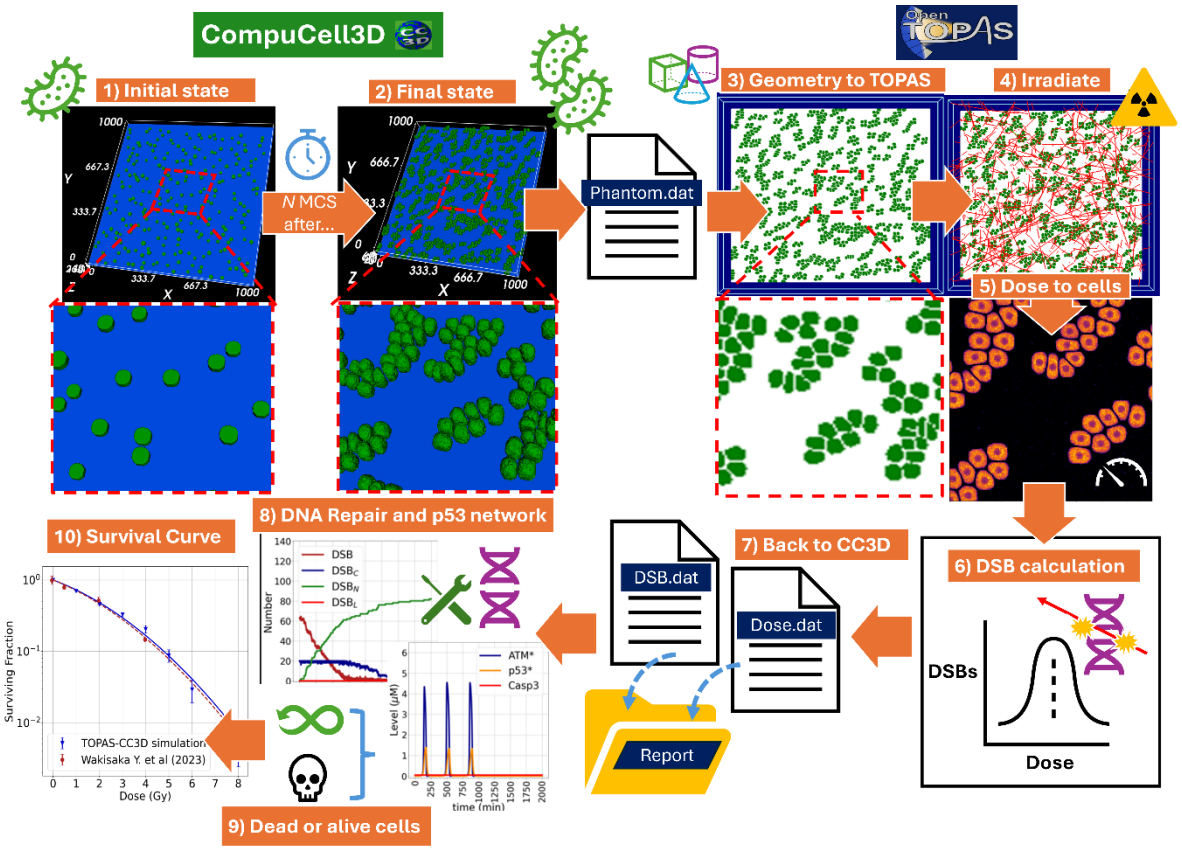

Figure 3.31. scheme of the general operation of the TOPAS-CC3D coupling where **1)** an initial seeded cell population grows for a predefined period until it reaches a **2)** final state which is **3)** transferred to TOPAS in a data format that it can read, then it is **4)** irradiated by a user defined radiation source and the **5)** the deposited dose is retrieved on each cell and used to **6)** calculate the initial number of DSBs that will be **7)** transferred back to CC3D to continue the simulation of the **8)** DNA repair and the p53 protein network, together they will determinate if the **9)** cell survive or die the damage and finally report the **10)** survival curve and compare it to experimental data to validate the platform.

This coupling of Monte Carlo codes resulted in the development of a new multiscale platform baptized as TOPAS-Tissue that will be discussed in the results section. To achieve its development several preliminary tests were performed to implement and calibrate the DNA repair and p53 protein network, first as a free-floating model and then associated a small test cell culture in CC3D.

3.3.1 p53 protein network implementation on Tellurium: Preliminary tests

The DNA damage response model by [Zhang X.P., et al (2009, 2011)] was implemented in CC3D and tested to ensure that its operation was identical to the one described in the original publication. The protein reaction scheme was implemented in the Antimony language and handled by the Tellurium tool using a free-floating model, this means that the model was not attached to any particular simulated cell and instead existed as a global biochemical system.

Following the authors methodology the number of initial DSBs for a uniformly irradiated population of cells with a deposited dose D_{Ir} can be sampled by a Poisson distribution [Rothkamm K., et al (2003)], with a mean value $\overline{N}_{DSB} = 35 \cdot D_{Ir}$ distributed on a fraction $f = 0.51$ of complex DSBs and the complementary fraction $(1 - f)$ as simple, for low LET irradiation like X-Rays [Zhang X.P., et al (2011)]. It is important to mention that for the free-floating model tests the number of initial DSBs

was the mean value of the Poisson distribution, without randomly sampling for each test run in order to simplify the procedure and make fair comparisons. However, once the model was assigned to a population of cells, each individual cell was assigned a random number of initial DSBS accordingly to the Poisson sampling procedure.

The first test was to reproduce the repair module kinetics for a simulated irradiation of 3Gy, and a corresponding $N_{DSB} = 105$. On figure 3.32. the implementation of the results of the repair module implementation on CC3D is demonstrated by showing the average of 10 repetitions of the time evolution of $\mathrm{DSB_C}$, using different random seeds on the **Left** image while several runs are shown on the **Right** images and compared to the reported behavior in [Zhang X.P., et al (2011)].

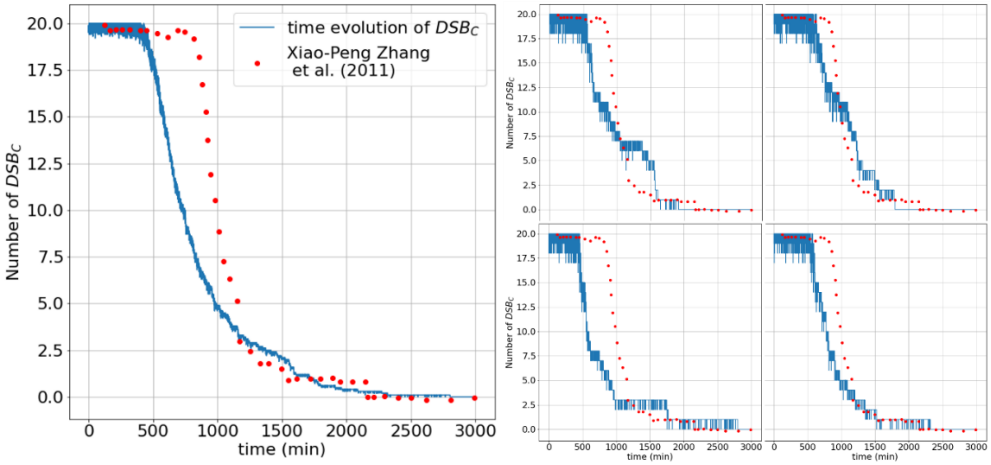

Figure 3.32: **Left.** Comparison between the repair module implemented on CC3D (solid line) and the reported $\mathrm{DSB_C}$ time evolution on [Zhang X.P., et al (2011)]. **Right**. Four individual repair processes to demonstrate the variability between individual runs of the model.

The authors recognize that, due to the stochastic nature of the DNA damage generation and repair process, there exists a considerable variability in the response of individual cells, even for the same radiation doses. This statement is appreciable in the results on the noisy individual runs of the model with different random seeds, that represent the repair of individual cells, sometimes under or above the reference data. Since no number of repetitions is provided in the original publication and the noisy nature of the graph indicates that this it is also a single run of the model for demonstration purposes instead of a mean value of the model after many repetitions, explaining the differences between our tests and the reference data. In addition, the number of $\mathrm{DSB_C}$ always reach 0 around 2200 minutes, agreeing with the original publication.

To ensure that the stochastic DNA repair model used by [Zhang X.P., et al (2009,2011)], solved by MC methods, was equivalent to the original TLK model by [Stewart R.D. (2001)] solved by deterministic numerical methods, a test was performed to compare both models under identical initial conditions: An irradiation of 5Gy with 122 initial DSBs spread between complex DSBs with a fraction $f = 0.51$ and the rest as simple DSBs. Since the original TLK model didn't consider DSBs attached to repair protein complex, an intermediate state was introduced to that model, and both $\mathrm{DSB_C}$ and available repair proteins N_R were considered to make a fair comparison. The modified TLK model is described by the next system of differential equations with the values of the parameters of the modified LLK listed below on table 3.5:

$$\frac{dDSB_{1D}}{dt} = -k_{fb1}N_R \cdot DSB_{1D} - k_{cross}NR \cdot DSB_{1D}(DSB_{1D} + DSB_{2D}) + k_{fr1}DSB_{1D}$$

$$\frac{dDSB_{2D}}{dt} = -k_{fb2}N_R \cdot DSB_{2D} - k_{cross}NR \cdot DSB_{2D}(DSB_{1D} + DSB_{2D}) + k_{fr2}DSB_{2D}$$

$$\frac{dDSB_{1C}}{dt} = k_{fb1}N_R \cdot DSB_{1D} + k_{cross}N_R \cdot DSB_{1D}(DSB_{1D} + DSB_{2D}) - k_{fr1}DSB_{1C} - k_{fix1}DSB_{1C}$$

$$\frac{dDSB_{2C}}{dt} = k_{fb2}N_R \cdot DSB_{2D} + k_{cross}N_R \cdot DSB_{2D}(DSB_{1D} + DSB_{2D}) - k_{fr2}DSB_{2C} - k_{fix2}DSB_{2C}$$

$$\frac{dDSB_{1F}}{dt} = k_{fix1}DSB_{1C}$$

$$\frac{dDSB_{2F}}{dt} = k_{fix2}DSB_{2C}$$

$$\frac{dN_R}{dt} = (k_{fix1} + k_{fr1})DSB_{1D} + (k_{fix2} + k_{fr2})DSB_{2D}$$

$$-N_R[k_{fb1}DSB_{1D} + k_{fb2}DSB_{2D} + k_{cross}(DSB_{1D} + DSB_{2D})^2]$$

Table 3.5. Values for the modified TLK parameters

$k_{fb1} = 1.3$	$k_{fix1} = 0.02$
$k_{fb2} = 0.13$	$k_{fix2} = 0.002$
$k_{rb1} = 0.3$	$k_{cross} = 0.0007$
$k_{rb2} = 0.03$	$N_R = 20$

10 repetitions for the MC model were performed from identical initial conditions and were compared with the deterministic numerical solution of the extended TLK, an equal time step of $dt = 0.01\text{min}$ was employed for both models and the 4th degree Runge-Kutta method was used to solve the TLK model.

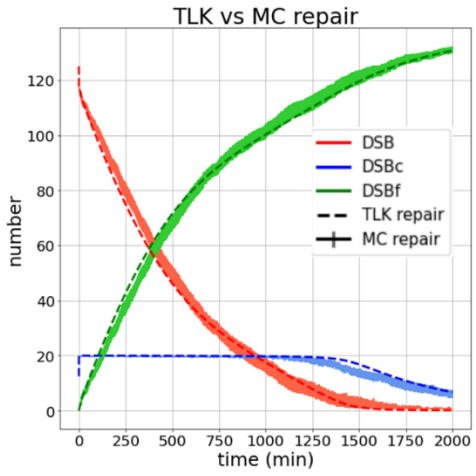

Figure 3.33. comparison between the TLK model by [Stewart R.D. (2001)] and the average of 20 repetitions of the MC DNA repair model by [Zhang X.P., et al (2009,2011)].

Another preliminary test was to ensure that the implementation of the protein network kinetics is reproduced correctly, for this we compared the individual ATM^*, $\mathrm{p53}^*$ and $\mathrm{Wip1}$ pulse profiles with the ones reported on [Zhang X.P., et al (2011)], shown below on figure 3.34.

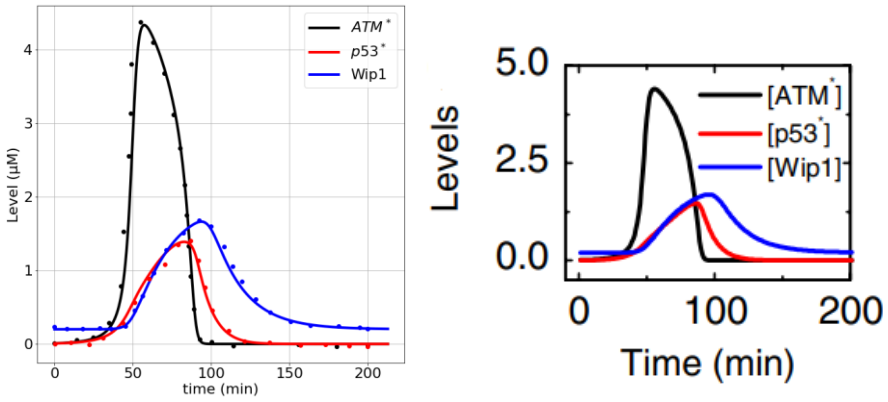

Figure 3.34. comparison between the ATM^*, $\mathrm{p53}^*$ and $\mathrm{Wip1}$ pulses (solid lines) produced by the CC3D implementation of the p53 protein network and the data reported on [Zhang X.P. et al (2011)] (dots) next to the original graph of the reported pulse profile.

The frequency and amplitude were also tested since the reported interval between pulses was around 6hr or 360 min, and the amplitude was nearly invariable for all ATM^*, $\mathrm{p53}^*$ and $\mathrm{Wip1}$ pulses [Zhang X.P., et al (2011)], results are shown below on figure 3.35.

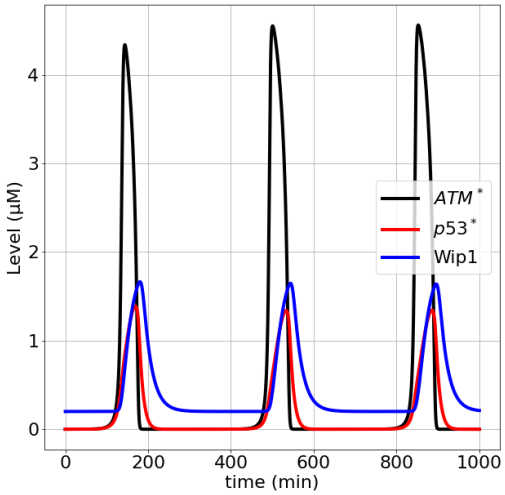

Figure 3.35. a train of ATM^*, $\mathrm{p53}^*$and $\mathrm{Wip1}$ pulses demonstrating an interval of around 360 minutes between pulses.

The work of [Zhang X.P., et al (2011)] also shows how the dynamic of the protein network changes at higher radiation doses. At 5Gy, corresponding to $N_{DSB} = 175$ initial DSBs, the number of ATM^*, $\mathrm{p53}^*$ and $\mathrm{Wip1}$ pulses increase to a maximum of 4 if the cell manages to repair on time, otherwise, the fifth pulse results in a sustained level of these proteins and then the triggering of the Casp3 apoptosis signal for cells that are beyond repair. These results, shown below in figure 3.36., are consistent with the data from the original publication.

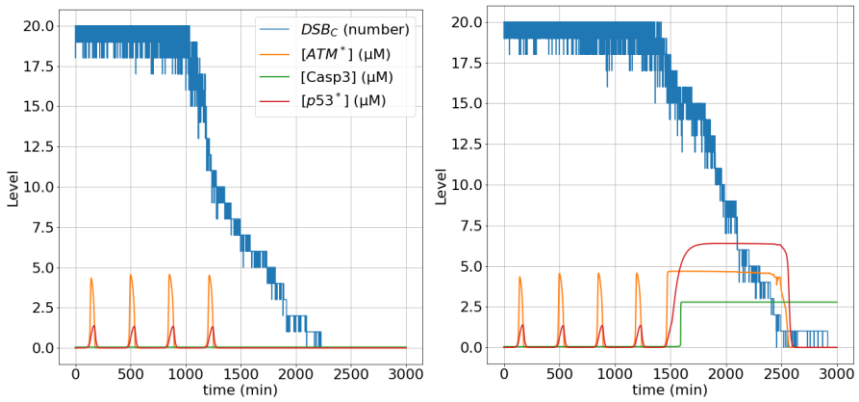

Figure 3.36. Comparison between a successfully repaired cell (left) and a cell that didn't repaired in time (right) with the same initial conditions, the time evolution of the number of $\mathrm{DSB_C}$ and the protein levels of $\mathrm{ATM^*}, \mathrm{p53^*}$ and $\mathrm{Casp3}$ are shown, and in the case of the failed DNA repair the trigger of the Casp3 apoptosis signal can be appreciated in green.

The next preliminary test was performed to check the sensibility of the p53 pulses depending on the number of initial repair proteins N_R, to explore a possible way to differentiate cells lines with specific radio sensitivities. The hypothesis was that fewer repair proteins available implied a longer repair period and consequently more cells would die. To test this assumption test were performed where the number of repair proteins was decreased in steps of 5 between the original value 20 to a minimum of 5. A simulated irradiation of 6Gy with a corresponding expected number of initial DSBs = 210 was used as an initial condition for all tests.

On figure 3.37. the comparison of the time evolution of $\mathrm{DSB_C}$ of all tested repair proteins configurations are shown. It can be observed that indeed the repair time increases as N_R decreases. However, the number of p53 pulses decreases and shifts in time, making the frequency longer until no pulses are generated at N_R = 5 and no cells die as a consequence. This means that the [Zhang X.P., et al (2009, 2011)] model was calibrated to reproduce the experimental frequency and maximum number of p53 pulses, and it is very sensitive to the changes in the number of repair proteins. Thus, this variable should remain untouched.

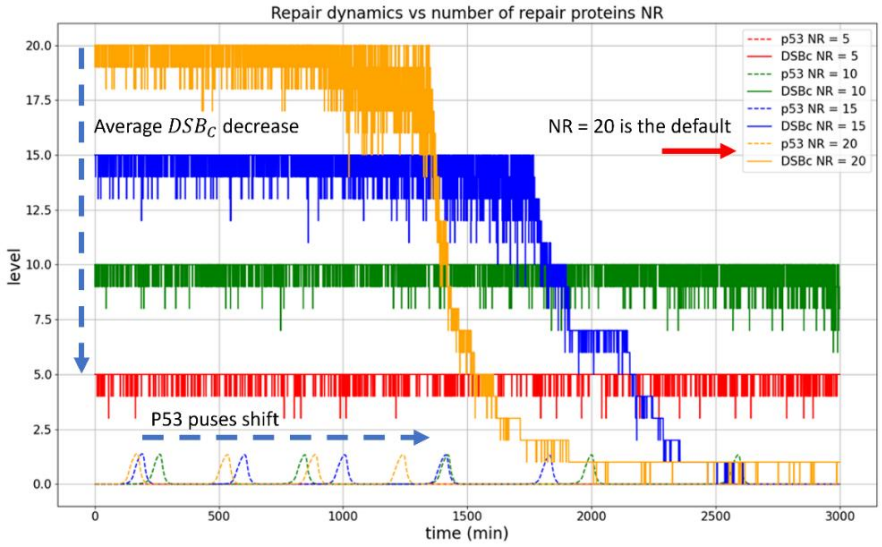

Figure 3.37 Sensibility test for the p53 pulse generation as a function of available repair proteins N_R

This result can be explained by the dependence of the ATM activation rate, in the form of a Michaelis-Menten formula shown below, with the dependance on the number of $\mathrm{DSB_C}$ framed on a square:

$$\frac{\mathrm{d[ATM^*]}}{\mathrm{dt}} = \mathrm{k_{act}} \cdot [\mathrm{ATM^*}] \boxed{\frac{\mathrm{DSB_C}}{\mathrm{DSB_C} + \mathrm{j_{DSB_C}}}} \cdot \frac{[\mathrm{ATM}]}{[\mathrm{ATM}] + \mathrm{j_{act}}}$$

Since ATM is the sensor of DNA damage and the initial signal for the rest of the protein network, with less repair proteins and fewer $\mathrm{DSB_C}$, the activation rate of ATM decreases and the other protein process, like the p53 pulses and ultimately the Casp3 apoptosis trigger, are not activated. Therefore, cells don't die at lower N_R numbers even if the repair process takes longer.

Finally, the free-floating model implemented in Tellurium was assigned to a 2-D culture of *dummy* cells with two identical *alive* types (yellow and brown) just for clarity purposes in the image, this means that both types of cells have the same adhesion and volume properties and no growth nor division processes.

The CC3D simulation consisted of simulating a uniform irradiation of 5Gy assigning the DSBs for each individual cell from a random Poisson sampling with mean value $\bar{N}_{DSB} = 175$, described at the start of this section. The $\mathrm{ATM^*}$ and $\mathrm{Casp3}$ levels were tracked automatically by an internal CC3D tool that displays the distribution of extra fields. Cells were programed to change type to *apoptotic* (blue), if the level of $\mathrm{Casp3}$ was superior to a maximum of $2.5\mu\mathrm{M}$ according to the original publication [Zhang X.P., et al (2009,2011)]. The results for the cell culture evolution can be seen below in figure 3.38.

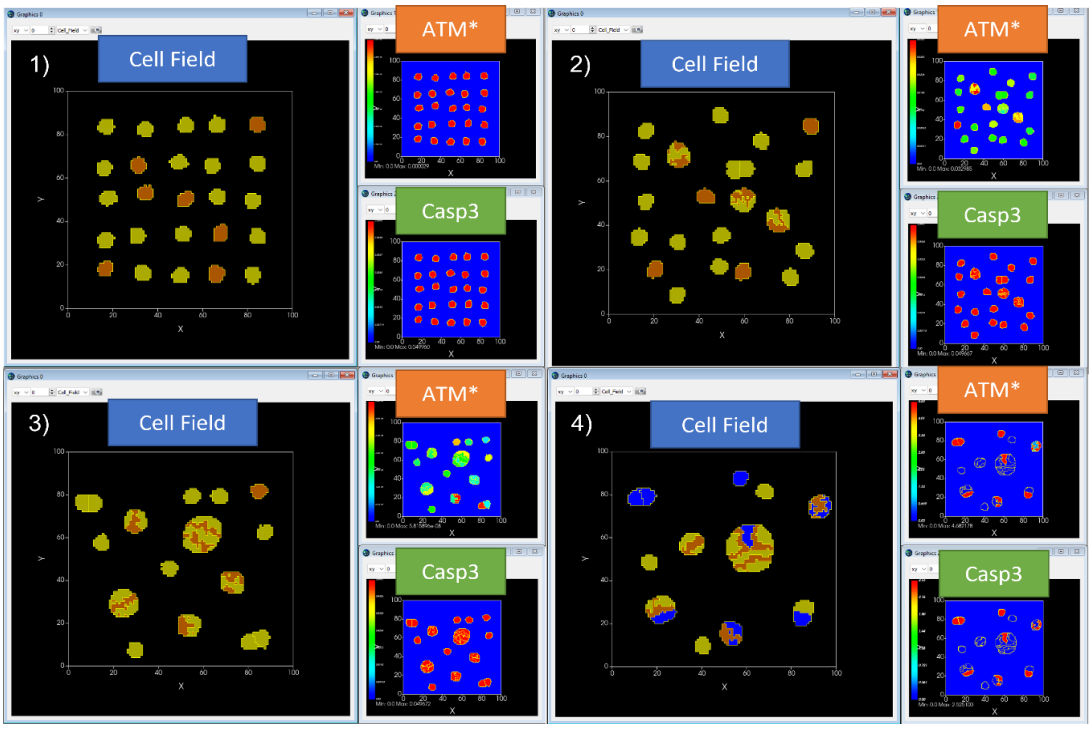

Figure 3.38. Time evolution of a dummy cell culture test with alive cells (brown and yellow) and apoptotic (blue) cells, the level of $\mathrm{ATM^*}$ and $\mathrm{Casp3}$ is tracked, and in the last image 4) it can be observed that the cell that changed to apoptotic are the ones with high levels of Casp3.

The last test was carried out in this dummy culture of 25 cells to evaluate the sensitivity of the model to a change in the value of the time step dt, since a smaller time step implies a longer simulation period and a larger computational cost, especially as the number of cells grows and the simulation jumps to 3-D space. A 6Gy irradiation corresponding to a mean value of DSBs $\bar{N}_{DSB} = 210$ was the initial condition for every run and 10 repetitions were performed for each time step value. The time step was changed from 0.1 to 4.0 simulated minutes in steps of 0.5 min, and a decrease on the total apoptotic cells was found as the time step increase, with a small *flat* region between 0.5 to 1.0 reaching just a couple of apoptotic cells at $\mathrm{dt} = 4\mathrm{min}$ in contrast to the 14 at $\mathrm{dt} = 0.1\mathrm{min}$. With these results, shown on figure 3.39., it was decided that the value of dt shouldn't surpass a value of 0.5 min, making a compromise between accuracy of the model and computational cost.

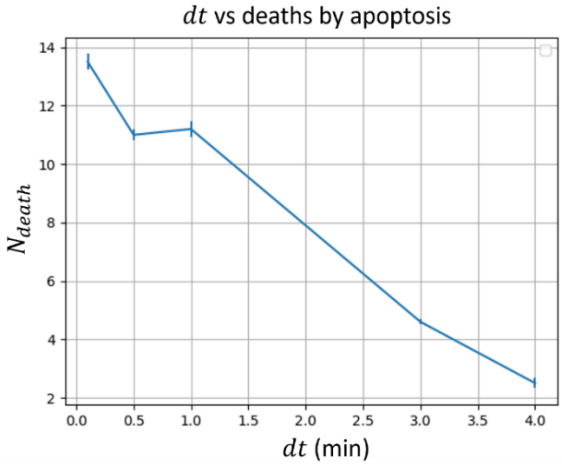

Figure 3.39. sensitivity of the p53 protein network to the value of the time step, measured by the number of alive cells that transform into apoptotic cells under identical irradiation conditions.

4. Results

4.1 Publication of the results for DNA breaks induction as a function of temperature using TOPAS

The publication titled "TOPAS-nBio simulation of temperature-dependent indirect DNA strand break yields" by José Ramos-Méndez, Omar García-García, Jorge Domínguez-Kondo, Jay A. LaVerne, Jan Schuemann, Eduardo Moreno-Barbosa and Bruce Faddegon (2022) was written and revised during the first year of PhD studies of M.Cs. Omar Rodrigo García García, containing contributions previously developed for the implementation on TOPAS-nBio of the temperature effect on the radiochemistry of water. It was sent to the journal *Physics in Medicine & Biology,* of the editorial *Institute Of Physics* (IOP), the 22th of December 2021, it was revised the 23 of May 2022 and finally published on 8th July 2022. It can be found online following the next link https://doi.org/10.1088/1361-6560/ac79f9.

IOP Publishing Phys. Med. Biol. 67 (2022) 145007 https://doi.org/10.1088/1361-6560/ac79f9

Physics in Medicine & Biology

IPEM Institute of Physics and Engineering in Medicine

PAPER

RECEIVED
22 December 2021

REVISED
23 May 2022

ACCEPTED FOR PUBLICATION
17 June 2022

PUBLISHED
8 July 2022

TOPAS-nBio simulation of temperature-dependent indirect DNA strand break yields

José Ramos-Méndez[1], Omar García-García[2], Jorge Domínguez-Kondo[1,2], Jay A LaVerne[3], Jan Schuemann[4], Eduardo Moreno-Barbosa[2] and Bruce Faddegon[1]

[1] Department of Radiation Oncology, University of California San Francisco, San Francisco, California CA-94115, United States of America
[2] Facultad de Ciencias Físico Matemáticas, Benemérita Universidad Autónoma de Puebla, Puebla, 72000, Mexico
[3] Radiation Laboratory and Department of Physics, University of Notre Dame, Notre Dame, Indiana IN-46556, United States of America
[4] Physics Division, Department of Radiation Oncology, Massachusetts General Hospital & Harvard Medical School, Boston, MA, United States of America

E-mail: Jose.RamosMendez@ucsf.edu

Keywords: TOPAS-nBio, DNA strand break, temperature, Monte Carlo, Geant4-DNA, radiation chemistry

Abstract

Current Monte Carlo simulations of DNA damage have been reported only at ambient temperature. The aim of this work is to use TOPAS-nBio to simulate the yields of DNA single-strand breaks (SSBs) and double-strand breaks (DSBs) produced in plasmids under low-LET irradiation incorporating the effect of the temperature changes in the environment. A new feature was implemented in TOPAS-nBio to incorporate reaction rates used in the simulation of the chemical stage of water radiolysis as a function of temperature. The implemented feature was verified by simulating temperature-dependent G-values of chemical species in liquid water from 20 °C to 90 °C. For radiobiology applications, temperature dependent SSB and DSB yields were calculated from 0 °C to 42 °C, the range of available published measured data. For that, supercoiled DNA plasmids dissolved in aerated solutions containing EDTA irradiated by Cobalt-60 gamma-rays were simulated. TOPAS-nBio well reproduced published temperature-dependent G-values in liquid water and the yields of SSB and DSB for the temperature range considered. For strand break simulations, the model shows that the yield of SSB and DSB increased linearly with the temperature at a rate of $(2.94 \pm 0.17) \times 10^{-10}$ Gy^{-1} Da^{-1} °C^{-1} ($R^2 = 0.99$) and $(0.13 \pm 0.01) \times 10^{-10}$ Gy^{-1} Da^{-1} °C^{-1} ($R^2 = 0.99$), respectively. The extended capability of TOPAS-nBio is a complementary tool to simulate realistic conditions for a large range of environmental temperatures, allowing refined investigations of the biological effects of radiation.

4.2 Results for TOPAS-kinetoscope coupling

The result for the scape yields of pure water; water with biomolecules and the model for the cellular environment, water, biomolecules and antioxidants; recovered at the end of the heterogeneous chemical stage at 100µs after the start of irradiation, using TOPAS simulation of a single pulse of conventional and FLASH irradiation are presented next. 400 repetitions for each configuration were performed and the average value is presented, TOPAS can report the number of each radiolitic species produced, the energy deposited in MeV and the G-value in Molecules per 100eV. Knowing that the volume used in these simulations was a cube with sides of 3µm, with a volume $V = 21\mu\text{m}^3$, we can convert the number of molecules N into molar concentration $[M]$ with the formula:

$$[M] = N/N_A V$$

Where $N_A = 6.022 \times 10^{23}\text{mol}^{-1}$ is the Avogadro number, and the volume V needs to be expressed on liters ($1\text{m}^3 = 1000l$). We can also consider the water density of $\rho_{water} = 1kg/l$ and the

equivalence from $1\text{J} = 6.242 \times 10^{18}\text{eV}$ to convert the G-values reported in TOPAS into units of molar concentration per dose delivered following the transformation $1molecule/100eV = 0.1036\ \mu\text{M/Gy}$ as described in [Wardman P. (2020)]. Then this scape yield in $\mu\text{M/Gy}$ can be used to calculate the production of molecules per unit time considering the dose rate (Gy/s) of each irradiation mode.

4.2.1 Results for the escape yields and generation rates using TOPAS

4.2.1.1 Pure Water

For pure water we can observe that the result of the scape yields is different for each mode of irradiation, not just because the FLASH pulse delivers a dose of 5Gy in contrast to the 0.028Gy by a CONV pulse, meaning that the higher number of molecules produced by the FLASH irradiation is also divided by a larger dose when calculating the G-values. This is instead explained by the intertrack effect: The density of ionizations increases with a higher dose rate, then the excited and ionized water molecules are in closer proximity and their radiolytic products have a higher probability of reaction. A concrete example is the yield of the hydrogen peroxide $G_{FLASH}(\text{H}_2\text{O}_2) = 1.0 \times 10^{-7}\ \text{M/Gy}$ for FLASH irradiation is about 20% higher that the yield on conventional dose rate $G_{CONV}(\text{H}_2\text{O}_2) = 8.1 \times 10^{-8}\text{M/Gy}$, in contrast the FLASH yield of hydroxyl $G_{FLASH}(\text{OH}) = 1.6 \times 10^{-7}\text{M/Gy}$ is around 40% smaller than the conventional yield of $G_{CONV}(\text{OH}) = 2.7 \times 10^{-7}\text{M/Gy}$, this can be explained by the fact that the main reaction on pure water that contributes to the production of hydrogen peroxide is the bimolecular reaction between hydroxyl radicals $\text{OH} + \text{OH} \rightarrow \text{H}_2\text{O}_2$, and in the high ionization density environment of FLASH irradiation this reaction occurs more often than conventional irradiation. The complete results for both types of irradiations are shown next on tables 4.1 and 4.2.

Table 4.1. Pure water CONV irradiation ($dD/dt = 2.86 \times 10^4\text{Gy/s}$)

Specie	N_{mol}	concentration (M)	Yield (M/Gy)	Generation rate (M/s)
H_2O_2	37.5	2.3×10^{-9}	8.1×10^{-8}	2.3×10^{-3}
H_3O^+	144.9	8.9×10^{-9}	3.1×10^{-7}	8.9×10^{-3}
HO_2	12.1	7.4×10^{-10}	2.6×10^{-8}	7.5×10^{-4}
H	2.8	1.7×10^{-10}	6.1×10^{-9}	1.7×10^{-4}
H_2	21.8	1.3×10^{-9}	4.7×10^{-8}	1.3×10^{-3}
O_2^-	110.7	6.8×10^{-9}	2.4×10^{-7}	6.8×10^{-3}
O_2	0.7	4.2×10^{-11}	1.5×10^{-9}	4.3×10^{-5}
OH^-	24.3	1.5×10^{-9}	5.2×10^{-8}	1.5×10^{-3}
OH	123.8	7.6×10^{-9}	2.7×10^{-7}	7.6×10^{-3}
e_{aq}^-	12.9	7.9×10^{-10}	2.8×10^{-8}	7.9×10^{-4}

Table 4.2. Pure water Flash irradiation ($dD/dt = 2.78 \times 10^6 \mathrm{Gy/s}$)

Specie	N_{mol}	Concentration (M)	Yield (M/Gy)	Generation rate (M/s)
$\mathrm{H_2O_2}$	8310.9	5.1×10^{-7}	1.0×10^{-7}	0.28
$\mathrm{H_3O^+}$	11779.5	7.2×10^{-7}	1.4×10^{-7}	0.40
$\mathrm{HO_2}$	4821.2	3.0×10^{-7}	5.9×10^{-8}	0.16
H	350.6	2.1×10^{-8}	4.3×10^{-9}	0.01
$\mathrm{H_2}$	5089.3	3.1×10^{-7}	6.2×10^{-8}	0.17
$\mathrm{O_2^-}$	10313.5	6.3×10^{-7}	1.3×10^{-7}	0.35
$\mathrm{O_2}$	1157.4	7.1×10^{-8}	1.4×10^{-8}	0.04
$\mathrm{OH^-}$	2726.1	1.7×10^{-7}	3.4×10^{-8}	0.09
OH	12998.5	8.0×10^{-7}	1.6×10^{-7}	0.44
$\mathrm{e_{aq}^-}$	587.3	3.6×10^{-8}	7.2×10^{-9}	0.02

4.2.1.2 Water with Biomolecules

In the presence of biomolecules all hydroxyl, hydrogen atoms and aqueous electrons are consumed, this is explained because the biomolecules act as scavengers of these radicals. On the other hand, the differences between the yields of radiolytic species are less drastic than in pure water: The G-value for hydrogen peroxide for FLASH irradiation $G_{FLASH}(\mathrm{H_2O_2}) = 4.9 \times 10^{-8}\mathrm{M/Gy}$ is just around 4% higher than the conventional irradiation $G_{CONV}(\mathrm{H_2O_2}) = 4.7 \times 10^{-8}\mathrm{M/Gy}$. The most dramatic increase is the case of hydroxide radicals where the yield for FLASH irradiation $G_{FLASH}(\mathrm{OH^-}) = 3.5 \times 10^{-10}\mathrm{M/Gy}$ is about one order of magnitude smaller than the yield for conventional irradiation $G_{CONV}(\mathrm{OH^-}) = 5.2 \times 10^{-9}\mathrm{M/Gy}$. In the case of biomolecules radicals the difference between the two types of irradiation were in average 10% superior in FLASH compared to CONV irradiation. For example, the DNA hydrogen adduct in FLASH $G_{FLASH}(\mathrm{DNA_H^\bullet}) = 4.2 \times 10^{-9}\mathrm{M/Gy}$ is about 13% higher than the conventional irradiation $G_{CONV}(\mathrm{DNA_H^\bullet}) = 3.7 \times 10^{-9} M/Gy$. The complete results for both irradiation configurations are shown on tables 4.3 and 4.4.

Table 4.3. CONV irradiation with biomolecules

Specie	N_{mol}	concentration (M)	Yield (M/Gy)	Generation rate (M/s)
$\mathrm{H_2O_2}$	21.7	1.3×10^{-9}	4.7×10^{-8}	1.3×10^{-3}
$\mathrm{H_3O^+}$	162.5	1.0×10^{-8}	3.5×10^{-7}	1.0×10^{-2}
$\mathrm{HO_2}$	0.8	5.1×10^{-11}	1.8×10^{-9}	5.2×10^{-5}
$\mathrm{H_2}$	14.3	8.8×10^{-10}	3.1×10^{-8}	8.8×10^{-4}
$\mathrm{O_2^-}$	1.2	7.4×10^{-11}	2.6×10^{-9}	7.4×10^{-5}

O_2	0.01	6.8×10^{-13}	2.4×10^{-11}	6.8×10^{-7}
OH^-	2.4	1.5×10^{-10}	5.2×10^{-9}	1.5×10^{-4}
$DNA^{\bullet}_{H}$	1.7	1.1×10^{-10}	3.7×10^{-9}	1.1×10^{-4}
$DNA^{\bullet}_{OH}$	5.6	3.5×10^{-10}	1.2×10^{-8}	3.5×10^{-4}
$DNA^{\bullet}_{e^-_{aq}}$	4.5	2.8×10^{-10}	9.7×10^{-9}	2.8×10^{-4}
$RNA^{\bullet}$	61.4	3.8×10^{-9}	1.3×10^{-7}	3.8×10^{-3}
$Nc^{\bullet}$	161.2	1.0×10^{-10}	3.5×10^{-7}	9.9×10^{-3}
$Am^{\bullet}$	26.9	1.7×10^{-9}	5.8×10^{-8}	1.7×10^{-3}
$Pr^{\bullet}$	128.6	7.9×10^{-9}	2.8×10^{-7}	7.9×10^{-3}

Table 4.4. FLASH irradiation with biomolecules

Specie	N_{mol}	concentration (M)	Yield (M/Gy)	Generation rate (M/s)
H_2O_2	3975.0	2.4×10^{-7}	4.9×10^{-8}	0.14
H_3O^+	25251.2	1.6×10^{-6}	3.1×10^{-7}	0.86
HO_2	208.4	1.3×10^{-8}	2.6×10^{-9}	7.1×10^{-3}
H_2	2716.6	1.7×10^{-7}	3.3×10^{-8}	9.3×10^{-2}
O_2^-	160.0	9.8×10^{-9}	2.0×10^{-9}	5.5×10^{-3}
O_2	1.0	6.2×10^{-11}	1.2×10^{-11}	3.4×10^{-5}
OH^-	28.2	1.7×10^{-9}	3.5×10^{-10}	9.6×10^{-4}
$DNA^{\bullet}_{H}$	339.8	2.1×10^{-8}	4.8×10^{-9}	1.2×10^{-2}
$DNA^{\bullet}_{OH}$	916.8	5.6×10^{-8}	1.1×10^{-8}	3.1×10^{-2}
$DNA^{\bullet}_{e^-_{aq}}$	770.4	4.7×10^{-8}	9.5×10^{-9}	2.6×10^{-2}
$RNA^{\bullet}$	10278.2	6.3×10^{-7}	1.3×10^{-7}	0.35
$Nc^{\bullet}$	27884.4	1.7×10^{-6}	3.4×10^{-7}	0.95
$Am^{\bullet}$	4442.4	2.7×10^{-7}	5.5×10^{-8}	0.15
$Pr^{\bullet}$	21485.4	1.3×10^{-6}	2.6×10^{-7}	0.73

4.2.1.3 Cellular environment model

The preventive action of antioxidants was modeled including them in the water-biomolecule mixture to complete the cell environment model. In comparison, there was a reduction of all biomolecule's radical yields of 3% on average for CONV and 2% for FLASH irradiations with the exception of a 7% jump on DNA-Hydrogen adducts for the conventional pulse, in the presence of antioxidants. These low values for radical reduction indicate that the antioxidants play a role of repair more than prevention and taking as an example the experimental results for protein radicals from [Nauser T. et al (2005)], where around 98% of the OH produced by radiolysis reacted with 1mM of lysozymes and an insignificant fraction with the 50 µM GSH present in the solution, which indicate that our results for the antioxidants damage prevention is consistent with the experimental data. The complete results for the irradiation of the cell environment model with one FLASH and CONV pulse are shown next on tables 4.5. and 4.6.

Table 4.5. CONV irradiation with biomolecules and antioxidants

Specie	N_{mol}	Concentration (M)	Yield (M/Gy)	Generation rate (M/s)
H_2O_2	21.0	1.3×10^{-9}	4.5×10^{-8}	1.3×10^{-3}
H_3O^+	162.8	1.0×10^{-8}	3.5×10^{-7}	1.0×10^{-2}
HO_2	0.8	4.9×10^{-11}	1.7×10^{-9}	4.9×10^{-5}
H_2	14.3	8.8×10^{-10}	3.1×10^{-8}	8.8×10^{-4}
O_2^-	1.2	7.4×10^{-11}	2.6×10^{-9}	7.4×10^{-5}
O_2	0.0	----------	----------	----------
OH^-	2.8	1.7×10^{-10}	6.0×10^{-9}	1.7×10^{-4}
$DNA^{\bullet}_{H}$	1.9	1.2×10^{-10}	4.1×10^{-9}	1.2×10^{-4}
$DNA^{\bullet}_{OH}$	5.3	3.3×10^{-10}	1.1×10^{-8}	3.3×10^{-4}
$DNA^{\bullet}_{e^-_{aq}}$	4.3	2.6×10^{-10}	9.2×10^{-9}	2.6×10^{-4}
$RNA^{\bullet}$	60.0	3.7×10^{-9}	1.3×10^{-7}	3.7×10^{-3}
$Nc^{\bullet}$	160.2	9.9×10^{-9}	3.4×10^{-7}	9.9×10^{-3}
$Am^{\bullet}$	26.1	1.6×10^{-9}	5.6×10^{-8}	1.6×10^{-3}
$Pr^{\bullet}$	125.1	7.7×10^{-9}	2.7×10^{-7}	7.7×10^{-3}
$GS^{\bullet}$	8.1	5.0×10^{-10}	1.7×10^{-8}	5.0×10^{-4}
Asc^-	0.24	1.5×10^{-11}	5.2×10^{-10}	1.5×10^{-5}

Table 4.6. FLASH irradiation with biomolecules and antioxidants

Specie	N_{mol}	Concentration (M)	Yield (M/Gy)	Generation rate (M/s)
H_2O_2	3960.6	2.4×10^{-7}	4.9×10^{-8}	0.13
H_3O^+	25298.2	1.6×10^{-6}	3.1×10^{-7}	0.86
HO_2	224.0	1.4×10^{-8}	2.8×10^{-9}	7.7×10^{-3}
H_2	2727.2	1.7×10^{-7}	3.4×10^{-8}	9.3×10^{-2}
O_2^-	153.2	9.4×10^{-9}	1.9×10^{-9}	5.2×10^{-3}
O_2	0.8	4.9×10^{-11}	9.8×10^{-12}	2.7×10^{-5}
OH^-	25.0	1.5×10^{-9}	3.1×10^{-10}	8.5×10^{-4}
$DNA^{\bullet}_{H}$	335.8	2.1×10^{-8}	4.1×10^{-9}	1.1×10^{-2}
$DNA^{\bullet}_{OH}$	885.4	5.4×10^{-8}	1.1×10^{-8}	3.0×10^{-2}
$DNA^{\bullet}_{e^-_{aq}}$	761.8	4.7×10^{-8}	9.4×10^{-9}	2.6×10^{-2}
$RNA^{\bullet}$	10096.6	6.2×10^{-7}	$1.2 \times 10\text{^} - 7$	0.34
$Nc^{\bullet}$	27650.6	1.7×10^{-6}	$3.4 \times 10\text{^} - 7$	0.95
$Am^{\bullet}$	4261.6	2.6×10^{-7}	5.2×10^{-8}	0.14
$Pr^{\bullet}$	20891.4	1.3×10^{-6}	2.6×10^{-7}	0.71
$GS^{\bullet}$	1297.0	8.0×10^{-8}	1.6×10^{-8}	4.4×10^{-2}
Asc^-	40.2	2.5×10^{-9}	4.9×10^{-10}	1.4×10^{-3}

Using these results, we can give an estimate of the number of DNA breaks, assuming that just the OH y H reactions with DNA can produce strand breaks, the total number of DNA reactions R_{DNA} is normalized by the deposited dose, 5Gy for FLASH and 0.028 for CONV irradiations, and by the simulated volume of $27\mu m^3$. Then we extrapolate this total number of reactions to the volume of a cell nucleus, represented by a sphere with a $5\mu m$ radius and a volume of around $524\mu m^3$ [Lammerding J. (2011)], then apply a damage efficiency of 20% to obtain the number of strand breaks, which is close to the measured number of single strand breaks per gray on huma cells of $\sim 1000\ SSB/Gy$ [Hall E. J. & Giaccia A. J. (2012)]. Results are presented next, on table 4.7.

Table 4.7. DNA radical yields and SSBs calculation

Irradiation	$R_{DNA}(OH + H)$	$R_{DNA}(Gy^{-1})$	$R_{DNA}Gy^{-1}(\mu m^{-3})$	Nucleus R_{DNA}	(20%) SSB/Gy
Without antioxidants					
CONV	7.3	260.7	9.6	5059.8	1011.9
FLASH	1221.2	244.4	9.1	4736.4	947.3

With antioxidants					
CONV	7.2	255.9	9.5	4961.8	992.4
FLASH	1220.8	244.1	9.0	4737.3	947.4

These overall results for the escape yields and generation rates for 1 pulse of CONV and FLASH irradiation were also used to feed chemical kinetic models on Kinetiscope to simulate the long-term time evolution for each system.

4.2.2 Cell environment model irradiation with Kinetiscope

The results from the TOPAS escape yields for the entire cell environment model, containing water, biomolecules and antioxidants; were used to feed Kinetiscope and simulate both FLASH and CONV irradiations using the user defined external stimulus to model the pulsated source and the overall irradiation time. For FLASH, this was done by multiplying the production rate (M/s) on table 4.6. of the las section by the pulse with (1.8μs) with a separation of 0.01s between pulses and considering that each pulse delivers 5Gy, a total delivered dose of 5 to 20Gy was simulated with 1 to 4 pulses respectively.

On the other hand, it was impossible to model the CONV irradiation with short pulses since the value of the production (M/s) rate per conventional pulse multiplied by the pulse duration (1.0μs) was too small for Kinetiscope, meaning that the individual propensities $a(\mathrm{R}^{\bullet}) = \Delta t \cdot d[\mathrm{R}^{\bullet}]/dt$ associated with the probability of generating molecules where too small and therefore improbable to occur, causing that no radicals were produced. Instead, we used the escape yields (M/Gy) on table 4.5. in the last section and multiply them by the overall dose rate with a reported value of 0.28Gy/s (10Gy/35s) [Montay-Gruel et al. (2019)] and then simulate a constant irradiation period accordingly to the desired dose: For 5Gy it was required 17.5s and for 20 Gy a corresponding 70s irradiation time was necessary. We performed tests for two different initial conditions of oxygen, 5 and 50μM for hypoxic and normal oxygenation respectively, on every irradiation configuration to compare the effect of the competence between the antioxidants and O_2. A scheme of this implementation is shown below in figure 4.1.

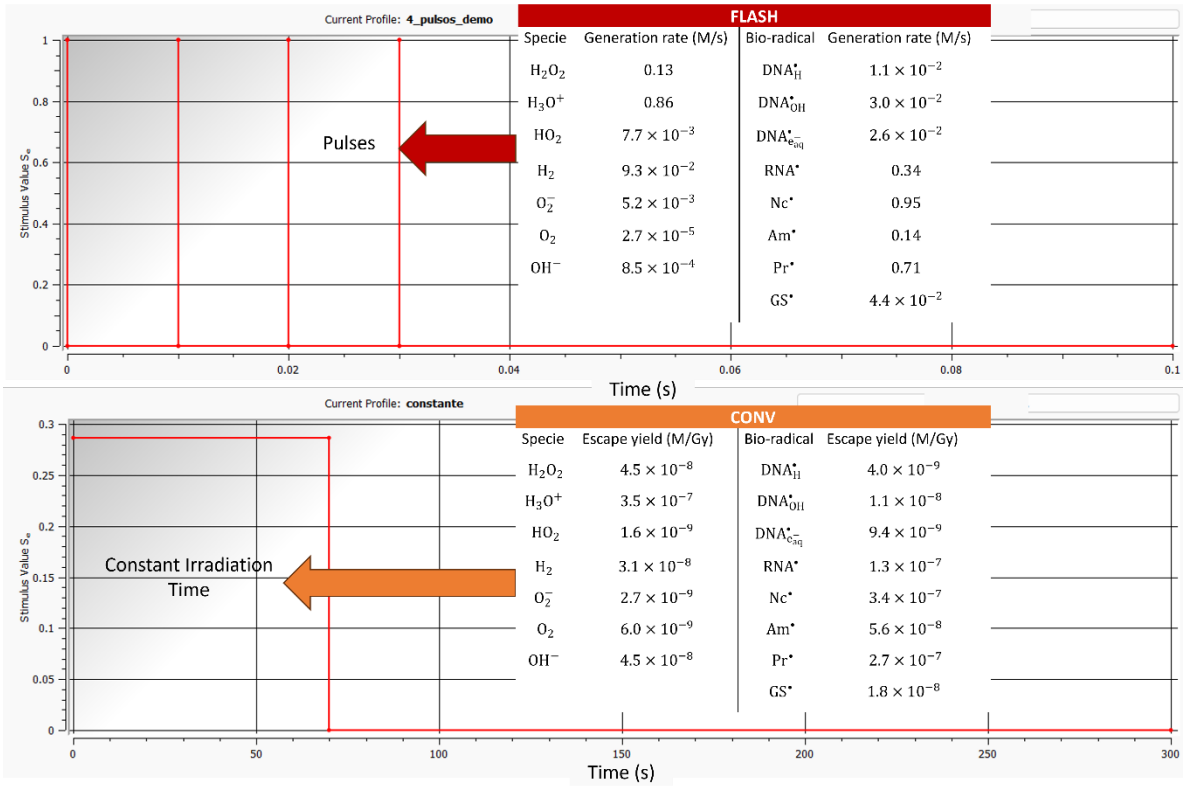

Figure 4.1. Scheme of the Kinetiscope configuration for FLASH, using pulses and the generation rate calculated, and CONV irradiation, using a constant irradiation with the escape yields simulated with TOPAS.

4.2.2.1 Single FLASH pulse

For a single pulse of FLASH irradiation, that represent a deposited dose of 5Gy, we can observe that the chemical repair by antioxidants is more effective at the lower concentration of oxygen (5μM), shown on the gap between the repaired (R) biological radicals and the hydroperoxyl radicals (ROOH), furthermore it doesn't even occur in the case of DNA. All the biological radicals ($R^{\bullet}$) and peroxyl radicals ($ROO^{\bullet}$) are transient states that end with a concentration of 0M because they are repaired or *patched* by an antioxidant. On table 4.8 a list of the final concentration of several biomolecules and radicals is presented for both oxygen initial concentration, with their absolute differences. The chemical repair of antioxidants is also shown represented by the percentage of repaired lesions (R) form the total radicals produced ($R + ROOH$), followed by the time evolution of several biomolecules and its radicals presented on figure 4.2.

Table 4.8. final concentration of biomolecules for 1FLASH pulse

Conc. (μM)	DNAOOH	DNA	PrOOH	Pr	NucOOH	Nuc	AmOOH	Am
$[O_2] = 5\mu M$	0.1	0.013	0.51	0.78	0.47	1.2	0.0	0.23
Repair (%)	11.5%		60.4%		71.8%		100%	
$[O_2] = 50\mu M$	0.076	0.0	1.1	0.1	0.14	0.33	2.6×10^{-3}	0.22
Repair (%)	0.0%		8%		70.2%		98.0%	
Difference (μM)	0.024	0.013	−0.59	0.61	0.33	0.87	-2.6×10^{-3}	0.01

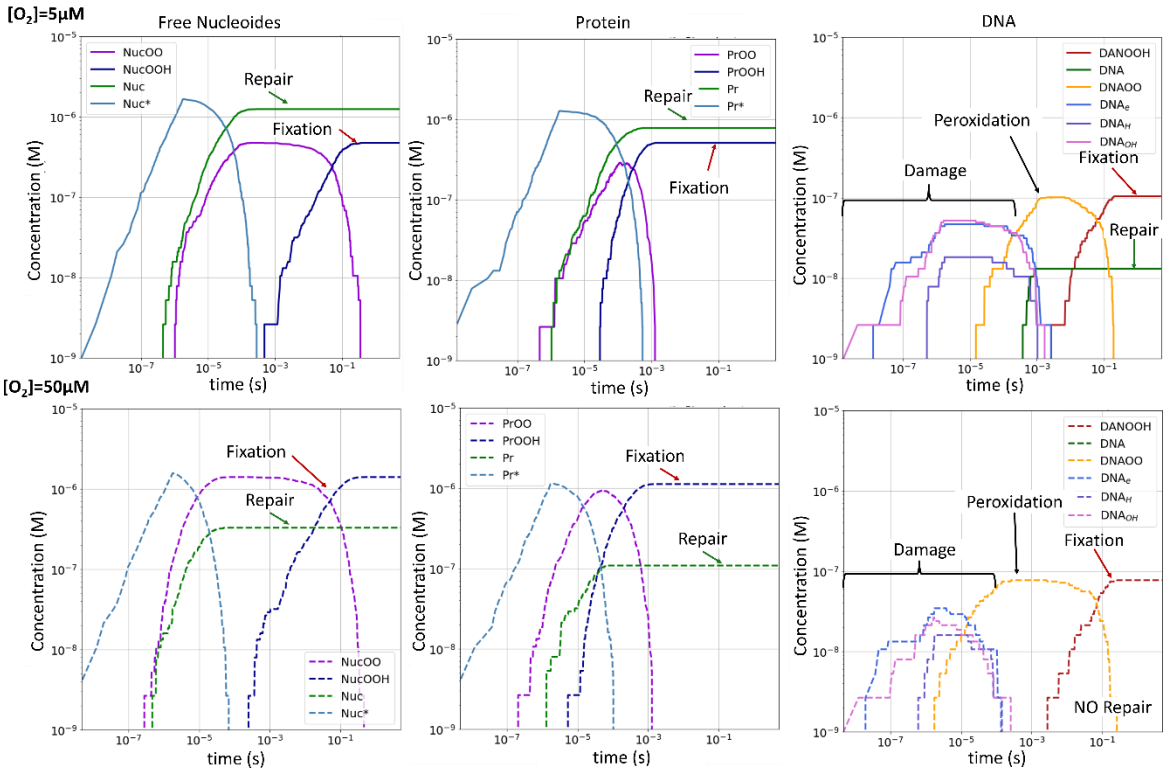

Figure 4.2. Time evolution for the free nucleotides, proteins and DNA biomolecules and their radicals for an Oxygen initial concentration of 5 or 50μM under 1FLASH pulse of 5Gy.

For antioxidants, there was a small decrease in in both GSH, with an initial concentration of $[\mathrm{GSH}]_0 = 2500\mu\mathrm{M}$, and AscH^-, with an initial concentration of $[\mathrm{AscH}^-]_0 = 100\mu\mathrm{M}$; of about $0.1\mu\mathrm{M}$ and $2\mu\mathrm{M}$, representing a depletion of the 0.004% and 2%, respectively for both oxygen initial concentrations. In the case of oxygen, the final concentration for both initial conditions were 3.3μM from 5.0μM, representing a 51.5 % depletion, and 46μM from 50μM, an 8.7% depletion of O_2. On the other hand, the concentration of some stable products like Asc^-, DHA or GSSG didn't show a large difference from both initial oxygen concentration, table 4.9. shows those results followed by a graph with the time evolution of the antioxidants, their products and the oxygen concentrations on figure 4.3.

Table 4.9. final concentration of antioxidants and O_2 for 1FLASH pulse

Conc. (μM)	GSH	O_2	AscH^-	Asc^-	DHA	GSSG
$O_2 = 5\mu\mathrm{M}$	2499.9	3.3	98	0.093	1.9	0.005
Depletion	0.004%	34.0%	2%			
$O_2 = 50\mu\mathrm{M}$	2499.9	46	98	0.095	1.9	0.002
Depletion	0.004%	8.7%	2%	----------	----------	----------

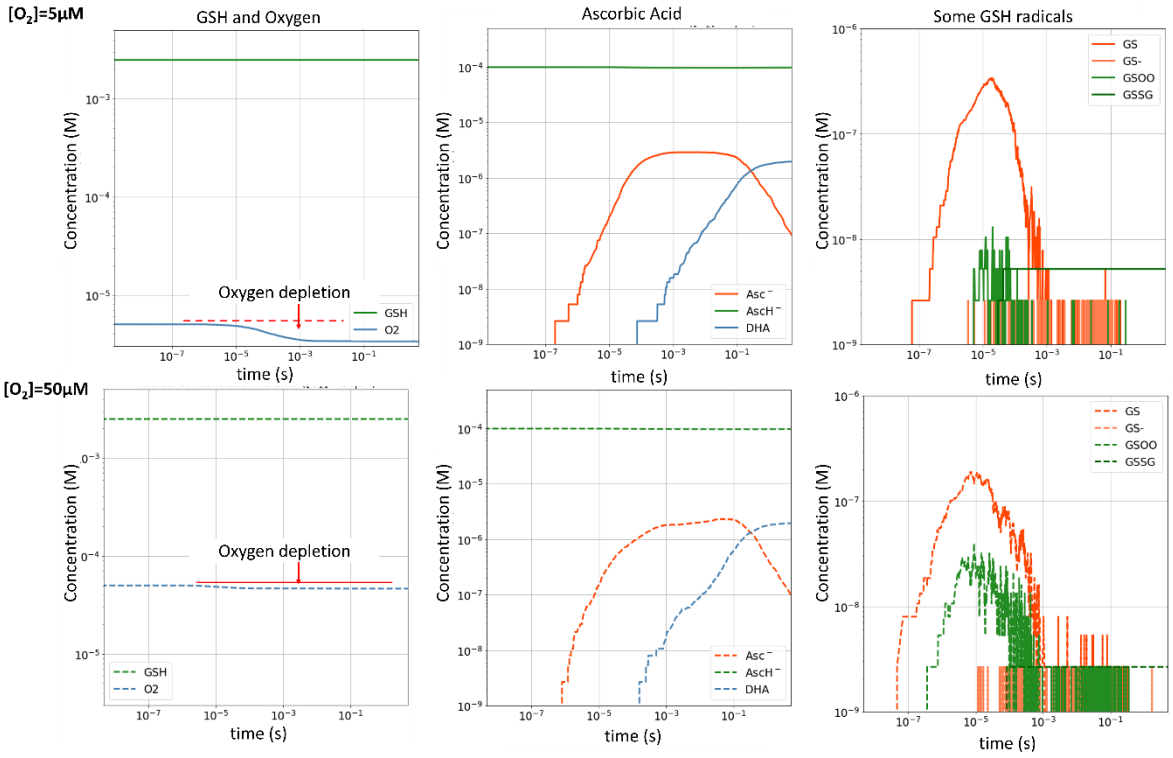

Figure 4.3. time evolution for O_2, GSH, $AscH^-$, Asc^-, DHA, GS, GS^-, GSOO and GSSG for an Oxygen initial concentration of 5 or 50µM under 1FLASH pulse of 5Gy.

4.2.2.2 Full FLASH irradiation.

The effects described for 1 Flash pulse are magnified by each subsequent pulse. In general, the number of stable repaired (R) or hydroperoxyl (ROOH) biological radicals increase linearly with dose, and the number of repaired radicals was greater at the lower oxygen concentration. For instance, antioxidants repair about 29.4% of the total DNA lesions at 20Gy on low oxygen concentrations (5µM) while only 1% are repaired for the same dose at 50µM O_2 concentration. The chemical repair is so overwhelmed by the competence with oxygen at this concentration that the same absolute quantity of DNA lesions (0.002µM) is repaired at 10 and 15Gy representing a 6.3% and 3.2% of the total DNA lesions induced respectively while 0% lesions are repaired at 5Gy.

Each pulse is delivered 0.01s after the previous one starting at 0s, this means that for the maximum of 4pulses, corresponding to 20G, the irradiation time never surpasses 0.03s and the species quickly stabilize saturating to their final concentrations around 1 second after the start of irradiation. The results for the final concentration of hydroperoxyl and repaired DNA, protein and nucleotide radicals, alongside the slope value for their lineal fittings, are shown below on table 4.10. for both initial oxygen conditions (5µM and 50µM) and all delivered doses from 5-20Gy, followed by the time evolution of these quantities shown in figures 4.4 to 4.6.

Table 4.10. final concentration for biological radicals under FLASH irradiation

Radical	DANOOH(µM)		DNA(µM)		PrOOH(µM)		Pr(µM)		NucOOH(µM)		NUC(µM)	
D/[O2]	5µM	50µM	5µM	50µM	5µM	50µM	5µM	50µM	5µM	50µM	5µM	50µM
5Gy	0.10	0.07	0.01	0.000	0.51	1.12	0.78	0.11	0.47	1.41	1.25	0.33
10Gy	0.23	0.20	0.03	0.002	0.90	2.22	1.64	0.29	0.86	2.77	2.47	0.73

15Gy	0.31	0.34	0.06	0.002	1.20	3.37	2.64	0.44	1.10	4.03	3.93	1.08
20Gy	0.36	0.43	0.15	0.005	1.32	4.49	3.73	0.64	1.20	5.29	5.47	1.49
Slope (µM/Gy)	0.017	0.024	0.009	0.0003	0.05	0.22	0.19	0.03	0.04	0.25	0.28	0.07

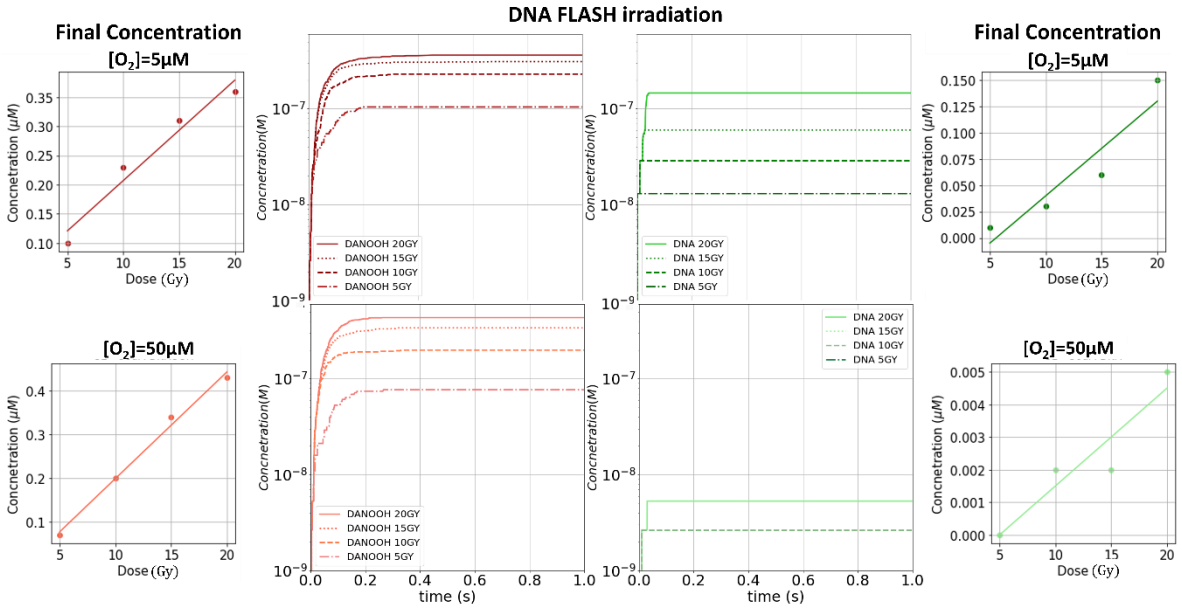

Figure 4.4. Time evolution of the concentration of DNA hydroperoxyl and repaired radicals (DNAOOH, DNA), and the lineal fitting for their final concentration, for 5 or 50µM initial concentration of oxygen under1-4 FLASH pulses irradiation corresponding to 5-20GY.

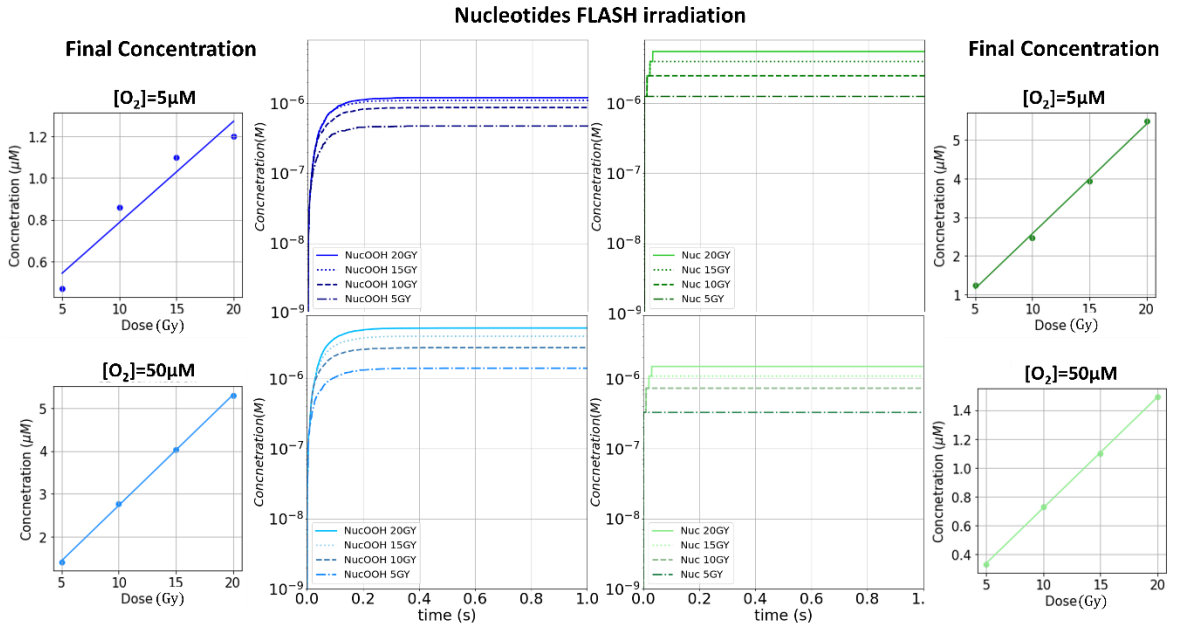

Figure 4.5. Time evolution of the concentration of Free Nucleotide hydroperoxyl and repaired radicals (NucOOH, Nuc), and the lineal fitting for their final concentration, for 5 or 50µM initial concentration of oxygen under1-4 FLASH pulses irradiation corresponding to 5-20GY.

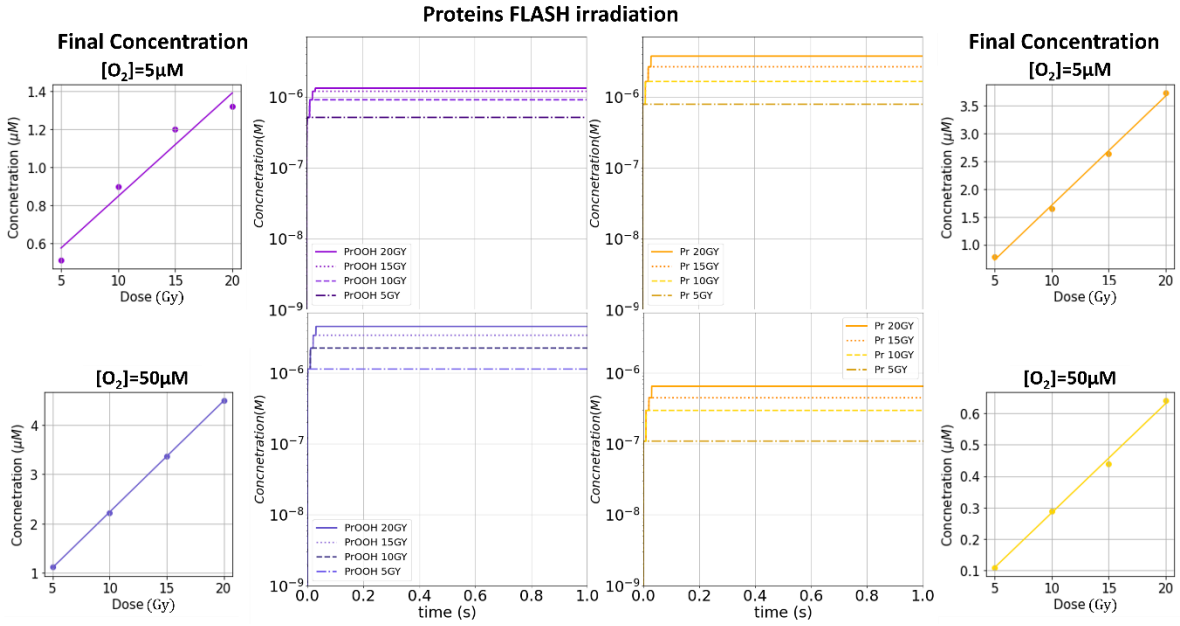

Figure 4.6. time evolution of the concentration of Free Protein hydroperoxyl and repaired radicals (PrOOH, Pr), and the lineal fitting for their final concentration, for 5 or 50µM initial concentration of oxygen under1-4 FLASH pulses irradiation corresponding to 5-20GY.

In the case of antioxidants and oxygen, the general observed behavior of the system as the number of pulses increased and deposited dose with them, was a decrease of the final concentration of these substances. This reduction also followed a linear relationship with dose. The depletion of oxygen went from 5µM to 0.18µM at 20Gy, representing a decrease of around 96.4% of the initial concentration and in the case of 50µM it decreased to 36.5µM with 4 FLASH pulses representing a 27% oxygen depletion. The case of GSH was less dramatic, the largest depletion is of 1µM for 20Gy on the higher oxygen concentration condition, representing a maximum of 0.04% reduction on the GSH concentration. It is notable that the Ascorbic acid had almost the same depletion on both oxygen conditions falling from 100 to 92.0µM, representing an 8% reduction, at the maximum deposited dose of 20Gy. This information is presented next, on table 4.11. followed by the time evolution and final concentration of the oxygen and antioxidants for all considered doses and both initial O_2 conditions on figure 4.7.

Table 4.11. Oxygen and antioxidant depletion by FLASH irradiation

Molecule	O2 (µM)		AscH- (µM)		GSH (µM)	
D/[O2]	5µM	50µM	5µM	50µM	5µM	50µM
5Gy	3.35	46.5	97.9	97.9	2499.9	2499.6
10Gy	1.91	43.1	95.9	95.9	2499.8	2499.4
15Gy	0.90	39.8	94.0	93.9	2499.8	2499.2
20Gy	0.18	36.5	92.0	91.9	2499.6	2499.0
Slopes(µM/Gy)	-0.21	-0.66	-0.39	-0.40	-0.018	-0.040

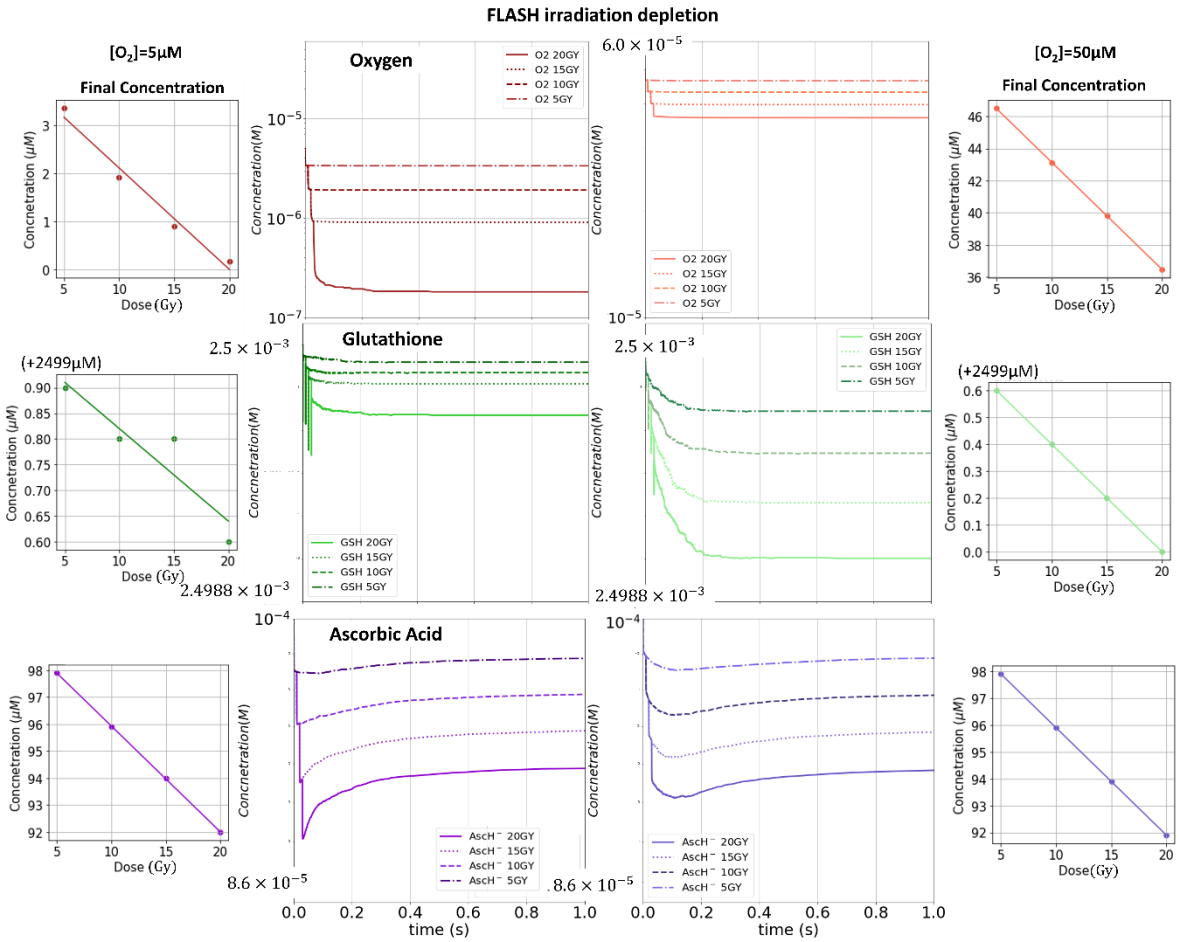

Figure 4.7. Time evolution of the concentration of O_2,GSH and $AscH^-$, showing the lineal fitting for their final concentration, for 5 or 50μM initial concentration of oxygen under 1-4 FLASH pulses irradiation corresponding to 5-20GY.

4.2.2.3 Conventional irradiation.

For conventional irradiation a constant delivery of radicals was simulated by multiplying the escape yield simulated (M/Gy) on TOPAS by the overall CONV dose rate (0.286Gy/s) during a period corresponding to the desired dose: 17.5s for 5Gy, 35s for 10Gy ,52.5s for 15Gy and 70s for 20Gy. In this case all simulations were stopped at 100s, steadily accumulating biological radicals until the irradiation stopped. At this point all configurations quickly stabilized within a few seconds. The final concentrations of radicals increased linearly with deposited dose and the number of repaired radicals (R) was superior on the 5μM oxygen initial concentration than the 50μM case. A difference between the simulated FLASH irradiation is that DNA repair occurred in every case with a 7.7 and 28.3% of the total DNA lesions being repaired for 5 and 20Gy doses respectively on a 5μM initial oxygen concentration condition while for 50μM O_2 it was 5.8 and 2.1% of the total DNS lesions induced for the same doses. The results for the final concentrations of several biological radicals for both oxygen concentrations conditions are presented next on table 4.12. alongside the slope (μM/Gy) of their lineal dependance with dose. Next, the time evolution of these biological radicals and linear fits for all conventional irradiation configurations on figures 4.8. to 4.10.

Table 12. final concentration for biological radicals under CONV irradiation

Radical	DANOOH(μM)		DNA(μM)		PrOOH(μM)		Pr(μM)		NucOOH(μM)		NUC(μM)	
D/[O2]	5μM	50μM	5μM	50μM	5μM	50μM	5μM	50μM	5μM	50μM	5μM	50μM
5Gy	0.12	0.08	0.01	0.005	0.53	1.25	0.90	0.17	0.50	1.46	1.30	0.34
10Gy	0.24	0.21	0.03	0.008	0.91	2.46	1.80	0.32	0.81	2.69	2.75	0.71
15Gy	0.31	0.34	0.08	0.008	1.13	3.68	2.90	0.51	1.02	4.03	4.29	1.12
20Gy	0.37	0.46	0.16	0.01	1.26	4.87	4.20	0.68	1.08	5.35	5.94	1.54
Slope (μM/Gy)	0.016	0.025	0.01	0.0003	0.04	0.24	0.22	0.03	0.06	0.26	0.31	0.08

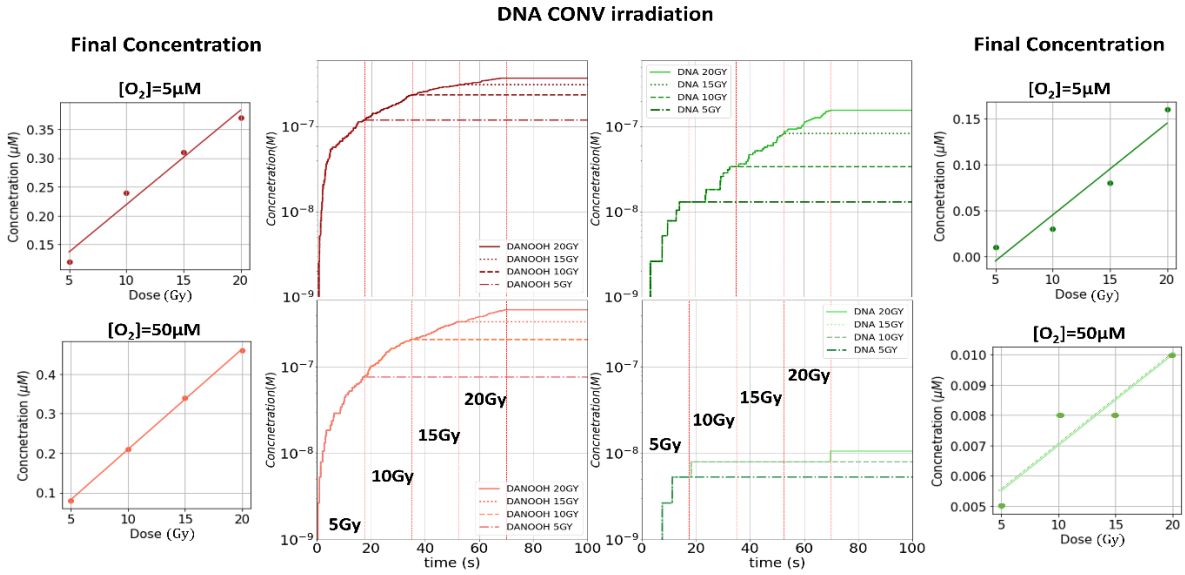

Figure 4.8. time evolution of the concentration of DNA hydroperoxyl and repaired radicals (DNAOOH, DNA), and the lineal fitting for their final concentration, for 5 or 50μM initial concentration of oxygen under 5-20 Gy CONV irradiation, their corresponding times are marked by vertical dotted red lines.

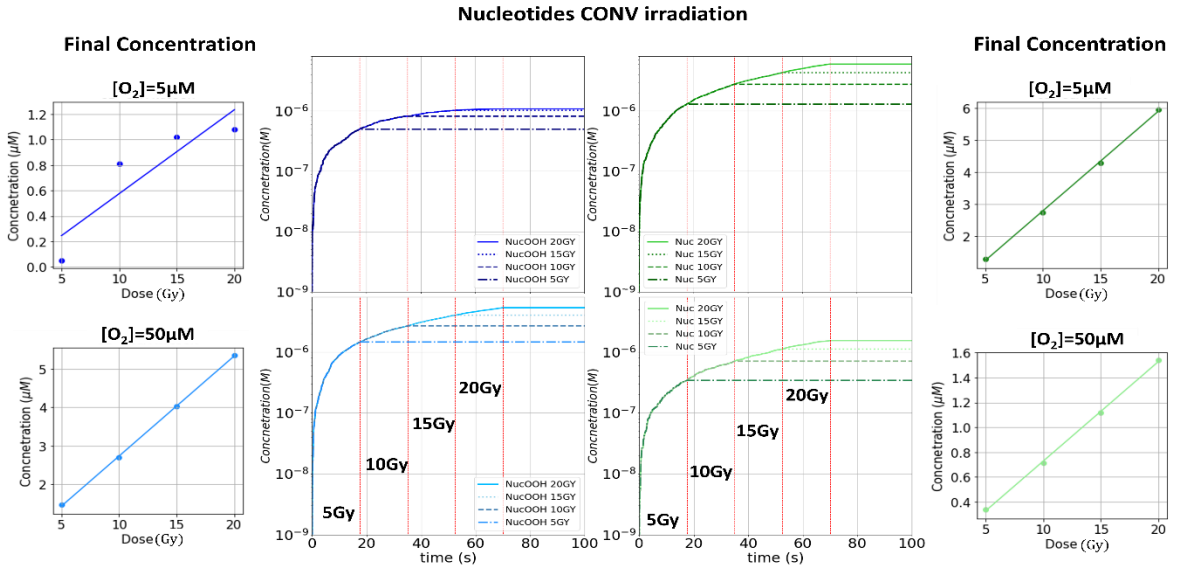

Figure 4.9. time evolution of the concentration of free nucleotides hydroperoxyl and repaired radicals (NucOOH, Nuc), and the lineal fitting for their final concentration, for 5 or 50μM initial concentration of oxygen under 5-20 Gy CONV irradiation, their corresponding times are marked by vertical dotted red lines.

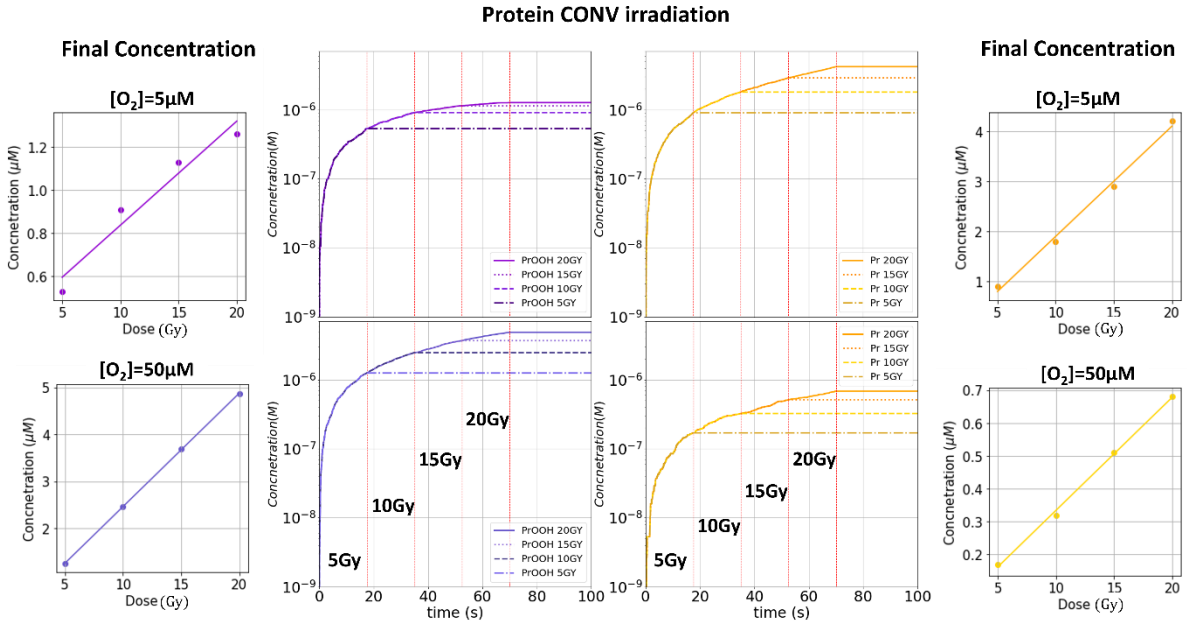

Figure 4.10. time evolution of the concentration of protein hydroperoxyl and repaired radicals (PrOOH, Pr), and the lineal fitting for their final concentration, for 5 or 50µM initial concentration of oxygen under 5-20 Gy CONV irradiation, their corresponding times are marked by vertical dotted red lines.

For the oxygen and antioxidants final concentration, results show a linear depletion as dose increase. For Oxygen, the concentration reduction was from 5 to 3.21µM at 5 Gy, representing a -35.8% depletion and to 0.18µM at 20Gy, representing a loss of 96.4% of oxygen. For the higher oxygen concentration, it went from 50 to 46.3µM at 5Gy irradiation, representing a 7.4% reduction, and to 36.0µM for 20Gy, representing a 28.0% oxygen depletion. The ascorbic acid followed a similar trend as the one described for FLASH irradiation where the depletion was practically the same both for 5 and 50µM of initial oxygen concentration: It experienced a reduction from 100 to 97.85µM for 5Gy and to 91.55µM for 20Gy, representing 2.2% and 8.5% depletion respectively. For GSH the reduction of the final concentration was very small: The maximum depletion of GSH was for 20Gy and $[O_2]$ = 50µM where it reduced from 2500µM to 2499µM, a 0.04% depletion. This information is provided next on table 4.13 followed by the time evolution of oxygen and antioxidants for all CONV irradiation configurations on figure 4.11.

Table 13. Oxygen and antioxidant depletion by CONV irradiation

Molecule	O2 (µM)		AscH- (µM)		GSH (µM)	
D/[O2]	5µM	50µM	5µM	50µM	5µM	50µM
5Gy	3.21	46.3	97.8	97.9	2499.9	2499.7
10Gy	1.87	43.0	95.6	95.8	2499.8	2499.5
15Gy	0.78	39.4	93.7	93.7	2499.7	2499.2
20Gy	0.18	36.0	91.5	91.6	2499.6	2499.0
Slopes(µM/Gy)	-0.20	-0.69	-0.42	-0.42	-0.02	-0.05

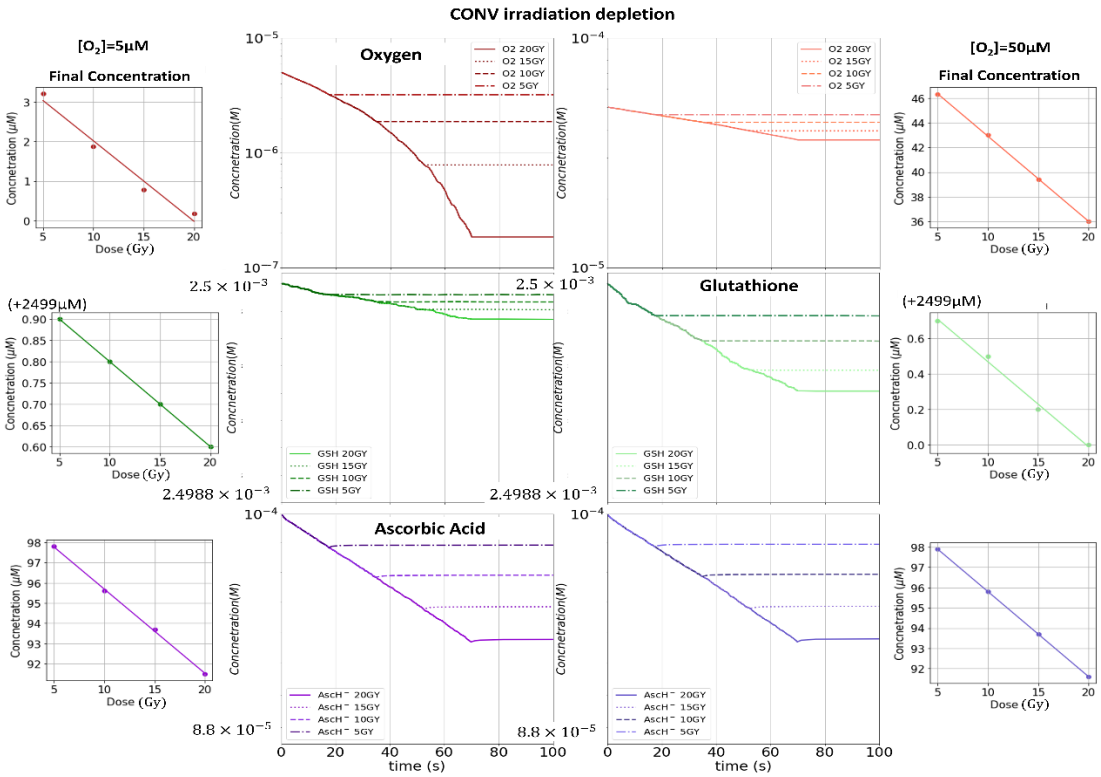

Figure 4.11. Time evolution of the concentration of O_2,GSH and $AscH^-$, showing the lineal fitting for their final concentration, for 5 or 50μM initial concentration of oxygen under 1-4 FLASH pulses irradiation corresponding to 5-20GY.

4.2.2.4 Differences between FLASH and Conv irradiations

A comparison between the final concentrations of FLASH and conventional irradiations was performed in terms of the percentage of their difference following the formula:

$$\text{dif}\ (\%) = \frac{[R]_{FLASH} - [R]_{CONV}}{[R]_{CONV}} \times 100\%$$

We used the actual difference instead of its absolute value to indicate the cases where conventional irradiation produced a larger final concentration of biological radicals than FLASH with a negative percentage. In the majority of cases CONV produced more hydroperoxyl radicals but also repaired more of the initially damaged biomolecules. The greatest differences were observed on the repair of DNA, where more than double the lesions were repaired under CONV irradiation. This is consistent with the lack of DNA repair on FLASH irradiation for 5Gy observed in the simulations. For the rest of biomolecules, the average difference was about 7.6% for 5μM of oxygen and 8.3% for 50μM with the maximum difference being the repaired proteins at 5Gy with a value of 42.9%. All this information is presented next, on table 4.14.

Table 4.14. Comparison between FLASH and CONV irradiations final concentrations

Radical	DANOOH(%)		DNA(%)		PrOOH(%)		Pr(%)		NucOOH(%)		Nuc(%)	
D/[O2]	5μM	50μM	5μM	50μM	5μM	50μM	5μM	50μM	5μM	50μM	5μM	50μM
5Gy	-16.6	-12.5	0.0	------	-3.8	-10.4	-13.3	-35.3	-6.0	-3.4	-3.8	-2.9
10Gy	-4.1	-4.8	0.0	-75.0	-1.1	-9.8	-8.9	-9.4	6.2	3.0	-10.2	2.8
15Gy	0.0	0.0	-25.0	-75.0	6.2	-8.4	-9.0	-13.7	7.8	0.0	-8.4	-1.8
20Gy	-2.7	-6.5	-6.5	-50.0	4.8	-7.8	-11.2	-5.9	11.1	-1.1	-7.9	-3.2

4.3 Implementation of the SSA in TOPAS

The python prototype of the Gillespie algorithm in Python served as a basis for its translation into a dedicated C++ file on the category of *processes* inside the extension library TOPAS-nBio (version 3.7.p1). Several *scorer* files, whose function is to register quantities of interest on the associated geometrical components, like energy, fluence, deposited dose and chemical yields among others; were modified to allow our SSA implementation to be recognized and compatible with those scorers. Specifically, the file "TsScoreWithIRTInTOPAS", a scorer that uses the IRT method for the time evolution of the system during the heterogeneous chemistry stage [Ramos-Méndez J., et al 2020] was extended to stop the operation of the IRT method and feed its results into the SSA at a predefined time, with a default value of $1\mu s$, and continue the simulation to a final time. Both of these parameters are tunable by the user. A screenshot showing the correct coupling and initialization of the Gillespie algorithm in TOPAS is shown next on figure 4.12:

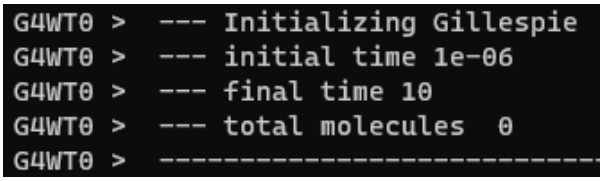

Figure 4.12. Terminal screenshot showing the correct initialization of the Gillespie algorithm on a TOPAS application $1\mu s$ after the beginning of the irradiation.

The next test was to compare the time evolution of the chemical species between the TOPAS-nBio implementation with Kinetoscope as a reference code. It was necessary to modify the scorer "TsScoreWithIRTCummulativeInTOPAS" since it tracks the deposited energy on the simulated volume at the same time that the IRT method is working. This allows the simulation of accumulated dose on pulsated radiation sources, like the high dose-rate sources used on FLASH irradiation. This test was performed on a $4\mu m$ side length cube made of water with a prescribed dose of 0.1Gy using an isotropic electron source with an initial energy of 1MeV, the same 10 main reaction scheme used on the test of the first Python prototype were also used here.

To make a fair comparison, the escape yield at the end of the heterogeneous chemical stage at $1\mu s$ after irradiation was fed into Kinetiscope as the initial condition for this reference code. The results for this test are shown below on figure 4.12 where the mark for the $1\mu s$ transition between the IRT method and the SSA is shown with a dashed vertical green line.

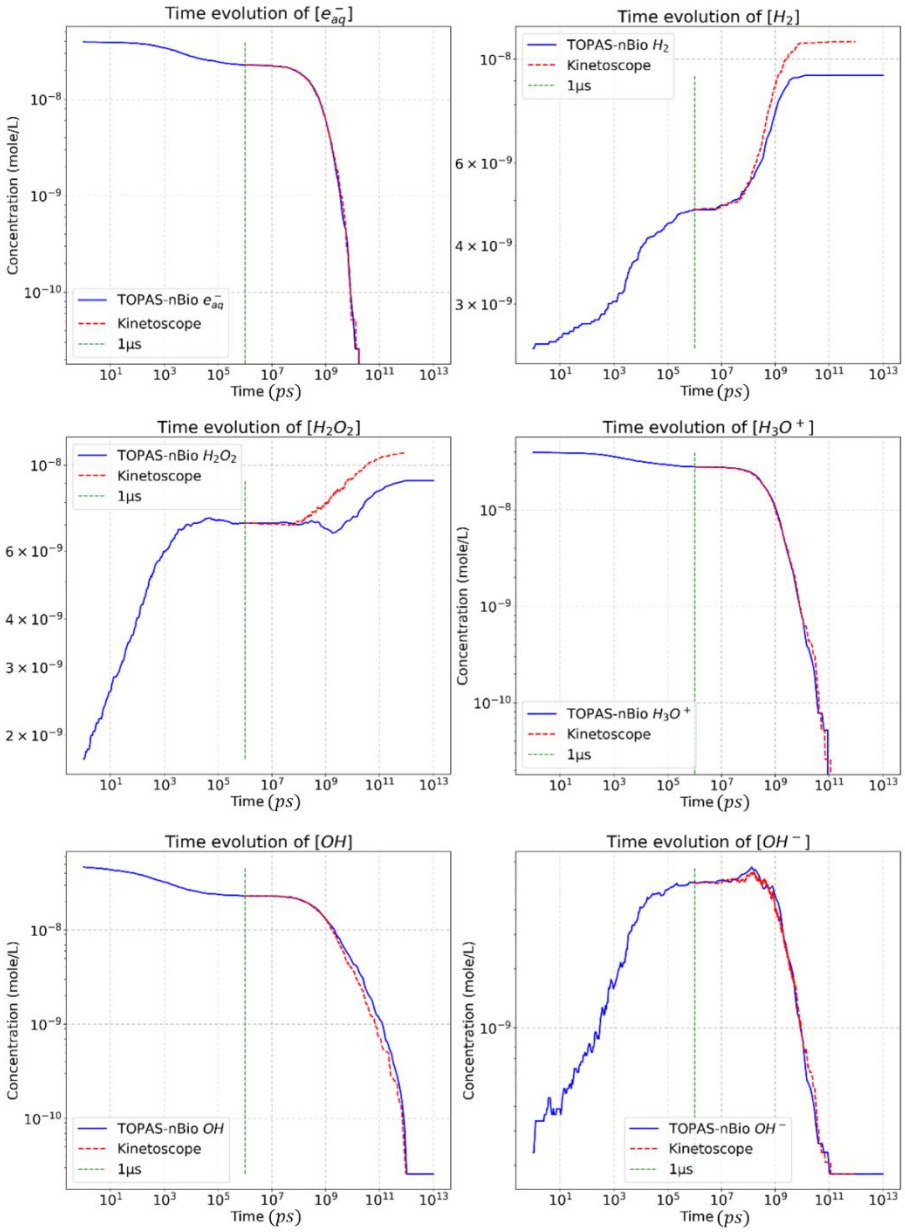

Figure 4.12. comparison between the time evolution for the concentration of some radiolytic chemical species of the IRT method coupled to the SSA implemented in TOPAS-nBio (solid blue line) against the results from Kinetiscope (dashed red line) after the escape yields at the end of heterogeneous chemical stage at 1µs (marked with a green dashed line) are feed as the initial condition for the simulation.

These results for the SSA implementation on TOPAS-nBio follow the same behaviors of the first Python prototype and almost all chemical species evolutions are identical to those simulated on Kinetiscope with the notable exceptions of H_2O_2 and H_2 for the same reasons described on section 3.2.1 *Prototype for the SSA implementation*. Other difficulties of this implementation arise from transforming the units of molar concentration inherited from Geant4 necessary for the SSA operation. Some reaction rates of the chemical scheme also need a statistical factor for the coupling of molecular spins [Plante I. & Devroye L. (2017)], that internally modify its value and need to be

compensated for the correct functioning of the Gillespie algorithm. These and many other issues were solved in the publication by [D-Kondo J.N., et al (2023)], where the contribution of this research work was the development of the SSA prototypes. The results for the correct functioning of the Gillespie algorithm implemented on TOPAS-nBio compared to Kinetoscope are shown below on figure 4.13 where the water chemical reaction scheme described on section 3.2 *TOPAS-Kinetiskope Coupling* was used and the transition time between the IRT method and the SSA was also changed from 1to 100μs.

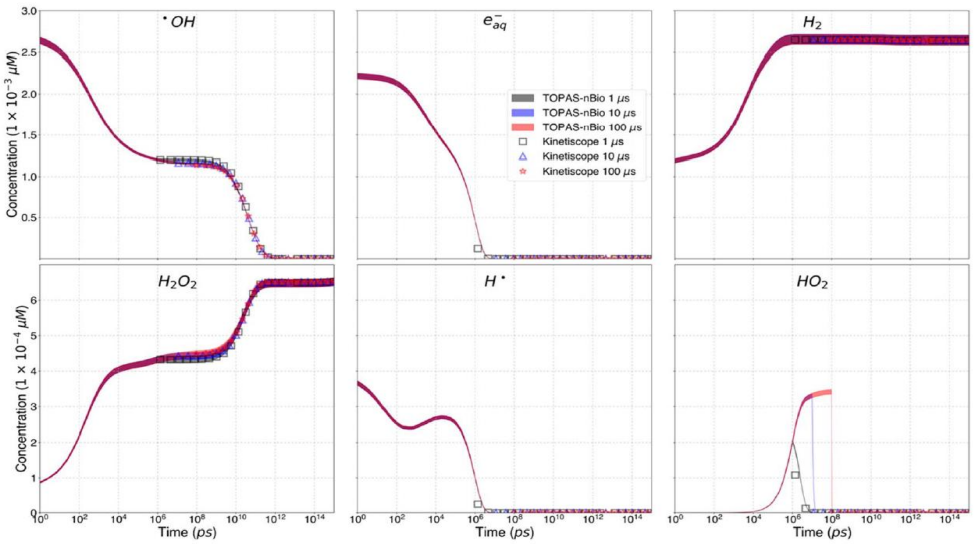

Figure 4.13. Time evolution of the concentration of OH,$\mathrm{e^-_{aq}}$. $\mathrm{H_2}$, $\mathrm{H_2O_2}$,H and $\mathrm{HO_2}$ free radicals produced by water radiolysis simulated using TOPAS-nBio and compared with the results of Kinetiscope for different time transition times (1, 10 and 100 μs) for the IRT method in the heterogeneous chemical stage to the SSA in the homogeneous chemical stage. Image taken from [D-Kondo J.N., et al (2023)].

This implementation of the SSA was ultimately used to calculate the escape values and the long-term evolution, until 1000s after the irradiation started, of the water radiolysis chemical species for a train of pulses for both conventional and FLASH irradiation, shown next on figure 4.14. demonstrating the newly implemented capacity of TOPAS to both simulate the heterogeneous and homogeneous chemical stages for this process.

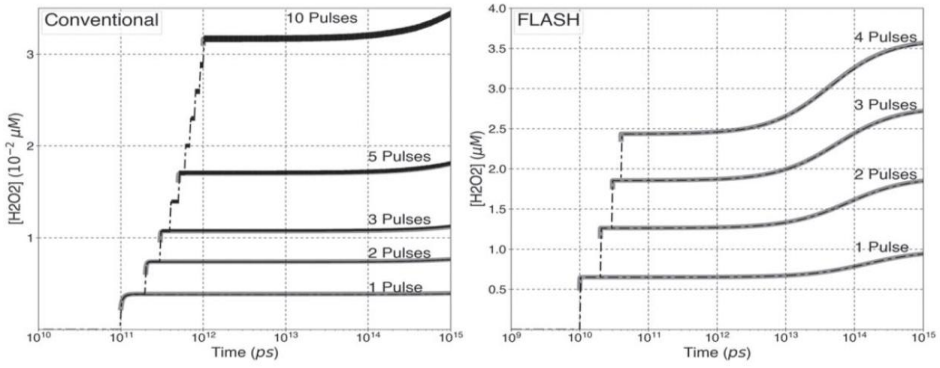

Figure 4.14. Time evolution of hydrogen peroxide concentration ($[\mathrm{H_2O_2}]$) for a train of CONV and FLASH pulses using TOPAS (dashed lines) and comparing it against Kinetiscope (solid lines) for the homogeneous stage. Image taken from [D-Kondo J.N., et al (2023)].

4.3.1 Publication of these Results

A paper titled “An integrated Monte Carlo track-structure simulation framework for modeling inter and intra-track effects on homogenous chemistry” by J. Naoki D-Kondo, Omar R. Garcia-Garcia, Jay A. LaVerne, Bruce Faddegon, Jan Schuemann, Wook-Geun Shin and José Ramos-Méndez (2023) was send to the journal *Physics in Medicine & Biology* of the editorial *Institute Of Physics* (IOP), on 20th December 2022, it was revised on 19th April 2023, accepted for publication the 18th May 2023 and published the 9th of June 2023, containing the contributions of this research work to the publication. It is available online on the following link https://doi.org/10.1088/1361-6560/acd6d0.

IOP Publishing Phys. Med. Biol. 68 (2023) 125008 https://doi.org/10.1088/1361-6560/acd6d0

Physics in Medicine & Biology

IPEM Institute of Physics and Engineering in Medicine

CrossMark

PAPER

RECEIVED
20 December 2022

REVISED
19 April 2023

ACCEPTED FOR PUBLICATION
18 May 2023

PUBLISHED
9 June 2023

An integrated Monte Carlo track-structure simulation framework for modeling inter and intra-track effects on homogenous chemistry

J Naoki D-Kondo[1], Omar R Garcia-Garcia[2], Jay A LaVerne[3], Bruce Faddegon[1], Jan Schuemann[4], Wook-Geun Shin[4] and José Ramos-Méndez[1,*]

[1] Department of Radiation Oncology, University of California San Francisco, San Francisco, CA 94115, United States of America
[2] Faculty of Mathematics and Physics Sciences, Benemérita Universidad Autónoma de Puebla, Puebla 72000, Mexico
[3] Radiation Laboratory and Department of Physics, University of Notre Dame, Notre Dame, IN 46556, United States of America
[4] Department of Radiation Oncology, Massachusetts General Hospital and Harvard Medical School, Boston, MA, United States of America
[*] Author to whom any correspondence should be addressed.

E-mail: Jose.RamosMendez@ucsf.edu

Keywords: Monte Carlo track-structure, water radiolysis, FLASH, TOPAS-nBio, Geant4-DNA

Abstract

Objective. The TOPAS-nBio Monte Carlo track structure simulation code, a wrapper of Geant4-DNA, was extended for its use in pulsed and longtime homogeneous chemistry simulations using the Gillespie algorithm. *Approach*. Three different tests were used to assess the reliability of the implementation and its ability to accurately reproduce published experimental results: (1) a simple model with a known analytical solution, (2) the temporal evolution of chemical yields during the homogeneous chemistry stage, and (3) radiolysis simulations conducted in pure water with dissolved oxygen at concentrations ranging from 10 μM to 1 mM with [H_2O_2] yields calculated for 100 MeV protons at conventional and FLASH dose rates of 0.286 Gy s^{-1} and 500 Gy s^{-1}, respectively. Simulated chemical yield results were compared closely with data calculated using the Kinetiscope software which also employs the Gillespie algorithm. *Main results*. Validation results in the third test agreed with experimental data of similar dose rates and oxygen concentrations within one standard deviation, with a maximum of 1% difference for both conventional and FLASH dose rates. In conclusion, the new implementation of TOPAS-nBio for the homogeneous long time chemistry simulation was capable of recreating the chemical evolution of the reactive intermediates that follow water radiolysis. *Significance*. Thus, TOPAS-nBio provides a reliable all-in-one chemistry simulation of the physical, physico-chemical, non-homogeneous, and homogeneous chemistry and could be of use for the study of FLASH dose rate effects on radiation chemistry.

4.4 Development of the simulation framework TOPAS-Tissue.

The coupling of TOPAS with CompuCell3D resulted in the development of a new computational framework for the multiscale simulation of the irradiation and biological response on a cell population level, baptized as TOPAS-Tissue. The first prototype called TOPAS-*Utils*, written in Python

within a CC3D application was used as the basis for the TOPAS-CC3D communication. Then it was extended and transferred to dedicated Python files where it is now a *class* designed to be imported as any other standard python library, such as NumPy or matplotlib, in the header of the file. The *object-oriented* nature of the Python programing language allowed that the class Utils could be imported in a CC3D application and associated to an object inside a *Steppable,* in the *Initialization* function, and this way inherit all the CC3D inner functions so the Utils class can use them and at the same time all TOPAS-Tissue's functions are available for the CompuCell3D application through this object that contains the Utils class.

```
class Utils:

    def __init__(self, CC3DSteppable,output_file = "output" ,output_directory = "./", seed = 1):
```

Figure 4.15. main class Utils, used to initialize TOPAS-Tissue

Besides the communication functions, other computational tools were developed to record the equivalence between metric to CC3D units: From length to number of voxels and time to MCS, in order to facilitate the translation of geometrical information from CC3D to TOPAS and back, while synchronizing all biological processes simulated on CompuCell3D.

The specific objectives of the TOPAS-Tissue development and validation were to reproduce the experimental configuration and survival curve for a prostate cancer cell culture assay under X-ray irradiation from [Wakisaka Y., et al. (2023)], as follows:

- Construct a geometrical model of PC-3 prostate cancer cells on CC3D based on the reported characteristics of this type of cell and let it evolve during a certain pre-irradiation period, from an initial number of seeded cells to a culture of a predefined confluency (cells per unit area).
- Develop a radiation source model from an experimental 6MV X-ray energy spectrum and irradiate the cell culture model in a 0-8Gy dose range.
- Extend the DNA repair model coupled to the p53 protein network proposed by [Zhang X.P., et al. (2009,2011)] to consider the accumulation of lethal lesions as an inevitable side effect of the DSBs repair and another independent condition for cellular death in the same way as the original TLK model [Sewart R.D 2001] and evaluated in parallel to the Casp3 apoptosis trigger.
- Finally, validate TOPAS-Tissue against the experimental survival curve reported on [Wakisaka Y., et al. (2023)] in terms of the alive cell colonies 2.7 simulated days after the irradiation.

On the next sections an in-depth review of the development and validation for the TOPAS-Tissue platform will be presented.

4.4.1 Main functions of TOPAS-Tissue

The main functions of the TOPAS-Tissue tool and their description are listed below:

- *cellField2Topas.*
  This is the central function that communicates TOPAS with CC3D. It writes automatically a TOPAS parameter file from the global information of the CC3D lattice, including the number of voxels in each direction and the equivalence of 1 voxel to metric length units. This lattice

information is used to construct a *virtual phantom* associated to a voxelated TsImageCube geometric component on TOPAS with the same number of voxels in each direction. This function takes as argument a *suffix* used to distinguish its output from other generated files, a string with the units that TOPAS will express the size of the phantom component, available units are nanometers (*nm*), micrometers (*um*) or millimeters (*mm*); and two lists with the cell types and the colors chosen to represent the for TOPAS visualization purposes.

```
def cellField2Topas(self, suffix, LenghtUnit = "um", cellTypes = {}, cellColors = {}):
    #-------------------------------------------------------------------------------#
    # Translation from the CC3D lattice to the voxelized virtual phantom that TOPAS  #
    # can read and asociate with a geometrical component for irradiation.            #
    #-------------------------------------------------------------------------------#
    oFile = open(self.output_directory+'/'+self.output_file + '.'+suffix+'.txt','w')

    #-----------------------------------#
    # Dimentions of the CC3D lattice    #
    #-----------------------------------#
    x = self.CC3D.dim.x
    y = self.CC3D.dim.y
    z = self.CC3D.dim.z

    #-----------------------------------#
    # Voxel equivalence to lenght unit #
    #-----------------------------------#
    VoxelSize = self.voxelLenghtEquivalence[LenghtUnit]

    hlx = 0.5 * x * VoxelSize
    hly = 0.5 * y * VoxelSize
    hlz = 0.5 * z * VoxelSize
```

Figure 4.16. *cellField2TOPAS* function, showing the necessary arguments and voxel to length conversion to construct the phantom component

A NumPy matrix called *phantom,* with the same dimensions as the CC3D lattice, is used to store the cell type Ids on each voxel and transferred to a binary file of 16 bits that can be referenced on the TOPAS parameter file. This is used to assign material to the virtual phantom on TOPAS corresponding to each type of cell. In this first implementation of TOPAS-Tissue all materials are water-copies, used for the differentiation of cell types. However, in future implementations, different cells that form specific kinds of tissue, like muscle or bone, can be assigned specific materials on the TOPAS virtual phantom.

It is important to note that the orientation of the geometrical components is different on CC3D $[x, y, z]$ than TOPAS $[z, x, y]$, because in the latter all objects are aligned along the Z axis. Therefore, this function is designed to automatically apply this transformation to prevent errors in the orientation of objects when the geometrical information is translated.

```
phantom = np.zeros([z, y, x])

for cell in self.CC3D.cell_list:

    cellPixelList = self.CC3D.get_cell_pixel_list(cell)

    if cellPixelList:
        for xyz in cellPixelList:
            phantom[xyz.pixel.z, xyz.pixel.y, xyz.pixel.x] = cell.type
```

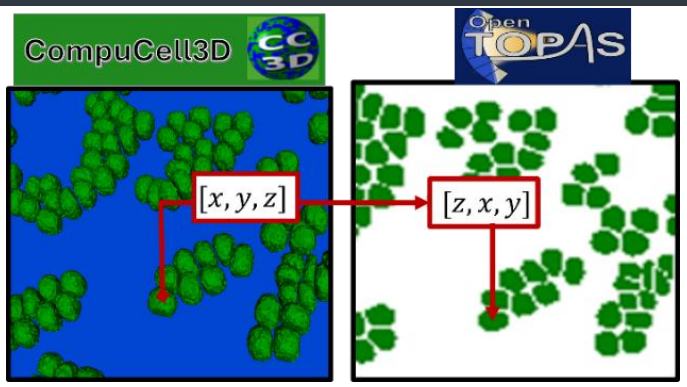

Figure 4.17. Translation of the CC3D lattice into the orientation of TOPAS

Due to the CC3D intrinsic nature of implementing geometrical models in a lattice and the capabilities of TOPAS/TOPAS-nBio to generate voxelized geometries, TOPAS-Tissue offers a flexible platform to irradiate any CC3D geometrical model. Other types of cells, cell population arrangements or even tissue can be incorporated using the current available tools. While the parameters that control the cell's behavior can be further specified by defining phenotypes in CC3D that might include, the growth rate, volume, and topological shape, among many others. This can be archived by incorporating the PhenoCellPy library (version 1.0) [Gianlupi J.F., et al (2023)], which is a tool capable of simulating the different cell phenotypes through all the stages of the cell cycle and is compatible with CC3D. Ongoing developments to integrate this library to TOPAS-Tissue shall be presented in future works.

- *irradiateWithTOPAS*

  First, this function checks for a file named "Source.txt" that contains the information of the particle source like the particle type, spatial distribution, angular momentum, energy spectrum, among others. This is an independent file that needs to be constructed by the user before running the simulation. In addition, there exists an option to use a default, predefined source that uses a volumetric source of 1MeV monoenergetic electrons and 5 million histories, written on a dedicated text file.

```
#-------------------------------------#
# Source is constructedon its own file #
#-------------------------------------#
oFile.write('#############################################################\n')
oFile.write('includeFile = Source.txt\n')
oFile.write('#############################################################\n')
```

Figure 4.17. Source file referenced on the main TOPAS parameter file that the user needs to independently construct before starting the simulation

Once the source file is located it will be used with the parameter file, previously generated by the function *cellField2Topas*, and perform the irradiation of the geometry by initiating TOPAS. This is done using the OS library on Python and running a shell script called "run_topas.sh" that contains the environment variables and the direction of the TOPAS executable. The same output file name used on the *cellField2Topas* function is part of the initializing instruction since it will be used to construct other .txt files to score the quantity of interest, in this case the deposited dose.

```
os.system('./run_topas.sh ' + self.output_file + '.' + suffix+'.txt')
```

```
#!/bin/bash

export TOPAS=$HOME/Applications/topas
export TOPAS_G4_DATA_DIR=$HOME/Applications/G4Data
export QT_QPA_PLATFORM_PLUGIN_PATH=$TOPAS/lib
export DYLD_LIBRARY_PATH=$TOPAS/lib

$TOPAS/bin/topas $1
```

Figure 4.18. TOPAS execution with OS library and the runtopas.sh shell script

Once irradiation is finished, this .txt file with the dose deposited in each voxel of the virtual phantom is opened as a NumPy array called *dosePerVoxel* that returns the TOPAS orientation $[z, x, y]$ to the original CC3D order $[x, y, z]$. Then three empty matrices with the same dimensions as the lattice are created called *doseMap, doseNuclMap* and *doseCytoMap* that will be used to register the dose in every voxel of the space, on every cell nucleus and every cytoplasm respectively.

In this implementation, the multiple compartment option in CC3D wasn't used, instead the dose in each cell's compartment is determined by taking advantage of a couple of functions on CC3D that tracks the cell's Center of Mass (COM), with the command *cell._COM* of the x, y, z components; and the list of all the voxels that forms each cell called *get_cell_pixel_list.* All the cell's voxels inside a sphere centered on the COM and located at a distance less than a user-defined nucleus radius $\mathrm{r_{nuc}}$ contribute to the nucleus dose, while the rest contribute to the cytoplasm dose. A scheme of this process is presented below in figure 4.19.

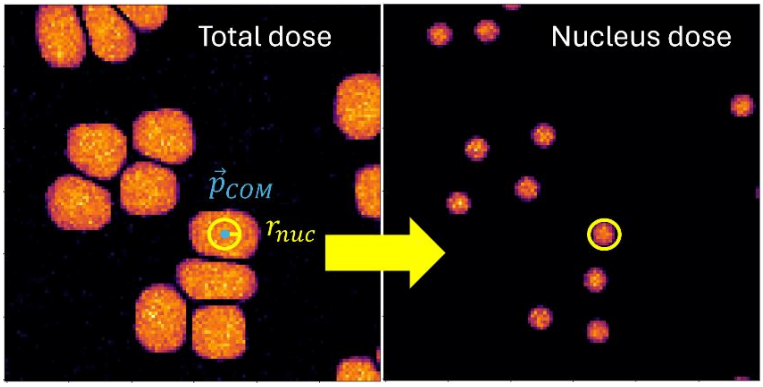

Figure 4.19. Selection of the voxels that contribute to the nuclear dose using the $\vec{p}_{COM}$ position and the nucleus radius defined by the user.

This is a straightforward method for simple cell geometry. Nevertheless, there is a CC3D option to construct cells with multiple compartments and it is compatible with TOPAS-Tissue since the ID that identifies a compartment to a cell number is also tracked by CC3D. Therefore, applications that consider tissue with complex, multicompartment cells can be developed on future works.

Finally, If the user decides to track the dose on each voxel an option is available to generate four files to write the dose deposited on the different parts of the geometry from the NumPy matrices: three of these are 36 bits binary files with floating-point format, one scores the dose in the lattice, the second and third on the cell's nucleus and cytoplasm respectively, and the last one is a plain text list with the information of the average dose deposited in each cell and its compartment, accompanied by other information like the COM, current volume of the cell, Its type and ID number, and the DSBs assigned from the nucleus dose, a process that will be explained next.

- *asignInitialDSBfromDose*
  This function uses the deposited dose in every cell's nucleus to calculate the initial number of DSBs on each cell. In the current implementation this is done randomly sampling a Poisson distribution with a mean value $\bar{N}_{DSB} = \alpha \cdot D_{nuc}$, here D_{nuc} is the deposited dose on the nucleus [Rothkamm K., et al (2003)] and α is parameter specific of the radiation quality used, from these initial DSBs a fraction of f will be classified as complex (DSB_2) and a complementary fraction $f - 1$ will be classified as simple (DSB_1), this fraction is also radiation type specific [Belov O., et al (2015)]. The α, f parameters are arguments in the function and need to be declared by the user.

  The calculated number of each type of DSBs are stored on the cell's dictionary, a list provided by CC3D to track external quantities. This step is also used to initialize the repair state of each cell with the necessary variables for the radiation response model stored in the same dictionary.

```
def asignInitialDSBfromDose(self, cell, dose = 0.0, NP = 35.0, k = 0.3):

        #-------------------------------------------------------------------#
        # After dose is asigned to each cell nucleus a dictionary with all the #
        # parameters needed for the repair model are asigned to each cell      #
        #-------------------------------------------------------------------#
        #    repair proteins  |-----  DSBs on diferent states -----|
    state = {"isRepairing" : False ,"NR": 20, "DSB": 0, "DSB_C": 0,\
    #                        |------ simple(1) and complex(2) DSBs ------|
    \"DSB_R": 0, "DSB_F": 0, "DSB1": 0, "DSB2": 0, "DSB1_C": 0,"DSB2_C": 0}

    if dose > 0.0:
        # DSBs follow a poisson distribution with mean value NP multiplied by the dose deposited
        DSB = np.random.poisson(NP * dose)
        # a fraction 1 - k of the initial DSBs are simple
        DSB1 = int((1.0 - k) * DSB)
        # and  a fraction of k are complex
        DSB2 = int(k * DSB)
        #-------------------------------------------------------------#
        # NOTE: NP and k are dependent on the radiation quality used #
        #-------------------------------------------------------------#
        state['DSB'] = DSB
        state['DSB1'] = DSB1
        state['DSB2'] = DSB2
        state["isRepairing"] = True

    cell.dict.update(state)
```

Figure 4.20. DSB assignment function from the sampling of a Poisson distribution and the starting repair state stored on the cell's internal dictionary that CC3D provides.

It is important to mention that we adopted this method to facilitate the CC3D-TOPAS coupling and speed up the testing of the other systems. However, TOPAS-Tissue is not limited to the Poisson DNA damage assignment. In fact, TOPAS-tissue is compatible with the TOPAS-nBio Monte Carlo track structure, in this way, the SSBs and DSBs that are fed to the DNA model repair can be simulated with TOPAS-nBio for a large set of particles and energies, including microdosimetric and nanodosimetric quantities [Faddegon B., et al (2023)]. Other, more advanced methods can be applied for the initial DSB calculation, for example the DBSCAN algorithm [Francis Z., et al (2011), Dos Santos M., et al (2014)] is already implemented and available within TOPAS scorers and precompiled DNA breaks databases, like the one proposed by [Thibaut Y., et al (2023)] on the MINAS TIRITH Geant4-DNA application, could be implemented in the future as well.

- *StepRepair*

  The DNA repair model adopted in TOPAS-Tissue was the one proposed in [Zhang X.P. et al (2009,2011)] and it is integrated in a function whose arguments are the cell being repaired and the time step dt that will synchronize the DNA repair with other simulated process. This gives the user control over a specific group of cells and the period of time that cells can be repaired. This function works by accessing the selected cell dictionary and modifying the repair variables in each step, for example the number of DSBs in each state or the number of available repair proteins, in almost the exact same process than the one described on section 2.3.4 *Protein DNA damage response networks*, with certain modifications that will be presented in a following section.

```
#----------------- DNA Repair Mechanism ------------------
    def StepRepair(self, cell, step_size = 0.1) :
```

```
#-------------------------------------------------------------------#
# 'state' is a filtered cell dictionary containing only the relevant #
# variables (represented by the cell dictionary keys) for the       #
# reparation process                                                #
#-------------------------------------------------------------------#
state = {key : cell.dict[key] for key in cell.dict.keys() and {"NR", "DSB", //
//"DSB_C", "DSB_R", "DSB_F", "DSB1", "DSB2", "DSB1_C", "DSB2_C" }}
#---------------------------------------#
#  fast repair process for simple DSB (1)  #
#---------------------------------------#
for d in range(int(state['DSB1'])):
    #-----------------------------------------#
    #  association with a repair protein (D => C) #
    #-----------------------------------------#
    r = np.random.uniform()

    PD = state['NR'] * (kfb1 + kcross * (state['DSB1'] + state['DSB2'])) * dt
```

Figure 4.21. Repair step function, DNA repair is performed by accessing and modifying the repair state of each cell, testing every DSB on each category to transition state using random sampling

The value of the time step is important since it is also involved in the probability of transition between DSBs states, the total simulation time and the synchronization with other biological models, like the p53 protein network model or the cellular growth and division process.

- Unit equivalence transformations and tables

  In order to define characteristics of cells in CC3D that involve geometric or temporal measurements, like the average size, growth rate or the doubling time and volume, need to be declared in terms of the number of voxels that represent these variables. However, this code doesn't have an internal system of metric units, and it is the responsibility of the user to ensure that all simulated biological models are calibrated to the chosen equivalence.

  Nevertheless. When CC3D is coupled with TOPAS it is imperative for the correct operation of TOPAS the precise communication of the voxels size in metric units. Therefore, computational tools that facilitate the register, conversion and rescaling of units in CC3D in the form of a series of functions that automatically fill tables of the temporal and length equivalence between MCS and voxel with metric units chosen by the user by declaring a known measurement the functions *setTimeUnitTable* and *setLenghtUnitTable* to assign certain number of MCS or voxels to its metric equivalence, for example if the user chooses a 1voxel : 2µm the corresponding function will take the arguments as follows:

$$\text{setLenghtUnitTable}(1, [2, \text{"um"}])$$

here the first argument is the number of voxels and the second an array with two entries, the number of equivalent units and a string with the length unit chosen. The available length units are nanometers ("*nm*"), micrometers ("*um*") and millimeters ("*mm*"), while temporal available units are the second ("*sec*"), minute, ("*min*"), hour ("*hr*") and days ("*day*"). The

available functions also automatically register the multiples of these units, following the previous example, if 1 vox = 2 um, the functions set the equivalence table for 0.1 vox = 2 nm and 1000 vox = 2 mm, and at the same time the opposite equivalence: 1 um = 0.5 vox and 1 mm = 500 vox. The time functions work in an identical way and the default equivalence chosen are 1 vox =1 um and 1 MCS = 1 min.

4.4.1.1 Geometry rescaling

One of the mechanisms that the unit equivalence tables facilitate is the rescaling of cells: In CC3D all simulated processes that modify the geometry and plasticity of cells use the index copy attempt to perform the changes. However, as the number of cells grow this process becomes too computationally expensive and the simulation slows down. Therefore, reducing the number of voxels that represent each cell by rescaling the whole geometry also reduces the number of operations required per step and the computation cost decreases, making the simulation more efficient consequently.

CompuCell3D has a dedicated function called *resize_and_shift_lattice* that accomplishes one of the objectives: Resizing the lattice size. This function allows the shifting of the whole cell array in a straight line defining a three-dimensional vector.

Nevertheless, the CC3D manual indicates that this function was designed to give more space to cells that are dividing and saturating the lattice. There are two condition for the correct operation of this function: First, when reducing the size of the lattice the function is not permitted to cut a portion of a cell, making the whole operation to fail; and second, if the displacement makes one of the cells to cross the lattice frontier, the shifting is canceled but the resize is carried out [Swat M.H., et al (2014)]. Therefore, particular care needs to be taken when reducing the lattice size.

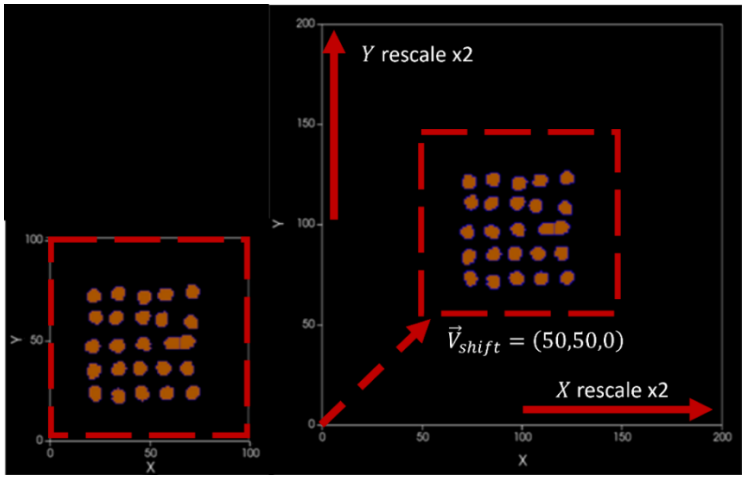

Figure 422. Normal action of the *resize_and_shift_lattice* function

Furthermore, this function restricts the shift of the whole cell array in a straight line. However, a displacement for a rescaling operation requires that each cell moves in the direction relative to the origin [0,0,0] of the lattice and proportional to the scaling function. Even if the resize and displacement operations are done correctly, other inconvenient on CC3D may occur when adjusting the cells volume accordingly to the rescale factor: If the target volume is changed the cell will

"deflate" to match the new target volume. However, if the maximum volume for the mitosis condition is changed at the same time, the current volume of the cell might be larger than the rescaled doubling volume and trigger the division process accidentally.

The method adopted in this work to solve this problem is to perform the rescaling process by stages. On figure 4.23., the whole process is shown: First a period is defined to carry out the rescaling, in preliminary test a 100 MCS was chosen. The first step **A)** is to rescale the target volume and growth rate, this causes in **B)** the cells to shrink and the growth rate to scale accordingly in the so-called *tolerance period*, that lasts until the middle of the period chosen. Then, once the cells have lost a certain percentage of their volume, the displacement is performed in **C)**, moving each cell in the direction relative to their current position with a magnitude proportional to the rescaling factor, preserving the geometric distribution at scale. The next step in **D)** is to use dummy cells called DEL (for delete), shown as yellow boxes that will act as barriers, to avoid cells from moving to the regions that will be chopped in the rescaling, and at the same time like cutters that will crop the cell's regions that fall outside of the resized lattice frontier, avoiding failure of the process. Then, in step **E)** DEL cells are eliminated, and the *resize_and_shift_lattice* function is used to scale the space. Finally, the doubling volume is rescaled to avoid accidental mitosis. Once the geometry resize has been performed on **F)** cells stabilize their volume very quickly and the simulation continues.

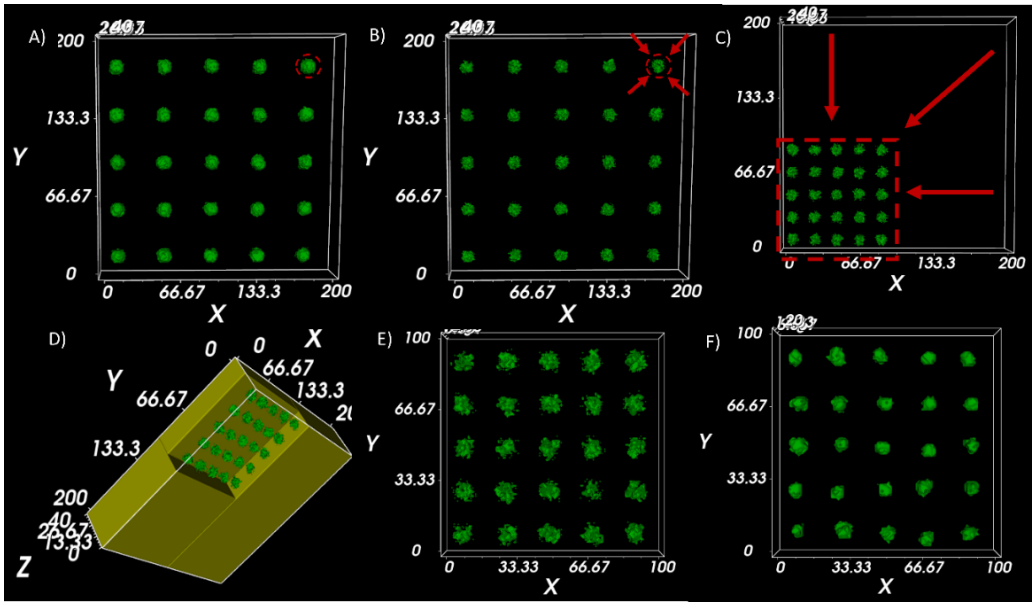

Figure 4.23. Stages of the rescaling process: **A)** original volume, **B)** volume reduction, **C)** displacement, **D)** auxiliar DEL cells on yellow, **E)** lattice resize and **F)** cell stabilization.

This method was tested in a 25-cell array (5x5) on 200x200x40 voxels, the initial target volume was 1000 voxels and the doubling period 500 MCS. Before a mitosis cycle is completed (on t = 50 MCS) a resize was applied with a reduction fraction of 20% (1:0.8) to 60% (1:0.4) and an increase of 10% (1:1.1), the total number of cells, the average volume and the normalized average volume was tracked as the simulation progressed to check if the resize process affected the other biological simulated processes, the results are presented below in figure 4.24.

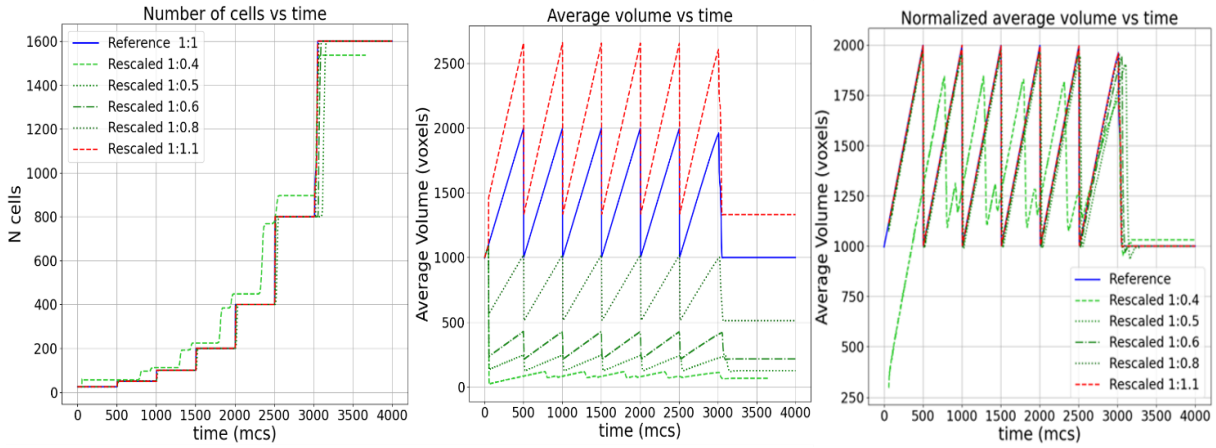

Figure 4.24. Rescaling test showing the time evolution of number of cells, average volume, and normalized average volume, for reduction fractions between 20-60% (greens) and an increase fraction of 10% (red) compared to the normal cell culture (blue).

Results indicate that the reductions between 20% to 50% and the 10% increase do not affect significantly the division process of 500 MCS and the division condition is correctly scaled. For example, a reductio of 50% implies a scaling of the target volume of $V_i \cdot 0.5^3 = V_i/8$, while a 10% increase implies a rescaling of $V_i \cdot 1.1^3 = V_i \cdot 1.331$. However, for a reduction larger than 60% the cellular division becomes unstable, in the sense that some cells divide too quickly or too slow. This might be explained since the cell's growth is controlled by the index copy attempt process and considering that a larger reduction implies that less voxels represent the same cells, each voxel represents a larger portion of the cell's total volume, and the stochastic rejection or acceptance of new cell voxels have a larger effect on the growth of the cell, making it erratic.

4.4.2 TOPAS-Tissue workflow

Once the general parameters of the simulation have been established and introduced to CC3D, like the size of the lattice, the initial number of cells, the time and length equivalences to MCS and voxels, the growth rates, radius and volumes of the cells among others, the operation of TOPAS-Tissue follows several stages: First, the *pre-irradiation* stage where the initial cells are *seeded*, creating the starting geometrical distribution with an initial density. They can grow and reproduce for a predefined period until they reach certain final density. Then in the *irradiation* stage TOPAS-Tissue translates the geometrical information from CC3D into a ready-to-run TOPAS-parameter control files and sets the irradiation conditions such as the type of incident particles, the number of histories, the energy spectrum among other parameters. It is used to perform irradiation and retrieve the dose in every cell. Then, it is used to calculate the DNA damage in each one of them. In the current implementation this is done within a single MCS of CC3D, however TOPAS has internal *time-features* [Shin J., et al. (2012] that can be incorporated into the framework in future works, to consider other types of irradiations like fractionated doses or pulsated sources that might take more than one MCS. Finally, on the *post-irradiation* stage, the damaged cells stop their growth and division processes to mimic the arrest of the cell cycle.

Since the DNA damage and every repair state is stored in each cell's dictionary, a scaling process can be performed at this point to make the simulations more efficient without losing geometrical

information. Then the DNA repair process working in parallel with the p53 protein network starts. Altogether they represent the cellular biological response to radiation damage.

The simulation internally tracks the *repair state* of every individual cell at each MCS, including the number of DSBs in each state, the concentration of proteins in the p53 pulse network, especially the level of Casp3 to trigger the apoptosis signal, and an identifier of the colony that the cell belongs to. This ID is an attribute assigned to each seeded cell at the beginning of the simulation, it is inherited to their daughter cells and facilitates the final counting for the survival fraction of the populations since experimentally the survival curves are constructed with the number of alive cell colonies after irradiation. A complete scheme of TOPAS-Tissue workflow is shown below on figure 4.25 and a table with all user's tunable parameters is provided next on table 4.14.

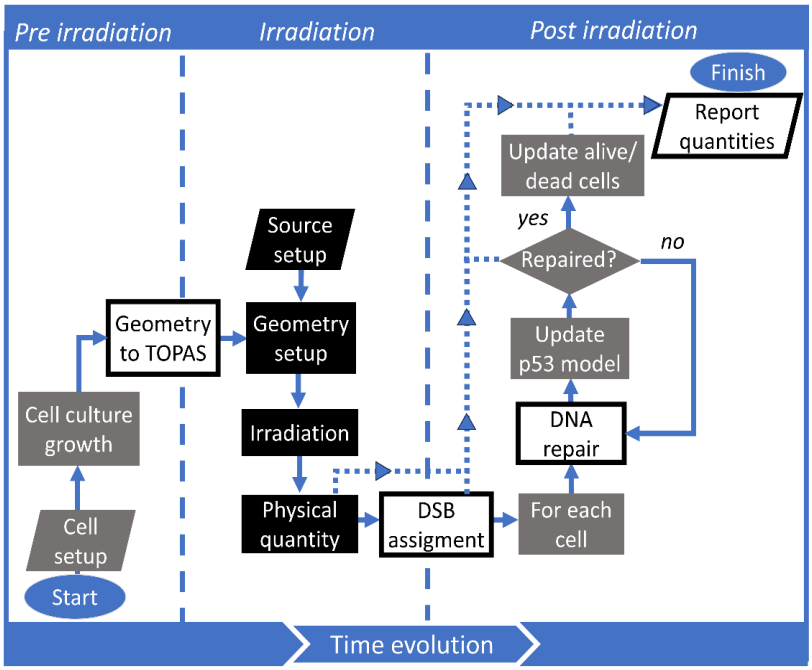

Figure 4.25. Schematic for the TOPAS-Tissue workflow

Table 4.14. List of the user tunable parameters and a brief description for each one.

Parameter	Description	Parameter	Description
X_{max}	Number of voxels on the X direction	t_{doub}	Cell's doubling volume time
Y_{max}	Number of voxels on the Y direction	k_{growth}	Cell's growth rate
Z_{max}	Number of voxels on the Z direction	T_{pre}	Pre-irradiation period duration
vox_{eq}	Equivalence from voxels to length units	$\overline{N}_{DSB}$	Average number of DSBs per Gy
dt	Equivalence from MCSs to time units	N_p	Number of primary particles
r_{cell}	Cell radius	D	Prescribed dose to the phantom
V_{cell}	Cell volume	f	Fraction of complex DSBs
r_{nuc}	Nuclear radius		

4.4.2.1 Simulation Configuration

The input parameter values used in the simulation framework are shown in Table 4.15. A detailed description of the culture geometry, the radiation source model and the changes made to the DNA repair model are presented in the following sections.

Table 4.15. Values for the parameters used in the simulation's configuration.

Parameter	CC3D Units	Metric Value	Parameter	CC3D Units	Metric Value
X_{max}	1000 vox	1000 µm	$1-f$	----------	49%
Y_{max}	1000 vox	1000 µm	p_{fatal}	----------	1.5%
Z_{max}	60 vox	60 µm			
vox_{eq}	1 vox	1 µm	Pre-irradiation stage		
r_{PC-3}	9 vox	9 µm	dt	1 MCS	2.88 min
V_{PC-3}	3053 vox	3053 μm^3	T_{pre}	2050 MCSs	4.1 days
r_{nuc}	4 vox	4 µm	t_{doub}	687 MCSs	33 h
$\overline{N}_{DSB}$	----------	27.5 DSB/Gy	k_{growth}	4.44 vox/MCS	1.54 $\mu m^3/min$
D	----------	0–8 Gy	Post-irradiation stage		
N_e^-	----------	18.2×10^6/Gy	dt	1 MCS	0.5 min
f	----------	51%	t_{doub}	3960 MCSs	33 h
			k_{growth}	0.77 vox/MCS	1.54 $\mu m^3/min$

4.4.3 PC-3 culture Geometrical model and the pre-irradiation stage

The experimental conditions chosen to validate the TOPAS-Tissue platform were the ones described in [Wakisaka Y., et al., (2023)]. Here, PC-3 prostate cancer cell cultures placed on flasks where irradiated with carbon ions of different energies to study the survival curves using X-rays as a reference radiation. A scheme of the irradiation configuration can be seen below in figure 4.26.

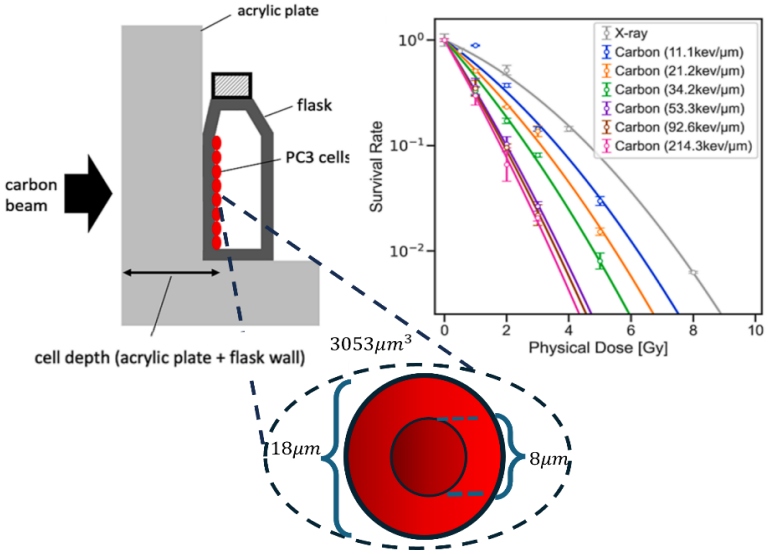

Figure 4.26. Scheme for the experimental configuration used the survival curves for the different radiation qualities and the geometrical characteristics of the P-C3 cells used in the experiment. Images adapted from [Wakisaka Y., et al, (2023)].

The geometrical model developed for this type of cells was constructed on CC3D and it was based on experimental measurements reported on literature: PC-3 cells have an average diameter of 18.08 ± 2.69 µm [Dolfi, S.C., et al (2013)], therefore a cell radius of $r_{\mathrm{PC-3}} = 9\mu\mathrm{m}$ was chose. Then, approximating the cells as spheres, this radius yields a volume of 3053 µm^3. The reported size of a cell's nucleus is between 3-5 µm of radius [Lammerding J. (2011)], therefore a value of$r_{\mathrm{nuc}} = 4\mu\mathrm{m}$ was used in this research work. An equivalence of 1 voxel = 1 µm was employed and the virtual phantom had a 1000 x 1000 µm^2 surface dimensions and 60 µm of height, this was chosen to avoid collisions between cells with the roof of the lattice.

One of the fundamental parameters of any CC3D simulation is the adhesion parameter between neighbor cells and their environment. For our geometrical model, the default parameters and the fact that there is not an option to control the adhesion between cells and the lattice frontier on CC3D, resulted in amorphous, blocky cell cultures stuck to one another, preventing any cellular mobility. A study was carried out to determinate the optimal parameters for adhesion. A 1 voxel layer was added to simulate the interface between cells and the flask material, resulting in rounded cells on well-defined colonies that allowed certain cell mobility. The results for the adhesion parameters are shown on table 4.16 followed by figure 4.27. with an image comparing the cultures that resulted from the CC3D default parameters, and the cell-flask interface shown on blue.

Table 4.16. Adhesion parameters used on the PC-3 cell culture geometrical model.

Type	Medium	Flask	Alive PC-3	Dead PC-3
Medium	0.0	0.0	1.0	10.0
Flask	-	0.0	100.0	100.0
Alive PC-3	-	-	10.0	1.0
Dead PC-3	-	-	-	100.0

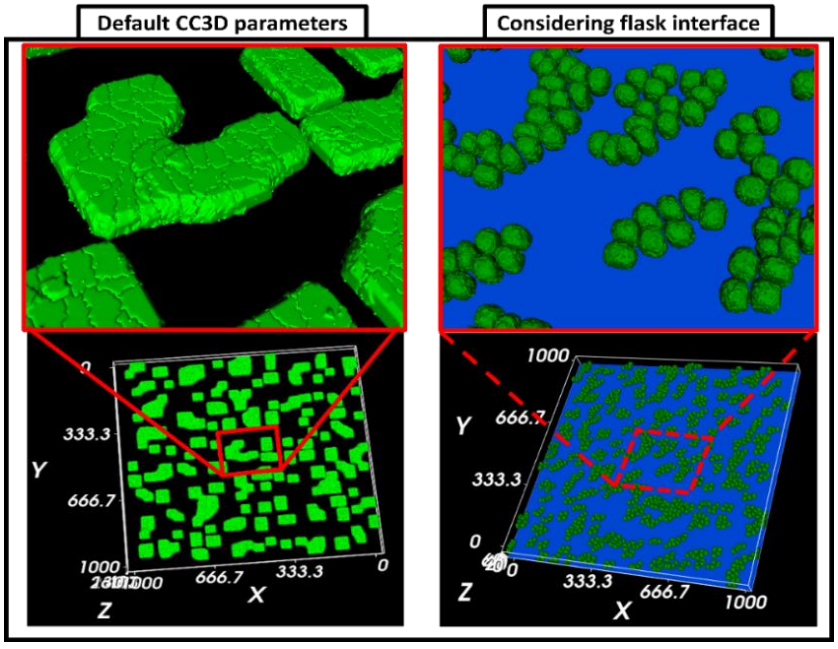

Figure 4.27. Comparison between the cell cultures that resulted from (**Left)** the default CC3D parameters and (**Right)** the optimized parameters that consider the cell-flask interface monolayer in blue.

The cell's doubling period reported on [Wakisaka Y., et al, (2023)] was 33h, the time equivalence in this stage was set to 1 day = 500 MCS, therefore the cell's growth rate was 3053 voxels every 687 MCSs to agree with the experimental measurement, the cell division was restricted to a random orientation on the X-Y plane to generate a cell monolayer.

The initial cell density, when the cells were seeded in the flask, was 6.0×10^5 cells per 25cm^2 or 2.4 per $(100\mu\text{m})^2$. To simulate this initial density the surface of the CC3D lattice was divided into regions of 100µm×100µm and randomly placed 2 or 3 cells, avoiding cell overlapping in each sub region. This resulted in an initial confluency of $2.48/(100\mu\text{m})^2$. In the experiment, the cells were left to grow for 4 days before irradiation and reached a confluency of 2.5×10^6 cells per 25cm^2 or 10.0 per$(100\mu\text{m})^2$ [Wakisaka Y., et al, (2023)] our simulated culture reached a density of 10.2 cells per (100 µm)^2 in 2050 MCS equivalent to 4.1days, a result within 1.6% from the reported value. The time evolution of the cell culture geometrical model is shown below on figure 4.28, where a 2D projection of the CC3D simulation is presented every 33 simulated hours.

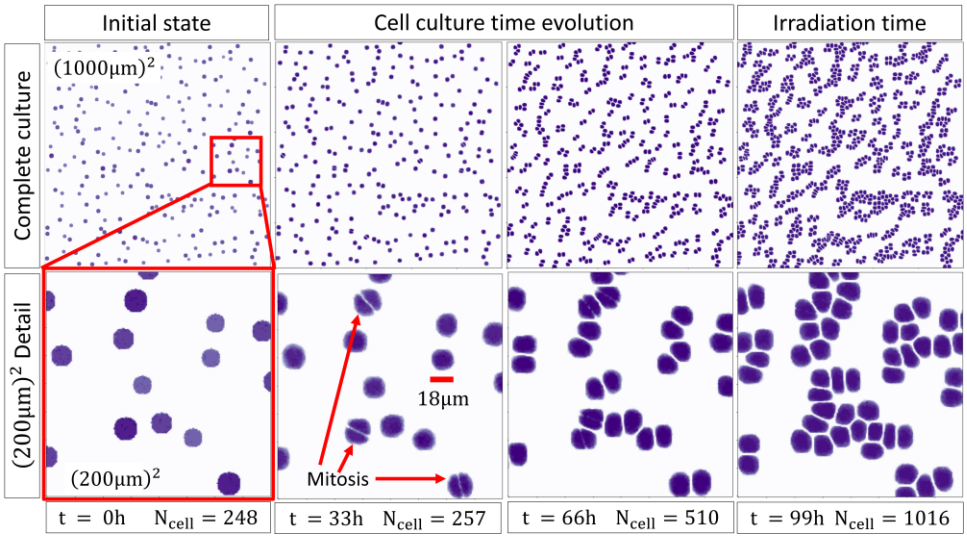

Figure 4.28. 2D projection of the CC3D cell culture geometrical model growth in the 4.1 days pre-irradiation period.

At the end of this stage the geometry was saved into a PIF file and served as the initial condition for all the irradiations performed, the evolution of the PC-3 cell culture from the initial density to the desired confluency after the pre irradiation period demonstrate that TOPAS-Tissue is capable to reproduce the growth of an in vitro experimental assay.

4.4.4 X-ray source modeling and the irradiation stage

At the irradiation stage, TOPAS-Tissue automatically transfers the geometrical information from CC3D to TOPAS with the function *cellField2Topas* in the form of a voxelated phantom using the TsImageCube component of TOPAS. The phantom dimensions are the same as the CC3D lattice, whereas the orientation was changed according to the TOPAS coordinate system. The virtual phantom contained the information of the cell number and cell compartment IDs in each voxel, this facilitates the cell identification in the postprocessing. In this implementation it was assumed the cell's volume, and its environment were made of water, thus the TsImageCube component set water

material to all voxels, regardless of the cell Id number in the voxel. Then, TOPAS is automatically called for a run using the function *irradiateWithTOPAS*.

The X-ray source was simulated with a 6MV TrueBeam LINAC phase space obtained from the database of MyVarian from www.myvarian.com/montecarlo (accessed 30 November 2023). It was considered that no significant differences existed between the phase space used in the simulations and the 4MV experimental X-Ray spectrum from [Wakisaka Y., et al., (2023)]. The phase space consisted of 10^9 histories, it was used in TOPAS to irradiate a water phantom of $10\text{cm} \times 10\text{cm} \times 20\text{cm}$ placed with a $5 \times 5\ \text{cm}^2$ field at 100cm surface-to-surface distance, the physics module selected for the simulations was "g4em-standard_opt4" with a production cut for secondary electrons of 1µm. At a depth of 10 cm a plane scorer was placed to register the kinetic energy of the secondary electrons produced by the incident X-rays that reached this plane. This region was chosen because transient charged-particle equilibrium exists.

Then, this kinetic energy spectrum was used to construct a volumetric source that produced electrons in random positions uniformly distributed across the voxelated cell culture geometry. On average, 18.2 million source electrons were needed to deliver a mean absorbed dose of 0.994 ± 0.001 Gy to every cell in the culture. The scheme for the complete development of the radiation source is shown below in figure 4.29.

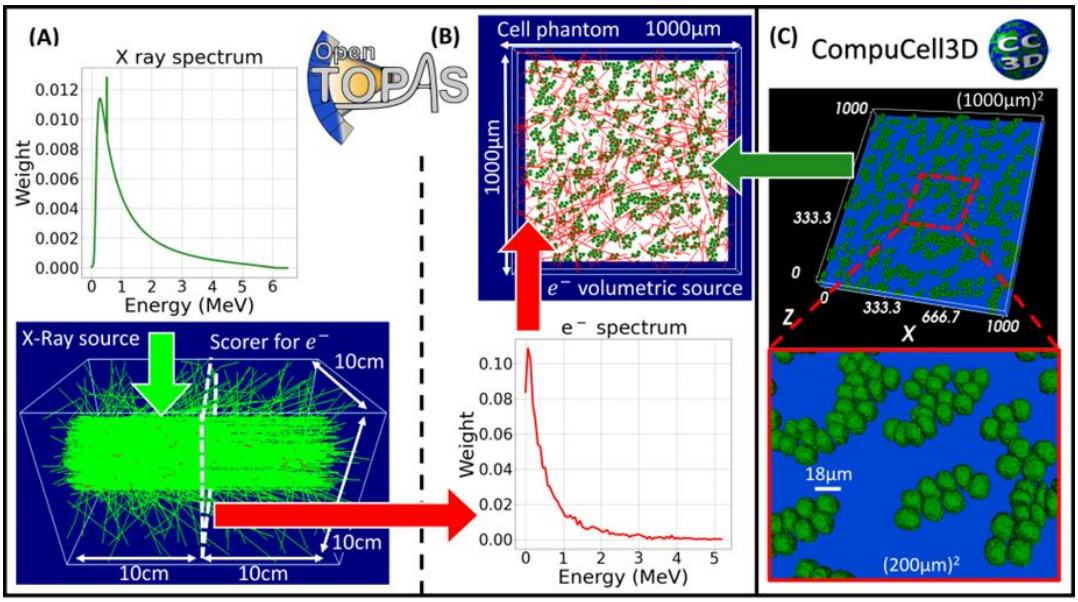

Figure 4.29. complete process of the radiation source construction. First on **A)** the X-ray spectrum is used to irradiate a 10 x 10 x 20 cm^3 water phantom and the secondary electron kinetic energy is retrieved on a plane score at 10 cm depth. Then, on **B)** this energy spectrum is used to construct a volumetric electron source and irradiate **the** virtual phantom that contains the **C)** geometrical information from CC3D.

After the irradiation is completed, the output file is processed by TOPAS-Tissue to assign the dose to the cell nucleus and cytoplasm before sending it back to CompuCell3D to continue the simulation. The nucleus dose is used to calculate the number of DSBs on every cell using the TOPAS-Tissue function *asignInitialDSBfromDose*: In a cell population irradiated with a uniform particle field at low LET (~0.2 keV/µm) radiation, a reasonable approximation to compute the number of DSBs is from a Poisson distribution, where the mean number of lesions increases linearly with the absorbed dose

and the mean value is equal to $N_{DSB} \cdot D_{nuc}$ [Rothkamm K. & Löbrich M. (2003)] which is depended on the radiation quality. For X-rays a N_{DSB} value of 27.5 DSBs/Gy was used accordingly to [Belov O.V., et al (2015)]. Complex DSBs (DSB_2) were given by a fraction f from the total number of DSBs. Consequently, simple DSBs were calculated as the complementary fraction $DSB_1 = (1 - f)$ DSB. We used a fraction value f = 0.51 for X-rays, obtained from [Rothkamm K. & Löbrich M. (2003), Belov O.V., et al (2015)]. DSBs were assigned to each cell using a Python dictionary provided by CC3D, which allowed the use of user-defined parameters during the simulation. We used such information to dynamically input the DNA repair model during each MCS.

Results for 20 simulations, with different random seeds, for the cell culture irradiation can be seen below on figure 4.30. where the deposited doses on both the cytoplasm and nucleus compartments of a group of cells on a small $(200\mu m)^2$ square region at the extremes of the dose range studied, 1 and 8Gy, are shown alongside a graph with the average number of DSBs, with the error bars representing the standard deviation, as a function of the dose deposited on the whole virtual phantom, demonstrating the lineal increase, with a slope of 25.1 DSBs/Gy, in the mean number of DSBs with dose and a Poisson distribution around it.

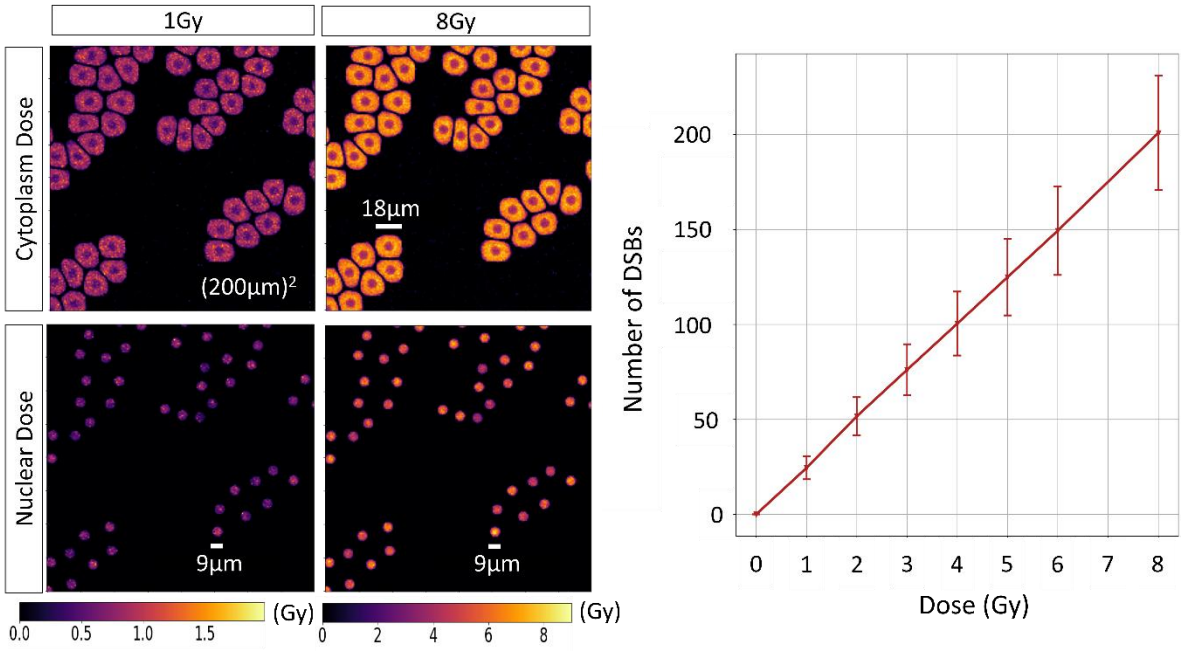

Figure 4.30 **Right**. Results for the deposited dose on a group of cells, in a $(200\mu m)^2$ region, in the cytoplasm and nucleus compartments at 1 and 8Gy. **Left**. Results for 20 independent simulations for the average number of DSBs produced as a function of deposited dose on the phantom with the error bars representing one standard deviation.

4.4.5 DNA repair model extension and cell survival evaluation

The base model for the biological radiation response is the one proposed by [Zhang X.P., et al (2009,2011)]. Briefly, it is a MC version of the TLK DNA repair model proposed by [Stewart R.D. (2001)] coupled with a model for the p53 protein network, however both models have limitations when evaluating the cell survival: The TLK model works by tracking the accumulation of lethal lesions that result as an inevitable byproduct of the DSBs mis repair, attributed to the formation of chromosomal aberrations [Pfeiffer P., et al. (2000), Forster J.C., et al. (2019)] and death by mitotic

catastrophe, when cells attempt and fail to divide [Douglass M., et al. (2015)], but simplifies the survival probability from an exponential function, not directly related to any biological processes.

On the other hand, the focus of the p53 protein network model was put on the number of DSBs attached to repair proteins ($\mathrm{DSB_C}$) since they influence the activation rate of the ATM proteins that initiate the operation of the rest of the protein network. The cellular death in this model was exclusively evaluated by the activation of the Casp3 apoptosis trigger when the level of this protein surpasses the maximum concentration by sustained p53 pulses as DNA is repaired. Whereas the lethality of the DSBs on the final stage of the repair module, the fixed DSBs ($\mathrm{DSB_F}$), was not considered, although the authors of the first version of the model recognized that the accumulation of lethal lesions had profound consequences on the final viability of affected cells [Ma L., et al (2005)].

Nevertheless, both models describe different and important aspects of the whole cellular response to DNA damage, therefore the solution proposed in this research work to account for both cellular death mechanisms were to extend the p53 protein network to include the lethality of mis repaired DSBs following the approach of the original TLK by separating the fixed DSBs after the repair process is finished into lethal lesions ($\mathrm{DSB_L}$) that occur with certain probability p_{lethal}, and non-lethal lesions ($\mathrm{DSB_N}$) with a complementary probability of $(1 - p_{lethal})$. The value of $p_{lethal} = 1.5\%$ was chosen from the fraction of γ-H2AX foci measured 24 h post-irradiation, considered as the fraction of non-repairable DSBs. The experimental value for 1 Gy γ-ray irradiation (LET ~0.2 keV/µm) was 1.35 ± 1.25 [Asaithamby A., et al (2008)]. The scheme that represents the DNA repair module is presented next, with the changes made to incorporate the lethality of DSBs marked by asterisks:

$$\mathrm{P(DSB_1 \rightarrow\ DSB_{C1}) = N_r[k_{fb1} + k_{cross}(DSB_1 + DSB_2)]\Delta t}$$

$$\mathrm{P(DSB_2 \rightarrow\ DSB_{C2}) = N_r[k_{fb2} + k_{cross}(DSB_1 + DSB_2)]\Delta t}$$

$$\mathrm{P(DSB_{C1} \rightarrow\ DSB_1)\ =\ k_{rb1}\Delta t}$$

$$\mathrm{P(DSB_{C2} \rightarrow\ DSB_2)\ =\ k_{rb2}\Delta t}$$

$$*\ \mathrm{P(DSB_{C1} \rightarrow DSB_{L1})\ =\ p_{lethal}k_{fix1}\ \Delta t}$$

$$*\ \mathrm{P(DSB_{C2} \rightarrow DSB_{L2})\ =\ p_{lethal}k_{fix2}\ \Delta t}$$

$$*\ \mathrm{P(DSB_{C1} \rightarrow DSB_{N1}) = (1 - p_{lethal})k_{fix1}\ \Delta t}$$

$$*\ \mathrm{P(DSB_{C2} \rightarrow DSB_{N2}) = (1 - p_{lethal})k_{fix2}\ \Delta t}$$

Then, the evaluation of cell death is done with two conditions: 1) the presence of at least one lethal lesion and 2) the triggering of the Casp3 apoptosis signal. On non-irradiated cells the Casp3 level remains low, close to its vasal value of 0.05 µM. However, once it was triggered by p53 sustained pulses, it rapidly increased and saturate at a concentration of 2.7 µM, which is considered as a condition for cell death.

The simulation tracked internally the information for every cell at each MCS, including the number of DSBs, the concentration of p53 and Casp3. The level of Casp3 is checked at each MCS and compared to the maximum level, while the presence of lethal lesions is checked at the end of the DNA repair process. On the other hand, if all DSBs are repaired correctly on time, without triggering

the Casp3 apoptosis signal, the cell returns to its proliferative state. A unique colony ID was assigned to each primary seeded cell at the time of irradiation as an external attribute that is tracked in the cell's dictionary as well. After cell division, the daughter cells were assigned to the same colony ID as their mother cell. This attribute allowed colony identification and counting at the end of the simulation when the cell survival curve is constructed.

For the post-irradiation stage, the time equivalence was changed to 1 MCS = 0.5 min, and as a consequence, the growth rate changed to 3053 voxels every 3960 MCSs (0.77 vox/MCS). One of the key consequences of cellular death is the loss of volume [Bortner C.D. & Cidlowski J.A. (2003)]. To simulate this process, dead cells reduce their target volume at a constant rate of $-1.54\mu m^3/min$ corresponding to the negative growth rate. The operation of the extended DNA repair module with the p53 protein network is shown on figure 4.31. alongside the model dynamics for two different uniform irradiations with deposited doses of 3 and 5 Gy.

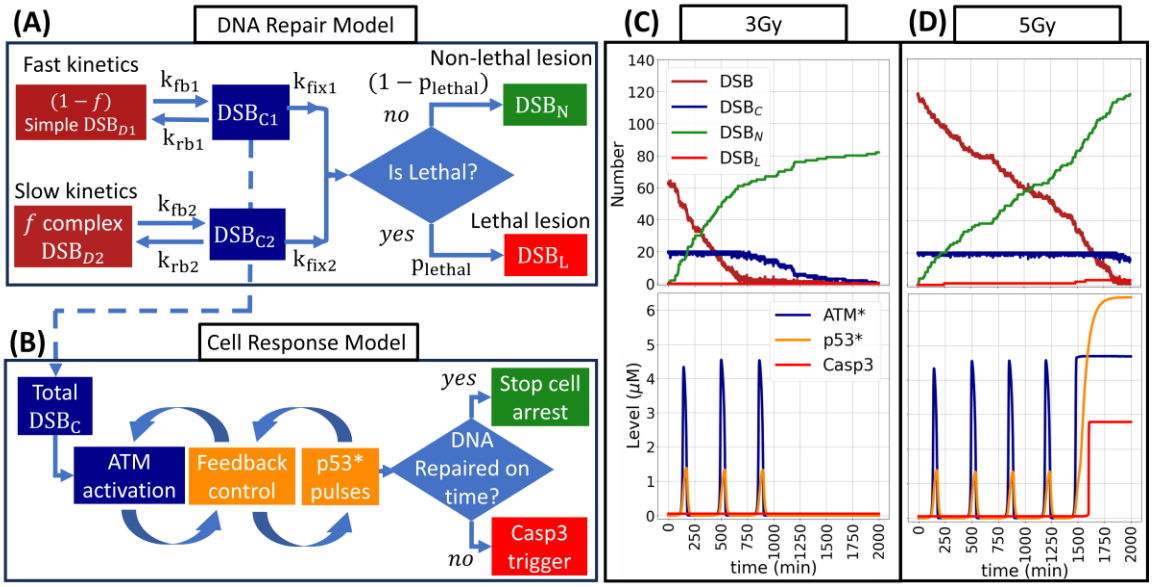

Figure 4.31. **A)** DNA repair module where the number of DSBs in state C influence the activation of ATM initiating the cellular response **B)** characterized by a protein reaction network centered around the p53 pulses. The kinetics of the whole model is presented in **C)** for 3Gy, showing a cell that repaired on time (before the 5th p53 pulse) without producing any lethal lesion, ensuring its survival, while on **D)** a 5Gy irradiation is shown, where the cell didn't repair its DNS on time and the Casp3 apoptosis signal is triggered, and a few lethal sessions are produced, resulting in the cell's death.

The time evolution of the number of cells was scored at user-defined step intervals (100 MCSs by default). The kinetic models reached equilibrium, about ~30 h after the beginning of irradiation. After this time, the survival was quantified from the number of remaining colonies as a function of the absorbed dose at 66 h, corresponding to 2 division cycles after irradiation.

4.4.6 Computational time: All systems working together

The complete scheme of all the mechanisms working together in TOPAS-Tissue is shown below in figure 4.32. The cell response diagram with the p53 protein network was adapted from [Zhang X.P., et al (2011)] directly. White ellipses represent biological processes and molecules, white parallelograms represent the irradiation process and products, and diamonds represent decisions. Solid lines with arrowheads represent a state transition, solid lines with white circles represent a

promotion of a process or biomolecule while black squares represent an inhibition of a process or degradation of a biomolecule.

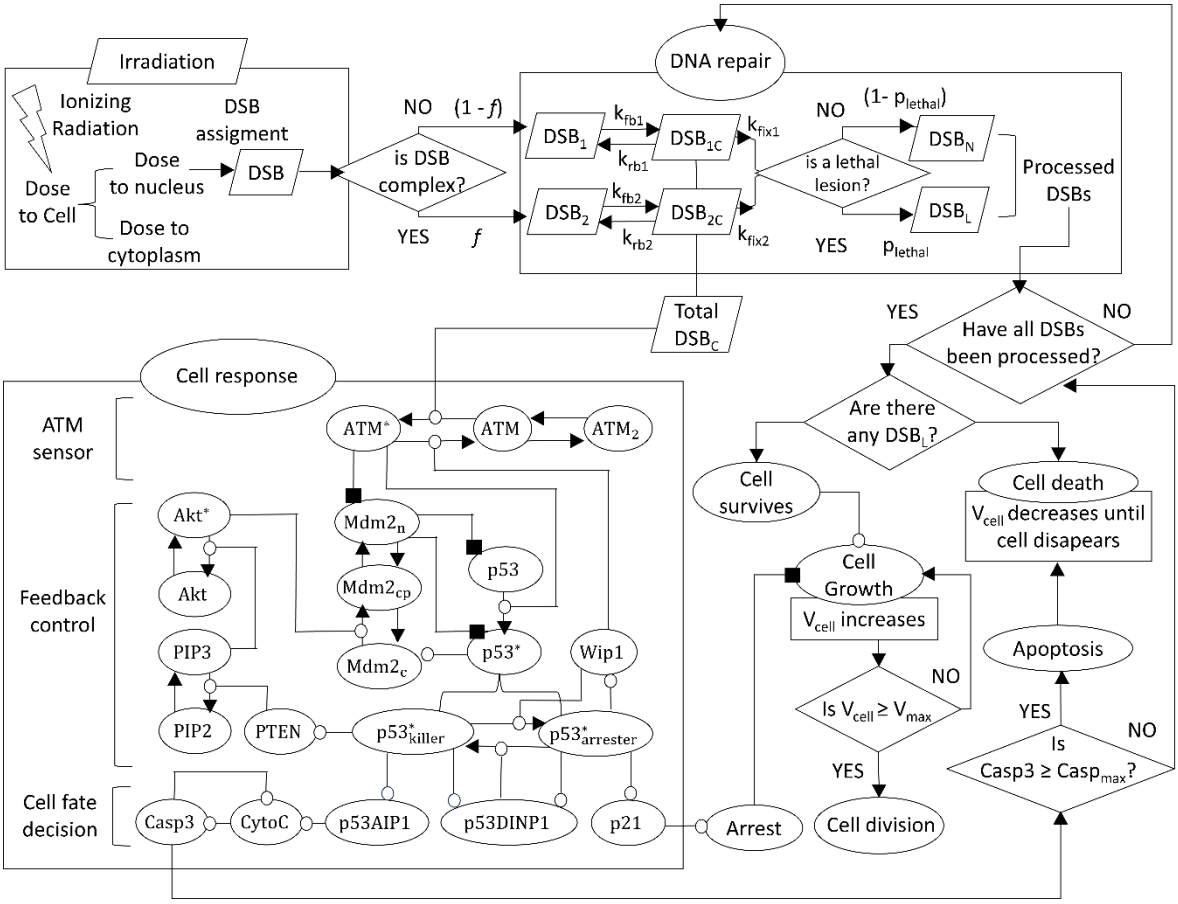

Figure 4.32. scheme for the complete TOPAS-Tissue operation, parallelograms represent irradiation process and products, ellipses biological process and molecules, while rhombus represent decisions. Arrows (→) represent a state transition, while straight lines ending on with white circles (○) represent promotions and black squares inhibitions (▪).

Results from 20 simulations running with different random seeds, using a Dell Precision 5820 Tower 20-CPU Intel Xeon W-2155 3.30 Ghz processor (Round Rock, TX, USA) were performed. The computation time per CPU for the execution of the TOPAS simulation, $\mathrm{T_{TOPAS}}$, scaled linearly with the number of simulated electrons, and consequently, with the deposited dose D, following the next expression: $\mathrm{T_{TOPAS}} = 2.9\ \mathrm{h} \cdot \mathrm{D/Gy} + 1.4\ \mathrm{h}$. On the other hand, CC3D execution time remained almost constant between 1 Gy to 4 Gy ($9.13\ \mathrm{h}$) and decreased linearly from 4 Gy to 8 Gy with a slope of $-0.55\ \mathrm{h/Gy}$. The reduction of computing time was caused by the decrease in the number of simulated cells due to the increase in killing with higher doses. This information is presented below in figure 4.33.

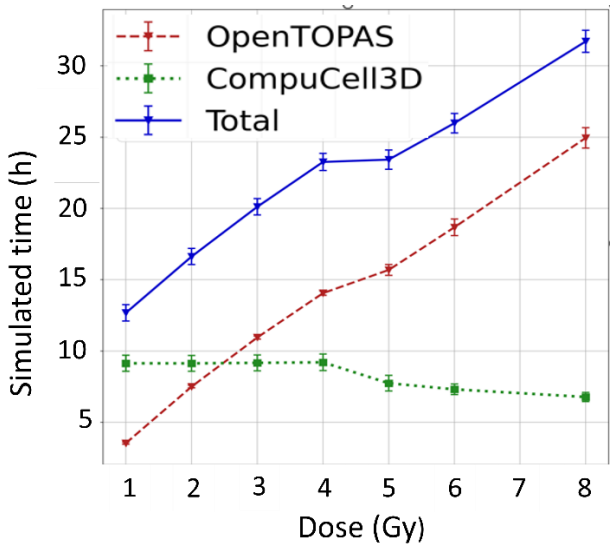

Figure 4.33. Simulation time for TOPAS, CC3D and their total sum as a function of the dose.

4.4.7 Cell survival curve

Results from the multiscale simulation of cell survival as a function of the dose are shown in figure 4.34. Each point corresponds to the average of 20 individual simulations at specific radiation doses. Error bars represent statistical uncertainties, measuring two standard deviations. Experimental values from [Wakisaka Y., et al (2023)] for a 4 MV X-ray beam are also displayed. As depicted, the simulated curve followed an exponential response. We fitted a linear–quadratic exponential function, obtaining parameters $\alpha = 0.280 \pm 0.025/\mathrm{Gy}$ and $\beta = 0.042 \pm 0.006/\mathrm{Gy}^2$. These values agreed within one standard deviation from the experimental parameters $\alpha_0 = 0.302 \pm 0.008/\mathrm{Gy}$ and $\beta_0 = 0.0417 \pm 0.0049/\mathrm{Gy}^2$ [Wakisaka Y., et al (2023)].

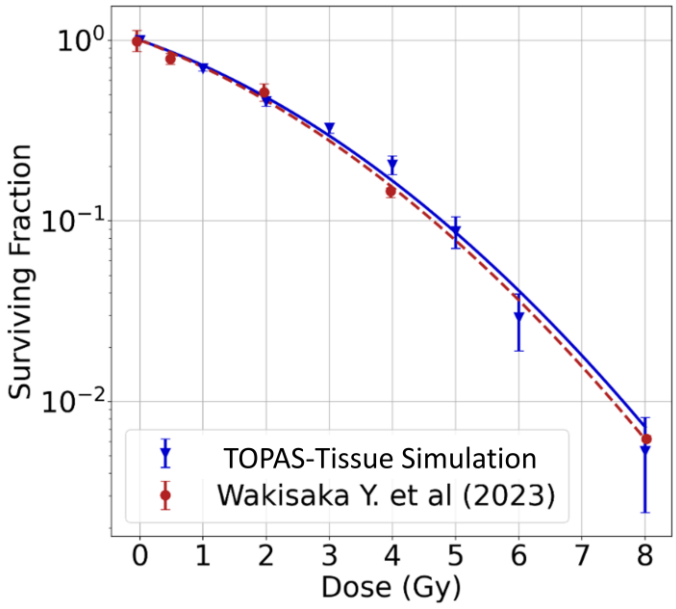

Figure 4.34. Simulated survival fraction compared to experimental data from [Wakisaka Y., et al (2023)].

4.4.8 Publication of these results

A publication titled “TOPAS-Tissue: A Framework for the Simulation of the Biological Response to Ionizing Radiation at the Multi-Cellular Level” by Omar Rodrigo García García, Ramon Ortiz, Eduardo Moreno-Barbosa, Naoki D-Kondo, Bruce Faddegon and Jose Ramos-Méndez (2024), with these results was sent to the International Journal of Molecular Science (IJMS) of the editorial Molecular Diversity Preservation International (MDPI) on 20 July 2024, it was revised the 21 August 2024, accepted on 17 September 2024 and finally published on 19 September 2024. It is accessible online on the next link: https://doi.org/10.3390/ijms251810061.

International Journal of *Molecular Sciences*

MDPI

Article

TOPAS-Tissue: A Framework for the Simulation of the Biological Response to Ionizing Radiation at the Multi-Cellular Level

Omar Rodrigo García García [1], Ramon Ortiz [2], Eduardo Moreno-Barbosa [1], Naoki D-Kondo [2], Bruce Faddegon [2] and Jose Ramos-Méndez [2,*]

[1] Facultad de Ciencias Físico Matemáticas, Benemérita Universidad Autónoma de Puebla, Puebla 72000, Mexico; omar.garciagarcia@alumno.buap.mx (O.R.G.G.); eduardo.morenoba@correo.buap.mx (E.M.-B.)
[2] Department of Radiation Oncology, University of California San Francisco, San Francisco, CA 94115, USA; ramon.ortizcatalan@ucsf.edu (R.O.); jorgenaoki.dominguezkondo@ucsf.edu (N.D.-K.); bruce.faddegon@ucsf.edu (B.F.)
* Correspondence: jose.ramosmendez@ucsf.edu

Abstract: This work aims to develop and validate a framework for the multiscale simulation of the biological response to ionizing radiation in a population of cells forming a tissue. We present TOPAS-Tissue, a framework to allow coupling two Monte Carlo (MC) codes: TOPAS with the TOPAS-nBio extension, capable of handling the track-structure simulation and subsequent chemistry, and CompuCell3D, an agent-based model simulator for biological and environmental behavior of a population of cells. We verified the implementation by simulating the experimental conditions for a clonogenic survival assay of a 2-D PC-3 cell culture model (10 cells in 10,000 μm^2) irradiated by MV X-rays at several absorbed dose values from 0–8 Gy. The simulation considered cell growth and division, irradiation, DSB induction, DNA repair, and cellular response. The survival was obtained by counting the number of colonies, defined as a surviving primary (or seeded) cell with progeny, at 2.7 simulated days after irradiation. DNA repair was simulated with an MC implementation of the two-lesion kinetic model and the cell response with a p53 protein-pulse model. The simulated survival curve followed the theoretical linear–quadratic response with dose. The fitted coefficients $\alpha = 0.280 \pm 0.025/Gy$ and $\beta = 0.042 \pm 0.006/Gy^2$ agreed with published experimental data within two standard deviations. TOPAS-Tissue extends previous works by simulating in an end-to-end way the effects of radiation in a cell population, from irradiation and DNA damage leading to the cell fate. In conclusion, TOPAS-Tissue offers an extensible all-in-one simulation framework that successfully couples Compucell3D and TOPAS for multiscale simulation of the biological response to radiation.

Keywords: Monte Carlo track-structure simulation; agent-based modeling; multiscale modeling; radiation damage response; PC-3 cell survival

Citation: García García, O.R.; Ortiz, R.; Moreno-Barbosa, E.; D-Kondo, N.; Faddegon, B.; Ramos-Méndez, J. TOPAS-Tissue: A Framework for the Simulation of the Biological Response to Ionizing Radiation at the Multi-Cellular Level. *Int. J. Mol. Sci.* **2024**, *25*, 10061. https://doi.org/10.3390/ijms251810061

5. Discussion

5.1 cellular environment model

The results from section "4.2 Results for TOPAS-kinetoscope coupling" quantifying chemical yields using a model of cellular environment are still under development. This is because there are several drawbacks with the approach followed. For instance, the DNA was modeled as a homogeneously distributed with reactions modeled as first order reactions with OH, H and $\mathrm{e}_{\mathrm{aq}}^{-}$ [Michaels H.B. & Hunts J.W. (1978)]. Thus, this approximation does not allow characterize the spatial distribution and complexity of the DNA breaks, and consequently, the subsequent biological processes like DSB repair cannot be fed by these results. Nevertheless, from the quantified yields of OH+DNA reactions, and using an efficiency of damage of 20%, the estimated the total SSBs is about 1000/Gy per cell, a value consistent with the value reported in the literature [Hall E.J. & Giaccia A.J. (2012)]. An efficiency value of 13% was experimentally measured in [Milligan J.R., et al (1993) and used in MCTS simulations elsewhere [Nikjoo H. et al (1997), D-Kondo N., et al (2021)].

In addition, other biological processes were not considered but that will be added in future work. These processes include the protein crosslinking resulting from a recombination of protein radicals ($\mathrm{Pr} = \mathrm{Pr}$) [Chen X., et al (2023)], the reoxygenation rate at times between flash pulses [Wardman P. (2020)] nor the enzymatic response to the damaged biomolecules or the radicals produced [Hurbain J., et al (2022)]. Therefore, to better represent and study the effect of radiation dose in the competence between oxygen and antioxidants in the early biological radiation response, the proposed model can be extended to contemplate all these factors in future works.

5.2 Implementation of the Gillespie algorithm and temperature influence on TOPAS-nBio

Nevertheless, the study of computational methods (that allows the simulation of the long-term time evolution of chemical systems [Gillespie D.T. (1976), Gillespie D.T., et al (2013)] performed during this research work contributed to the implementation and validation of the Gillespie Algorithm in TOPAS-nBio [D-Kondo J.N., et al (2023)]. In that work, three verification tests were performed: 1) a simple reaction scheme with three virtual molecules and a known analytical solution; 2) a test for establishing the time for the homogeneous chemistry transition; and 3) the implemented Gillespie algorithm. Results showed good agreement with Kinetiscope calculations, which was used as reference software. Finally, for the validation of pure water irradiations using FLASH and conventional dose rates, the results for the final concentration of hydrogen peroxide as a function of the dose and the initial oxygen concentration were compared with experimental data and Kinetiscope. The reported experimental results for the G-Value of $\mathrm{H_2O_2}$ on water under FLASH irradiation with an initial oxygen concentration of $1.0\mathrm{mM}$ was $0.205 \pm 0.006\mu\mathrm{M/Gy}$ [Anderson A.R. & Hart E.J. (1962)] and remained constant for an oxygen concentration of $1.2\mathrm{mM}$ [Sehested K., et al (1968)], while for conventional irradiation with an initial oxygen concentration of $0.25\mathrm{mM}$ the $\mathrm{H_2O_2}$ yield was $0.099 \pm 0.004\mu\mathrm{M/Gy}$ [Roth O. & LaVerne J.A. (2011)]. These experimental results were used to validate the TOPAS-nBio simulations, where the standard deviations were within 1.97% and 0.083% for conventional and FLASH dose rates respectively [D-Kondo J.N., et al (2023)].

During the first period of this research work the temperature-dependent radiation chemistry parameters were implemented in TOPAS-nBio, that contributed to the publication reported in

[Ramos-Méndez J., et al (2022)]. Whereas this paper is not directly related to this research work, it was an important contribution to the extension of this MCTS code since the temperature is not a variable that is often considered, despite the fact that it can affect the number of DNA breaks under the same irradiation conditions [Tomita K., et al (1995)].

Both the implementation of the temperature dependence of the chemical kinetic parameters and the Gillespie algorithms extended the capabilities of TOPAS-nBio to simulate the radiation chemistry of aqueous solutions at low-LET $\sim 0.3\ \mathrm{keV}\ \mu\mathrm{m}^{-1}$ $^{60}\mathrm{Co}$ gamma rays. The majority of DNA breaks are caused by the indirect radiation effect on this LET range [Von Sontang C. (2005), Ramos-Méndez J., et al (2022)].

5.3 Development of TOPAS-Tissue

This research work contributed to the development and validation of TOPAS-Tissue, a new framework for the coupling of two MC-based codes: TOPAS and Compucell3D. This tool allows the multiscale simulation of cell survival from the irradiation to the biological response that determinates the outcome of DNA damage. The verification of the framework was performed comparing our simulated results with the survival curve of PC-3 prostate cancer cells under X-ray irradiation [Wakisaka Y., et al (2023)].

TOPAS-Tissue, through its CC3D operation, is capable of modeling the growth and division processes of a cell population during a pre-irradiation period. We assumed optimal conditions for the cell culture in this first version of the framework, this means that all cells were synchronized, and their growth followed a constant rate.

However, a more realistic approach would consider other factors linked to the cell cycle regulation, cellular development and radiosensitivity, such as the biochemical signaling or the availability of oxygen and nutrients in the cellular environment or the mechanical stress it experiences [Shirinifard A., et al (2009), Adrian G., et al (2019)]. CC3D already considers several functions to simulate their action. It automatically tracks the internal pressure of cells with a dedicated Potts plugin, which is a quantity related to mechanical stress [Swat M.H., et al (2012)], and the cell's growth rate can be dependent on other variables, such as the level of oxygen, nutrients or biochemical signals. Furthermore, the consumption or section of such chemicals can be accounted for by the uptake or secretion functions of CC3D [Shirinifard A., et al (2009), Swat M.H., et al (2012)]. Since CC3D also allows access to the values of a chemical field and its customized modification, the perturbation of the oxygen field by physical-chemical effects, such as the high dose rate of FLASH irradiation could be precomputed [D-Kondo N., et al (2021, 2023)].

In this research work, the DSBs assignment on individual cells was sampled from the delivered dose in each nucleus. This is a reasonable estimate for a uniform irradiation with MV X-rays and homogeneously distributed dose deposits [Rothkamm K., et al (2003)]. This is not the case for other radiation qualities, for example, high LET particles like heavy ions or protons. These particles leave a more densely distribution of ionizations along their primary track. The detail of these energy deposits influence the distribution and complexity of DNA breaks and need to be considered to accurately describe the response to this type of radiation.

Nevertheless, there is ongoing work to implement alternative methods to assign DNA damage in TOPAS-Tissue. For example, clustering algorithms like DBSCAN are already available on TOPAS-nBio

for DNA damage distribution calculations [Francis Z., et al (2011), Dos Santos M., et al (2014)]. They have been successfully used in RADCELL via Geant4-DNA, which was the first work to report a coupling between CC3D and Geant4. But it requires further modifications to account for the contribution of radiolytic chemical species.

The TLK model used in this research work is a simplification of the two main DSB repair pathways in cell's NHEJ and HR processes, represented by a slow and fast kinetic component respectively. However, it does not simulate explicitly the reactions between the repair proteins involved. This approximation limits the application of the model for cells with deficient protein expression, such as the XPF-deficient human fibroblast (XFE). However, kinetic models that consider an extended set of protein reactions exist [Belov O.V., et al (2015)], whereas the cell fate after irradiation was not simulated. This presents another opportunity to extend TOPAS-Tissue with this kind of kinetic model and complement them with the implemented mechanisms to determinate the cellular outcome.

In this regard, the cell fate decision is simulated with the accumulation of lethal lesions as DNA repairs and with a p53 protein network model that captures the general dynamics of the biological response to radiation. However, mutations on the p53 pathway, such as the ones that affect the expression of the TP53 gene sensory layer, that modify the activation of the repair mechanisms [Brahme A. & Lorat Y. (2023)] are not considered. Other biological process triggered by DNA damage, such as the cel cycle regulation by the phosphorylation of the checkpoint kinases (Chk1 and Chk2) by ATM, which are all key players in the biological response to radiation [Kohn K.W (1999), Zhao M., et al (2020)] are not considered. To tackle these issues, we can make use of other existing models for the regulation networks that control these biological processes in response to radiation damage, such as the *Cell Cycle Database,* an online repository of 26 models for the interactions of proteins and genes that regulates the cell cycle of yeast and human beings, available in the SBML files [Alfieri R. & Milanesi L. (2013)], which is a compatible database format on CC3D.

The simulated results for the survival curve agreed with experimental data within two standard deviations, validating the TOPAS-Tissue framework and the implemented models. However, the current model for the cellular response to radiation just considers one explicit cellular death pathway: The triggering of the apoptosis signal by Casp3 integrated inside the p53 protein network model. Future extensions of TOPAS-Tissue might consider other cell fate modules with different death pathways. Even to consider explicitly the spatial distribution and complexity of DNA breaks to simulate the formation of chromosomal aberrations through the disrepair of DSBs [Pfeiffer P., et al (2000), Forster J.C., et al (2019)].

These facts indicate that TOPAS-Tissue offers a flexible and extensible tool that can take advantage of all the available functions, tools and methods from the two MC codes that it combines, and it could represent the bedrock for further computational simulations, modeling and the general study of radiobiological research aimed at the development of better and more effective cancer treatments based on radiation therapy.

6. Future Work

6.1 Extending the cellular environment model and oxygen diffusion incorporation.

The current version of cellular environment proposed model can be extended and complemented in several ways. The current model contemplates the action of the superoxide dismutase that partially resupplies oxygen while producing hydrogen peroxide as a byproduct of the reaction $2O_2^- \xrightarrow{\text{SOD}} H_2O_2 + O_2$ [Wardman P. (1999)]. However, H_2O_2 is toxic to the cells [Montay-Gruel P., et al (2019), Wardman P. (2020)] and the current implementation doesn't include the biological response to this free radical accumulation. Nevertheless, there is a kinetic model proposed by [Hurbain J., et al (2022)] for the enzymatic response to oxidative stress where the neutralization of hydrogen peroxide by specialized proteins is explicitly described that can be incorporated into the proposed model to contemplate this biological aspect. However, an important limitation of the current implementation is that the reaction rates laws in Kinetiscope can only be defined in terms of positive powers of the involved reagent's concentrations [Hinsberg W. & Houle F. (2020)]. Therefore, reactions that describe biological processes, such as the interaction between proteins or the metabolisms of oxygen, governed by more complex functions, such as a Michaelis-Menten equation, cannot be declared in Kinetiscope. As an alternative, we can employ the CC3D internal tool Tellurium [Swat M.H., et al (2014)] to translate the proposed model into its language Antimony to take full advantage of a more flexible platform to solve coupled differential equations systems.

Even more importantly, the reoxygenation process by diffusion is fundamental for a more complete study of the competence between the oxygen damage fixation against its chemical repair by antioxidants [Wardman P. (1999,2020)]. Experimental results of FLASH irradiation indicate that the timing between two consecutive radiation pulses is an important factor in the final survival of cells, showing that if two pulses are separated by a sufficiently long intermediate period the cell survival is reduced compared to a single pulse with equivalent deposited dose, shown in figure 6.1. This effect is attributed to the reoxygenation of the cells after the first pulse depletes the internal oxygen [Ling C. et al (1978)]. This publication also presents experimental measurements of the oxygen resupply of completely depleted cells and a model that approximates the process as a one-dimensional diffusion system.

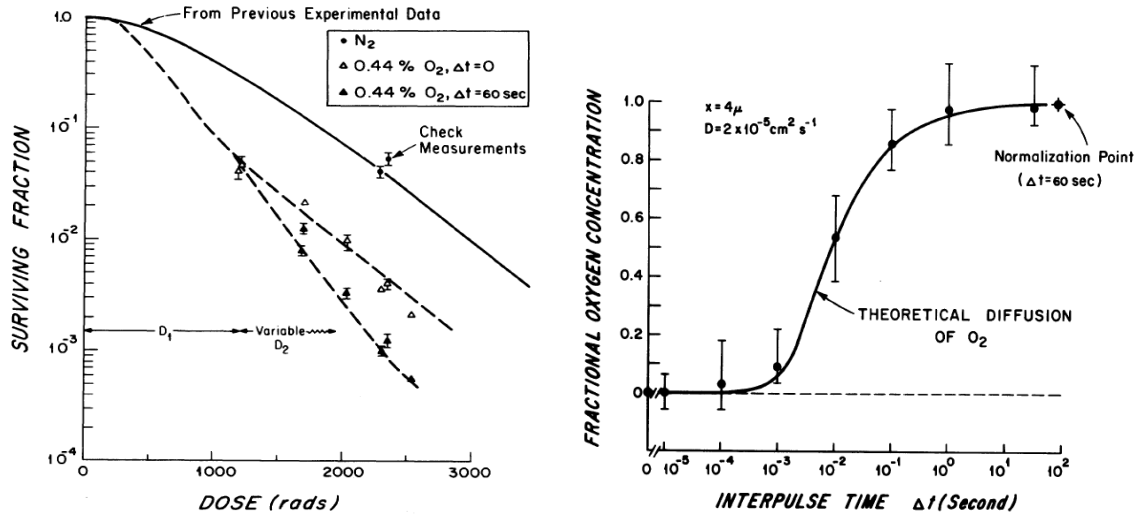

Figure 6.1. Experimental results of the reoxygenation process on FLASH irradiation. **Left**. The difference on the cell survival fraction for the same radiation dose distributed on a single pulse (white triangles) and two pulses separated by a 60 second period (black triangles) to allow reoxygenation. **Right**. Experimental measurements for the resupply of oxygen after complete depletion and the fitting of a theoretical 1-dimentional diffusion model. Images taken from [Ling C. et al (1978)].

To account for the effect of O_2 distribution of tissue, oxygen transport and consumption on a vascularized tumor model has been simulated before on CC3D [Shirinifard A., et al (2009)]. Thus, in future research works, this and other existing mechanisms that influence the early formation of DNA damage and the long term cellular outcomes can be integrated into the current cellular environment model and implemented into TOPAS-Tissue as an all-in-one simulation platform that controls all the parallel processes in order to develop a more complete understanding of the biological response to radiation damage of the cellular environment.

6.2 Cell Cycle simulation

The importance of explicitly simulating the cell cycle progression lays in the capacity to determine which DSBs repair pathways are available to the cells at the time of irradiation. This is reflected in part in the experimental results that demonstrate the changing radio sensitivity at the different stages of the cell division process [Sinclair W.K. & Morton R.A. (1966)], shown below on figure 6.2.

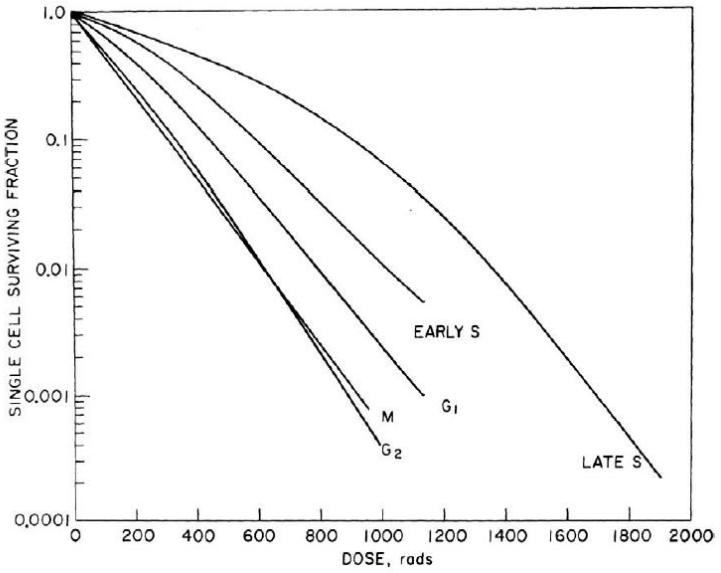

Figure 6.2. Results for the differences in the surviving fraction of synchronized Chinese Hamster cells on each cell cycle stage. Image taken from [Sinclair W.K. & Morton R.A. (1966)].

To achieve the simulation of the cell cycle regulation we can extend TOPAS-Tissue with an existing kinetic model proposed by [Iwamoto K., et al (2011)] to simulate the cell cycle natural transition for undamaged cells and consider the effect of ATM regulation, including the action of Chk1 for cellular arrest. In addition, we can make use of a tool compatible with CC3D, the PhenoCellPy package [Gianlupi J.F., et al (2023)], that has been used to simulate the explicit biochemical signaling for the transition between the cell cycle stages. Implementing this extension of CC3D could improve the modeling detail of this biological behavior. Therefore, future work is planned to include this and other models that describe distinct cell behaviors into TOPAS-Tissue, in a compatible SBML format through CC3D.

6.3 Long range bio-signaling

Complementary to the capacity of the Tellurium tool for handing the internal bio-signaling networks, the CC3D chemical field diffusion tools can handle the extracellular long-range signaling, such as the Prostaglandin E2 (PGE2) pro-mitotic factor, a protein produced by Casp3 apoptosis signal on dying cells that stimulate the growth of surviving cells and contributes to the post irradiation repopulation [Zhao M., et al (2020)]. An example of the PGE2 effect can be seen experimentally on in vitro assays where a small number of 4T1 breast cancer cells with a fluorescent tag were seeded on much larger populations of untagged cells, referred as “feeders”, irradiated under different X-ray doses (0-12Gy), the growth factor secreted by the dying cells influenced the growth of the tagged cells resulting on much larger populations after the same period [Huang Q., et al (2011)], these results are presented on figure 6.3.

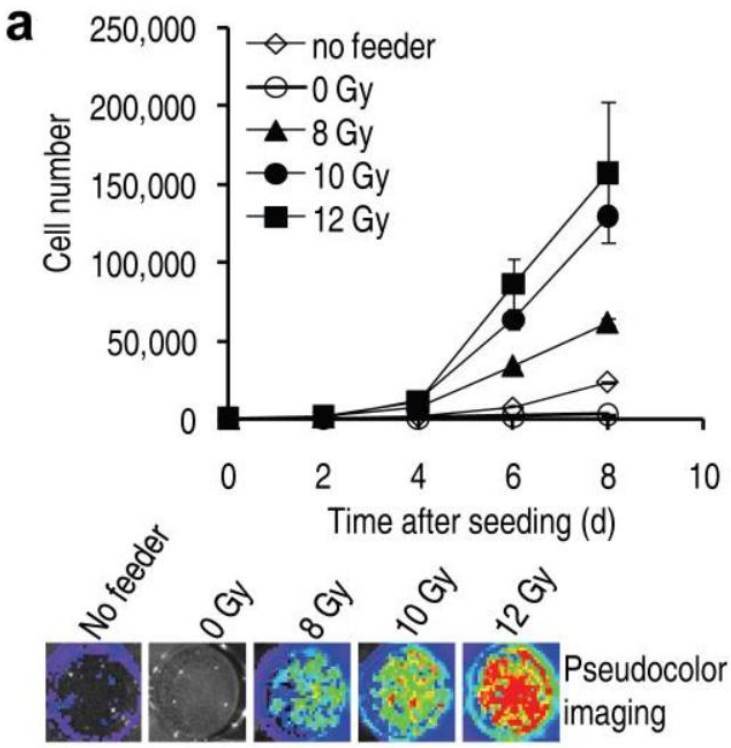

Figure 6.3. experimental results for the growth of 4T1 breast cancer cells stimulated by the PGE2 signal of irradiated feeder cells under different X-ray doses. Image taken from period [Huang Q., et al (2011)]

CC3D has been used to simulate the action of the *Vascular Endothelial Growth Factor* (VEGF), a stimulant for the growth of new vascular cells secreted by hypoxic cells, on a vascularized tumor model [Shirinifard A., et al (2009)]. This model accounts for the diffusion coefficient, the secretion and absorption rates of the bio-signal and the cellular growth rate dependent on the concentration of the VEGF. Taking this existing model as a starting point, other long-range bio-signaling such as the PGE2 repopulation effect can be implemented on TOPAS-Tissue on future research works.

6.4 Extending the DNA damage calculation model

In regards of the DNA damage calculation, we can go a step further than the use of the current phase spaces available on TOPAS-nBio. Precomputed lookup tables that relate micro and nanodosimetric quantities with the probability of DNA breaks induction that can reconstruct not only their spatial distribution but also their complexity, have been recently proposed [Thibaut Y., et al (2023)]. These lookup tables represent a very efficient tool for the calculation of radiation damage, especially at the cell population level where the calculation of lesions on individual cellular nucleus from the fundamental physical-chemical interactions of radiation could be computationally prohibitive.

These and other possible future projects can complement this research work and incorporated in the TOPAS-Tissue framework. The combined use of MCTS and ABM methods are the next step on the study of radiation biology from the computer simulation perspective and represents an important instrument for novel cancer treatments research.

7. Conclusions

This research work contributed to the combined use of specialized MC codes for the simulation of the distinct stages of the irradiation of a biological target and its consequences. The Gillespie algorithm, capable of simulating the long-term time evolution of chemical systems, and models for the kinetic chemical parameters, such as the reaction rate and diffusion coefficients, dependent on the temperature were studied for their subsequent implementation in TOPAS-nBio. Thus, this work contributed to extending the capacity of TOPAS-nBio to simulate both the heterogeneous and homogeneous chemical stages of the water radiolysis process.

A methodology for the simulation of the cellular environment consisting of five general families of biomolecules and the two most important antioxidants GSH and $AscH^-$, irradiated under FLASH and conventional dose rates, was implemented in TOPAS-nBio and Kinetiscope. The results are pending to be published. This model could serve as the basis of a more detailed version that considers the distribution and complexity of DNA breaks and the cellular response to other damaged biomolecules.

Finally, this work contributed to the development of a new framework for the multiscale simulation of the irradiation and biological evolution of a cell population TOPAS-Tissue, developed at the University of California San Francisco. This framework couples two well-established Monte Carlo-based codes: TOPAS-nBio and Compucell3D. The framework was used to construct a model of a PC-3 cell culture irradiated with an MV X-ray source in the range of 0–8 Gy. The framework allowed an easy simulation setup to reproduce the pre-irradiation growth of the cell culture from an initial number of seeded cells to a final confluency. The dose was scored in two distinct cellular compartments: Cytoplasm and nucleus. DSBs were randomly sampled, following a Poisson distribution, from the dose in each cell's nucleus, and assigned to them. A coupled model consisting of DNA repair and a cell response model were implemented. Two cell inactivation conditions were considered: The presence of lethal lesions and apoptosis triggered by the Caspase3 enzyme signal. The cell survival curve was simulated from the counting of colonies. The parameters from a fitted linear quadratic model differed by two standard deviations from published measured data.

The new framework offers an all-in-one multiscale platform for the irradiation of multi-cellular structures and their biological response modeling. It considers the spatial distribution of radiation-induced lesions, changes in the cellular environment, such as oxygen availability, and models for the radiation influence on internal cellular processes like cell cycle regulation, which is an ongoing work for future publications. Overall, this work provides the foundation to assist future research on the understanding of tissue response to radiation, which is crucial for the development of new radiotherapy techniques, by enabling coupled and versatile simulations of physical and biological processes using two dedicated and validated software.

Bibliography

Abdel-Wahab M., Gondhowiardjo S.S., Rosa A.A., Lievens Y., El-Haj N., Polo Rubio J.A., Prajogi G.B., Helgadottir H., Zubizarreta E., Meghzifene A., Ashraf V., Hahn S., Williams T. & Gospodarowicz M. (2021). Global Radiotherapy: Current Status and Future Directions-White Paper. *JCO global oncology*, *7*, 827–842. https://doi.org/10.1200/GO.21.00029

Adrian G., Konradsson E., Lempart M., Bäck S., Ceberg C. & Petersson K. (2019). The FLASH effect depends on oxygen concentration. *The British journal of radiology*, *93*(1106), 20190702. https://doi.org/10.1259/bjr.20190702

Agmon N. (1984). Diffusion with back reaction. J Chem Phys 81:2811–2817. doi:10.1063/1.447954

Alberts B., Johnson A., Lewis J., Raff M., Roberts K. & Walte P. (2002). Molecular Biology of the Cell. 4th edition. New York: Garland Science. The Shape and Structure of Proteins. Available from: https://www.ncbi.nlm.nih.gov/books/NBK26830/

Alfieri R. & Milanesi L. (2013). Cell Cycle Database. In: Dubitzky, W., Wolkenhauer, O., Cho, KH., Yokota, H. (eds) Encyclopedia of Systems Biology. Springer, New York, NY. https://doi.org/10.1007/978-1-4419-9863-7_1069

Alizadeh E. & Sanche L. (2012). Precursors of solvated electrons in radiobiological physics and chemistry. *Chemical reviews*, *112*(11), 5578–5602. https://doi.org/10.1021/cr300063r

Anderson A.R., & Hart E.J. (1962). Radiation Chemistry of Water with Pulsed High Intensity Electron Beams. *Journal of Physical Chemistry*, *66*(1). https://doi.org/10.1021/j100807a014

Andreo P., Burns D.T., Nahum A.E., Seuntjens J.P. & Attix F.H. (2017). *Fundamentals of ionizing radiation dosimetry* (2nd edition). WILEY-VCH.
https://search.ebscohost.com/login.aspx?direct=true&scope=site&db=nlebk&db=nlabk&AN=1535812

Arruebo M., Vilaboa N., Sáez-Gutierrez B., Lambea J., Tres A., Valladares M. & González-Fernández A. (2011). Assessment of the evolution of cancer treatment therapies. *Cancers*, *3*(3), 3279–3330. https://doi.org/10.3390/cancers3033279

Asaithamby A., Uematsu N., Chatterjee A., Story M.D., Burma S. & Chen D.J. (2008). Repair of HZE-particle-induced DNA double-strand breaks in normal human fibroblasts. *Radiation research*, *169*(4), 437–446.
https://doi.org/10.1667/RR1165.1

Atkins P.W. & De Paula J. (2006). Atkins' Physical Chemistry. 8th Edition, Oxford University Press, Oxford, New York.

Attix F.H. (1986). Introduction to Radiological Physics and Radiation Dosimetry. J. Wiley and Son, New York. http://dx.doi.org/10.1002/9783527617135

Ayene I.S., Koch C.J. & Krisch R.E. (1995). Modification of Radiation-Induced Strand Breaks by Glutathione: Comparison of Single- and Double-Strand Breaks in SV40 DNA. *Radiation Research*, *144*(1), 1–8. https://doi.org/10.2307/3579229

Ayene I.S., Koch C.J. & Krisch R.E. (1996). Simulation of the Cellular Oxygen Effect with an SV40 DNA Model System Using DNA Strand Breaks as an End Point. *Radiation Research*, *146*(5), 501–509. https://doi.org/10.2307/3579550

Azzam E.I., Jay-Gerin J.P. & Pain D. (2012). Ionizing radiation-induced metabolic oxidative stress and prolonged cell injury. *Cancer letters*, *327*(1-2), 48–60. https://doi.org/10.1016/j.canlet.2011.12.012

Balasubramanian B., Pogozelski W.K. & Tullius T.D. (1998). DNA strand breaking by the hydroxyl radical is governed by the accessible surface areas of the hydrogen atoms of the DNA backbone, *Proc. Natl. Acad. Sci. U.S.A.* 95 (17) 9738-9743,

Ballarini F., Biaggi M., Merzagora M., Ottolenghi A., Dingfelder M., Friedland W., Jacob P., Paretzke H.G. (2000). Stochastic Aspects and Uncertainties in the Prechemical and Chemical Stages of Electron Tracks in Liquid Water: A Quantitative Analysis Based on Monte Carlo Simulations. Radiation and Environmental Biophysics. 2000;39(3):179–88. doi: 10.1007/s004110000060.

Balter A., Merks R.M.H., Popławski N.J., Swat M. & Glazier J.A. (2007). The Glazier-Graner-Hogeweg Model: Extensions, Future Directions, and Opportunities for Further Study. In: Anderson, A.R.A., Chaplain, M.A.J., Rejniak, K.A. (eds) Single-Cell-Based Models in Biology and Medicine. Mathematics and Biosciences in Interaction. Birkhäuser Basel. https://doi.org/10.1007/978-3-7643-8123-3_7

Baron F., Nau F., Guérin-Dubiard C., Bonnassie S., Gautier M., Andrews S.C. & Jan S. (2016). Egg white versus Salmonella Enteritidis! A harsh medium meets a resilient pathogen. *Food microbiology*, *53*(Pt B), 82–93. https://doi.org/10.1016/j.fm.2015.09.009

Baskar R., Lee K.A., Yeo R. & Yeoh K.W. (2012). Cancer and radiation therapy: current advances and future directions. *International journal of medical sciences*, *9*(3), 193–199. https://doi.org/10.7150/ijms.3635

Becker D., Summerfield S., Gillich S. & Sevilla M.D. (1994). Influence of oxygen on the repair of direct radiation damage to DNA by thiols in model systems. *International journal of radiation biology*, *65*(5), 537–548. https://doi.org/10.1080/09553009414550631

Belmonte J.M., Clendenon S.G., Oliveira G.M., Swat M.H., Greene E.V., Jeyaraman S., Glazier J.A. & Bacallao R.L. (2016). Virtual-tissue computer simulations define the roles of cell adhesion and proliferation in the onset of kidney cystic disease. *Molecular biology of the cell*, *27*(22), 3673–3685. https://doi.org/10.1091/mbc.E16-01-0059

Belov O.V., Krasavin E.A., Lyashko M.S., Batmunkh M. & Sweilam N.H. (2015). A quantitative model of the major pathways for radiation-induced DNA double-strand break repair. *Journal of theoretical biology*, *366*, 115–130. https://doi.org/10.1016/j.jtbi.2014.09.024

Bernal M.A., Bordage M.C., Brown J.M.C., Davídková M., Delage E., El Bitar Z., Enger S.A., Francis Z., Guatelli S., Ivanchenko V.N., Karamitros M., Kyriakou I., Maigne L., Meylan S., Murakami K., Okada S., Payno H., Perrot Y., Petrovic I., Pham Q.T., Ristic-Fira A., Sasaki T., Štěpán V., Tran H.N., Villagrasa C. & Incerti S. (2015). Track structure modeling in liquid water: A review of the Geant4-DNA very low energy extension of the Geant4 Monte Carlo simulation toolkit. *Physica medica : PM : an international journal devoted to the applications of physics to medicine and biology : official journal of the Italian Association of Biomedical Physics (AIFB)*, *31*(8), 861–874. https://doi.org/10.1016/j.ejmp.2015.10.08

Bernhardt Ph., Friedland W., Jacob P. & Paretzke H.G. (2003). Modeling of ultrasoft X-ray induced DNA damage using structured higher order DNA targets, International Journal of Mass Spectrometry, Volumes 223–224, 2003, Pages 579-597, ISSN 1387-3806, https://doi.org/10.1016/S1387-3806(02)00879-5.

Bortner C.D. & Cidlowski J.A. (2003). Uncoupling cell shrinkage from apoptosis reveals that Na+ influx is required for volume loss during programmed cell death. *The Journal of biological chemistry*, *278*(40), 39176–39184. https://doi.org/10.1074/jbc.M303516200

Brahme A. & Lorat Y. (2023). Dual Nucleosomal Double-Strand Breaks Are the Key Effectors of Curative Radiation Therapy. *Biophysica*. 2023; 3(4):668-694. https://doi.org/10.3390/biophysica3040045

Brahme A. (2014). Accurate analytical description of the cell survival and dose-response relationships at low and high doses and LETs. In Comprehensive Biomedical Physics. Elsevier; 2014:121-142. Pages 121-142, ISBN 9780444536334, https://doi.org/10.1016/B978-0-444-53632-7.00807-8.

Buxton G.V., Greenstock C.L., Helman W.P. & Ross A.B. (1988). Critical Review of rate constants for reactions of hydrated electrons, hydrogen atoms and hydroxyl radicals (·OH/·O^- in Aqueous Solution. *J. Phys. Chem. Ref. Data* 1 April 1988; 17 (2): 513–886. https://doi.org/10.1063/1.555805

Canoy R.J., Shmakova A., Karpukhina A., Shepelev M., Germini D. & Vassetzky Y. (2022). Factors That Affect the Formation of Chromosomal Translocations in Cells. *Cancers*, *14*(20), 5110. https://doi.org/10.3390/cancers14205110

Carrasco-Hernandez J., Ramos-Méndez J., Padilla-Rodal E. & Avila-Rodriguez M.A. (2023). Cellular lethal damage of ^{64}Cu incorporated in mammalian genome evaluated with Monte Carlo methods. *Frontiers in medicine*, *10*, 1253746. https://doi.org/10.3389/fmed.2023.1253746

Casas F. Bese N., van der Merwe D., Hendry J. & Jeremic B. (2008). Radiation Therapy, Editor(s): Harald Kristian (Kris) Heggenhougen, International Encyclopedia of Public Health, Academic Press, Pages 483-491, ISBN 9780123739605, https://doi.org/10.1016/B978-012373960-5.00261-6.

Chang H.H.Y., Pannunzio N.R., Adachi N. & Lieber M.R. (2017). Non-homologous DNA end joining and alternative pathways to double-strand break repair. *Nature reviews. Molecular cell biology*, *18*(8), 495–506. https://doi.org/10.1038/nrm.2017.48

Chang, D. S., Lasley, F. D., Das, I. J., Mendonca, M. S., & Dynlacht, J. R. (2022). *Basic radiotherapy physics and biology*. Springer International Publishing. ISBN 978-3-030-61899-5. DOI https://doi.org/10.1007/978-3-030-61899-5

Charlton D.E., Nikjoo H. & Humm J.L. (1989). Calculation of Initial Yields of Single-Strand and Double-Strand Breaks in Cell-Nuclei From Electrons, Protons and Alpha-Particles. International Journal of Radiation Biology, 56(1), 1–19. 10.1080/09553008914551141

Chatzipapas K.P., Tran N.H., Dordevic M., Zivkovic S., Zein S., Shin G-W., Sakata D., Lampe N., Brown J.M.C., Ristic-Fira A., Petrovic I., Kyriakou I., Emfietzoglou D., Guatelli S. & Incerti S. (2023). Simulation of DNA damage using Geant4-DNA: an overview of the "molecularDNA" example application. *Prec Radiat Oncol*. 2023; 7: 4–14. https://doi.org/10.1002/pro6.1186

Chen X., Josephson B. & Davis B.G. (2023). Carbon-Centered Radicals in Protein Manipulation. *ACS central science*, *9*(4), 614–638. https://doi.org/10.1021/acscentsci.3c00051

Choi K., Medley J.K., König M., Stocking K., Smith L., Gu S. & Sauro H.M. (2018). Tellurium: An extensible python-based modeling environment for systems and synthetic biology. *Bio Systems*, *171*, 74–79. https://doi.org/10.1016/j.biosystems.2018.07.006

Claydon C.R., Segal G.A. & Taylor H.S. (1971) Theoretical Interpretation of the Optical and Electron Scattering Spectra of H_2O. *J. Chem. Phys.* 1 May 1971; 54 (9): 3799–3816. https://doi.org/10.1063/1.1675431

Cobut V., Frongillo Y., Patau J.P., Goulet T., Fraser M. & Jay-Gerin J. (1998). Monte Carlo simulation of fast electron and proton tracks in liquid water -- I. physical and physicochemical aspects. *Radiation Physics and Chemistry, 51*, 229-243.

Curtis S.B. (1986). Lethal and potentially lethal lesions induced by radiation--a unified repair model. *Radiation research*, *106*(2), 252–270.

Dal Castel P. (2022 August 3). "CompuCell3D Workshop 3.1 Secretion Absorption and Avascular Tumor" [Video] https://www.youtube.com/watch?v=tAcoRmNkVqo

Datta N.R. & Bodis S. (2019). Hyperthermia with radiotherapy reduces tumour alpha/beta: Insights from trials of thermoradiotherapy vs radiotherapy alone, Radiotherapy and Oncology, Volume 138, 2019, Pages 1-8, ISSN 0167-8140, https://doi.org/10.1016/j.radonc.2019.05.002

Debela D.T., Muzazu S.G., Heraro K.D., Ndalama M.T., Mesele B.W., Haile D.C., Kitui S.K. & Manyazewal T. (2021). New approaches and procedures for cancer treatment: Current perspectives. *SAGE open medicine*, *9*, 20503121211034366. https://doi.org/10.1177/20503121211034366

Diercksen G.H.F., Kraemer W.P., Rescigno T.N., Bender C.F., McKoy B.V., Langhoff S.R. & Langhoff P.W. (1982). Theoretical studies of photoexcitation and ionization in H_2O. *J. Chem. Phys.* 15 January 1982; 76 (2): 1043–1057. https://doi.org/10.1063/1.443072

Dietzen D.J. (2018). Amino acids, peptides, and proteins. In *Principles and Applications of Molecular Diagnostics* (pp. 345-380). Elsevier. https://doi.org/10.1016/B978-0-12-816061-9.00013-8

Dizdaroglu M. & Jaruga P. (2012). Mechanisms of free radical-induced damage to DNA. *Free radical research*, *46*(4), 382–419. https://doi.org/10.3109/10715762.2011.653969

D-Kondo J. N., Garcia-Garcia O.R., LaVerne J.A., Faddegon B., Schuemann J., Shin W.G. & Ramos-Méndez J. (2023). An integrated Monte Carlo track-structure simulation framework for modeling inter and intra-track effects on homogenous chemistry. *Physics in medicine and biology*, *68*(12), 10.1088/1361-6560/acd6d0. https://doi.org/10.1088/1361-6560/acd6d0

D-Kondo N., Moreno-Barbosa E., Štěphán V., Stefanová K., Perrot Y., Villagrasa C., Incerti S., De Celis Alonso B., Schuemann J., Faddegon B. & Ramos-Méndez J. (2021). DNA damage modeled with Geant4-DNA: effects of plasmid DNA conformation and experimental conditions. *Physics in medicine and biology*, *66*(24), 10.1088/1361-6560/ac3a22. https://doi.org/10.1088/1361-6560/ac3a22

Dos Santos M., Clairand I., Gruel G., Barquinero J.F., Incerti S. & Villagrasa C. (2014). Influence of chromatin condensation on the number of direct DSB damages induced by ions studied using a Monte Carlo code. *Radiation protection dosimetry*, *161*(1-4), 469–473. https://doi.org/10.1093/rpd/ncu029

Douglass M., Bezak E. & Penfold S. (2015). Development of a radiation track structure clustering algorithm for the prediction of DNA DSB yields and radiation induced cell death in Eukaryotic cells. *Physics in medicine and biology*, *60*(8), 3217–3236. https://doi.org/10.1088/0031-9155/60/8/3217

Edel S., Terrissol M., Peudon A., Kümmerle E. & Pomplun E. (2006). Computer simulation of strand break yields in plasmid pBR322: DNA damage following 125I decay. *Radiation protection dosimetry*, *122*(1-4), 136–140. https://doi.org/10.1093/rpd/ncl453

Edgren M., Nishidai T., Scott, O.C. & Révész L. (1985). Combined effect of misonidazole and glutathione depletion by buthionine sulphoximine on cellular radiation response. *International journal of radiation biology and related studies in physics, chemistry, and medicine*, *47*(4), 463–474.

Elliot A.J. & Bartels D. (2009). The reaction Set, rate constants and g-values for the simulation of the radiolysis of light water At. Energy Canada Ltd. Rep. 41 153–127160 (https://inis.iaea.org/search/search.aspx?orig_q=RN:41057263)

Elliot A.J. & McCracken D.R. (1990). Computer modelling of the radiolysis in an aqueous lithium salt blanket: Suppression of radiolysis by addition of hydrogen, Fusion Engineering and Design, Volume 13, Issue 1, 1990, Pages 21-27, ISSN 0920-3796, https://doi.org/10.1016/0920-3796(90)90028-5.

Elliot A.J. (1994). Rate constants and g-values for the simulation of the radiolysis of light water over the range 0-300 deg C (AECL--11073). Canada

Faddegon B., Blakely E.A., Burigo L., Censor Y., Dokic I., Domínguez Kondo N., Ortiz R., Ramos Méndez J., Rucinski A., Schubert K., Wahl N. & Schulte R. (2023). Ionization detail parameters and cluster dose: a mathematical model for selection of nanodosimetric quantities for use in treatment planning in charged particle radiotherapy. *Physics in medicine and biology*, *68*(17), 10.1088/1361-6560/acea16. https://doi.org/10.1088/1361-6560/acea16

Faddegon B., Ramos-Méndez J., Schuemann J., McNamara A., Shin J., Perl J. & Paganetti H. (2020). The TOPAS tool for particle simulation, a Monte Carlo simulation tool for physics, biology and clinical research. *Physica medica : PM : an international journal devoted to the applications of physics to medicine and biology : official journal of the Italian Association of Biomedical Physics (AIFB)*, *72*, 114–121. https://doi.org/10.1016/j.ejmp.2020.03.019

Favaudon V., Caplier L., Monceau V., Pouzoulet F., Sayarath M., Fouillade C., Poupon M.F., Brito I., Hupé P., Bourhis J., Hall J., Fontaine J.J. & Vozenin M.C. (2014). Ultrahigh dose-rate FLASH irradiation increases the differential response between normal and tumor tissue in mice. *Science translational medicine*, *6*(245), 245ra93. https://doi.org/10.1126/scitranslmed.3008973

Favaudon V., Caplier L., Monceau V., Pouzoulet F., Sayarath M., Fouillade C., Poupon M.F., Brito I., Hupé P., Bourhis J., Hall J., Fontaine J.J. & Vozenin M.C. (2014). Ultrahigh dose-rate FLASH irradiation increases the differential response between normal and tumor tissue in mice. *Science translational medicine*, *6*(245), 245ra93. https://doi.org/10.1126/scitranslmed.3008973

Felsenfeld G., & Groudine M. (2003). Controlling the double helix. *Nature*, *421*(6921), 448–453. https://doi.org/10.1038/nature01411

Fernández-Varea J.M., Salvat F., Dingfelder M. & Liljequist D. (2005). A relativistic optical-data model for inelastic scattering of electrons and positrons in condensed matter, Nuclear Instruments and Methods in Physics Research Section B: Beam Interactions with Materials and Atoms, Volume 229, Issue 2, Pages 187-218, ISSN 0168-583X, https://doi.org/10.1016/j.nimb.2004.12.002.

Field S.B. & Bewley D.K. (1974). Effects of dose-rate on the radiation response of rat skin. *International journal of radiation biology and related studies in physics, chemistry, and medicine*, *26*(3), 259–267. https://doi.org/10.1080/09553007414551221

Fink C.C., Slepchenko B., Moraru I.I., Watras J., Schaff J.C. & Loew L.M. (2000). An image-based model of calcium waves in differentiated neuroblastoma cells. *Biophysical journal*, *79*(1), 163–183. https://doi.org/10.1016/S0006-3495(00)76281-3

Forster J.C., Douglass M.J.J., Phillips W.M. & Bezak E. (2019). Stochastic multicellular modeling of x-ray irradiation, DNA damage induction, DNA free-end misrejoining and cell death. *Scientific reports*, *9*(1), 18888. https://doi.org/10.1038/s41598-019-54941-1

Francis Z., Villagrasa C. & Clairand I. (2011). Simulation of DNA damage clustering after proton irradiation using an adapted DBSCAN algorithm. *Computer methods and programs in biomedicine*, *101*(3), 265–270. https://doi.org/10.1016/j.cmpb.2010.12.012

Friedland W., Jacob P., Bernhardt P., Paretzke H.G. & Dingfelder M. (2003). Simulation of DNA damage after proton irradiation. *Radiation research*, *159*(3), 401–410. https://doi.org/10.1667/0033-7587(2003)159[0401:soddap]2.0.co;2

Friedland W., Schmitt E., Kundrát P., Dingfelder M., Baiocco G., Barbieri S. & Ottolenghi A. (2017). Comprehensive track-structure based evaluation of DNA damage by light ions from radiotherapy-relevant energies down to stopping. *Scientific reports*, *7*, 45161. https://doi.org/10.1038/srep45161

Frongillo Y., Goulet T., Fraser M., Cobut V., Patau J.P. & Jay-Gerin J. (1998). Monte Carlo simulation of fast electron and proton tracks in liquid water -- II. nonhomogeneous chemistry. *Radiation Physics and Chemistry, 51*, 245-254.

Galano A. & Alvarez-Idaboy J. (2011). Glutathione: Mechanism and kinetics of its non-enzymatic defense action against free radicals. RSC Advances. 1. 1763. 10.1039/c1ra00474c.

Gebicki J.M., Nauser T., Domazou A., Steinmann D., Bounds P.L. & Koppenol W.H. (2010). Reduction of protein radicals by GSH and ascorbate: Potential biological significance. *Amino Acids*, *39*(5), 1131-1137. https://doi.org/10.1007/s00726-010-0610-7

Ghosh R., Das D. & Franco S. (2018). The Role for the DSB Response Pathway in Regulating Chromosome Translocations. *Advances in experimental medicine and biology*, *1044*, 65–87. https://doi.org/10.1007/978-981-13-0593-1_6

Gianlupi J.F., Sego T.J., Sluka J.P. & Glazier J.A. (2023). PhenoCellPy: A Python package for biological cell behavior modeling. bioRxiv 2023. doi: https://doi.org/10.1101/2023.04.12.535625

Gilchrist D.A. (2024). *Mitosis*, *Genome.gov*. Available at: https://www.genome.gov/genetics-glossary/Mitosis (Accessed: 14 November 2024).

Gillespie D.T. (1976). A general method for numerically simulating the stochastic time evolution of coupled chemical reactions, Journal of Computational Physics, Volume 22, Issue 4, Pages 403-434, ISSN 0021-9991, https://doi.org/10.1016/0021-9991(76)90041-3.

Gillespie D.T. (2000). The chemical Langevin equation. *J. Chem. Phys.* 1 July 2000; 113 (1): 297–306. https://doi.org/10.1063/1.481811

Gillespie D.T., Hellander A. & Petzold L.R. (2013). Perspective: Stochastic algorithms for chemical kinetics. *J. Chem. Phys.* 7 May 2013; 138 (17): 170901.

Glazier, J.A., Balter, A., Popławski, N.J. (2007). Magnetization to Morphogenesis: A Brief History of the Glazier-Graner-Hogeweg Model. In: Anderson, A.R.A., Chaplain, M.A.J., Rejniak, K.A. (eds) Single-Cell-Based Models in Biology and Medicine. Mathematics and Biosciences in Interaction. Birkhäuser Basel. https://doi.org/10.1007/978-3-7643-8123-3_4

Goulet T. & Jay-Gerin J.P. (1989). Thermalization of Subexcitation Electrons in Solid Water. *Radiation Research*, *118*(1), 46–62. https://doi.org/10.2307/3577422

Goulet T., Jay-Gerin J.P. & Patau J. (1990). Influence of the parent cation on the thermalization of subexcitation electrons in solid water. United States. https://doi.org/10.1021/j100381a065

Hall E.J. & Giaccia A.J. (2012). Radiobiology for the Radiologist. 7th Edition, Wolters Kluwer Health/Lippincott Williams & Wilkins, Philadelphia.

Hefferin M.L. & Tomkinson A.E. (2005). Mechanism of DNA double-strand break repair by non-homologous end joining. *DNA repair*, *4*(6), 639–648. https://doi.org/10.1016/j.dnarep.2004.12.005

Heller J.M., Hamm R.N., Birkhoff R.D. & Painter L.R. (1974). Collective oscillation in liquid water. *J. Chem. Phys.* 1 May 1974; 60 (9): 3483–3486. https://doi.org/10.1063/1.1681563

Hendry J.H., Moore J.V., Hodgson B.W. & Keene J.P. (1982). The constant low oxygen concentration in all the target cells for mouse tail radionecrosis. *Radiation research*, *92*(1), 172–181.

Hervé du Penhoat M.A., Goulet T., Frongillo Y., Fraser M.J., Bernat P. & Jay-Gerin J.P. (2000) Radiolysis of Liquid Water at Temperatures up to 300 C: A Monte Carlo Simulation Study. The Journal of Physical Chemistry A. 50. Vol. 104. American Chemical Society; 2000.; pp. 11757–70

Hinsberg W. & Houle F. (2020) kinetiscope online user's manual Version 1.1. Available online: https://hinsberg.net/kinetiscope/manual/toc.htm (accessed on 15 September 2024)

Houle F.A., & Hinsberg W.D. (1995). Stochastic simulations of temperature programmed desorption kinetics. *Surface Science, 338(1-3), 329–346.* doi:10.1016/0039-6028(95)00554-4

Howard-Flanders P. (1960) Effect of Oxygen on the Radiosensitivity of Bacteriophage in the Presence of Sulphydryl Compounds. *Nature* **186**, 485–487 (1960). https://doi.org/10.1038/186485a0

Huang Q., Li F., Liu X., Li W., Shi W., Liu F.F., O'Sullivan B., He Z., Peng Y., Tan A.C., Zhou L., Shen J., Han G., Wang X.J., Thorburn J., Thorburn A., Jimeno A., Raben D., Bedford J.S., & Li C.Y. (2011). Caspase 3-mediated stimulation of tumor cell repopulation during cancer radiotherapy. *Nature medicine*, *17*(7), 860–866. https://doi.org/10.1038/nm.2385

Hucka M., Bergmann F., Dräger A., Hoops S., Keating S., Le Novère N., Myers C., Olivier B., Sahle S., Schaff J., Smith L., Waltemath D. & Wilkinson D. (2018). The Systems Biology Markup Language (SBML): Language Specification for Level 3 Version 2 Core. *Journal of Integrative Bioinformatics*, *15*(1), 20170081. https://doi.org/10.1515/jib-2017-0081

Hughes J.R. & Parsons J.L. (2020). FLASH Radiotherapy: Current Knowledge and Future Insights Using Proton-Beam Therapy. *International journal of molecular sciences*, *21*(18), 6492. https://doi.org/10.3390/ijms21186492

Hurbain J., Thommen Q., Anquez F. & Pfeuty B. (2022). Quantitative modeling of pentose phosphate pathway response to oxidative stress reveals a cooperative regulatory strategy. *iScience*, *25*(8), 104681. https://doi.org/10.1016/j.isci.2022.104681

Iarovaia O.V., Rubtsov M., Ioudinkova E., Tsfasman T., Razin S.V. & Vassetzky Y.S. (2014). Dynamics of double strand breaks and chromosomal translocations. *Molecular cancer*, *13*, 249. https://doi.org/10.1186/1476-4598-13-249

Incerti S., Baldacchino G., Bernal M., Capra R., Champion C., Francis Z., Guatelli S., Guèye P., Mantero A., Mascialino B., Moretto P., Nieminen P., Rosenfeld A., Villagrasa C. & Zacharatou C. (2010). THE Geant4-DNA project. International Journal of Modeling, Simulation, and Scientific Computing, 1(2), 157–178. 10.1142/S1793962310000122

Incerti S., Kyriakou I., Bernal M.A., Bordage M.C., Francis Z., Guatelli S., Ivanchenko V., Karamitros M., Lampe N., Lee S.B., Meylan S., Min C.H., Shin W.G., Nieminen P., Sakata D., Tang N., Villagrasa C., Tran H. & Brown J.M.C. (2018). Geant4-DNA example applications for track structure simulations in liquid water: A report from the Geant4-DNA Project. Medical Physics, 0(0), 1–18. 10.1002/mp.13048

INEGI (2023) Estadísticas a propósito del día mundial contra el cáncer (4 de febrero) datos nacionales. COMUNICADO DE PRENSA NÚM. 77/23

Iwamoto K., Hamada H., Eguchi Y., & Okamoto M. (2011). Mathematical modeling of cell cycle regulation in response to DNA damage: exploring mechanisms of cell-fate determination. *Bio Systems*, *103*(3), 384–391. https://doi.org/10.1016/j.biosystems.2010.11.011

Jafari Nivlouei S., Soltani M., Shirani E., Salimpour M.R., Travasso R. & Carvalho J. (2022). A multiscale cell-based model of tumor growth for chemotherapy assessment and tumor-targeted therapy through a 3D computational approach. *Cell proliferation*, *55*(3), e13187. https://doi.org/10.1111/cpr.13187

Jin F., Leitich J. & Sonntag C.V. (1993). The superoxide radical reacts with tyrosine-derived phenoxyl radicals by addition rather than by electron transfer. *Journal of The Chemical Society-perkin Transactions 1*, 1583-1588.

Kang S., Kahan S., McDermott J., Flann N., & Shmulevich I. (2014). Biocellion: accelerating computer simulation of multicellular biological system models. *Bioinformatics (Oxford, England)*, *30*(21), 3101–3108. https://doi.org/10.1093/bioinformatics/btu498

Karamitros M., Mantero A., Incerti S., Friedland W., Baldacchino G., Barberet P., Bernal M., Capra R., Champion C., El Bitar Z., Francis Z., Guèye P., Ivanchenko A., Ivanchenko V., Kurashige H., Mascialino B., Moretto P., Mieminen P., Santin G., Seznec H., Tran H.N., Villagrasa C. & Zacharatou C. (2011) Modeling Radiation Chemistry and Biology in the Geant4 Toolkit. Progress in NUCLEAR SCIENCE and TECHNOLOGY, Vol. 2, pp.503-508

Kohn K.W. (1999). Molecular interaction map of the mammalian cell cycle control and DNA repair systems. *Molecular biology of the cell*, *10*(8), 2703–2734. https://doi.org/10.1091/mbc.10.8.2703

Kreipl M.S., Friedland W. & Paretzke H.G. (2009). Time- and space-resolved Monte Carlo study of water radiolysis for photon, electron and ion irradiation. *Radiation and environmental biophysics*, *48*(1), 11–20. https://doi.org/10.1007/s00411-008-0194-8

Kutcher G.J. & Green A.E.S. (1976). A Model for Energy Deposition in Liquid Water. *Radiation Research*, *67*(3), 408–425. https://doi.org/10.2307/3574338

Labarbe R., Hotoiu L., Barbier J. & Favaudon V. (2020). A physicochemical model of reaction kinetics supports peroxyl radical recombination as the main determinant of the FLASH effect. *Radiotherapy and oncology : journal of the European Society for Therapeutic Radiology and Oncology*, *153*, 303–310. https://doi.org/10.1016/j.radonc.2020.06.001

Lahalle A., Lacroix M., De Blasio C., Cissé M.Y., Linares L.K. & Le Cam L. (2021). The p53 Pathway and Metabolism: The Tree That Hides the Forest. *Cancers*, *13*(1), 133. https://doi.org/10.3390/cancers13010133

Lampe N., Karamitros M., Breton V., Brown J.M.C., Sakata D., Sarramia D. & Incerti S. (2018). Mechanistic DNA damage simulations in Geant4-DNA Part 2: Electron and proton damage in a bacterial cell, Physica Medica, Volume 48, 2018, Pages 146-155, ISSN 1120-1797, https://doi.org/10.1016/j.ejmp.2017.12.008.

Lee J.H. & Paull T.T. (2005). ATM activation by DNA double-strand breaks through the Mre11-Rad50-Nbs1 complex. *Science (New York, N.Y.)*, *308*(5721), 551–554. https://doi.org/10.1126/science.1108297

Ling C.C., Michaels H B., Epp E.R. & Peterson E.C. (1978). Oxygen diffusion into mammalian cells following ultrahigh dose rate irradiation and lifetime estimates of oxygen-sensitive species. *Radiation research*, *76*(3), 522–532.

Liu R. (2017). *Integrated Spatial and Temporal Stochastic Model in Radiation Biology : Design, Implementation, and Application.* : Oregon State University.

Liu R., Higley K.A., Swat M.H., Chaplain M.A.J., Powathil G.G. & Glazier J.A. (2021). Development of a coupled simulation toolkit for computational radiation biology based on Geant4 and CompuCell3D. *Physics in medicine and biology*, *66*(4), 045026. https://doi.org/10.1088/1361-6560/abd4f9

Luke D.A. & Stamatakis K.A. (2012). Systems science methods in public health: dynamics, networks, and agents. *Annual review of public health*, *33*, 357–376. https://doi.org/10.1146/annurev-publhealth-031210-101222

Mark F., Becker U., Herak J.N., & Schulte-Frohlinde D. (1989). Radiolysis of DNA in aqueous solution in the presence of a scavenger: a kinetic model based on a nonhomogeneous reaction of OH radicals with DNA molecules of spherical or cylindrical shape. *Radiation and environmental biophysics*, *28*(2), 81–99. https://doi.org/10.1007/BF01210293

McMahon S J. & Prise K.M. (2019). Mechanistic Modelling of Radiation Responses. *Cancers*, *11*(2), 205. https://doi.org/10.3390/cancers11020205

Meesungnoen J. & Jay-Gerin J.P. (2005). High-LET radiolysis of liquid water with 1H+, 4He2+, 12C6+, and 20Ne9+ ions: effects of multiple ionization. *The journal of physical chemistry. A*, *109*(29), 6406–6419. https://doi.org/10.1021/jp058037z

Meylan S., Incerti S., Karamitros M., Tang N., Bueno M., Clairand I. & Villagrasa C. (2017). Simulation of early DNA damage after the irradiation of a fibroblast cell nucleus using Geant4-DNA. *Scientific reports*, *7*(1), 11923. https://doi.org/10.1038/s41598-017-11851-4

Michaels H.B. & Hunt J.W. (1973). Reactions of the Hydroxyl Radical with Polynucleotides. *Radiation Research*, *56*(1), 57–70. https://doi.org/10.2307/3573791

Michaels H.B. & Hunt J.W. (1977). Reaction of Oxygen with Radiation-Induced Free Radicals on Single-Stranded Polynucleotides. *Radiation Research*, *72*(1), 18–31. https://doi.org/10.2307/3574553

Michaels H.B. & Hunt J.W. (1978). Model for radiation damage in cells by direct effect and by indirect effect: a radiation chemistry approach. Radiation Research, 74(1), 23-34.

Milligan J.R., Aguilera J.A. & Ward J.F. (1993). Variation of single-strand break yield with scavenger concentration for plasmid DNA irradiated in aqueous solution. Radiation Research, 133(2), 151–157. 10.2307/3578350

Milligan J.R., Arnold A.D. & Ward J.F. (1992). The effect of superhelical density on the yield of single-strand breaks in γ-irradiated plasmid DNA. Radiation Research, 132(1), 69–73. 10.2307/3578335

Milligan J.R., Wu C.C.L., Ng J.Y-Y., Aguilera J.A. & Ward J.F. (1996). Characterization of the Reaction Rate Coefficient of DNA with the Hydroxyl Radical. Radiation Research, 146(5), 510. 10.2307/3579551

Mohammad N., Talton L., Dalgan S., Hetzler Z., Steksova A. & Wei Q. (2024). Ratiometric nonfluorescent CRISPR assay utilizing Cas12a-induced plasmid supercoil relaxation. *Communications chemistry*, *7*(1), 130. https://doi.org/10.1038/s42004-024-01214-2

Montay-Gruel P., Acharya M.M., Petersson K., Alikhani L., Yakkala C., Allen B.D., Ollivier J., Petit B., Jorge P.G., Syage A.R., Nguyen T. A., Baddour A.A.D., Lu C., Singh P., Moeckli R., Bochud F., Germond J.F., Froidevaux P., Bailat C., Bourhis J., Vozenin M.C. & Limoli C.L. (2019). Long-term neurocognitive benefits of FLASH radiotherapy driven by reduced reactive oxygen species. *Proceedings of the National Academy of Sciences of the United States of America*, *116*(22), 10943–10951. https://doi.org/10.1073/pnas.1901777116

Murthy S.S., Trapani D., Cao B., Bray F., Murthy S., Kingham T.P., Are C. & Ilbawi A.M. (2024). Premature mortality trends in 183 countries by cancer type, sex, WHO region, and World Bank income level in 2000-19: a retrospective, cross-sectional, population-based study. The Lancet. Oncology, S1470-2045(24)00274-2. Advance online publication. https://doi.org/10.1016/S1470-2045(24)00274-2

National Center for Biotechnology Information (2024). PubChem Compound Summary for CID 6131, 5'-Cytidylic acid. (Retrieved October 24, 2024) from https://pubchem.ncbi.nlm.nih.gov/compound/5_-Cytidylic-acid.

Nauser T., Koppenol W.H. & Gebicki J.M. (2005). The kinetics of oxidation of GSH by protein radicals. *The Biochemical journal*, *392*(Pt 3), 693–701. https://doi.org/10.1042/BJ20050539

Neal J.A., Dang V., Douglas P., Wold M.S., Lees-Miller S.P. & Meek K. (2011). Inhibition of homologous recombination by DNA-dependent protein kinase requires kinase activity, is titratable, and is modulated by autophosphorylation. *Molecular and cellular biology*, *31*(8), 1719–1733. https://doi.org/10.1128/MCB.01298-10

Nestler E.J. & Greengard P. (1999) Protein Phosphorylation is of Fundamental Importance in Biological Regulation. In: Siegel GJ, Agranoff BW, Albers RW, et al., editors. Basic Neurochemistry: Molecular, Cellular and Medical Aspects. 6th edition. Philadelphia: Lippincott-Raven; 1999. Available from: https://www.ncbi.nlm.nih.gov/books/NBK28063/

Niki E. (2021). Lipid oxidation that is, and is not, inhibited by vitamin E: Consideration about physiological functions of vitamin E. *Free radical biology & medicine*, *176*, 1–15. https://doi.org/10.1016/j.freeradbiomed.2021.09.001

Nikjoo H., Emfietzoglou D., Liamsuwan T., Taleei R., Liljequist D. & Uehara S. (2016). Radiation track, DNA damage and response-a review. *Reports on progress in physics. Physical Society (Great Britain)*, *79*(11), 116601. https://doi.org/10.1088/0034-4885/79/11/116601

Nikjoo H., O'Neill P., Goodhead D.T. & Terrissol M. (1997). Computational modelling of low-energy electron-induced DNA damage by early physical and chemical events. *International journal of radiation biology*, *71*(5), 467–483. https://doi.org/10.1080/095530097143798

Nikjoo H., Uehara S. & Emfietzoglou D. (2012). Interaction of Radiation with Matter (1st ed.). CRC Press. https://doi.org/10.1201/b12109

O'Neill P. (1983). Pulse Radiolytic Study of the Interaction of Thiols and Ascorbate with OH Adducts of dGMP and dG: Implications for DNA Repair Processes. *Radiation Research*, *96*(1), 198–210. https://doi.org/10.2307/3576178

Oei A.L., Vriend L.E., Crezee J., Franken N.A. & Krawczyk P.M. (2015). Effects of hyperthermia on DNA repair pathways: one treatment to inhibit them all. *Radiation oncology (London, England)*, *10*, 165. https://doi.org/10.1186/s13014-015-0462-0

Oh J.M. & Myung K. (2022). Crosstalk between different DNA repair pathways for DNA double strand break repairs. *Mutation research. Genetic toxicology and environmental mutagenesis*, *873*, 503438. https://doi.org/10.1016/j.mrgentox.2021.503438

Pastina B. & LaVerne J.A. (2021) *The Journal of Physical Chemistry A*. *105* (40), 9316-9322 DOI: 10.1021/jp012245j

Paull T. T. (2015). Mechanisms of ATM Activation. *Annual review of biochemistry*, *84*, 711–738. https://doi.org/10.1146/annurev-biochem-060614-034335

Perl J., Shin J., Schumann J., Faddegon B. & Paganetti H. (2012). TOPAS: an innovative proton Monte Carlo platform for research and clinical applications. *Medical physics*, *39*(11), 6818–6837. https://doi.org/10.1118/1.4758060

Perricone C., De Carolis C. & Perricone R. (2009) Glutathione: A key player in autoimmunity, Autoimmunity Reviews, Volume 8, Issue 8, 2009, Pages 697-701, ISSN 1568-9972, https://doi.org/10.1016/j.autrev.2009.02.020.

Pfeiffer P., Goedecke W. & Obe G. (2000). Mechanisms of DNA double-strand break repair and their potential to induce chromosomal aberrations. *Mutagenesis*, *15*(4), 289–302. https://doi.org/10.1093/mutage/15.4.289

Plante I (2011). A Monte-Carlo step-by-step simulation code of the non-homogeneous chemistry of the radiolysis of water and aqueous solutions. Part I: Theoretical framework and implementation. Radiation and Environmental Biophysics, 50(3), 389–403. 10.1007/s00411-011-0367-8

Plante I. & Devroye L. (2017). Considerations for the independent reaction times and step-by-step methods for radiation chemistry simulations, Radiation Physics and Chemistry, Volume 139, 2017, Pages 157-172, ISSN 0969-806X, https://doi.org/10.1016/j.radphyschem.2017.03.021.

Plante I. (2016) Calculation of the second term of the exact Green's function of the diffusion equation for diffusion-controlled chemical reactions, Computer Physics Communications, Volume 198, 2016, Pages 41-46, ISSN 0010-4655, https://doi.org/10.1016/j.cpc.2015.09.001.

Plante I. (2021). A review of simulation codes and approaches for radiation chemistry. *Physics in medicine and biology*, *66*(3), 03TR02. https://doi.org/10.1088/1361-6560/abbd19

Plante I., Ponomarev A., Patel Z., Slaba T. & Hada M. (2019). RITCARD: Radiation-Induced Tracks, Chromosome Aberrations, Repair and Damage. *Radiation research*, *192*(3), 282–298. https://doi.org/10.1667/RR15250.1

Pogozelski W.K. & Tullius T.D. (1998). Oxidative Strand Scission of Nucleic Acids: Routes Initiated by Hydrogen Abstraction from the Sugar Moiety. *Chemical reviews*, *98*(3), 1089–1108. https://doi.org/10.1021/cr960437i

Poignant F., Plante I., Patel Z.S., Huff J.L. & Slaba T.C. (2022). Geometrical Properties of the Nucleus and Chromosome Intermingling Are Possible Major Parameters of Chromosome Aberration Formation. *International journal of molecular sciences*, *23*(15), 8638. https://doi.org/10.3390/ijms23158638

Porter A. & Jänicke R. (1999) Emerging roles of caspase-3 in apoptosis. *Cell Death Differ* **6**, 99–104. https://doi.org/10.1038/sj.cdd.4400476

Potts R.B. (1952). Some Generalized Order-Disorder Transformations. Mathematical Proceedings of the Cambridge Philosophical Society, 48, 106-109.https://doi.org/10.1017/S0305004100027419

Prager G.W., Braga S., Bystricky B., Qvortrup C., Criscitiello C., Esin E., Sonke G.S., Martínez G.A., Frenel J.S., Karamouzis M., Strijbos M., Yazici O., Bossi P., Banerjee S., Troiani T., Eniu A., Ciardiello F., Tabernero J., Zielinski C.C., Casali P.G., … Ilbawi A. (2018). Global cancer control: responding to the growing burden, rising costs and inequalities in access. *ESMO open*, *3*(2), e000285. https://doi.org/10.1136/esmoopen-2017-000285

Pramanik D., Jolly M.K. & Bhat R. (2021). Matrix adhesion and remodeling diversifies modes of cancer invasion across spatial scales. *Journal of theoretical biology*, *524*, 110733. https://doi.org/10.1016/j.jtbi.2021.110733

Raldow A.C., Chen A.B., Russell M., Lee P.P., Hong T.S., Ryan D.P., Cusack J.C. & Wo J.Y. (2019). Cost-effectiveness of Short-Course Radiation Therapy vs Long-Course Chemoradiation for Locally Advanced Rectal Cancer. *JAMA network open*, *2*(4), e192249. https://doi.org/10.1001/jamanetworkopen.2019.2249

Ramos-Méndez J., Domínguez-Kondo N., Schuemann J., McNamara A., Moreno-Barbosa E. & Faddegon B. (2020). LET-Dependent Intertrack Yields in Proton Irradiation at Ultra-High Dose Rates Relevant for FLASH Therapy. *Radiation research*, *194*(4), 351–362. https://doi.org/10.1667/RADE-20-00084.1

Ramos-Méndez J., García-García O., Domínguez-Kondo J., LaVerne J.A., Schuemann J., Moreno-Barbosa E., & Faddegon B. (2022). TOPAS-nBio simulation of temperature-dependent indirect DNA strand break yields. *Physics in medicine and biology*, *67*(14), 10.1088/1361-6560/ac79f9. https://doi.org/10.1088/1361-6560/ac79f9

Ramos-Méndez J., Perl J., Schuemann J., McNamara A., Paganetti H. & Faddegon B. (2018). Monte Carlo simulation of chemistry following radiolysis with TOPAS-nBio. *Physics in medicine and biology*, *63*(10), 105014. https://doi.org/10.1088/1361-6560/aac04c

Rehman I., Gulani A., Farooq M. & Simpson B. (2023). Genetics, Mitosis. In *StatPearls*. StatPearls Publishing.

Reynolds P., Anderson J.A., Harper J.V., Hill M.A., Botchway S.W., Parker A.W. & O'Neill P. (2012). The dynamics of Ku70/80 and DNA-PKcs at DSBs induced by ionizing radiation is dependent on the complexity of damage. *Nucleic acids research*, *40*(21), 10821–10831. https://doi.org/10.1093/nar/gks879

Rice S.A. (1985) Comprehensive chemical kinetics, vol 25 (diffusion limited reactions). Elsevier, Amsterdam

Roth, O., & LaVerne, J. A. (2011). Effect of pH on H2O2 production in the radiolysis of water. *The journal of physical chemistry. A*, *115*(5), 700–708. https://doi.org/10.1021/jp1099927

Rothkamm K. & Löbrich M. (2003). Evidence for a lack of DNA double-strand break repair in human cells exposed to very low x-ray doses. *Proceedings of the National Academy of Sciences of the United States of America*, *100*(9), 5057–5062. https://doi.org/10.1073/pnas.0830918100

Rudek B., McNamara A., Ramos-Méndez J., Byrne H., Kuncic Z. & Schuemann J. (2019). Radio-enhancement by gold nanoparticles and their impact on water radiolysis for x-ray, proton and carbon-ion beams. *Physics in medicine and biology*, *64*(17), 175005. https://doi.org/10.1088/1361-6560/ab314c

Ruff S.E., Logan S.K., Garabedian M.J. & Huang T.T. (2020). Roles for MDC1 in cancer development and treatment. *DNA repair*, *95*, 102948. https://doi.org/10.1016/j.dnarep.2020.102948

Sakata D., Belov O., Bordage M.C., Emfietzoglou D., Guatelli S., Inaniwa T., Ivanchenko V., Karamitros M., Kyriakou I., Lampe N., Petrovic I., Ristic-Fira A., Shin W.G. & Incerti S. (2020). Fully integrated Monte Carlo simulation for evaluating radiation induced DNA damage and subsequent repair using Geant4-DNA. *Scientific reports*, *10*(1), 20788. https://doi.org/10.1038/s41598-020-75982-x

Sanche L. (2008). Low Energy Electron Damage To DNA. In: Shukla, M.K., Leszczynski, J. (eds) Radiation Induced Molecular Phenomena in Nucleic Acids. Challenges and Advances In Computational Chemistry and Physics, vol 5. Springer, Dordrecht. https://doi.org/10.1007/978-1-4020-8184-2_19

Saunders N. & Miodownik A.P. (1998 Editors) Chapter 3 - Basic Thermodynamics, Pergamon Materials Series, Pergamon, Volume 1, 1998, Pages 33-57, ISSN 1470-1804, ISBN 9780080421292, https://doi.org/10.1016/S1470-1804(98)80023-0. (https://www.sciencedirect.com/science/article/pii/S1470180498800230)

Schuemann J., McNamara A.L., Ramos-Méndez J., Perl J., Held K.D., Paganetti H., Incerti S. & Faddegon B. (2019). TOPAS-nBio: An Extension to the TOPAS Simulation Toolkit for Cellular and Sub-cellular Radiobiology. *Radiation research*, *191*(2), 125–138. https://doi.org/10.1667/RR15226.1

Schulte-Frohlinde D. & Bothe E. (1990). Determination of the constants of the Alper formula for single-strand breaks from kinetic measurements on DNA in aqueous solution and comparison with data from cells. *International journal of radiation biology*, *58*(4), 603–611. https://doi.org/10.1080/09553009014551961

Scully R., Panday A., Elango R. & Willis N.A. (2019). DNA double-strand break repair-pathway choice in somatic mammalian cells. *Nature reviews. Molecular cell biology*, *20*(11), 698–714. https://doi.org/10.1038/s41580-019-0152-0

Šefl M., Incerti S., Papamichael G. & Emfietzoglou D. (2015). Calculation of cellular S-values using Geant4-DNA: The effect of cell geometry. *Applied radiation and isotopes : including data, instrumentation and methods for use in agriculture, industry and medicine*, *104*, 113–123. https://doi.org/10.1016/j.apradiso.2015.06.027

Shen J., Griffiths P.T., Campbell S.J., Utinger B., Kalberer M. & Paulson S E. (2021). Ascorbate oxidation by iron, copper and reactive oxygen species: review, model development, and derivation of key rate constants. *Scientific reports*, *11*(1), 7417. https://doi.org/10.1038/s41598-021-86477-8

Shibata A., & Jeggo P.A. (2021). ATM's Role in the Repair of DNA Double-Strand Breaks. *Genes*, *12*(9), 1370. https://doi.org/10.3390/genes12091370

Shin W-G., D-Kondo J.N., Ramos-Méndez J., LaVerne J.A., Rothwell B., Bertolet A., McNamara A., Faddegon B., Paganetti H. & Schuemann J. (2025) Investigation of hydrogen peroxide yields and oxygen consumption in high dose rate irradiation: a TOPAS-nBio Monte Carlo study Phys. Med. Biol. 70 015012

Shin W-G., Sakata D., Lampe N., Belov O., Tran N.H., Petrovic I., Ristic-Fira A., Dordevic M., Bernal M.A., Bordage M-C., Francis Z., Kyriakou I., Perrot Y., Sasaki T., Villagrasa C., Guatelli S., Breton V., Emfietzoglou D. & Incerti S.(2021). A Geant4-DNA Evaluation of Radiation-Induced DNA Damage on a Human Fibroblast. Cancers. 2021; 13(19):4940. https://doi.org/10.3390/cancers13194940

Shirinifard A., Gens J.S., Zaitlen B.L., Popławski N.J., Swat M. & Glazier J.A. (2009). 3D multi-cell simulation of tumor growth and angiogenesis. *PloS one*, *4*(10), e7190. https://doi.org/10.1371/journal.pone.0007190

Sinclair W.K. & Morton R.A. (1966). X-ray sensitivity during the cell generation cycle of cultured Chinese hamster cells. *Radiation research*, *29*(3), 450–474.

Somogyi E.T., Bouteiller J.M. Glazier J.A., Konig M., Medley J.K., Swat M.H. & Sauro H.M. (2015). libRoadRunner: A high performance SBML simulation and analysis library. Bioinformatics, 31, 3315‑3321, https://doi.org/10.1093/bioinformatics/btv363

Spinks J.W.T. & Woods R.J. (1990). An Introduction to Radiation Chemistry 3rd edn (New York: Wiley)

Stewart R. D. (2001). Two-lesion kinetic model of double-strand break rejoining and cell killing. *Radiation research*, *156*(4), 365–378. https://doi.org/10.1667/0033-7587(2001)156[0365:tlkmod]2.0.co;2

Stewart R.D., Yu V. K., Georgakilas A.G., Koumenis C., Park J.H. & Carlson D.J. (2011). Effects of radiation quality and oxygen on clustered DNA lesions and cell death. *Radiation research*, *176*(5), 587–602. https://doi.org/10.1667/rr2663.1

Stucki M., & Jackson S.P. (2006). gammaH2AX and MDC1: anchoring the DNA-damage-response machinery to broken chromosomes. *DNA repair*, *5*(5), 534–543. https://doi.org/10.1016/j.dnarep.2006.01.012

Sung H., Ferlay J., Siegel R.L., Laversanne M., Soerjomataram I., Jemal A., & Bray F. (2021). Global Cancer Statistics 2020: GLOBOCAN Estimates of Incidence and Mortality Worldwide for 36 Cancers in 185 Countries. *CA: a cancer journal for clinicians*, *71*(3), 209–249. https://doi.org/10.3322/caac.21660

Swat M.H., Belmonte J., Heiland R.W., Zaitlen B.L., Glazier J.A. & Shirinifard A. (2014) CompuCell3D Reference Manual Version 3.7.4. Available online: https://compucell3d.org/BinDoc/cc3d_binaries/Manuals/PythonScriptingManual_v.3.7.4.pdf (accessed on 15 November 2023).

Swat M.H., Thomas G.L., Belmonte J.M., Shirinifard A., Hmeljak D. & Glazier J.A. (2012). Multi-scale modeling of tissues using CompuCell3D. *Methods in cell biology*, *110*, 325–366. https://doi.org/10.1016/B978-0-12-388403-9.00013-8

Taucher-Scholz G. & Kraft G. (1999). Influence of radiation quality on the yield of DNA strand breaks in SV40 DNA irradiated in solution. *Radiation research*, *151*(5), 595–604.

Thibaut Y., Gonon G., Martinez J.S., Petit M., Vaurijoux A., Gruel G., Villagrasa C., Incerti S. & Perrot Y. (2023). MINAS TIRITH: A new tool for simulating radiation-induced DNA damage at the cell population level. Phys. Med. Biol. 2023, 68, 034002.

Tomita H., Kai M., Kusama T. & Ito A. (1998). Monte Carlo simulation of DNA strand-break induction in supercoiled plasmid pBR322 DNA from indirect effects. Radiation and Environmental Biophysics, 36(4), 235–241. 10.1007/s004110050077

Tomita H., Kai Y., & Kusama A.T. (1995). Strand Break Formation in Plasmid DNA Irradiated in Aqueous Solution: Effect of Medium Temperature and Hydroxyl Radical Scavenger Concentration. Radiat. Res, 36, 46–55.

Tran H.N., Chappuis F., Incerti S., Bochud F. & Desorgher L. (2021). Geant4-DNA Modeling of Water Radiolysis beyond the Microsecond: An On-Lattice Stochastic Approach. *International journal of molecular sciences*, *22*(11), 6023. https://doi.org/10.3390/ijms22116023

Tran H.N., Ramos-Méndez J., Shin W.G., Perrot Y., Faddegon B., Okada S., Karamitros M., Davídková M., Štěpán V., Incerti S. & Villagrasa C. (2021). Assessment of DNA damage with an adapted independent reaction time approach implemented in Geant4-DNA for the simulation of diffusion-controlled reactions between radio-induced reactive species and a chromatin fiber. *Medical physics*, *48*(2), 890–901. https://doi.org/10.1002/mp.14612

Tsabar M., Mock C.S., Venkatachalam V., Reyes J., Karhohs K.W., Oliver T.G., Regev A., Jambhekar A. & Lahav G. (2020). A Switch in p53 Dynamics Marks Cells That Escape from DSB-Induced Cell Cycle Arrest. *Cell reports*, *32*(5), 107995. https://doi.org/10.1016/j.celrep.2020.107995

van Zon J.S. & ten Wolde P.R. (2005). Green's-function reaction dynamics: a particle-based approach for simulating biochemical networks in time and space. *The Journal of chemical physics*, *123*(23), 234910. https://doi.org/10.1063/1.2137716

Wakisaka Y., Minami K., Okada N., Tsubouchi T., Hamatani N., Yagi M., Takashina M. & Kanai T. (2023). Treatment planning of carbon ion radiotherapy for prostate cancer based on cellular experiments with PC3 human prostate cancer cells. *Physica medica : PM : an international journal devoted to the applications of physics to medicine and biology : official journal of the Italian Association of Biomedical Physics (AIFB)*, *107*, 102537. https://doi.org/10.1016/j.ejmp.2023.102537

Wang D. & Farhana A. (2023). Biochemistry, RNA Structure. In *StatPearls*. StatPearls Publishing.

Wang H., Guo M., Wei H. & Chen Y. (2023). Targeting p53 pathways: mechanisms, structures, and advances in therapy. *Signal transduction and targeted therapy*, *8*(1), 92. https://doi.org/10.1038/s41392-023-01347-1

Wang P., Wang H.Y., Gao X.J., Zhu H.X., Zhang X.P., Liu F. & Wang W. (2023). Encoding and Decoding of p53 Dynamics in Cellular Response to Stresses. *Cells*, *12*(3), 490. https://doi.org/10.3390/cells12030490

Wardman P. (1999). Thiyl radicals in biology: their role as a 'molecular switch' central to cellular oxidative stress. In Alfassi, Z. B. (Eds.), *S-centered radicals*. (1st ed., pp. 289-309). Wiley.

Wardman P. (2020). Radiotherapy using high-intensity pulsed radiation beams (FLASH): a radiation-chemical perspective Radiat. Res. 194607–17

Warmenhoven J.W., Henthorn N.T., Ingram S.P., Chadwick A.L., Sotiropoulos M., Korabel N., Fedotov S., Mackay R.I., Kirkby K.J. & Merchant M.J. (2020). Insights into the non-homologous end joining pathway and double strand break end mobility provided by mechanistic in silico modelling. *DNA repair*, *85*, 102743.

Wilson J.D., Hammond E.M., Higgins G.S. & Petersson K. (2020). Ultra-High Dose Rate (FLASH) Radiotherapy: Silver Bullet or Fool's Gold?. *Frontiers in oncology*, *9*, 1563. https://doi.org/10.3389/fonc.2019.01563

World Health Organization (2024, September 14) Cancer https://www.who.int/es/news-room/fact-sheets/detail/cancer

Wu M., Ye H., Tang Z., Shao C., Lu G., Chen B., Yang Y. & Wang G. (2017). p53 dynamics orchestrates with binding affinity to target genes for cell fate decision. *Cell Death Dis* **8**, e3130. https://doi.org/10.1038/cddis.2017.492

Yin H., Xu L. & Porter N.A. (2011). Free radical lipid peroxidation: mechanisms and analysis. *Chemical reviews*, *111*(10), 5944–5972. https://doi.org/10.1021/cr200084z

Zhang T., Brazhnik P. & Tyson J.J. (2007). Exploring mechanisms of the DNA-damage response: p53 pulses and their possible relevance to apoptosis. *Cell cycle (Georgetown, Tex.)*, *6*(1), 85–94. https://doi.org/10.4161/cc.6.1.3705

Zhang X., Zhang N., Schuchmann H.P. & von Sonntag C. (1994) Pulse Radiolysis of 2-Mercaptoethanol in Oxygenated Aqueous Solution. Generation and Reactions of the Thiylperoxyl Radical. *The Journal of Physical Chemistry* **1994** *98* (26), 6541-6547. DOI: 10.1021/j100077a020

Zhang X.P., Liu F. & Wang W. (2011). Two-phase dynamics of p53 in the DNA damage response. *Proceedings of the National Academy of Sciences of the United States of America*, *108*(22), 8990–8995. https://doi.org/10.1073/pnas.1100600108

Zhang X.P., Liu F. & Wang W. (2011). Two-phase dynamics of p53 in the DNA damage response. *Proceedings of the National Academy of Sciences of the United States of America*, *108*(22), 8990–8995. https://doi.org/10.1073/pnas.1100600108

Zhao M., Wang Y., Zhao Y., He S., Zhao R., Song Y., Cheng J., Gong Y., Xie J., Wang Y., Hu B., Tian L. & Huang Q. (2020). Caspase-3 knockout attenuates radiation-induced tumor repopulation via impairing the ATM/p53/Cox-2/PGE_2 pathway in non-small cell lung cancer. *Aging*, *12*(21), 21758–21776. https://doi.org/10.18632/aging.103984